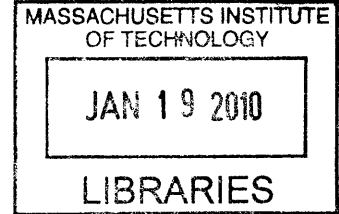# New Paradigm to Design Micro and Nano-Patterned Membranes.

By

Damien Eggenspieler

Ingénieur de l'Ecole Polytechnique
Ecole Polytechnique, France, 2008

Submitted to the Department of Mechanical Engineering
in partial fulfillment of the requirements for the degree of

MASTER OF SCIENCE IN MECHANICAL ENGINEERING
at the
MASSACHUSETTS INSTITUTE OF TECHNOLOGY
JUNE 2010
© Massachusetts Institute of Technology 2010. All rights reserved.

Author . . . .
Department of Mechanical Engineering
May 18th, 2010

Certified by . . . .
Mary C. Boyce
Gail E. Kendall Professor of Mechanical Engineering
Thesis Supervisor

Accepted by . . . .
David Hardt
Chairman, Department Committee on Graduate Students

New Paradigm to Design Micro and Nano-Patterned Membranes.

By

Damien Eggenspieler

Submitted to the Department of Mechanical Engineering
on May 18th, 2010, in partial fulfillment
of the requirements for the degree of
MASTER OF SCIENCE IN MECHANICAL ENGINEERING

Abstract

Access to drinking water is a growing issue and one of the key challenging of the twenty first century. The rapid depletion of current supply sources (aquifers, rivers, lake...) urges to find solutions, especially cost and energy efficient processes to desalinate seawater.

Reverse osmosis is a membrane process for purification of seawater, invented in 1940's, which has evolved ever since, to become nowadays the most efficient process for desalination. We discuss the shortcomings of this technology, and identify bio-fouling to be the main cause of irreversibility (thus costs) in this process. After observation of solutions developed by Nature to deter bio-fouling (especially for marine species), surface micro-topography and chemistry have been identified as the two effective anti-fouling strategies.

We introduce a brand new technology to create micro- and nano-patterned surfaces that is compatible with a wide variety of chemical compounds. A proof of concept is introduced with the first prototypes of wrinkled surfaces created with Initiated Chemical Vapor Deposition; Stiff polymeric coatings form wrinkles when deposited on pre-stretched soft elastomeric substrates. We are showing, both theoretically and experimentally, that the characteristics of these wrinkles can be tuned very easily.

Mimicking Nature requires creating more complicated micro-topographies than the sinusoid-like pattern obtained with uniform coatings and substrates. We are showing with a numerical model that local stiffening of the substrate can be used to direct and control the buckling of the coating. In order to gain the full control of this design strategy, an inverse method is needed to establish how to treat the substrate in order to obtain a desired micro-topography. We set up the foundations of this inverse mechanical model, and develop an algorithm for a simple case.

Thesis Supervisor: Mary C. Boyce
Title: Gail E. Kendall Professor of Mechanical Engineering

TABLE OF CONTENTS

ACKNOWLEDGMENTS

First, I would like to thank my advisor, prof. Boyce. Your attention to details, your capacity to transform ideas into great ideas as well as your ability to understand and analyze any problem instantaneously keep amazing me. Committed to excellence, respectful and visionary, always in search of innovative ideas and meaningful questions to tackle you really embodied my vision of MIT.

I would also like to thank the people who help me to come at MIT, and provided me with this great opportunity to discover this wonderful working environment, where passion and hard-work combine to create meaningful innovations. Prof. Salençon, Molinari, Guest, I am really thankful and pleased to have been your student. Chiara, I cannot be grateful enough, for the few months I spent working for you at CalTech. Your boundless passion and enthusiasm, the content of your character are truly inspiring.

I am also thankful to all my labmates and coworkers for their advice and support, especially to Gozde and Renaud, as well as all the people who contributed to making the past two years at MIT really enjoyable; Una, Laure-Anne.

But I guess my experience at MIT would have been tasteless without my friends and family. Across Atlantic, friends who experienced the "Pura-Vida" and roommates, I feel truly blessed to know you, and have lived those years with you! Tite-Mum, dad, Flo & Alice… you are beyond all expectations. I could not have been luckier and cannot dream of a more perfect family.

INTRODUCTION

More than 1 billion people lack access to a drinking water supply. Between 1.3 and 1.8 million people died due to water related diseases in 2001(1). The list of the impact of water scarcity and lack of drinking water on health, established by the UNESCO is daunting. But most importantly water scarcity has been a growing problem. Based on the latest available population and freshwater data, somewhere between 2.4 billion and 3.2 billion people may be living in either water-scarce or water-stressed conditions by 2025, depending on future rates of growth, compared to 505 million people in the year 2000 (2).

In this context, and with the always improving technologies to treat water, desalination plants have gained a huge interest in the past few decades. From 225 in 1953, the number of installed desalination plants has reached 15000 in 2002, for a total desalination capacity of 32 million m^3/day (3) in 125 countries. Seawater desalination accounts for some 59% of those plants, and the Middle East region or 49% of the worldwide capacity. Achieving low costs with small energy footprint, membrane desalination and more specifically reverse osmosis is growing at a fast pace and accounts for most of the new installed capacities. Benefiting from the very active domain of nano-materials and membrane science, reverse osmosis is definitely a very promising technology.

This work is the result of a two-year study of this technology. We have carried out meticulous research on reverse osmosis to understand the full environment of the reverse osmosis membrane. While some major drawbacks seemed out of our reach for the moment (e.g. capital costs, possibility to scale down plants), we have identified bio-fouling on the membrane as a major transverse problem, which not only affects the membrane but the whole plant design (pretreatment, membrane operations, disposal of the rejection stream) and the overall desalination costs. To overcome bio-fouling, Nature has provided every seawater macro-organisms with different anti-fouling strategies. While some of them are active mechanisms (e.g. secretion of an antimicrobial epidermal substance by Dolphins, grooming of epibiosis by other macro-species) and seem difficult to adapt to the current technology, we are showing that the control of surface topography is an efficient passive anti-fouling strategy (e.g. used in mussel shells or shark skin) that might be applied to reverse osmosis with only slight modifications to the current manufacturing of membranes. Chapter II offers an introduction to the wrinkling of stiff coating on compliant substrate, with first experimental and numerical results. Chapter III goes one step further and proposed a new paradigm for designing any desired micro-patterned membranes.

Chapter I: Review of reverse osmosis operation and definition of relevant failure modes to be addressed

A. CONTENT

B.   Introduction

Two types of processes are competing for high salinity water treatment: thermal distillation and membrane treatment. More energy intensive, thermal processes encompass MSF (Multi stage Flash) and MED (Multi Effect Distillation). Despite its poor energy efficiency, MSF still accounts for most of the thermal capacity in the Middle East region, due to the advantageous cost of energy compared to the cost of electricity in this area. Going through a set of pressure vessels at lower and lower pressure, a preheated stream of feed water is flashed and the vapor is condensed into a clean distillate water stream. On the other side, in a MED (Multi-Effect Distillation), water is evaporated through tanks at higher and higher temperature as the brine stream gets more and more concentrated. The distillate of each effect is condensed into a clean water stream. These two technologies have similar advantages: a tolerance to high salinity and can operate with a source of energy other than electricity (e.g., cogeneration, oil). Capital investment is pretty high especially to provide non-corrosive material working at high temperature and high salinity, and both energy requirements and final desalination cost (MED: 1.15 $/$m^3$ MSF: 1.10 $/$m^3$) tend to be higher than the cost of RO (.82 $/$m^3$). This is why we have chosen to work on reverse osmosis.

The first chapter is organized as a review aiming at understanding the full environment of reverse osmosis technology, from the full operation of an RO plant to membrane permeation modeling and membrane manufacturing. This rather short summary of RO systems operation allows us to identify the main "failure mode" of these systems, bio-fouling, as well as the "relevant parameters" for innovation.

We then introduce an innovative solution for membrane manufacturing in the subsequent chapters of this thesis.

C. Engineering consideration in Reverse osmosis

A reverse osmosis (RO) plant divides a feed water stream into two streams, one with a lower concentration in salt and impurities, the permeate, and another with higher concentration, the concentrate or concentrated brine stream.

The function of salt removal is performed by a polymeric membrane. This thesis aims at improving current design and manufacturing of this membrane itself. Before focusing on the membrane itself, the first section of this work describes all the stages of a reverse osmosis plant, in order to study the environment, and define the major failure modes of these polymeric membranes.

1. From the intake to the outtake

a) Sources of water and Bio-fouling

Reverse osmosis plants are used to decrease the salinity of the water, from mainly three sources:

- **seawater.**
  Seawater is difficult to treat. The salt concentrations are high and the biological life is important, resulting in bio-fouling. To measure the salt concentration, we often use the Total Dissolve Salt (TDS) measure. It is the sum of the concentration of organic and inorganic material in the water. For coastal regions, seawater, TDS are usually above 38,000 ppm. ((4),(5))
- **brackish surface water**
  Brackish surface water is less concentrated in salt than seawater; TDS is usually in the range 1,000 to 10,000ppm. However, it is often contaminated with sulfates. As a result, the major problem with surface water is scaling, or fouling with inorganic materials. Calcium carbonates, calcium sulfates and barium sulfates are the most problematic scalants. Surface water is also affected by marine life, and bio-fouling might be a risk.
- **brackish groundwater**
  Groundwater has only medium level of TDS (1,000 to 10,000 ppm) but with very high level of scalants and very low level of bio-life (the water has been filtered by the geological sand layers to penetrate in the aquifer). Scaling is the major problem.

Sources of brackish water are often far from large human communities, already depleted (over-exploited aquifers in India (6)), or highly polluted. As a result, many projects are targeting the desalination of seawater. This is why our primary goal is to design a membrane robust to bio-fouling.

b) pre-treatments

Before going into the RO stage itself, the feed water is pretreated. Different pre-treatment methods are used in series in the feed water stream.

Insufficiently pre-treated water is responsible for three failure modes of RO membranes: Bio-fouling, scaling and hydrocarbon clogging.

(1) Bio-fouling

A rapidly growing bio-film may grow and clog on the membrane. This is the main failure mode mechanism for the membrane. To lower the probability of bio-fouling on an RO membrane, chemical, physical and membrane pre-treatments are used:

Chlorine is the most used chemical. The active species, hypochlorous acid HOCl, has a high germinicid efficiency. For instance, the World Health Organization identifies that at pH7, a concentration of chlorine of .08mg/L is enough to remove all bacteria in one minute (1). Ozone (more efficient than chlorine but much less stable), or DBNPA ,(i.e. 2,2, dibromo-3-nitrilo-proprionamide, an effective and membrane compatible biocide) might be substituted for chlorine to disinfect the feed water. However, these chemical treatments have strong oxidizing properties, and a step to lower this potential (dechlorination) has to be performed before the RO module.

Ultraviolet (UV) irradiation is also known to have a germinicide effect, and is used for clean water (colloids in water limit the penetration of UV in water and limit the efficiency of UV treatment).

Media-filtration is also used to lower the bio-fouling potential. The water is poured onto a granular material (sand and other mineral granular materials), and filtrates through these medium. For slow enough filtration (2 m/h) and an appropriate choice and thickness of the filtering material (2-3m high), the filtrate is almost free of bacteria. This filtration step is used in most plants, but is associated with high capital and operating costs (requires a lot of space and needs to be carefully maintained and cleaned very often). This is why active research is trying to develop micro- and ultra-filtrations that are robust to fouling. This ultra-filtration step is often used in combination with media filtration to achieve a high quality of feed water for RO modules, but may forecast to replace media-filtration.

Figure 1: Ashkelon SWRO plant. The multi-media filtration (on the left of the picture) requires a lot of space, are labour intensive and are associated with high capital costs. Chemical treatment can be more automized but operation costs are still high, and anti-fouling membranes might lower the need of those costly pre-treatment (photo credit to Sauvet-Goichon (7))

Figure 2: Close-up on the Multi-media filtration in Ashkelon SWRO plant. (photo credit to Sauvet-Goichon (7))
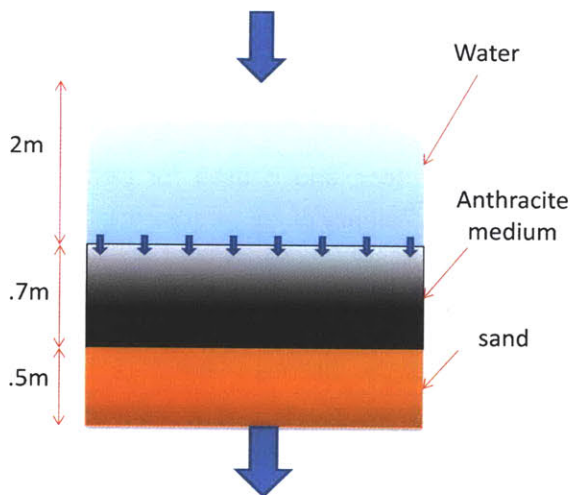
Figure 3: Schematic of multi-layer filtration: water is poured on top of granular media, and slowly permeate through this filter. Depending on the exact composition of the granular media and the filtration rate, most of the bio-life can be retained on the top layer and is removed by backwash.

Figure 4: Cartridge micronic filters in Ashkelon SWRO plant. Micro-filtration is the last step to remove any particles (bio-foulants, agregates and colloids) above 1-5μm. (photo credit to Sauvet-Goichon (7))

Bio-fouling is the most important failure mode of RO membranes. Bio-films develop on these membranes and eventually decrease their performance. The pre-treatment methods to lower bio-fouling potential are associated with high costs (capital and operating costs) and require a lot of manpower. Furthermore, the cost of water pre-treatment is so high that most plants operate at high recovery ratio (i.e. ratio of permeate flux to feed flux), which is detrimental to their performance.

This is why developing a non/low fouling membrane is very topical and would be very beneficial for the cost of water.

(2)   Scaling

Scaling is the second most common failure mode for RO membranes. Inorganic salts precipitate on the membranes and lower the performance of RO membranes. It is often a problem associated with high recovery ratio, where the final concentrate has a very high concentration in calcium sulfate (CaSO4), calcium carbonate (CaCO3) or other silica. Lime softening, pH adjustment, use of anti-scalant or acid-cation exchange resin are the main common techniques used to treat the water.

The reaction of calcium carbonate scale formation $Ca^{2+}_{(aq)} + CO_3^{2-}{}_{(aq)} \leftrightarrow CaCO_{3\ (s)}$ has a low solubility limit: $K_s = 4.8 * 10^{-9}$ (at 25C) (8). At the same time, carbonate (like all the alkaline scalant) is conjugate with acid bicarbonate with this equilibrium:

$$\begin{cases} CO_3^{2-}{}_{(aq)} + H_3O^+_{(aq)} \leftrightarrow HCO_3^-{}_{(aq)} + H_2O & pKa_1 = 10.25\ (@25C) \\ HCO_3^-{}_{(aq)} + H_3O^+_{(aq)} \leftrightarrow H_2CO_{3\ (aq)} + H_2O & pKa_2 = 3.60\ (@25C) \end{cases}$$
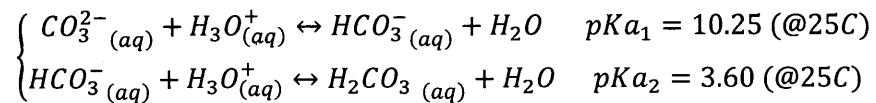
Maintaining pH lower than 9-10 will reduce the concentration of carbonate, reducing the rate of scaling formation. This is the mode of operating of lime treatment or pH adjustment for scaling. However, the addition of lime or other acid in the feed water increases the TDS (Total Dissolved Salts) in the feed water, and if overdosed, might damage the membrane.

Acid exchange resins are used to substitute scale forming cations (Ca2+, Ba2+ ...) by H+. It is mainly use for small brackish water plants.

The mode of operation of anti-scalants is more intricate. Polymeric anti-scalants may form a complex with the salts and increase the constant of solubility. It can also coat the surface of micro-crystal and prevent further growth of the crystal. Anti-scalants are generally specific to one type of scaling and might be detrimental to RO operation (increasing the fouling rate, ...). (9) (10).

Due to relatively low recovery rate, scaling is less important for seawater treatment than bio-fouling. It also requires less capital costs and only precise chemical dosing is needed.

(3)   coagulant and particulate fouling.

Particulate fouling is the third type of fouling. This problem is more acute in waste water reclamation than seawater. The major particulates are removed through flocculation –coagulation or filtration.

In coagulation-flocculation, chemicals are added for particulates (clays, colloids silica, organics material or oils) to aggregate. The sludge is removed in a flocculation stage, while the rest of colloidal material is trapped during media- or ultra-filtration process.

Coagulation/ flocculation → Dual media filtration → Chlorination → Cartridge filtration / Membrane filtration → dechlorination
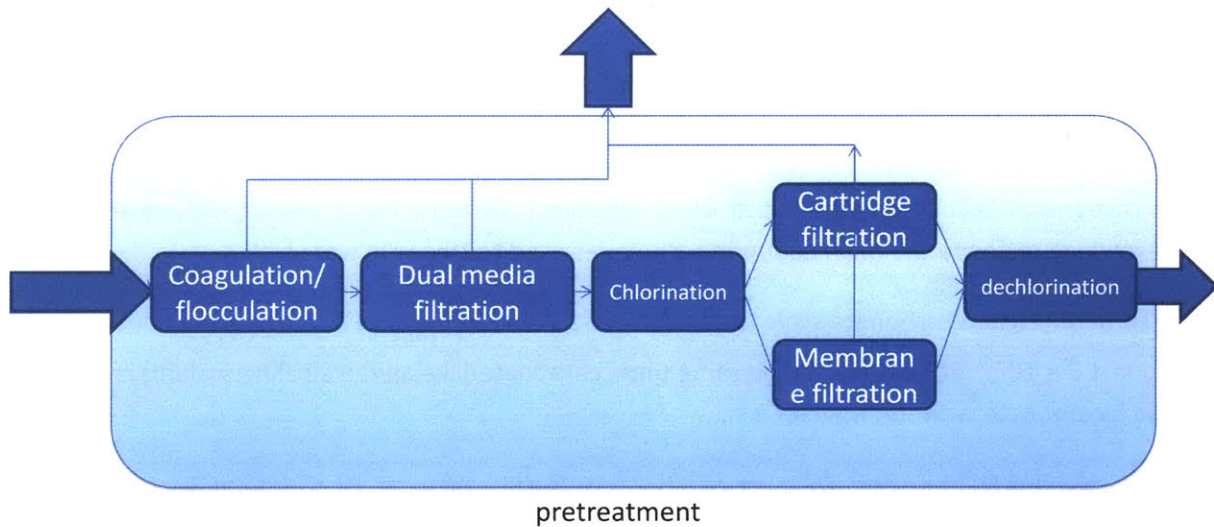
pretreatment

Figure 5: multiple pretreatment steps are needed before the RO step. From coagulation-flocculation to granular media filtration, and ultra or/and cartridge filtration, the water is purified and finer and finer particules are removed. The addition of chemicals (either biocids, flocculants and anti-scalants) is used in parallel to those filtration process. For low output plants, other physical treatment (UV) can also be used.

Pretreatment	CaCO$_3$	CaSO$_4$	BaSO$_4$	SrSO$_4$	CaF$_2$	SiO$_2$	SDI	Fe	Al	Bacteria	Oxid. agents	Org. matter
Acid addition	●							○				
Scale inhibitor antifoulant	○	●	●	●	●	○		○				
Softening with IX	●	●	●	●	●							
Dealkalization with IX	○	○	○	○	○							
Lime softening	○	○	○	○	○	○	○	○				○
Preventive cleaning	○					○	○	○	○	○		○
Adjustment of operation parameter	○	○	○	○	○	●						
Media filtration						○	○	○	○			
Oxidation filtration							○	●				
In-line coagulation							○	○	○			○
Coagulation-flocculation						○	●	○	○			●
Microfiltration/Ultrafiltration						●	●	○	○	○		●
Cartridge filtration						○	○	○	○	○		
Chlorination										●		
Dechlorination											●	
Shock treatment										○		
Preventive biocidal treatment										○		
GAC filtration										○	●	●

○ Possible   ● Very effective

Table 1: Summary of pre-treatment options for bio-fouling, scaling and organic fouling (from (11))

All in all, costly pre-treatments are used to treat water. For seawater, the major costs are associated with bio-fouling, which is also the main failure mode of RO membranes.

c)   *post-treatment*

Post-treatment consists most of the time of the addition of chlorine to prevent bio-contamination during stocking and distribution, as well as hardness addition to prevent corrosion from pipes downstream. Cheap hypochlorous acid or sodium hypochlorite (12) are usually used to dose free chlorine above 0.2ppm, the level recommended in the distribution network by the WHO (1).

Brine disposal is sometimes disregarded in scientific studies. Growing environmental concerns helped by new regulations is resulting in more and more expensive disposal options. Surface water disposal is the least environment-friendly but also the preferred option, especially due to low cost (.03 to .2 $/m^3$) (13). Often time, recovery rate is limited in order not to exceed 70,000ppm of TDS in the concentrate and to keep low concentration of chemical used for pretreatment.

If water retreatment installations can support the extra-load, sewer disposal is also often chosen for its low cost (.30 to .66 $/m^3$). Then comes the solution of deep well injection (.33 to 2.64 $/m^3$). Space permitting, evaporation ponds (1.18 to 10.04 $/m^3$) and brine concentrators (.66 to 26.41 $/m^3$) are expensive but very clean alternatives. When compared to the cost of membrane replacement (.008 to .05 $/m^3$) or chemicals (.008 to .05 $/m^3$), it can be understood why disposal is such an issue in practical cases.

d)   *energy recovering*

SWRO is a very energy intensive process. In the first plants, designed without energy recovery devices, throttling accounted for the major parts of this energy (up to 57% of the total energy destruction (14)), much more than the permeation through the membrane itself. As a result, the second law efficiency (ratio of the theoretical power needed to separate salt water in two streams over the consumed power) was as low as 4.1%.

Nowadays, the processes are much more efficient (second law efficient can be as high as 50%), especially due to the use of energy recovery devices. The first devices used were Pelton wheel and Francis turbine. In the first case, a wheel is propelled by the pressurized brine rejection water. The power is mechanically transmitted to the high pressure pumps through a drive shaft. Those systems can operate at 80% (the pelton wheel itself operates at 88% and pump efficiency is no more than 90%, while turbines usually operate at 72%). With those systems, energy can account for more than 40% of the overall costs of a SWRO (15), 85% of which is used by the high pressure pumps. A disruptive technology came to market in 1997: isobaric pressure exchangers. Those exchangers avoid the double conversion from pressure to torque and torque to pressure. Energy Recovery Inc. manufactured a piston-free pressure exchanger. Feed water enters these pressure exchanger systems in low pressure inlet, and pulls brine water out of the chamber of a rotor. Once the chamber is full, the other end is connected to the high pressure brine water which pressurizes the feed water. The process is continuous, and due to high rotation speed, the mixing between feed water and brine is moderated. A 2.5% salinity increase is

usually observed (16). Though, in terms of pressure power, the system has an outstanding 92% efficiency.

Improvement in energy recovery devices drove the cost reduction in RO technology during the last ten years, as emphasized by Gluekstern (for a red sea project, Gluekstern (17) shows that the improvement in Pelton technology from 1995 to 2008 are lowering the energy consumption from .86 to .57 kWh/m^3, while going for Isobaric pressure exchangers would lower this consumption to a mere .53 kWh/m^3). As the processes upstream and downstream become more and more efficient, the second law irreversibility due to the membrane has a larger and larger relative impact.
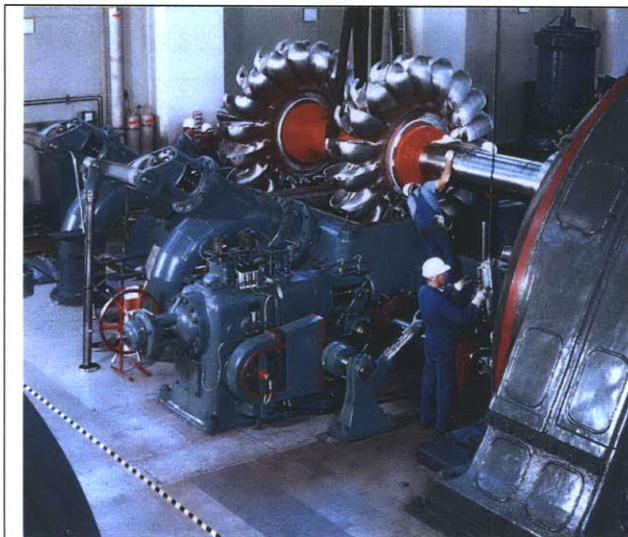

Figure 6: Pelton wheels are widely used. The wheel itself is powered by the high-pressure brine rejection water stream, and is connected via a mechanical shaft to a compressor, which pressurizes the feed line (photo credit Voith Siemens Hydro Power)
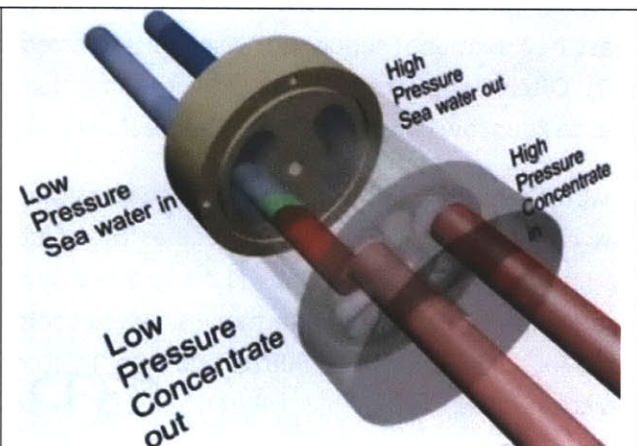

Figure 7: Isobaric piston-free pressure exchangers use a rotary ceramic part (transparent). The high-pressure concentrate (red) is pushed through one end, and pressurize the feed (blue) on the other end. The rotation velocity is enough so that the two flows do not mix (green part), and this is associated with only a slight increase in salinity (photo credit Energy Recovery Inc.).

We have seen that the upstream treatments (pre-treatments) would be eased with the invention of better membrane, especially with improved anti-fouling properties. On the other hand, downstream processes are more and more efficient (energy recovery), and any improvement in membrane efficiency is leveraged by this high efficiency.

To understand better the context of the membrane, the next section reviews the elements, which contain the RO membrane, and their assembly in the pressure vessel.
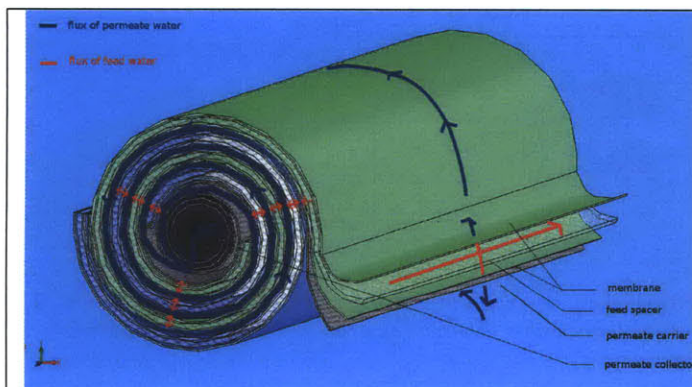
2. RO elements

a) Description of the assembly

Focusing on the membrane itself, many designs have been created to increase the efficiency of those systems. Out of those many systems, only two are commercialized: hollow fiber and spiral wounded membranes. The first ones have a better packing density (active membrane area per unit volume). But due to lower fouling rates (18), and a better control of pressure gradient, spiral-wound membranes are the preferred type of unit in commercial desalination and reverse osmosis water treatment.

Spiral wound elements are composed of 3 layers wrapped around a permeate collector: RO membranes (in green in Figure 8), a permeate carrier (grey mesh in Figure 8) and a feed spacer (transparent in Figure 8). During the wrapping process, the feed spacer is introduced to allow the creation of a feed channel of finite thickness between two consecutive membrane leaves, and a membrane carrier allows the permeate water to flow down to the permeate collector.

The water is going in the element by one of the sides. Glue lines are sealing the sides of the permeate channel, and avoid water to pass directly from the feed to the permeate side, without going through the membrane. More precisely, pressurized feed water enters the element from the side of the element (directly in the feed spacer, as shown in Figure 8). It is running in the feed spacer along the z axis (red arrow in Figure 8). Some water permeates through the membrane into the permeate channel. It then spirals down to the permeate collector (blue arrow) in the middle of the element. The brine concentrated stream exits the element on the right side of the element.


Figure 8: RO element, section view. The feed (transparent) and permeate (grey) channels are separated by the membrane (green). The feed water enters the element axially into the feed channel (the permeate being sealed in each side of the element). Part of it flows only in the axial direction and becomes the concentrated brine stream. Part of the water permeate through the membrane, goes into the permeate channel, spirals around the element to go into the permeate collector in the center. This is the permeate stream (shematics made with Solidworks)

Figure 9: Picture of the cross section of a Filmtech 8inch element. Several sheets are wrapped uround the permeate collector. The element is inserted into a fiberglass case (green), which is itself inserted into a pressure vessel.

This whole module is inserted inside in membrane housings, usually made of fiber glass. Depending on the size and configuration of the module, from 5 to 8 elements are used in series in a pressure vessel.

In order to increase the recovery rate, brine of those modules is often collected to enter a second pressure vessel. Since the salinity of the brine is increased at the end of the first pressure vessel, a boosting stage can be inserted before the second pressure vessel, to keep the same permeation performance despite the higher osmostic pressure. Also as pressure vessels often work in parallel, several designs are used: a one to one pressure vessel is called series array while a N for N is called a parallel. Considering that the flux of brine of the firsts pressure vessel is less than their feed, a N to M (N>M) design can also be adopted. This is the tapered array design. A lot of consideration enters in this configuration choice during the design of a plant. As the pressure is decreasing over the elements and the position in the array, and the salinity is increased, the rejection is smaller and smaller, while the scaling potential is increased.
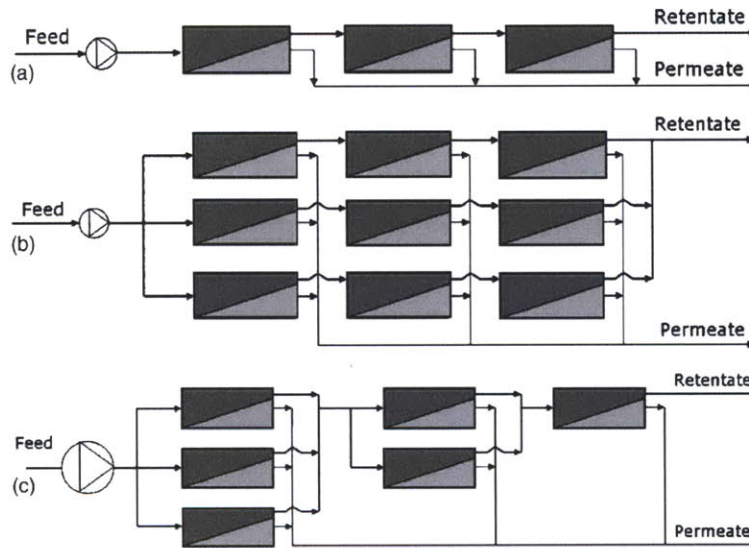
Figure 10: Elements and pressure vessel are combined to form a plant. Usually, a pressure vessel contains between 8 and 10 elements in series. Those pressure vessels are organized in arrays, either in series (a), in parallel (b) or in a tappered configuration (c).

On the contrary, high salinity or complex (high boron concentration…) feed water may require a second pass. Instead of filtering the brine, pressure vessels of a second pass are filtering permeate from the firsts ones to come down to very low permeate concentration. The biggest and most recent SWRO plant in Ashkelon (Israel) is the epitome of this multi-pass process. It uses four passes. The first one uses more than 25000 RO modules for a 45% recovery pass. Part of this permeate is further treated with some 15000 brackish water modules organized in 3 passes at high recovery (85 to 90%) at high and then low pH to decrease boron level.

b) *Optimal design of the feed spacer*

Feed spacers have been improved over the last 20 years. But the most recent studies show that there is still room for improvement (19)

In fact, spacers mainly act as a stirring agent to increase the convection parameter (this parameter is measuring the stirring of the layers close to the membrane), and as a result reduce the polarization effect (this is the increase of salt concentration in the feed channel due to the differential permeation fluxes of salts and water). Flux enhancement up to five times has been reported (20). On the other hand, spacers are detrimental to the pressure losses in feed channel (20) (21) (22), and a trade-off between both phenomena has to be found. Even more so as bio-films can develop directly on the spacer itself (23), (24).

Most autopsies to determine flux and hydraulic performance declines of modules are performed on the membrane itself. Though, it has been shown (23) that the hydrodynamic resistance of the feed channel (the Feed Channel Pressure drop) can be triple in full size plant due to fouling on the spacer, over very short period of time. Since Energy Recovery Devices operate at high efficiencies (above 92%), energy losses in the feed channel (FCP increases) are paramount to booster sizing, and more generally, to the energy efficiency of the RO plant.

D. Manufacturing an RO membrane

While the idea of osmotic pressure has been formulated in the beginning of the 19th century, it is only in 1877 that Wilhelm Pfeffer actually measured the relation between the pressure differential across a semi-permeable membrane separating two sugar solutions, and their concentration. In 1901 (25) Van't Hoff set up the theory of osmotic pressure in dilute solutions as reported in his Nobel lecture. The osmotic pressure π of a dilute solution can be expressed as $\pi = -c.R.T$, where c is total concentration of solute in the solution, T is the absolute temperature and R is the gas constant.

If two solutions of different concentration are separated by a semi-permeable membrane (permeable to the solvent, but impermeable to the solute), this imbalance will induce a flux of the solvent through the membrane from the dilute solution to the concentrated one. This flow can be reversed if a physical pressure greater than the osmotic is applied: in this case, the less concentrated water becomes even less concentrated and the more concentrated one becomes more so. This is the principle of reverse osmosis. Manufacturing the membrane with the right chemistry, permeation properties and mechanical strength is so involved that it took over a century to see the first successful membrane, with Loeb and Sourirajan in 1964.

While the performances of the reverse osmosis (RO) membrane have dramatically improved since the first RO membranes by Loeb and Sourirajan, the processing of those membranes is still the same. Cadotte (26) listed nine criteria that need to be achieved simultaneously to characterize a good RO membrane. Apart from the obvious water flux and salt rejection, compaction resistance, resistance to free chlorine and to other oxidizing agents, stability over a wide pH range, wet/dry reversibility and stability at high temperature are to be taken into account during the design of new membranes. Almost 30 years later, those criteria have only slightly changed. New regulations have imposed new type of rejection (boron (1), Trihalomethane (27)...) while less and less clean feed water has increased the need for anti-fouling properties (13) of new membranes.

1. What does an RO membranes look like?

The active part of a reverse osmosis membrane is a very thin dense layer. But since this layer has to be both ultra thin (to have good permeation properties the layer should be less than a micron thick) and be strong enough (to sustain quite a lot of force due to high pressure), this layer is cast on top of porous support layers. Whether of the same material (Loeb and Sourirajan asymmetric cellulose acetate type of membrane) or made of different materials (Cadotte composite membrane), the membrane is structurally heterogeneous: the active layer is dense while the support layer has to be as porous as possible to have the least hydraulic resistance possible. In Figure 11, the 3 different layers (PET non woven support layer, PSf support layer and the active layer) are clearly shown in the THC-HR membrane by KMS (Koch Membrane System).
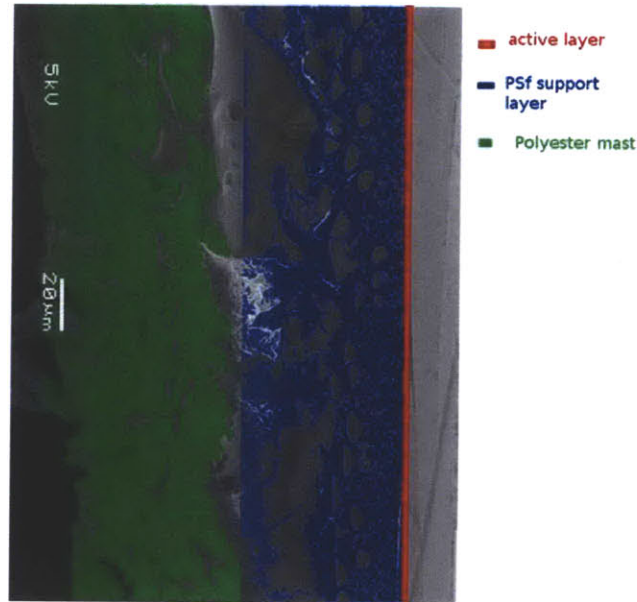
Figure 11: Micrograph of the cross section of a Cadotte composite RO membrane (Koch membrane, TFC-HR). This micrograph, taken by Dr Gozde Ince-Ozaydin, collaborator in Chemical Engineering at MIT, clearly represents the active layer (highlighted in red), the porous polysulfone (in blue) and the fibous mast of Polyethylene (in green). Colors have been added to vizualize the cross section. The membrane was cut at very low temperature in Liquid nitrogen, to avoid the partial crushing of the top layer on the Polysulfone layer.

The role of each layer is more apparent on Figure 12: the PET non woven mat is composed of large fibers randomly distributed that provide the required mechanical stiffness to the membrane, while the porous polysulfone layer is engineered to be very smooth to support the active layer without inducing too much stress concentration due to "topographical defects".
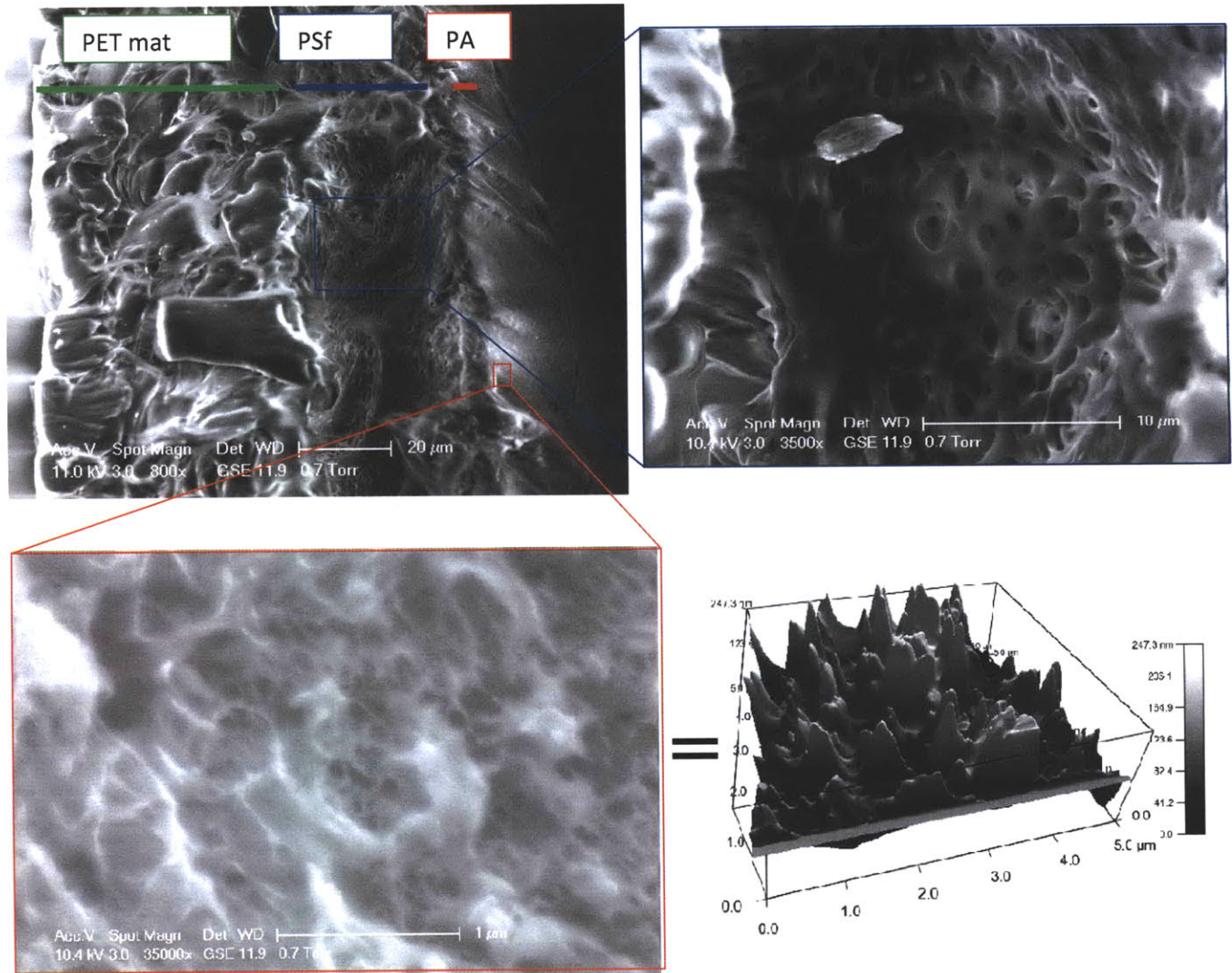
Figure 12: a/Micrograph of the cross section of a composite RO membrane (GE osmonics, SW-AD) - b/zoom in the PSf region - c/zoom on the active layer at higher magnification d/ surface topology by AFM imaging of the top layer

2.   What makes a good membrane?

While defining the performance criteria of RO membranes is quite easy, it is very difficult to conclude on the physical and chemical composition of a "best membrane". Indeed, improving the performance of a membrane toward one criterion often degrades its performance toward the others: in membrane manufacturing, it is all about trade-off.

The influence of a few physical parameters of a membrane on its performance will be discussed. As far as chemistry is concerned, some of the "good practices" or choices that have been made over the years will be reviewed. This review provides a better understanding of the dos and don'ts in reverse osmosis membranes and guides the innovative ideas that we are developing in chapter 2 and 3.

a) *Physical parameters*

(1)   Membrane thickness and its role on permeability

The thickness of the active layer is the most obvious physical parameter which will affect the performance of the membrane. Theoretically, the classical solution-diffusion theory predicts that water flux in operation varies as the inverse of the thickness of the active layer. The same conclusion holds for the limiting flux of the water in both the pervaporation mode or the limit of infinite pressure (28). This conclusion led to the successful manufacturing of higher flux, lower pressure polyamide membrane (29) in the early 80's, by manufacturing thinner defect-free active layers.

On the other hand, reducing the thickness will also degrade both the durability of the membrane and its mechanical strength. It is also thought (30) that thinner membranes are more prone to pinholes or local defects, which affect the salt rejection.

Overall, the thickness of the active layer will be determined by the conditions of interfacial polymerization (31) (including chemical composition of the support layer, the chemistry of the two reacting solutions, temperature and relative humidity during polymerization...). For instance, Hoek et al. (31) have shown that the hydrophilicity of the support layer plays a significant role during the interfacial polymerization of the active layer. While the ideal membrane is composed of hydrophilic active and support layers, the conditions for interfacial polymerization require a hydrophobic support layer. As a result, a trade-off specific to each chemistry and polymerization condition has to be found to meet those two objectives.

(2)   Hydrophilicity and surface charges, key parameters to fouling potential

Another important set of physical parameters are surface hydrophilicity and surface charge of a reverse osmosis membrane. Those quantities are usually mentioned together, as they both involve a particular configuration of the electrical state of the membrane. Hydrophylicity is commonly measured by the contact angle between a dry membrane and the surface of a drop of purified water sitting on this membrane. The surface charge (or surface zeta potential) is measured using an electro kinetic analyzer to get the streaming potential in an electrolyte solution.

The surface zeta potential has been shown to have an important role in the fouling mechanisms. While negatively charged membranes do not exhibit a decrease in flux in presence of anionic surfactants, the cationic surfactant will be attracted by the membrane resulting in a rapid fouling (32) of the membrane. The opposite phenomenon is observed for positively charged membranes. This is why membrane surface charge should be maintained as neutral as possible (at all pH). In practice, most of the reverse osmosis membranes are negatively charged, likely due to the deprotonation of the carboxylic groups present in the polyamide of the active layer. In order to reduce this surface charge, many commercially available RO membranes which are to be used in fouling environment are coated with a neutral polyvinyl alcohol (PVA). This coating reduces surface zeta potential from -25mV;-37mV (for uncoated membranes) down to -2mV;-15mV (for coated ones). This range of surface potential from -10 to -5mV has been shown to exhibit the lowest fouling rate.

Hydrophilicity also plays an important role in the permeation and fouling properties. Bacteria adhesion is often stronger on hydrophobic substrates.

(3)   Roughness, an ill-understood parameter
Roughness is the third important physiochemical property of a reverse osmosis membrane. However, its influence is not always well understood (33).

For example, Hirose et al. (34) concluded that, in non fouling conditions, a linear relation existed between the membrane flux and the roughness (roughness root mean square). It is thought that this surface unevenness can be regarded as an enlargement of the effective RO area. The membranes tested in this study were prepared by varying the concentration of isopropyl alcohol in the amine solution use during the interfacial polymerization. Gerard (32) got similar conclusions with a corrugated skin layer obtained by modifying the conditions during this interfacial polymerization. It was further observed that fouling behavior was similar for those membranes compared to conventional ones.

On the other hand, surface roughness is often seen as a fouling promoter or smoothness as a passive anti-fouling characteristic. Elimelech (35) compared cellulose acetate and polyamide modified membranes, which have been pretreated with anionic surfactants to have the same electro kinetic (zeta) potential. The higher fouling rate on the composite polyamide layer has been attributed to its rougher surface.

Chapter 2 of this thesis describes in greater details very recent studies in which several surfaces with "controlled roughness" (or micro and nano-patterning) were shown to have lower fouling properties.

This short review of physical parameters shows that thickness, roughness, hydrophilicity and surface charges are important. While the role of thickness is well understood and affects mostly the water flux and rejection (through pinholes and defects), the other three properties are more complex. They affect mostly fouling and scaling properties.

An exhaustive review of the chemistry is far beyond the scope of this review. Though, few "good practices" will be mentioned as to which material is or has been used for membrane manufacturing, and why so.

b)   Chemistry
RO membranes are either composite or asymmetric. Asymmetric membranes are made of a single material with a gradient in porosity perpendicular to the in-plane directions, composite membranes are composed of several layers of different chemistry and porosity.

(1)   Cellulose acetate: a good tradeoff between permeability and chlorine resistance
Cellulose acetate asymmetric membranes were first introduced in the early 1970's by Loeb and Sourirajan. Since then, Cellulose triacetate has progressively replaced the cellulose acetate. But those membranes are still produced (36) either in the flat type sheet (Toray, Dow, Hydranautics, …) or in the

hollow fiber arrangement (Dow, Toyobo,…), especially for their good chlorine tolerance capacities. They can operate in environment with free chlorine up to 1mg/L (15).

While their permeation properties can almost compare with the composite membranes, they suffer from a lack of stability toward pH of the feed water. The hydrolysis reaction involved in the damaging mechanism is removing the acetate group of the cellulose acetate (37) (38): $R_1 - COOH + R_2 - OH \leftrightarrow R_1CO - OR_2 + H_2O$. Fritzmann (15) showed that CA membrane life time can be shortened from the usual 4 years at pH 4-5 to 2.5 years if operated at pH 6, and down to a couple of days if the pH goes down to 1 or up to 9. This lifetime is even further shortened with an increase of temperature (increasing Temperature from 23°C to 51°C increases the hydrolysis rate by a factor of 8) (39). Cellulose acetate asymmetric membranes also compact and their flux gradually declines over their lifetimes (15).

A comparative study of their permeation properties shows that salt passage in those membranes is slightly less than for composite membranes, but that water passage is almost as high as the most recent composite membranes (cf Figure 13). The performance of cellulose acetate membrane can be further improved by increasing the level of acetylation and heat treating (annealing) after formation. Both improve significantly the salt rejection without degrading too much the water passage as shown in Figure 14 and Figure 15. Figure 14 represents the salt rejection versus the water flux for membranes after heat treatment at different temperatures. Figure 15 represents the water permeability versus the salt permeability for cellulose acetate of different degree of acetylation.
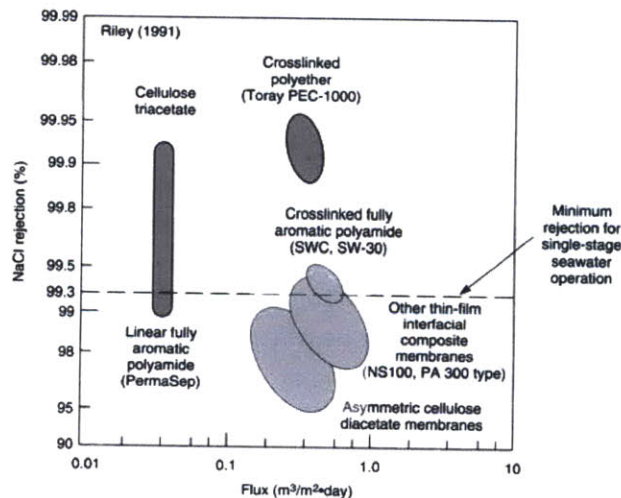
Figure 13: Flux rejection versus NaCl rejection for commonly used materials. (from Baker (40))
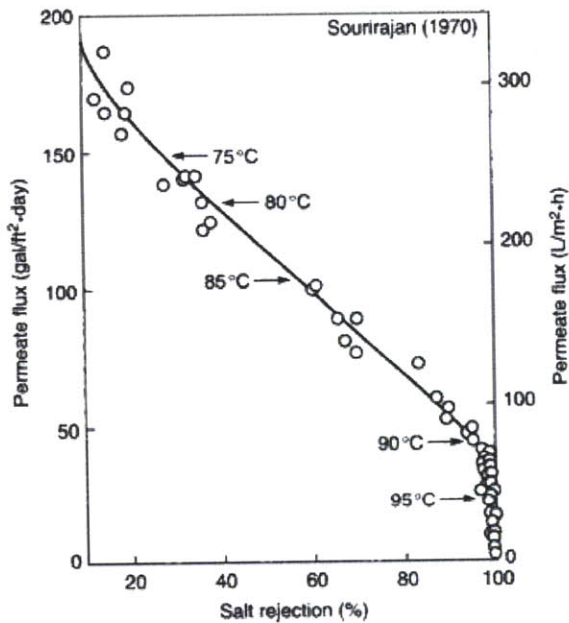
Figure 14: Influence of the heat treatment on permeation properties of a cellulose acetate membrane. (from Baker (40))
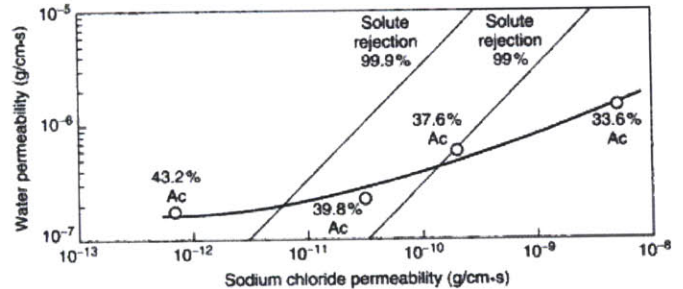

Figure 15: Influence of Acetylation on properties of cellulose acetate membrane. (from Baker (40))

(2)   Composite polyamide: the choice for high permeation performances on pretreated water with low level of free chlorine.

The other type of successful membranes is composite polyamide membranes formed by interfacial polymerization. Cadotte described in his patent (29) one of the most successful active layers used in RO, the FT30, along with the conclusions that lead to the chemistry of the active layer.

This active layer is made by interfacial polymerization, achieved by contacting a polyamine and an acyl halide. More precisely, the porous support layer usually made of polysulfone, is immersed in a solution of m-phenylenediamine (MPD). After removal of the excess, it is immersed in tremesoyl chloride (TMC). A very thin layer (200nm (11)) will be formed at the interface between MPD and TMC.

Those membranes have great permeation properties: salt rejection up to 99.6% with flux of 33gfd (gallon per square foot per day). The "Achilles' heel" of those membranes is the poor resistance to chlorine. While Cadotte (26) showed some chlorine resistance of his membrane to level of chlorine of 100ppm during 72h, polyamide membranes often require a continuous chlorine concentration lower than .1ppm in the feed water (41), and a membrane should not be exposed more than 200-1000h to level of free chlorine higher than 1ppm. The mechanism of degradation can be attributed to a reversible N-chlorination (the hydrogen atom link to the nitrogen of the amide is replaced by a chloride atom) and an irreversible ring-chlorination (due to an interaction between the ring of the aromatic group and a chloride).

Used as a disinfectant, chlorine is the most common preventive and curative method to combat fouling on membranes and pipes. This is why the lack of chlorine resistance of the active layer is of huge practical importance. We are seeing here again the cause of the main failure mode of RO plants: lack of chlorine resistance leading to lower level of chlorine in the feed and eventually higher fouling rates.

3.   Processing of a membrane.

a)   Forming a porous layer by phase inversion method

Over the years, phase inversion method has proven to be a great technology to form membranes with asymmetric porous structure. It is of common use in ultra- and micro-filtration, but all types of RO membranes also benefit from this technique, either to form the whole membrane in the case of cellulose acetate asymmetric membrane, or to process the porous layer supporting the active layer in the case of composite membranes. The main advantage of this method is the small size of the pores that is possible to achieve. This method is using the thermodynamics of demixing, and pore sizes are generally quite well controlled, down to 20nm.

The basic principle (42) of this method is to bring a ternary system, composed of a Solvent, a Non-Solvent and a Polymer in a meta-stable state. This meta-stable state will form two stable phases: one rich in polymer (blue on the simulation- Figure 16) is fixed by gelation, vitrification or crystallization and another poor in polymer (red on the simulation Figure 16) evaporates and corresponds to the pores of the porous membranes obtained. This process is called demixing.

(a) $\tilde{t} = 0$ (b) $\tilde{t} = 8.01 * 10^{-5}$ (c) $\tilde{t} = 0.0001301$ (d) $\tilde{t} = 0.0004776$
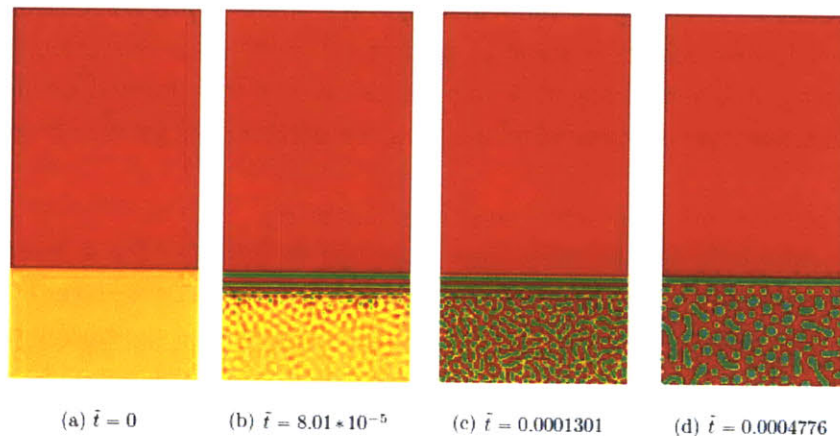
Figure 16: 2D morphology evolution (change of polymer fraction) during the demixing of a PVDF membrane formed by immersion precipitation (adapted from (42))

Mainly two techniques are used to bring the Solvent-Polymer mixture into the meta-stable configuration.

The other process for membrane manufacturing is called immersion precipitation. The mixture solvent-polymer is dipped into a coagulation bath composed of a Non-solvent reactant. Two phenomena are coupled during this process: the diffusion of the non-solvent and solvent into the mixture and coagulation bath and the demixing/solidification of the polymer rich phase. This method is widely used in the case of composite membrane

Either the mixture will be thermally precipitated: the solvent quality usually decreases when the temperature is decreased, resulting in a meta-stable state. The solvent then evaporates.

Inversion methods are widely used because they are versatile and tunable. Provided that the polymer is soluble in the solvent, almost any polymer can be used. Moreover, by changing the reaction conditions (temperature, time of residency in the liquid …), the reactants (solvent, non solvent), using a vapor phase instead of a coagulation bath or using additives, this membrane formation can be accurately controlled.

b) *Forming a thin active layer.*
Once this porous support layer is formed, the very thin active layer is created. This layer is meant to be the thinnest possible, with a smooth and flawless surface and a favorable chemistry with good permeation properties.

(1) Low rate demixing
Asymmetric membranes (also known as Loeb-Sourirajan membranes) are composed of mainly one material, oftentimes cellulose acetate. Instead of dipping the multi-phase mixture in the coagulation bath right after casting, it is first draught. A thin dense layer is thus formed on the surface. The characteristics of the active layer will depend on the time, temperature and gelation properties.

(2) Interfacial polymerization for active layer manufacturing
Interfacial polymerization is by far the most used technique to form the active layer for composite membranes. Two reactive monomers are contacted, and react to form a dense layer at their interface. More specifically, the porous support layer is first dipped into an amine pre-polymer and the whole system is then dipped into an acid chloride solution, resulting in a thin coating on top of the support layer. The huge advantage of this method is that the film growth is "self-inhibiting": as the film grows in thickness, the diffusion of one substance in the other is reduced. It results in very thin films (down to 50nm). The drawback is the high and uncontrolled surface roughness of the membranes prepared with this technique.

4.   Conclusions

The membrane is a complex system composed mainly of two types of layers: a support to resist the macroscopic stresses imposed by the high pressure and the active layer to provide the membrane with its permeation performance. The current processing methods are quite versatile in terms of the usable chemicals, and haven't changed much since the beginning of membrane filtration. A lot of effort in chemical engineering goes into designing new molecules to achieve high permeation performances while improving strategies against fouling (either by tolerating higher level of free chlorine, by decreasing surface roughness or improving electro-kinetics properties of the surface of the active layer).

E.   Permeation through a membrane

Understanding the precise transport phenomenon, to come up with a relation between water, salt passage and pressure has been a key to engineer better membrane desalination systems. This analysis shows that polarization gradient, due to differential flow of solute and solvent, is the key element in both permeation and fouling/scaling problems.

1.   Water and salt passage in a membrane

a)   Attempt to physically describe the transport phenomenon on the active membrane

Transport phenomenon in the system membrane/solvent/solute includes diffusion of salt and solvent in the non-porous active layer, as well as adsorption/desorption at the two interfaces membrane/solution.

Nomenclature

	upstream solution	membrane	downstream solution
pressure	$= \quad p_0$	p_m	p_ℓ
solvent (1):	$C_{10}^s, \ a_{10}^s$	$C_1^m, \ a_1^m$	$C_{1\ell}^s, \ a_{1\ell}^s$
solute (2):	$C_{20}^s, \ a_{20}^s$	$C_2^m, \ a_2^m$	$C_{2\ell}^s, \ a_{2\ell}^s$

Osmotic pressure: $\quad n_1$

$$\pi_0 = -\frac{RT}{V_1} \ln a_{10}^s \qquad \qquad \pi_\ell = -\frac{RT}{V_1} \ln a_{1\ell}^s$$

$$n_2$$

$$z = 0 \qquad \qquad \ell$$

$n_1 \quad = \quad$ mass flux of solvent (1)

$n_2 \quad = \quad$ mass flux of solute (2)

$$\frac{n_2}{n_1} = \frac{C_{2\ell}^s}{C_{1\ell}^s} \qquad \text{mass balance}$$

$$R \equiv 1 - \frac{C_{2\ell}^s}{C_{20}^s} = 1 - \frac{C_{1\ell}^s}{C_{20}^s}\frac{n_2}{n_1} \qquad = \quad \text{solute rejection}$$

$$SP \equiv \frac{C_{2\ell}^s}{C_{20}^s} = 1 - R \qquad \qquad = \quad \text{solute passage}$$

for dilute solutions $C_{1\ell}^s \cong \rho_1 \quad = \quad$ solvent density

Figure 17: Nomenclature for the reverse osmosis permeation (from (28))

A good description of the system (28) {membrane/water/salt} is achieved by the ternary Maxwell-Stephan equation, which couples the "diffusive"force d_i on the component i, the velocity v_i of i, the mole fraction x_i and the multicomponent diffusion coefficients D_{ij}:

$$d_i = -\sum_{j \neq i} \frac{x_i x_j}{D_{ij}}(v_i - v_j)$$

Adding to this relation the definition of the chemical potential: $\nabla \mu_i^m = RT \, \nabla \ln(a_i^m) + \overline{V}_i \nabla p_m$, a general expression for d_i: $c \, R \, T \, \mathrm{d_i} = \mathrm{c_i} \nabla \mu_i^m$ and the assumption relatively well accepted that the pressure is uniform inside the membrane, and we link the activity of the components to their velocity in the membrane:

$$x_i \nabla \ln\left(a_i^m\right) = -\sum_{j \neq i} \frac{x_i x_j}{D_{ij}} (v_i - v_j)$$

After some algebra, the expressions for a binary mixture {salt/water} become:

$$J_w + \left(\frac{w_2 J_w - w_1 J_s}{w_m}\right) \epsilon_1 = -\frac{\rho \omega_1 D_{1m}}{w_m} \nabla \ln(a_1^m)$$

$$\text{and } J_s - \left(\frac{w_2 J_w - w_1 J_s}{w_m}\right) \epsilon_2 = -\frac{\rho \omega_2 D_{2m}}{w_m} \nabla \ln(a_2^m),$$

where ϵ_1 and ϵ_2 are coupling coefficients, which couple the diffusion of the water to the diffusion of the salts. Also, before any simplifications, the pressure does intervene in the diffusion of the salt, contrary to the solution-diffusion model.

> It should be noted that outside the active layer, the salt is diffusing in the water, while in the active layer, the polymer is the medium in which both water and salts are diffusing. This nuance is tremendously important when using less general expressions to describe the diffusion, like Fick's law in the solution-diffusion model. This raises complexity for the continuity of the simplified equations.
> The second hypothesis that has been discussed and seems now to be well accepted is the absence of a pressure gradient in the membrane. The pressure only intervenes in the adsorption equation on the sides of the active layer.
> The last remark addressed by Paul et al. (28) is the inability for those models to describe very accurately composite membranes. They are only accurately applicable to asymmetric Cellulose-acetate membranes.

The strength of this model is to capture two limiting phenomena observed experimentally:

> **The ultimate flow**. Simplified models used in industry use a linear relation between the water flux and the trans-membrane pressure applied. Experimentally, as shown on Figure 18, the concentration gradient induced by the pressure difference is bounded hence the flux. More precisely, this limiting flux is: $\frac{C_{10}^m D_{1m}}{l < w_m >}$ (cf schematics for definition of those quantities).
> In this model, the rejection admits an upper bound. This is an important parameter of the membrane.
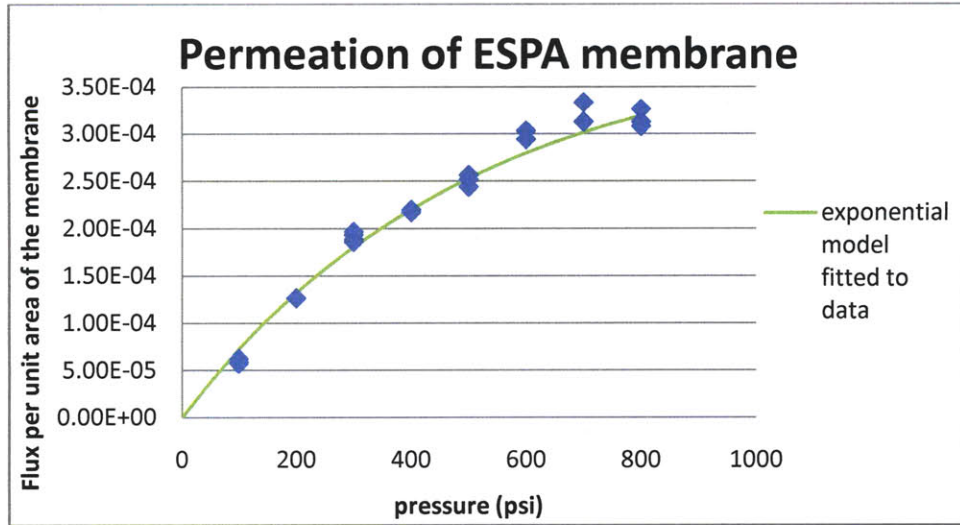
Figure 18: Experimental measurements on the water flux as a function of the trans-membrane pressure. These measurements were taken on a lab-scale RO system that we built around a SEPA CF42 crossflow cell by Sterlitech. Omega sensors (pressure transducers, flowmeters) were installed in the permeate and concentrate streams.

More fundamentally, it introduces a coupling between the salt and the water. Also, a dependence of diffusion coefficient with concentration can be introduced.

Few important subtleties:

> We can't define a mole fraction of the system, since it may be infinite for very crosslinked polymers. So mass fraction or volume fraction are the preferred quantities.
> Up to now, no unified multiscale model has successfully described this permeation through the active layer. As a result, the coefficients are found experimentally.

b)   *Simplified model*

In a first approximation, it is often very convenient to assess flux and salt rejection of a membrane from a simple permeation experiment at a certain pressure and feed concentration. To do so, Fick's law is used in lieu of Maxwell-Stephan equation:

$$J_w = D_{1m} \frac{dc_1^m}{dz}.$$

Assuming that

- the diffusion coefficients are concentration independent
- derivative are equal to variation across thin layers
- the membrane-solvent mixture is thermodynamically ideal (ie $\mu_1^m = \mu_1^0 + RT \ln (c_1^m)$)
- difference in chemical potential across the membrane is the same taken in the membrane or in the solution

Concentration gradient of the solvent in the membrane can be estimated with $c_{10}^m - c_{1l}^m = c_{10}^s - c_{1l}^s = \frac{c_1^m V_1 (\Delta p - \Delta \pi)}{RT}$. On the other hand, pressure effect is neglected on the diffusion of solute in the membrane. As a result, water and solute fluxes through the membrane are estimated by:

$$J_w = \frac{D_{1m} c_1^m V_1 (\Delta p - \Delta \pi)}{lRT}.$$

$$J_s = \frac{D_{2m} K_2 \, (c_{20}^s - c_{21}^s)}{l}.$$

Furthermore, permeability is often seen as a product of solubility and diffusion: $P_2 = K_2 D_{2m}$ and $P_1 = K_1 D_{1m}$. Together with the approximation of dilute solutions $(K_1 = \frac{c_1^m}{c_1^s} \cong \frac{c_1^m}{\rho_1})$, it forms the simplified expression for water and salts fluxes, as well as rejection:

$$J_w = \frac{P_1 \rho_1 V_1}{l} * \frac{\Delta P}{RT}, J_s = \frac{P_2 c_{20}^s}{l} * (1 - \frac{c_{21}^s}{c_{20}^s})$$

$$R = 1 - \frac{c_{2l}^s}{c_{2l}^s} = \frac{\Delta P}{\alpha + \Delta P} \text{ i.e., with } \alpha = \frac{RT \, P_2 c_{20}^s}{P_1 \rho_1 V_1}.$$

This model is very broadly used, and the water passage through cellulose acetate membranes is quite accurately predicted (43). Though, recent experimental data indicate that salt permeation is not well described by this purely linear model, and propose phenomenological corrections. Mainly having $\Delta \pi$ be the average of the osmotic pressure between both side of the active layer, and salt flux being $J_s = B * (c_0 - c_p)^\alpha$, and α has been reported to be in the range 1.02-1.51 for several commercial membranes (44).

c) Conclusion from the models for permeation properties
From those expressions, we can see that flux of salt and water are both inversely proportional to the thickness of the active layer, while rejection doesn't depend on it. Similarly, Lonsdale et al. (43) reported that water flux is inversely proportional to the temperature, but they did not observe a significant change in salt rejection (which is a second order effect in this model for relatively high rejection).

We should also note that the membrane performances are to be distinguished from the module performance, which can be significantly different, as reported by Tay et al. (45). Due to concentration effect along the module, as well as hydrodynamic resistance, we observe an increase in trans-membrane pressure resulting in a decrease of salt rejection.

d) Other layers

We understand fairly well the mass transfer theory in the active layer. Similarly, mass transfer for ultrafiltration membranes are very well described, either with Poiseuille type of flow (flux is proportional to the applied pressure, for large enough pores) or Knudsen flow (for small pores, based on collision of solvent with the membrane) (46).

Whether a RO membrane can just be considered as 2 membranes in series, with hydraulic resistance calculated independently is still unclear. Only little literature has been found on this subject, precisely because it is hardly possible to test only active layers. Though, this question does play a huge role in forward osmosis type of treatment, where polarization gradient are created inside the pores. Loeb (47) himself raised the question in 1997 by demonstrating that the support fabric itself does play a role in permeation properties.

2. Limiting factors

As water permeates through the membrane, the salt and other particulate concentration increases in the vicinity of the surface of the active layer. This is the polarization concentration, and constitutes one of the most detrimental effects of membrane filtration.

We review here the salt polarization and its effect on permeation performance. This polarization gradient also results in scaling and fouling, two phenomena, which will be described.

a) Polarization gradient decreases permeation performances

While a complete model of this complex convection-diffusion problem seems to be out of reach, three simple analytical models are predicting relatively well polarization effect (48) (49), two of which are commonly used in reverse osmosis.

The first one is very basic and just accounts for a classic Fick diffusion and the salt flux across the membrane (50): in steady operation, we assume that the transverse flux of salt in a boundary layer of thickness δ is everywhere equal to the flux of salt through the membrane:

$$J_s(x) = C_p(x) * J_w(x)$$

,where C_p is the concentration of salt in the permeate and J_w the water flux. And flux of salt along y axis is $J_w(x) * c(x,y) + D_s * \frac{dc}{dy}(x,y)$. Introducing the two boundary conditions: $c(x,\delta) = c_b(x)$ and $c(x,0) = c_w(x)$, where c_w is the wall concentration, and c_b the bulk concentration in the feed channel. It comes: $\frac{c_w - c_p}{c_b - c_p} = \exp\left(\frac{J_w \delta}{D}\right)$. And introducing the intrinsic retention of the membrane, $R_{int} = 1 - \frac{c_p}{c_m}$ we obtain the polarization concentration:

$$\frac{c_w}{c_b} = \frac{\exp\left(\frac{J_w\delta}{D}\right)}{R_{int}+(1-R_{int})\exp\left(\frac{J_w\delta}{D}\right)}.$$
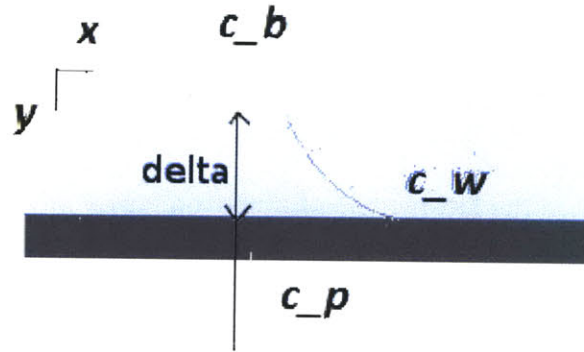
The last step in this analysis is to relate the thickness of this boundary layer to parameters of the problem. While there is no ultimate answer for this problem, a dimensionless Sherwood coefficient is often introduced $Sh = \frac{kd_h}{D} = a * Re^b * Sc^c * \left(\frac{d_h}{L}\right)^d$, where Re is the Reynolds number, Sc is the Schmidt number (measureing viscosity and mass diffusion ratio) and d_h is the hydraulic diameter. Usually, experimental studies/ theoretical calculations in laminar flow for different geometry of the channel help find the right parameters a,b,c,d. Two interesting configurations are the laminar flow in rectangular channel, for which $Sh = 1.85 * \left(\frac{Re\,.Sc.d_h}{L}\right)^{1/3}$ and the turbulent flow with $Sh = 0.04.\,Re^{0.75}Sc^{.33}$. Those are the configurations without a feed spacer. Feed spacers are used as mass transfer enhancers, and will reduce the polarization concentration. As an example, Schock and Da Costa obtained Sherwood numbers for some spacers: $Sh = k.\frac{d_h}{D} = 0.0096.\,Re^{.5}.Sc^{.6}$. For reverse osmosis, assuming Re=200 and Sc=600, we get a reduction from 1200 to 6 of the Sherwood number in turbular condition, by adding a permeate spacer.

This model has the huge advantage to be analytical, and is used by many process engineers. It over-predicts water passage and salt rejection due to an under-prediction of the polarization. Though, in this model, the boundary layer thickness does not depend on the water passage across the membrane, and it seems to be an important drawback. Other semi-numerical solutions (51) have been developed for more accuracy.

The model presented fails to capture the notion of maximum flux. As the flux of water increases, the polarization gradient becomes more and more important. The osmotic pressure seen by the membrane also increases. The membrane reaches a point where an increase in pressure does not significantly increase the water flux. This is the limiting flux, one other membrane characteristic.

The increase in the osmotic pressure due to the polarization gradient is thus very important. But by increasing the concentration of salts and organic materials just at the surface of RO membranes, polarization is also the triggering effect for scaling, organic fouling and bio-fouling.

b) *Scaling or Inorganic salt precipitation*

(1)   Preferred element for scaling.
Scaling is often detected when the last module of a pressure vessel has a flux decline (24). The salt concentration in the feed of the last RO element is always significantly higher than the concentration in the first (especially if the recovery ratio is high). As a result, scaling will mostly affect these elements.

(2)   Importance of scaling in Reverse Osmosis.
Scaling is detrimental to RO membrane for several reasons. The first and most obvious reason is that the scaled area of a membrane will not show the same permeation properties. The "cake" is blocking the passage of the water (see Figure 19). This cake also increases the drag for the axial flow, and thus increases the hydrodynamic loss in the element. Then, inorganic crystal growth is easier than the nucleation of those crystals. As a result, formation of scale is self-triggering and exponential. Last, scale might damage the membrane, resulting in pinholes and contamination of the permeate water by feed water.

| Figure 19: Severe scaling of an element. The cake formed in this element blocking both the flow through the membrane as well as the feed channel. As a result, this element is (from (52)). | Figure 20: Silica deposition on a RO membrane (From (52)). |
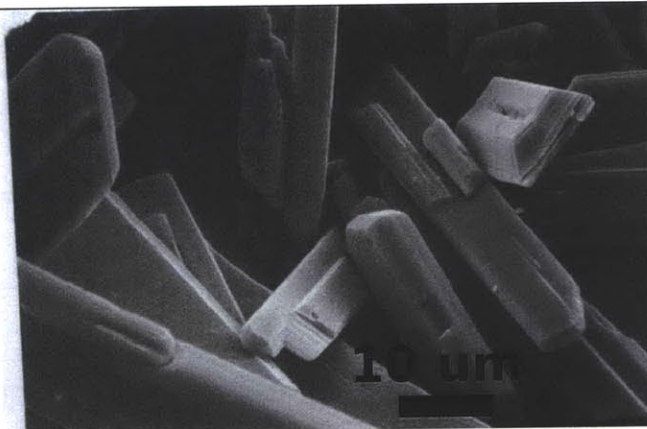
(3)   Treatments.
The chemical preventive treatments (anti-scalant, alkalinity treatment) have been mentioned in the pre-treatments for RO plant in the first section of this chapter. Another preventive solution for the scaling is

the feed spacer. This mesh, inserted in the feed channel, serves both as a spacer, and a method to stir the feed stream, and decrease the polarization gradient. This reduces the risk of scaling, at least when the design of the feed spacer does not create eddies and recirculation regions ((53), (19)).

Curative treatments exist. But they are scale specific (carbonate requires hypochloric acid, while sulfate scale requires soda, ...). Furthermore, the chance of success of these treatments might be very low, and the active layer may be damaged in the process of cleaning.

c) Bio-fouling

(1) Bio-fouling: a sequential process
Biofouling is the third important reason for flux decline after scaling and polarization concentration, letting aside membrane degradation (chlorine attack, compaction ...). It has been reported that less than 3 days were required for a biofilm to cover completely a reverse osmosis membrane. (24)

As shown by Goosen (54) and Wahl (55), fouling is a sequential process.

- Transport of the fouling agent up to the surface: the fouling macro-molecule are conveyed by the water and have a tendency to be directed onto the membrane. Both the polarization gradient, Brownian motion and the electrostatic forces between the molecules and the surface have their importance at this stage.
- Attachment to the substratum and growth at the surface: A macromolecular film composed of proteins, lipids, DNA and polysaccharides first colonize the surface during a phase of biochemical conditioning: the physical and chemical properties of the surface are altered. This film is well known under the name of EPS (extracellular Polymeric Substance).

(a) PA01 dead cell layer

(b) PA01 biofilm layer
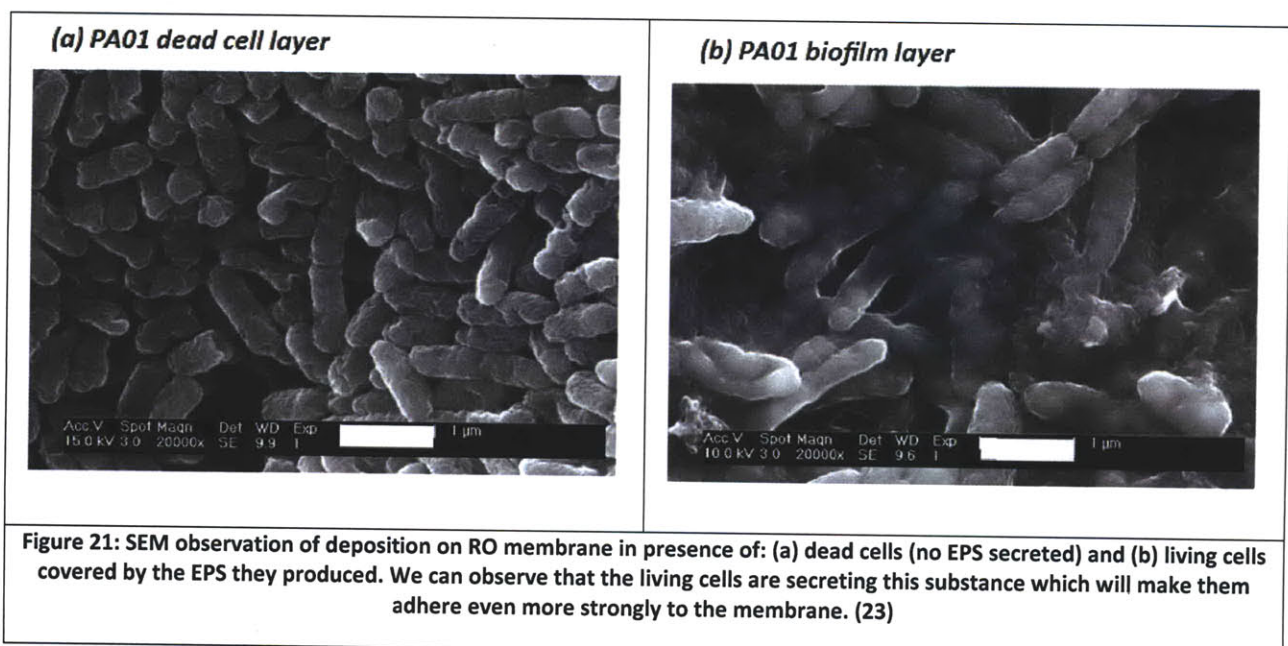
Figure 21: SEM observation of deposition on RO membrane in presence of: (a) dead cells (no EPS secreted) and (b) living cells covered by the EPS they produced. We can observe that the living cells are secreting this substance which will make them adhere even more strongly to the membrane. (23)

- This film allows a bacterial colonization of the surface first with a reversible adsorption and then with the irreversible adhesion of bacteria to the film.
- The surface is then colonized by unicellular eukaryonts (diatoms, protozoa and yeasts), first form of biological activity to settle. The cells can secrete substance to form the EPS film around them, and be even more robustly anchored on the membrane.

(2)   Role of membrane properties on fouling sequence

A number of membrane properties play an important role in the microbial adhesion (roughness, hydrophilicity, surface charge, affinity with bacteria,...). Most of these are bacteria specific. For example, if the size of the features on the surface of the membrane is smaller than the macromolecule, it might prevent a strong attachment to the membrane. On the other hand, larger features might provide settlement area. Charge configuration is also very macromolecular specific.
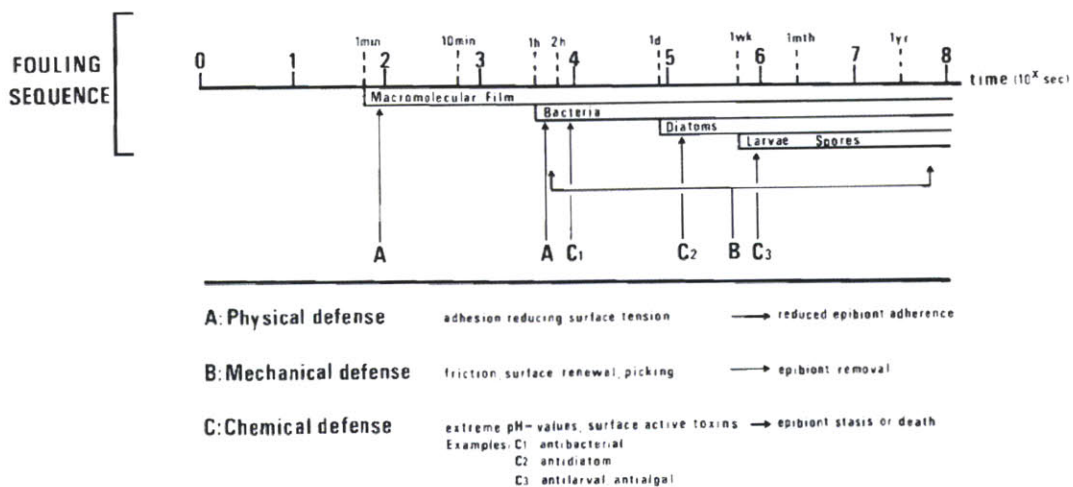
Fig 3 Examples of antifouling defense adaptations with their respective target zones during the fouling sequence. For example while physical defense activity is limited to the processes of initial adsorption onto a young surface, sloughing may act at all levels

Figure 22: Examples of antifouling defenses and target zones during the fouling sequence in seawater environment (from (55))

(3)   Importance of bio-fouling on permeation properties.

Once again, bio-fouling has several impacts on the permeation properties of RO membranes:

- As observed by Elimelech et al. (35), the cell layer is thought to enhance polarization by decreasing the mixing parameter of the boundary layer. It results in a change in permeation properties: salt concentration is increased on the outer surface of the active layer, decreasing both salt rejection and water flux (increased osmotic pressure).

- The formation of the dense EPS film (see Figure 21) explains the irreversible decrease in flux of the membrane. The cells attached to the membrane produce this matrix, which forms a 10-20 microns (54) thick film, which degrades both the adsorption and permeability parameters.
- The hydraulic resistance of the film (i.e. in the feed channel between the inlet and concentrate outlet) is also degraded with the formation of the bio-fouling layer. It is due both to the fouling on the spacer and on the membrane itself.
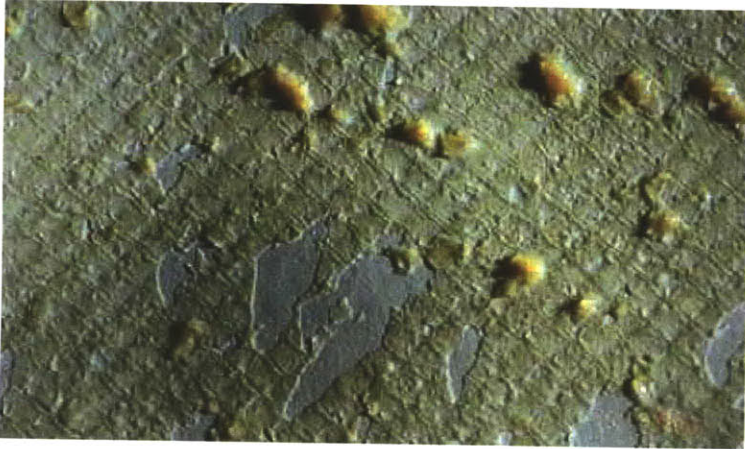
Figure 23: bio-film can develop in 3 to 5 days on a membrane (24)
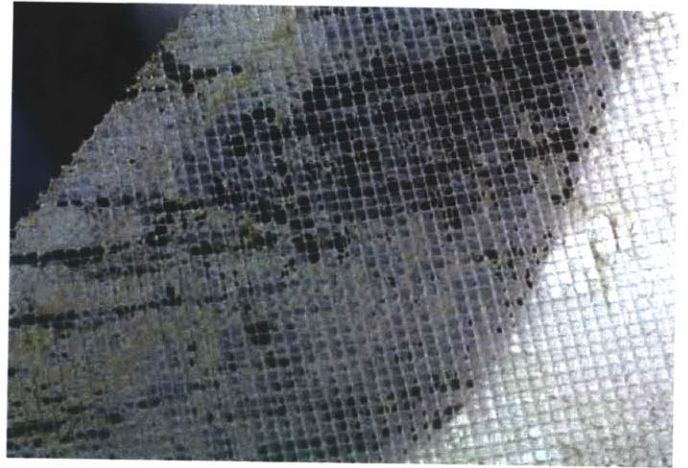
Figure 24: picture of a feed spacer with bio-fouling (24)

(4)   treatment for bio-fouling RO on membranes

We have already described the chemical preventive methods for bio-fouling, mainly with the addition in the feed water of biocids (chlorine, ozone ...).

A very frequent physical preventive/ curative (for early treatment) method is the backwash of membranes. the flow is reverse, and clean water goes from the permeate channel to the feed channel. In the event of reversible fouling, this allows to remove most of the bio-fouling and recover the initial permeation properties.

Chemical curative treatments depend on the stage of the bio-fouling. Soda can be used when the element is still in-line (i.e. producing clean water). Peroxide hydrogen, hot water or even a shock injection of free chlorine can be used for off-line elements that are more severely fouled.

d)   Boron removal

(1)   Relevance of Boron

Among all salts, one has gained a tremendous interest for reverse osmosis in the last few decades: Boron. Boron is used in large quantities for making detergents, and reclamation and surface water can have relatively large concentration of Boron. WHO set up a guideline value for Boron concentration of

.5mg/L in drinking water (1) , and some trees requires an irrigation water with as low as .2mg/L (56), while Boron concentration in seawater is usually in the range 5-6ppm.

(2)   Low rejection of boron due to its apolar complex at normal pH.

The reason why Boron gains such an interest is due to the low rejection rates of the membranes. At neutral pH, Boron is present in water as boric acid, which dissociates only at high concentration and high pH, according to:

$$\begin{cases} H_3BO_3 \leftrightarrow H_3O^+ + H_2BO_3^-, \text{with } pKa_1 = 9.14 \\ H_2BO_3^- \leftrightarrow H_3O^+ + HBO_3^{2-}, \text{with } pKa_3 = 12.74 \\ BO_3^{2-} \leftrightarrow H_3O^+ + BO_3^{3-}, \text{with } pKa_3 = 13.8 \end{cases}$$
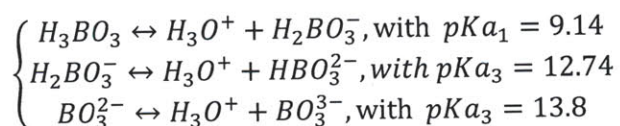
As a result, most of the Boron is in a non ionic and apolar form and weakly hydrated. This is very detrimental to the rejection performance of membranes (see Figure 25). Rejection of H_3BO_3 can be as low as 60 to 90% for membranes whose TDS or $H_2BO_3^-$ rejection are from 99 to 99.8%.
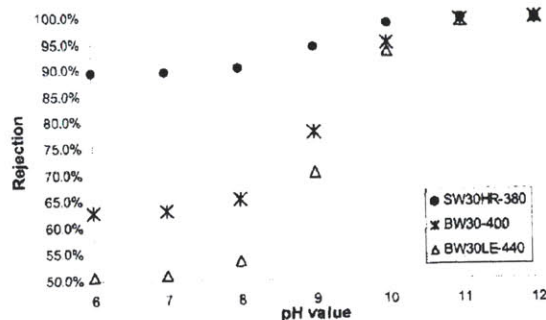
Figure 25: Boron rejection of 3 different Filmtec RO membranes (from (57))

(3)   Design of RO plants around Boron rejection

This alone brought the development of multi-passes desalination plants. The epitome of multi-passes reverse osmosis is Ashkelon plant, where the water is treated through a 4 pass process (7) to achieve desalination and Boron reduction to values lower than .4mg/L. The first pass is operated at low recovery (45%) and decreases drastically the TDS. A second pass at high pH and high recovery (85%) was added to remove Boron. The brine of this pass was treated at low pH (to avoid scaling) and high recovery (85%). To reduce the Boron concentration even more, the permeate of the third pass goes through a Boron specific RO pass: high pH-high recovery (90%).

F. Conclusion

In normal operation, seawater reverse osmosis is a very efficient technology. However, the chore of the technology (the polymeric reverse osmotic membranes) is very sensitive to fouling and treatment that are usually used to deter bio-life. This results in high capital costs to install adapted pre-treatments, requires a relatively high manpower for maintenance and translates into degraded permeation performance (due to the formation of a bio-film). In the end, non fouling (or low fouling) reverse osmosis membranes are one of the most needed technologies to lower the cost of water production in many aspects.
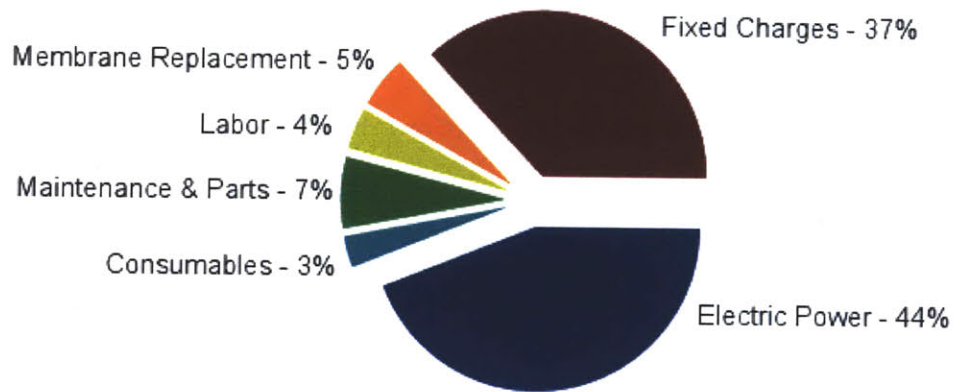
Figure 26: Cost breakdown for seawater RO systems. Non fouling membranes would allow to lower the cost of most of the important budgets of RO plants (from (58))

G. Bibliography for chapter I.

1. **World Health Organization.** *Guideline for drinking water (3rd edition).* 2006.

2. **Robert Engelman (Population Action International).** *People in the balance- Population and Natural resources at the Turn of the Millennium.* 2000.

3. **(US), National Research Council.** *Review of the desalination and water purification technology roadmap.* s.l. : Committee to Review the Desalination and Water Purification, 2002.

4. **Cashman, Preene.** *Groundwater lowering in construction: a practical guide.* s.l. : Spon press, 2001.

5. Water Quality Association, Glossary . [Online] as of October 2009. http://www.wqa.org/.

6. **Pearce.** *When the Rivers Run Dry: Water--The Defining Crisis of the Twenty-first Century .* s.l. : Beacon Press books, 2006.

7. *Ashkelon desalination plant — A successful challenge.* **Sauvet-Goichon.** 2007, Desalination, Vol. 203, pp. 75–81.

8. *Handbook of Inorganic Chemical Compounds.* s.l. : McGraw-Hill, 2003.

9. *Enhancing RO system performance utilizing antiscalants.* **Ghafour.** 2002, Desalination, Vol. 153, pp. 149-153.

10. *Limits of RO recovery imposed by calcium phosphate precipitation.* **Greenberg.** 2005, Desalination, Vol. 183 , pp. 273–288.

11. **Dow water solution.** *Filmtech reverse osmosis membrane: Technical manual.* 2003.

12. *Engineering design of Skikda Seawater Desalination Plant, Desalination and Water Treatment.* **Fanjul.** 2009, Desalination and Water Treatment, Vol. 7, pp. 206–213.

13. *Reverse osmosis desalination: Water sources, technology, and today's challenges.* **Greenlee.** 2009, Water Research, Vol. 43, pp. 2317-2348.

14. *Second law analysis of a reverse osmosis plant in Jordan.* **Aljundi.** 2009, Desalination, Vol. 239, pp. 207-215.

15. *State of the art of reverse osmosis desalination.* **Fritzmann.** 2007, Desalination, Vol. 216, pp. 1-76.

16. *Development of the fourth generation energy recovery device. A CTO's Notebook.* **Stover.** 2004, Desalination, Vol. 165, pp. 313-321.

17. *Effect of recent technological developments on SWRO incorporated in the Red-Dead project.* **Glueckstern.** 2009, Desalination and Water treatment, Vol. 5, pp. 132-136.

18. *Hollow fine fiber vs. spiral-wound RO desalination membranes Part 2: Membrane autopsy.* **Butt.** 1997, Desalination, Vol. 109 , pp. 83-94.

19. *Modeling the impacts of feed spacer geometry on reverse osmosis and nanofiltration processes.* **Gilllen.** 2009, Chemical Engineering Journal, Vol. 149, pp. 221–231.

20. *Spiral wound modules and spacers Review and analysis.* **Ribeiro.** 2004, Journal of Membrane Science, Vol. 242, pp. 129–153.

21. *Characterization of a zigzag spacer for ultrafiltration.* **Schwinge.** 2000, Journal of Membrane Science, Vol. 172, pp. 19–31.

22. *Study of the effects of spacer geometry in membrane feed channels using three-dimensional computational flow modeling.* **Shakaib.** 2007, Journal of membrane science, Vol. 297, pp. 74-89.

23. *Biofouling of reverse osmosis membranes: Role of biofilm-enhanced osmotic pressure.* **Herzberg.** 2007, Journal of Membrane Science, Vol. 295, pp. 11–20.

24. **Dow Chemical.** *Technical manual, Form No. 609-00071-0309.*

25. **Hoff, Jacobus Henricus van 't.** *Osmotic pressure and chemical equilibrium, Nabel lecture.* 1901.

26. *A new thin-film composite seawater reverse osmosis membrane.* **Cadotte.** 32, 1980, Desalination, pp. 25-31.

27. *Development of crosslinked fully aromatic polyamide ultra-thin composite membranes for seawater desalination.* **Kurihara.** 1994, Desalination, pp. 133-144.

28. *Reformulation of the solution-diffusion theory of reverse osmosis .* **Paul.** 2004, Journal of membrane science, Vol. 241, pp. 371-389.

29. **Cadotte.** *Interfacially synthesized reverse osmosis membrane. 4,277,344* 1981.

30. *Effect of membrane chemistry and coating layer on physiochemical properties of thin film composite polyamide RO and NF membranes.* **Tang.** 2009, Desalination, Vol. 242, pp. 168-182.

31. *Impacts of support membrane structure and chemistry on polyamide-polysulfone interfacial composite membranes.* **Ghosh.** 2009, Journal of Membrane Science, Vol. 336, pp. 140-148.

32. *New membrane developments expanding the horizon for the application of reverse osmosis technology.* **Gerard.** 1998, Desalination, Vol. 119, pp. 47-55.

33. *Surface properties of Reverse Osmosis Membrane.* **Yao.** 2007, Journal of Applied polymer science, Vols. 105-3, pp. 1261 – 1266.

34. *Effect of skin layer surface on the flux behavior of RO membranes.* **Hirose.** 1996, Journal of membrane science, Vol. 121, pp. 209-215.

35. *Role of membrane surface morphology in colloidal fouling of cellulose acetate and composite aromatic polyamide reverse osmosis membranes.* **Elimelech.** 1997, Journal of membrane science, Vol. 127, pp. 101-109.

36. *Leading Edge Technology on Commercially Available Membranes vs. Innovative Membranes in the R&D Stages.* Asilomar, CA : s.n., Feb. 2009. ACS conference.

37. *The Reaction of Cellulose Acetate with Acetic Acid and Water.* **Hiller.** 1953, Journal of polymer science, Vols. 10-4, pp. 385-423.

38. *Optimization of the intermittent chlorine injection (ICI) method for seawater desalination RO plants.* **Fujiwara.** 2008, Desalination, Vol. 229, pp. 231-244.

39. *Kinetic study of the hydrolysis of cellulose acetate in the pH range of 2-10.* **Kenneth.** 1966, Journal of applied polymer science, Vol. 10, pp. 825-832.

40. **Baker.** *Membrane technology and application.* s.l. : Jahn Wiley and sons editions , 2004.

41. *Study on hypochlorite degradation of aromatic polyamide reverse osmosis membrane.* **Kang.** 2007, Journal of membrane science, Vol. 300, pp. 165-171.

42. **Zhou.** *Simulations of Polymeric Membrane Formation in 2D and 3D.* s.l. : PhD thesis at MIT , 2006.

43. *Transport properties of cellulose acetate osmotic membranes.* **Lonsdale.** 1965, Journal of applied polymer science, Vol. 9, pp. 1341-1362.

44. *Experimental study of water and salt fluxes through reverse osmosis membranes.* **Zhou.** 2005, Environment science technology, Vol. 39, pp. 3382-3387.

45. *Non-linear behavior of permeate flux in full-scale reverse osmosis process.* **Tay.** 2005, Journal of environmental engineering, pp. 1481-1487.

46. **Mudler.** chap. 4: Transport in membrane. *Basic principle of membrane technology.* s.l. : Kluwer academic publishers, 1996.

47. *Effect of porous support fabric on osmosis through a Loeb-Sourirajan type asymmetric membrane.* **Loeb.** 1997, Journal of Membrane Science, Vol. 129, pp. 243-249.

48. *Concentration polarization in ultrafiltration and reverse osmosis: a critical review.* **Sablani.** 2001, Desalination, Vol. 141, pp. 269-289.

49. *Estimation of mass transfer coefficient using a combined nonlinear membrane transport and film theory model.* **Murthy.** 1997, Desalination, Vol. 109, pp. 39-49.

50. **Mudler.** chap. 7: Polarisation phenomena and membrane fouling. *Basic principle of membrane technology.* s.l. : Kluwer academic publishers, p. 1996.

51. *Modeling concentration polarization in reverse osmosis processes.* **Kim.** 2005, Desalination, Vol. 186, pp. 111-128.

52. **Amjad.** *Reverse Osmosis; Membrane Technology, Water Chemistry and Industrial Application.* [ed.] Van Nostrand Reinhold. 1992.

53. **Costa, Da.** *Fluid flow and mass transfer in spacer-filled channels for ultrafiltration, PhD thesis.* s.l. : School of chemical engineering and industrial engineering, University of New South Wales, 1993.

54. *Fouling of reverse osmosis and ultrafiltration membranes: a critical review.* **Goosen.** 2004, Separation Science and Technology, Vol. 39 (10), pp. 2261-2298.

55. *Marine epibiosis. I.Fouling and antifouling: some basics aspects.* **Wahl.** 1989, Mar. Ecol. Prog. Ser. , Vol. 58, pp. 175-189.

56. *Boron removal from desalinated seawater and brackish water by improved electrodialysis.* **Oren.** 2006, Desalination, Vol. 199, pp. 52–54.

57. *Boron removal from seawater using FILMTECTM high rejection SWRO membranes.* **Redondo.** 2003, Desalination, Vol. 156, pp. 229-238.

58. **Miller.** *Review of Water Ressources and Desalination Technoloies.* Sandia National Laboratories. 2003.

59. *Marine epibiosis. I.Fouling and antifouling: some basics aspects.* **Wahl.** 1989, Mar. Ecol. Prog. Ser. , Vol. 58, pp. 175-189.

60. Volume 4: Marine and Industrial Biofouling. *Surface Modification Approach to Control Biofouling, Marine and Industrial Biofouling.* s.l. : Springer Series on Biofilms.

61. *Settlement of Ulva Zoospores on Patterned Fluorinated and PEGylatedMonolayer Surfaces.* 2008, Langmuir, Vol. 24, pp. 503-510.

62. *Engineered Nanoforce Gradients for Inhibition of Settlement (Attachment) of Swimming Algal Spores.* **Schumacher.** Langmuir : s.n., 2008, Vol. 24, pp. 4931-4937.

63. *Bioinspiration—the solution for biofouling control?* 2009, Bioinsp. Biomim. , Vol. 4, p. 015007.

64. *Approaches in designing non-toxic polymer surfaces to deter marine biofouling.* 2009, Soft matter, Vol. 5, pp. 4088–4100.

65. **Fleming.** Biofouling in RO systems. [book auth.] Amjad. *Reverse Osmosis. Membrane Technology Water Chemistry and Industrial Applications.* s.l. : Van Nostrand Reinhold, 1993.

66. *Bioinspiration—the solution for biofouling control?* **Ralston.** 2009, Bioinsp. Biomim., Vol. 4, pp. 1-9.

67. *A preliminary approach to epidermal antimicrobial defense in the Delphinidae.* **Meyer.** 2004, Marine Biology, Vol. 144, pp. 841–844.

68. *The influence of Natural Surface Microtopographies on Fouling.* **Bers.** 2004, Biofouling, Vol. 20, pp. 43-51.

69. *Learning from nature: Non-toxic biofouling control by.* **A. Kesel, R. Liedert.** 2007. Comparative Biochemistry and Physiology, Part A 146 ; A7–BIOMIMETICS AND BIOMECHANICS — SMART SOLUTIONS FROM NATURE. pp. S129–S141.

70. *Cells lying on a bed of microneedles: An approach to isolate mechanical force.* 4, 2003, PNAS (Proc. of Nat. Ac. of Science), Vol. 100, pp. 1484–1489.

71. *Engineering Shark skin and other solutions.* **Ball.** 1999, Nature, Vol. 400, pp. 507-509.

72. *Development and Testing of Hierarchically Wrinkled Coatings for Marine Antifouling.* **Efimenko.** 2009, Applied material and interface, Vol. 1;5, pp. 1031–1040.

73. **Wierzbicki.** *Lecture notes for the class "Plate and Shells" at MIT.* s.l. : MIT, 2009.

74. *Herringbone Buckling Patterns of Compressed Thin Films on Compliant Substrates.* **Chen.** 2004, Journal of Applied Mechanics, Vol. 71, pp. 597-603.

75. *Nonlinear analyses of wrinkles in a film bonded to a compliant substrate.* **Huang.** 2005, Journal of the Mechanics and Physics of Solids, Vol. 53, pp. 2101–2118.

76. **Dowling.** 15.10: Energy dissipation in materials. *Mechanical behavior of materials, engineering methods for deformation, fracture and fatigue.* 1999.

77. *Initiated chemical vapor deposition (iCVD) of polymeric nanocoatings.* **Gleason.** 2007, Surface & Coatings Technology, Vol. 201, pp. 9400–9405.

78. *Wrinkled surface topographies of electrospun polymer fibers.* **Wang.** 2009, Appl. Phys. Lett., Vol. 94, p. 151916.

79. *A Stretchable Form of Single-Crystal Silicon for High-Performance Electronics on Rubber Substrates.* **Khang.** 2006, science, Vol. 311.

80. *Ordering of Spontaneously Formed Buckles on Planar.* **Huck.** 2000, langmuir, Vol. 16.

81. —. **Wilhelm T. S. Huck, Ned Bowden, Patrick Onck, Thomas Pardoen, John W. Hutchinson and George M. Whitesides.** 2000, langmuir, Vol. 16, pp. 3497-3501.

82. **Anand, L.** *Mechanics of solids, Lecture notes (MIT 2.071).* 2009.

83. **Nguyen, Q.S.** *Stability and nonlinear solid mechanics.* s.l. : Wiley, 2000.

84. **R., Cook.** *Concepts and applicatoins of Finite Element Analysis, second edition.* s.l. : John Wiley, 1974.

85. **Moler, Cleve.** Eigenvalues and Singular Values. *Numerical Computing with MATLAB.* s.l. : Mathworks, 2004.

86. **Organization), UNESCO-WWAP (World Health.** *World Health Report, Water, a shared responsibility.* 2006.

87. *The search for a chlorine-resistant reverse osmosis Membrane.* **Glater.** 1994, Desalination, Vol. 95, pp. 325-345.

88. *Backwash of RO spiral wound membranes.* **Sagiv.** 2005, Desalination, Vol. 179, pp. 1-9.

89. *Overview of systems engineering approaches for a large-scale seawater desalination plant with a reverse osmosis network.* **Kim.** 2009, Desalination, Vol. 238, pp. 312-332.

90. *Pilot Tests of Multibore UF Membrane at Addur SWRO Desalination Plant, Bahrain.* **Bu-Rashid.** 2007, Desalination, Vol. 203, pp. 229–242.

91. **Wilf.** *Guidebook, membrane desalination technology, Reverse Osmosis, Nanofiltration and Hybrid Systems Process, Design, Applications and Economics.* ISBN 0-86689-065-3.

92. *UF membranes for RO desalination pretreatment.* **Wolf.** 2005, Desalination, Vol. 182 , pp. 293–300.

93. *Le dessalement des eaux par osmose inverse: l'expérience de Véolia Water.* **Gaid.** 2007, Desalination, Vol. 203, pp. 1–14.

94. *Microscopy as a tool for analysis of membrane failure and fouling.* **Roever, De.** 2007, Desalination, Vol. 207, pp. 35–44.

95. **Organization, World Health.** chap 7: Microbial aspects. *Guideline for drinking water (3rd edition),.* 2006.

96. *Pretreatment for desalination of seawater from an open intake by dual-media filtration: Pilot testing and comparison of two different media.* **Mitrouli.** 2008, Desalination, Vol. 222, pp. 24–37.

97. *Seawater filtration for fouling prevention under stormy conditions.* **Tenzer.** 1999, Desalination, Vol. 125, pp. 77-88.

98. *Performance of the Gabès desalination plant.* **Fethi.** 2001, Desalination, Vol. 136, pp. 263–272.

99. *UF/MF as RO pre-treatment: the real benefit.* **Bonnélye.** 2008, Desalination, Vol. 222, pp. 59–65.

100. *Theoretical optimization of spiral-wound and capillary nanofiltration modules.* **Meer, Van der.** 1997, Desalination, Vol. 113, pp. 129-146.

101. *Modeling concentration polarization in reverse osmosis spiral wound elements.* **Marinas.** 1996, Journal of environmental Eng. , pp. 292-298.

102. *Biofouling of spiral-wound nanofiltration and reverse osmosis membranes: A feed spacer problem.* **Vrouwenvelder.** 2009, water research, Vol. 43, pp. 583-594.

103. **Schwinge.** *Experimental & simulation studies of fluid flow in spacer-filled channels in spiral wound modules, Ph.D. Thesis.* s.l. : School of Chemical Engineering and Industrial Chemistry, University of New South Wales, 2003.

104. **GOSS, V.G.A.** *Snap buckling, writhing and loop formation in twisted rods, PhD thesis.* s.l. : Center for Nonlinear Dynamics, University College London, 2003.

105. **Millard P., Ballard A.** *Modelling of slender structures, lecture note.* Palaiseau : Ecole Polytechnique, 2008.

106. *Using Euler buckling springs for vibration isolation.* **Winterflood.** 2002, Class. Quantum Grav., Vol. 19, pp. 1639–1645.

CHAPTER II: A new manufacturing technique

A. Content

B. Introduction

The analysis of the failure modes for current membranes used for water treatment shows a pressing need for membranes with anti-fouling properties. To design an anti-fouling strategy, we have been looking into solutions observed in fouling environments both in the living world and engineered solutions outside the membrane field.

In this chapter, we review two solutions that have recently been found to mitigate fouling. One is based on periodic features that mimic shark-skin. The second is based on a sinusoid-like texture of the membrane. We then use iCVD (initiated Chemical Vapor Deposition) coating to combine the benefits of the chemistry developed by a coworker, Dr Goze Ince Ozaydin, in the lab of Professor Karen Gleason in chemical engineering at MIT and the sinusoidal like texture. After characterization of these samples, we develop a dimensionless analysis along with a numerical model for the formation of those wrinkles (buckling and post-buckling analysis). This direct approach provides a robust method to predict the final coating surface micro-topography for a wide range of stretch conditions, material properties.

C. State of the art of surface topography modification for mitigation of fouling

1. Sequential process of fouling and consequences on anti-fouling coating design strategy

As shown by Wahl (59), fouling is a sequential process, and those antifouling strategies often target different steps of this fouling sequence.

- A macromolecular film (the so called EPS film described in I.B.c)) composed of glycoproteins, proteoglucans and polysaccharides first colonizes the surface during a phase of biochemical conditioning: the physical and chemical properties of the surface are altered.

- This allows a bacterial colonization of the surface first with a reversible adsorption and then with the irreversible adhesion of bacteria to the film.

- The surface is then colonized by unicellular eukaryonts (diatoms, protozoa and yeasts), the first form of biological activity to settle.
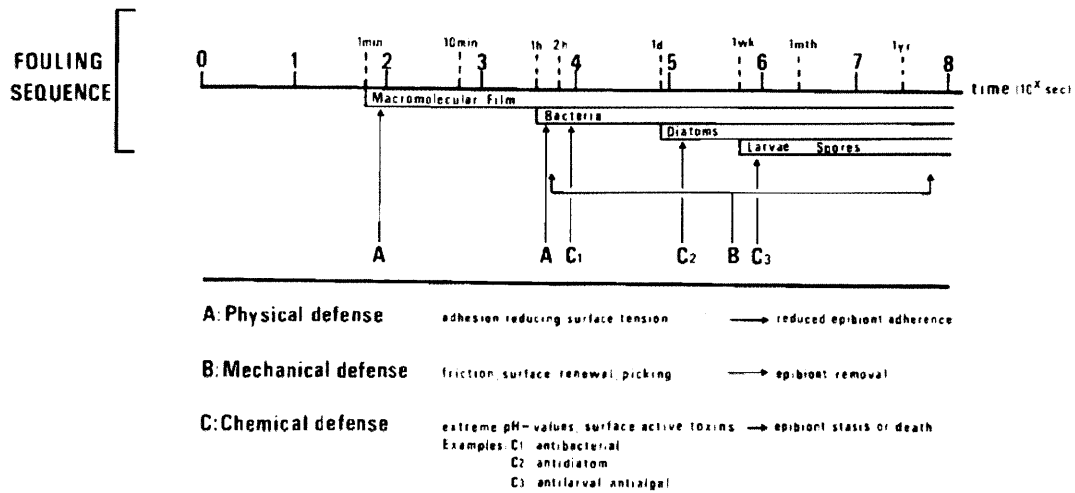
Fig 3 Examples of antifouling defense adaptations with their respective target zones during the fouling sequence. For example while physical defense activity is limited to the processes of initial adsorption onto a young surface, sloughing may act at all levels

Figure 27: Examples of antifouling defenses and target zones during the fouling sequence in seawater environment (from Mar. Ecol. Prog. Ser. 58: 175-189, 1989)

There are mainly three types of antifouling-strategies (60), depending on which step of the fouling sequence it is focusing on:

1. mechanical detachment of biofoulers;
2. killing or inactivation of biofouling organisms
3. surface modification turning the substrate material into a low-fouling or non-sticking (non-adhesive) one.

However, as pointed out by T. Vladkova, the mechanisms of bio-adhesion are still poorly understood. If surface free energy, mechanical properties, and wettability are often recalled as the main parameters for fouling on homogeneous substrates, some other parameters such as heterogeneous chemistry (61), 3D surface patterning (62) or most probably a combination of all those properties (63) are suspected to be keys to the design of anti-fouling substrates (64).

As soon as the EPS film starts to form, the performance of the filtration membrane starts to degrade (65): membrane water flux gradually decreases, trans-membrane pressure increases and salt rejection decreases. Furthermore, it has been shown that it is more difficult to remove attached cells than to inhibit their adhesion in the first place. As a result, we are aiming for a solution to limit the formation of the film in the very early steps, essentially by altering the physical forces (electrostatic interaction, Van-der-Waal forces,...) between the membrane and the polysaccharides.

2. Bio-inspired surface morphology

a) four anti-fouling strategies employed by marine species.
An increasing interest is shown for surface morphology modification, as a way to deter fouling in its early stages. It is thought that certain types of features on the surface of membranes act as unfavorable sites for bacterial adhesion. The efficiency of the micro-topography of the membrane largely depends on the relative length scales of the fouling agents and the features, the height of those features and their exact pattern.

We expect that modern photolithographic techniques will soon enable a better understanding of the relations between surface topology and fouling of bio-organisms and pave the way for patterned membranes with improved anti-fouling properties.

Under pressure of the ship industry (to invent non-harmful antifouling coatings for seawater), bio-medical industry (to provide designers with bio-compatible materials that do not clog and whose properties are not hidden by a bio-film) and membrane industry (especially to advance fouling on membrane for water treatment), intense research is focusing on bio-mimicking, and replicating the strategies applied by marine species to limit fouling (66).

- Among those strategies, secretion of protective substances has been known for a long time (67) to serve as a non-specific defense against bacteria and fungi.

- Behavioral strategies have also been observed in marine species (change in salinity, bury into the ground or emerge into air).

- Chemistry of the surface of those organisms is also very important (surface energy, chemical components...). We are working on this project with collaborators in the Chemical Engineering Department at MIT who are working on this aspect.

- Physical considerations are also part of marine species anti-fouling strategy, most importantly with surface topography. Ultra-smooth surfaces are often seen as beneficial as they do not offer refuge from shear stresses. However, a few topographies have been shown to exhibit good anti-fouling performance. We are reviewing in the next section the transient anti-fouling property of several shellfish, before presenting a new artificial patterning method based on Shark skins and wrinkled membranes.

b)   Transitory anti-fouling property of shellfishes

Bers et al. (68) used high resolution resins to replicate surface mircotopographies of four marine organisms, known to have low fouling properties: *Cancer pagurus, Mytilus edulis, Ophiura texturata* and the eggcase of *Scyliorhinus canicula*. As shown in Figure 28, those species exhibit rough surfaces over different length scales. Depending on the species, the features range from several hundreds of microns to one micron. They replicate those topographies to decouple chemistry and physical effects from the surface topology of those organisms.
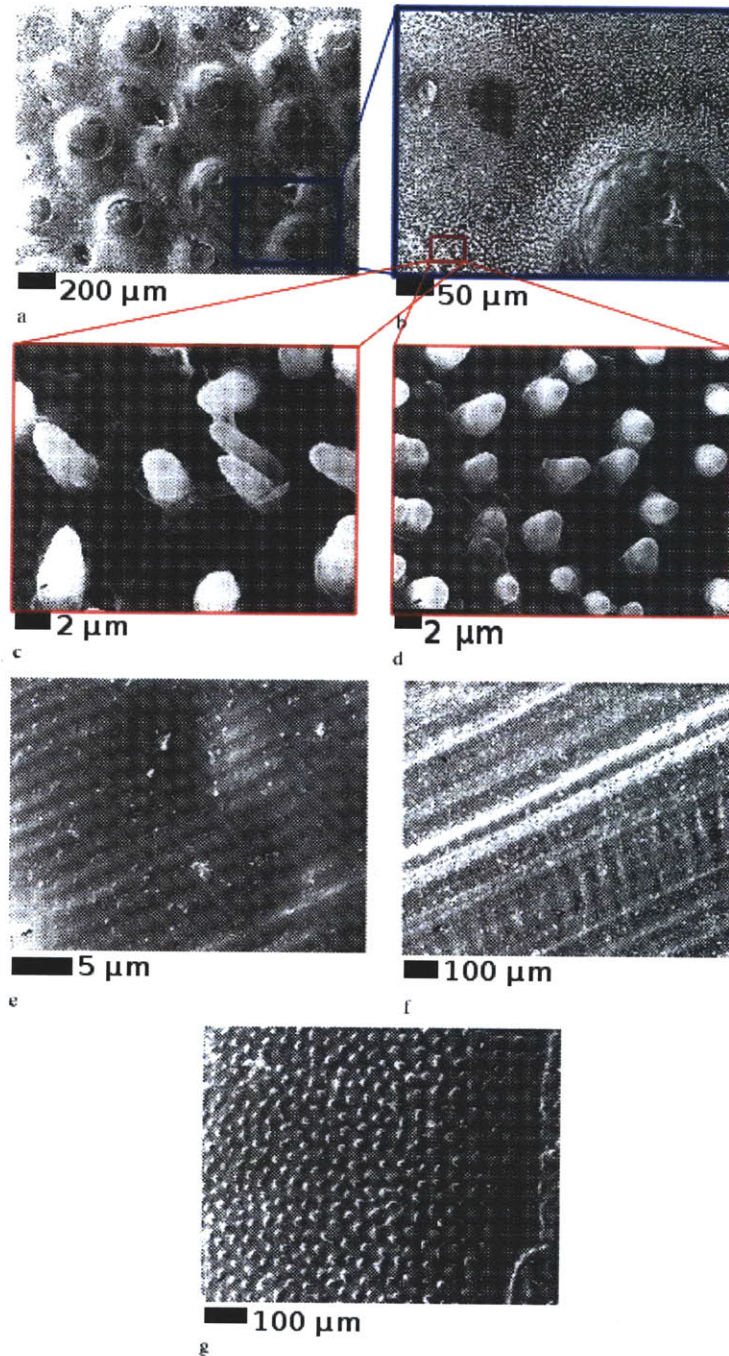
Figure 28: SEM images of surface micro-structure of 4 differents marine organisms (a-c/ carapace of C. pagurus, d/surface structure of high resolution resin replicate of C. paragurus micro-topography; e/periostracum of M. edulis; f/ structure of high resolution replica of egg case of S. canicula; g/ surface structure of O texturata) from (68). These micro-structures were studied for their low fouling performance especially with macrofoulers (e.g. fungi, diatoms, protozoans)

After exposition to natural fouling in field experiments, the performance of the topography was determined by computing the surface relative recruitment. This surface recruitment is defined by the relative number of fouling particles on the textured surface and on the smooth one, after a given period of time. Their conclusions are very positive. Although the anti-fouling characteristic is mostly transitory

and foulant specific, a clear drop (up to 60%) in the surface recruitment is observed in the first few days as represented on Figure 29.
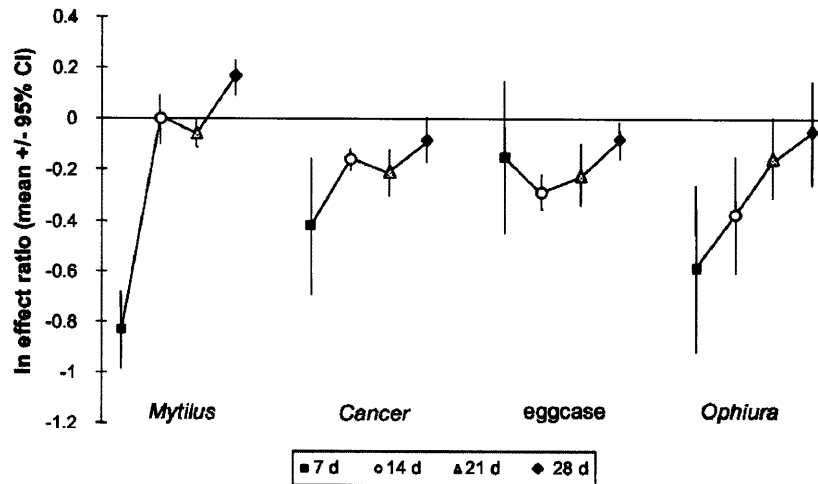
Figure 29: recruitment ratio of macro-foulers in field tests between micro-structured and smoothen substrate. From (68).

c) *Shark skin AF: a bio-inspired material*

In 2008, Shumacher et al. (62) focused on replicating shark skin. They fabricate a PDMS substrate with patterned surfaces composed of small micrometer-size features. Similarly to shark scales (Figure 30), their features are organized within diamond shape repeating unit (Figure 31). Each unit is composed of seven posts of same height (3µm) and width (2µm) but different length (from 4 to 16 µm). They expect to reproduce the low fouling properties (up to 67% of reduction of fouling by barnacle settlement as shown in (69)) of these shark skins.

Those patterned surfaces are astonishingly efficient as anti-fouling surfaces, and as shown by Figure 35, the Ulva spore settlement is reduced by a factor 3 compared to the smooth surface.

The proposed explanation for the anti-fouling property is a disturbance in the 1st step of the fouling sequence. By varying the size of neighbor features, they create what they described as nano-force gradient surfaces. Based on an equal deflection at the top of two neighbor features of different sizes (and bending stiffness), the author predicted that a force would be applied on any particle bridging any two features.

The spore is surrounded by a lipoprotein plasma membrane, which searches the surface of the substrate, looking for a favorable spot. The inhomogeneities of the patterned surface would result in sliding of this medium, allowing only a reduced number of spores to permanently attach to the substrate. More specifically, they assume that the difference in stiffness of the features is responsible for a nano-force gradient (shown in Figure 32) which disrupts the normal process of cementing of the protein membranes.

[This reasoning for nano-force gradient is based on the method developed by Tan et al.(70) to study an array of PDMS posts. In this article, Tan et al. had described the behavior of the slender posts by a classic Euler beam theory in bending. Modeling the force F exerting by a post as a function of the deflection w at the top of the post of Young's modulus E, height L and moment of inertia I by $F = \left(\frac{3EI}{L^3}\right)^{-1} w$. Though, Shumacher et al. further suppose that two neighbor features should deflect of the same amount, without justifying this hypothesis. They also suppose that their features (which are no longer slender structures) will not deform in torsion but still in a global bending].
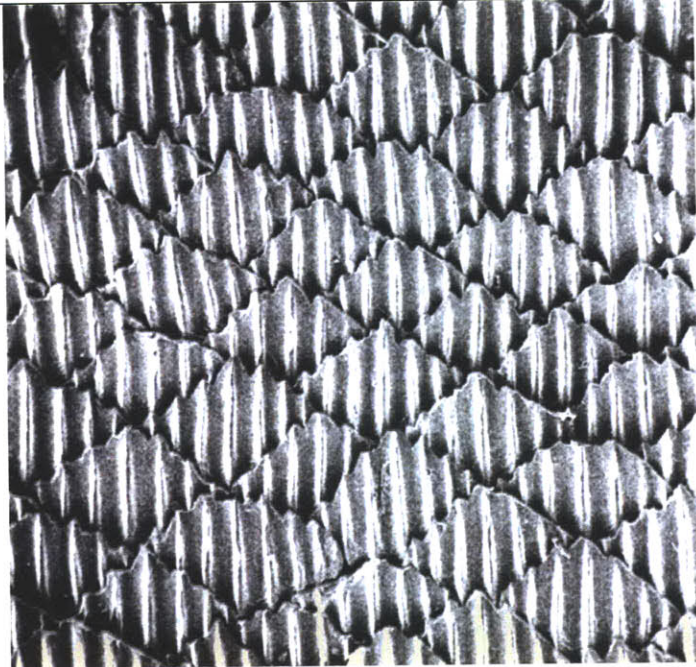
Figure 30: Riblets on a Shark skin provides superior aerodynamics properties (from (71)). No lengthscale bar was displayed in the source, but Shark scale are 100μm to 1mm long. One scale is composed of several riblets (here seven per scale)
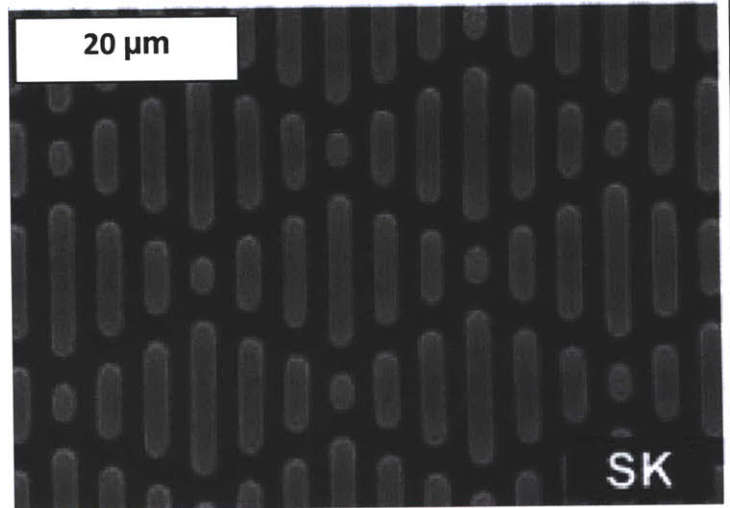
Figure 31: Shark skin AF is a PDMS substrate reproducing the pattern of the real shark skin. The PDMS casted onto a mold and peeled off. The features are 3μm high. (from (62))
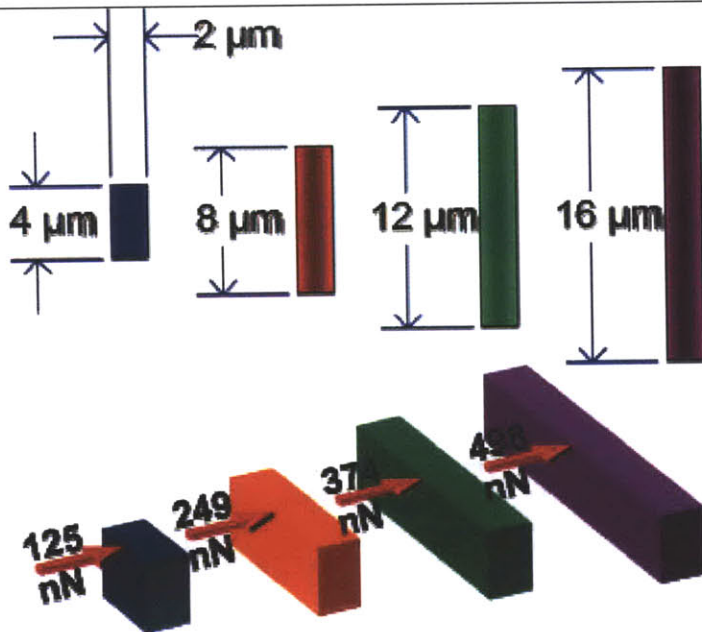
Figure 32: Nano-force gradient are supposed to explain the antifouling properties of the Shark skin AF. Supposing an equal deflection of two neighbor features, the difference of bending rigidity of those features results in a force named the nano-force. By repeating periodically those pattern with features of different size, we obtain a surface of "nano-force gradient". From (62)
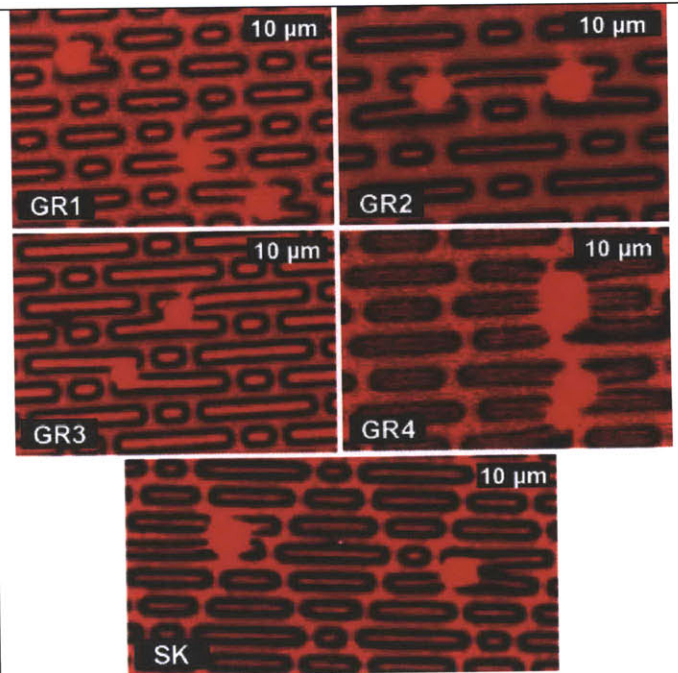
Figure 33: Light micrograph of spores bridging the gap between two neighboring features. Most spores are sitting on so called preferred settlement regions, and the deflection of the PDMS features is noticeable. From (62)
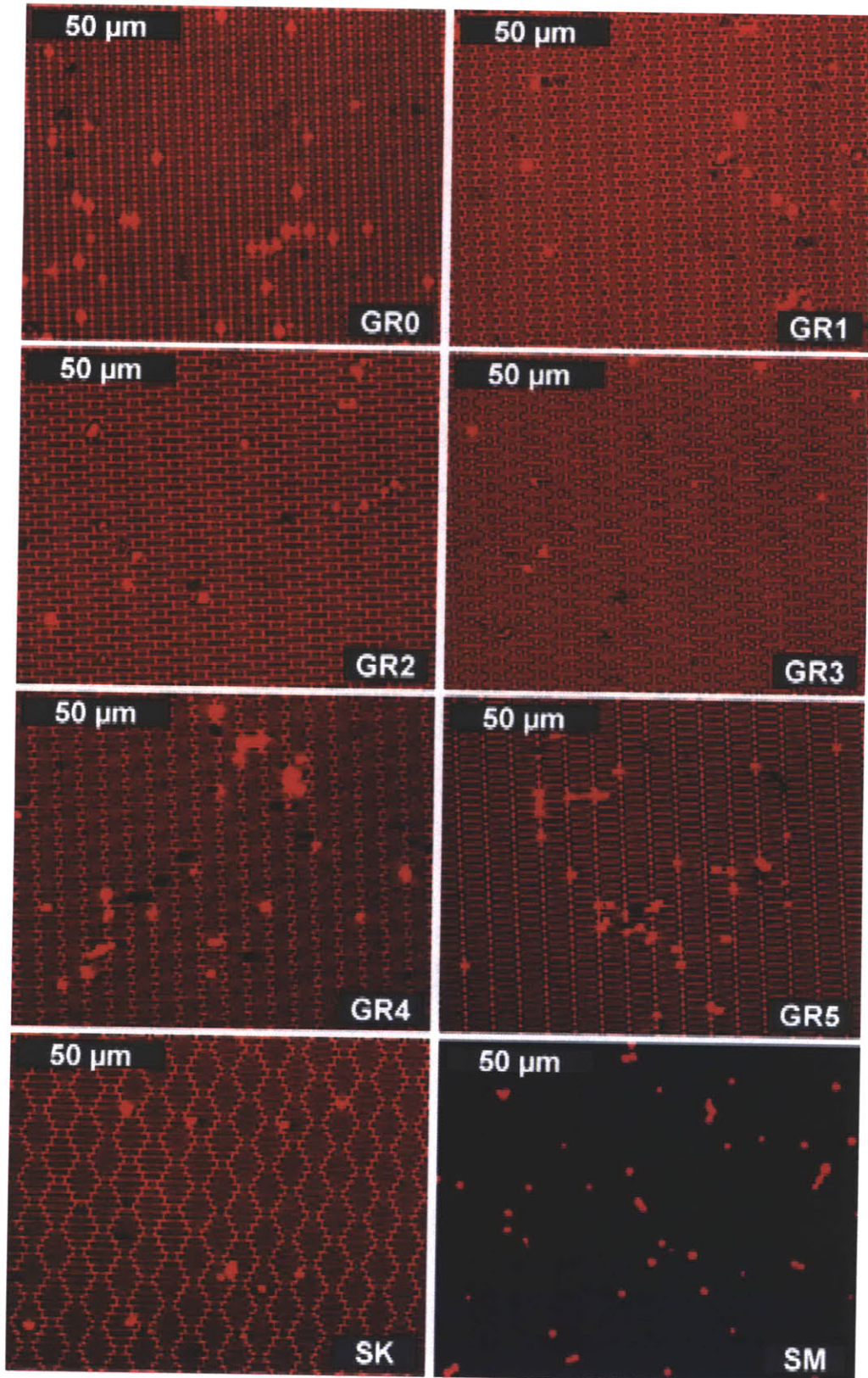
Figure 34: Light micrographs of spores (ulva) colonizing gradient surfaces (GR0 -> GR5 are surface with respective nano-force gradient 0nN;125nN;249nN;374nN;125nN;0nN ; SK is the Shark-Skin; SM is the smooth surface) from (62)

Spore Density (spores/mm^2)

	SM	GR5	GR0	GR4	GR2	GR1	GR3	SK
Mean	484	442	358	358	297	258	229	160
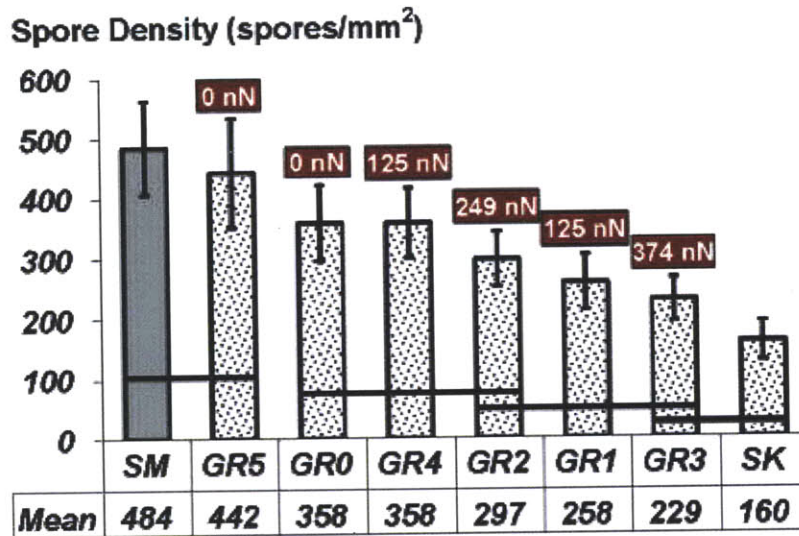
Figure 35: Spore density settlement on pattern surface. The mean spore density is represented on this histogram as a function of the type of patterning (see Figure 34). The "nano-force" is highlighted in red. From (62)

3.   Wrinkles and low fouling properties.

Extending on the idea of patterning membranes to improve their anti-fouling properties, Efimenko et al. (72) formed wrinkles on a PDMS membrane. Those wrinkles naturally appear upon buckling of a stiff skin on a soft substrate. More precisely, a flat PDMS substrate is cast, before being stretched. Once stretched, a UV treatment will form a stiff skin layer on this membrane. Upon release of the stretch, the skin layer is put in compression and will buckle in a sinusoid-like shape.

After making this membrane, Efimenko et al. exposed a PDMS flat sample and a wrinkled sample in seawater for 4 weeks. The two samples are collected (Figure 36 left column) and rinsed with a water stream (Figure 36 right column). This seawater field study shows the effectiveness of the wrinkles in limiting the adhesion of macro-fouling organisms, as well as improving their removal.

However, their laboratory fouling tests show that spores settle in valleys of wrinkles or cracks in the coating (see Figure 37). As a result, improving the quality of the coating (reducing crack size and frequency, obtaining a more conformal coating to not lose the smallest features and defining better patterning) is crucial to the success of this method.

as collected after 4 weeks in seawater

after water stream cleaning

Flat substrate

micro-wrinkled substrate

Figure 36: Comparison of flat PDMS (top figures) and unidirectional wrinkled PDMS (bottom figures) after 4 weeks exposure in a marine environment. Anti-adhesion performances are assesed by the differencial color of the two samples as remove from the seawater. Removal properties are assessed by the differential color before and after rinsing the sample with a water stream (from (72))
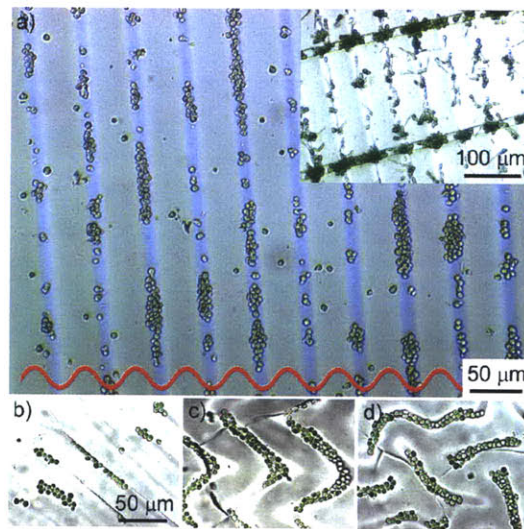
Figure 37: Optical micrograph of a wrinkled sample exposed to a micro-fouling test. The Ulva spores settle in the valleys of the wrinkles or in the cracks of the coating. (from (72))

Those are the reasons why we have developed a method to efficiently combine chemistry and surface topography. Instead of using a pre-patterned surface that we coat, we think that taking benefit from the mechanics of the thin coating to form the wrinkles is a new and a very promising method for high-rate production of low-fouling surfaces applied to many different type substrates.

D. Buckling instability of a hard coating on a soft elastic foundation

1. Scaling analysis: energy in the coating and in the substrate

This example of wrinkles, along with the following experimental and numerical sections, is based on the buckling instability of a stiff coating in compression on a soft elastic foundation. This instability is due to the fact the situation with the energy of the coating in compression is larger than the sum of the bending energy and the energy due to the substrate deformation. An example of a first buckling mode is shown in 2D for a plane strain configuration in Figure 38.
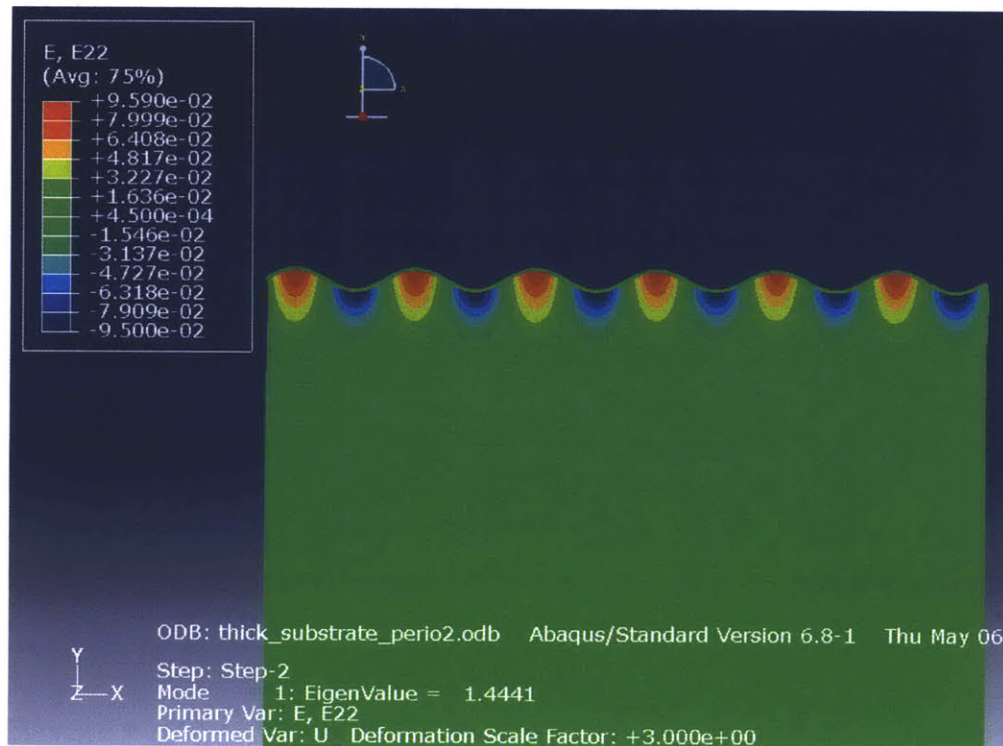
Figure 38: First buckling mode for a hard coating in compression on top of an elastic substrate in the 2D case. The strain in the direction normal to the coating is shown here. This simulation was performed on the Finite Element Code Abaqus, for a relative thickness coating-substrate of 1/200 and a relative stiffness of 500, using plane strain elements.

Wang et al. recently developed a scaling analysis based on the energy of the coating and the substrate.

It is assumed that the deflection is given by

$$u_y(x) = A sin\left(\frac{2\pi x}{\lambda}\right).$$

The bending energy carried by the buckled coating depends on the amplitude A of the wrinkles and their wavelength λ. Writing ρ the curvature, λ the wave length and t the thickness of the coating, the bending energy E_{bend} for a section of sine wavelength and unit width of the coating becomes:

$$E_{bend} = \int_{coating} \frac{1}{2}\overline{E}_c I.\left(\frac{1}{\rho(x)}\right)^2 dxdy$$

$$\sim \overline{E_c} t^3 \left(\frac{A}{\lambda^2}\right)^2 . \lambda$$

$$\text{since} \frac{1}{\rho} \sim \frac{d^2 w}{dx^2} \sim \frac{A}{\lambda^2}$$

For the substrate, we estimate the stored energy E_{subst}, to be:

$$E_{subst} = \int \bar{E}_s \epsilon^2 dx dy dz$$

$$\sim \bar{E}_s \left(\frac{A}{\lambda}\right)^2 . \lambda^2$$

where the substrate strain is $\epsilon \sim \frac{A}{\lambda}$ and affects a height λ of the substrate

The total energy of the system then scales by:

$$U \sim E_{bend} + E_{subst}$$

$$\sim \frac{\overline{\overline{E_c}} t^3 A^2}{\lambda^3} + E_s A^2$$

At equilibrium,

$$\frac{\partial U}{\partial \lambda} = 0$$

Given the wavelength scaling:

$$\lambda^3 \sim t^3 \frac{\overline{\overline{E_c}}}{E_s}$$

This scaling analysis provides a scaling law for the wavelength of the oscillations. We should extend this analysis to determine a critical stretch ϵ_0 for which structure will buckle.

The sum of the bending energy of the coating and the substrate energy should be compared to the in-plane energy of the coating in compression:

$$E_{memb} = \int_{coating} \overline{E_c} S . \epsilon_0^2 da$$

$$\sim \overline{E_c} . t . \epsilon_0^2$$

We should relate the amplitude of the oscillation to the strain, in the limit of small oscillations:

$$\epsilon_0 = \frac{l - l_0}{l_0} = \left(\int_0^\lambda \sqrt{1 + \left(\frac{2\pi A}{\lambda} . sin\left(\frac{2\pi x}{\lambda}\right)\right)^2} \, dx - 1 \right) * \frac{1}{\lambda}$$

$$\sim \left(\int_0^\lambda 1 + \frac{1}{2}\left(\frac{2\pi A}{\lambda} . sin\left(\frac{2\pi x}{\lambda}\right)\right)^2 dx - 1 \right) * \frac{1}{\lambda}$$

$$\epsilon_0 \sim \left(\frac{\pi A}{\lambda}\right)^2$$

This relation allows a comparison of the energies in the fundamental and first buckling mode. The critical stretch is the value of the stretch for which the two situations have equal energy.

Hence,

$$E_{memb} \sim E_{bend} + E_{subst}$$

$$\overline{E_c}.t.\epsilon_c^2.\lambda \sim \frac{\overline{\overline{E_c}}t^3 A^2}{\lambda^3} + E_s A^2$$

$$\overline{E_c}.t.\epsilon_c^2 \sim \frac{\bar{E_c}t^3}{\lambda^2}.\epsilon_c + E_s\lambda.\epsilon_c$$

$$\overline{E_c}.t.\epsilon_c \sim \frac{\bar{E_c}t^3}{\lambda^2} + E_s.\lambda$$

$$\epsilon_c \sim \frac{t^2}{\lambda^2} + \frac{E_s\lambda}{\overline{E_c}.t}$$

$$\epsilon_c \sim \frac{t^2}{\left(t^3\frac{\overline{\overline{E_c}}}{E_s}\right)^{\frac{2}{3}}} + \frac{E_s\left(t^3\frac{\overline{\overline{E_c}}}{E_s}\right)^{\frac{1}{3}}}{\overline{E_c}.t}$$

$$\epsilon_c \sim \left(\frac{\bar{E_c}}{E_s}\right)^{-\frac{2}{3}}$$

This critical strain is the maximum strain that can be applied to the coating without buckling. This scaling law is very different from the linear buckling of plates or wide beams without the elastic substrate.

In this case of plates, calling D the bending stiffness, w the width, l the length of the plate and $k_{c;m}(l,w) = \left(\frac{mw}{l} + \frac{l}{mw}\right)^2$ the critical form parameter of mode m, we classically determine that(73):

$$\epsilon_c = \frac{k_c\pi^2 D}{\overline{E_c}.w^2.t} \sim \frac{k_c t^2}{w^2}$$

In the case of wide beams with a second moment of rotation I, we have similarly:

$$\epsilon_c = \frac{\pi^2 I}{t.w.l^2} \sim \frac{\pi^2 t^2}{l^2}$$

For those two cases, the buckling is a global phenomenon, which depends on the aspect ratio, but not on the material properties. On the other end, the wrinkling of a hard coating on a soft elastic foundation depends only on material properties, and not on aspect ratio (provided the wavelength is smaller than the width and length of the sample).

We should also note that the summation of the equivalents is rigorous here since we are considering only positive quantities (energies). This would not be the case otherwise ($\frac{1}{x} \sim -\frac{1}{x} + \frac{4}{x^2}$ but $\frac{4}{x^2} \sim 0$ does not hold).

2. Analytical solutions

a) Results for buckling wavelength and one case of post-buckling analysis.

Precising this scaling analysis, Chen et Hutchinson (74) have computed the energy of the modes, solutions of the linear buckling problem about the pre-buckling state: $D.\nabla^4 w + \sigma_0 t \nabla^2 w = -p$

These modes are defined by their deflection:

$$w = w.\cos\left(\frac{2\pi x}{\lambda_1}\right).\cos\left(\frac{2\pi y}{\lambda_2}\right)$$

The minimum of energy is found for

$$\frac{2\pi}{\lambda} = \frac{1}{t} * \left(3.\frac{E_s}{1-v_s^2}.\frac{1}{E_c}\right)^{\frac{1}{3}}$$

The buckling load is then:

$$\sigma_c = \frac{E_c}{4}.\left(3.\frac{E_s}{1-v_s^2}.\frac{1}{E_c}\right)^{\frac{2}{3}}$$

They also carried out a non-linear analysis of the post buckling solution in the one dimensional mode (i.e. uni-axial stretching), based on the von-Karman plate theory. They showed that the optimal wavelength for the buckling problem (i.e. the wavelength assocated with the lower critical stress) is also the state of minimal potential energy in the post-buckling mode (at least among the sinusoidal solutions). This is shown in Figure 39: as the load is increased above the critical load σ_0^c, the mode associated with the lowest buckling load has a lower energy than any other mode.
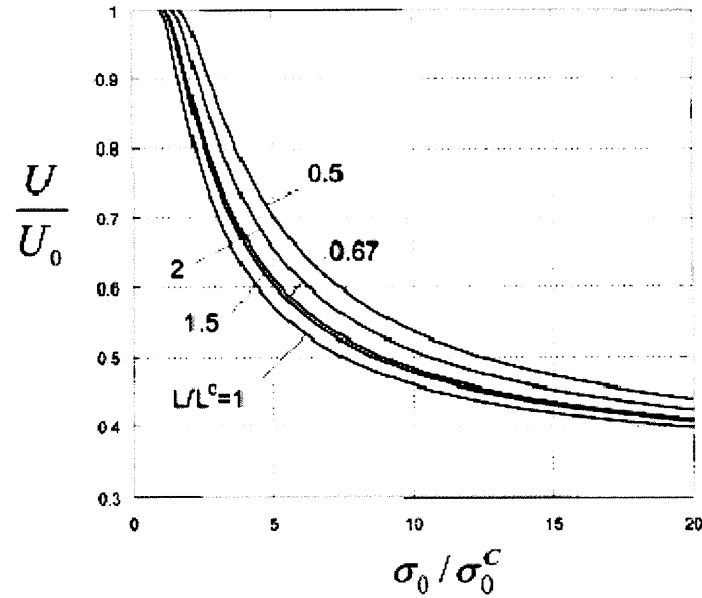
Figure 39: Ratio of the average elastic energy per unit area in the film/substrate system in the buckled state to that in the unbuckled state, $\frac{U}{U_0}$, as a function of the in plane stress, normalized by the buckling load $\frac{\sigma_0}{\sigma_0^c}$, for one dimensional modes. The mode associated with the lowest critical load ($\frac{L}{L_c} = 1$) remains the mode with the lowest energy even when the load is increased above the critical value. From (75)

Their non-linear analysis also reveals a very interesting phenomenon associated with the post-buckling problem. In the case of an equal loading in both directions, they computed the energy for 3 specified solutions: one-dimensional buckling, checker-board buckling and herringbone mode. They found out that buckling load associated with the Herringbone pattern is higher than the one associated with either the one-directional of the checker-board pattern. It means that the pre-buckling solution will most likely bifurcates in the direction of one of these two modes. However, when the load is further increase above the critical load of the Herringbone pattern, the energy of this mode becomes smaller than the energy of any of the two previous buckling modes (see Figure 40). As a result, the structure will bifurcate again in the Herringbone pattern.
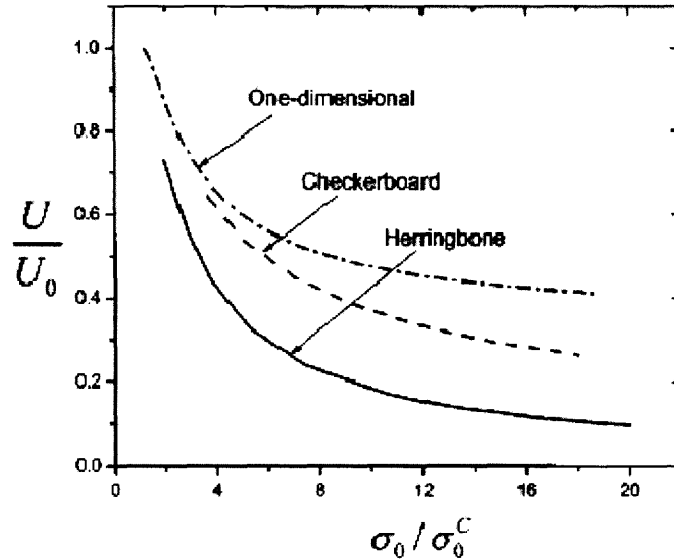
Figure 40: The Energy of three different equilibrium solutions for the bi-axial stretching is represented. The One-dimensional (or sinusoidal like) solution has the highest energy, but also the lowest buckling mode. We think that the plot for the cherker-board should be extended to lower relative loads, since it bifurcation load should be lower than the one of the Herringbone pattern. The Herringbone pattern should have the highest buckling load. But when it exists, the Herringbone mode is the mode of lowest energy (among those three). From (75)

We mention this phenomenon for two reasons.

- The first reason is that this phenomenon provides a really interesting test for our numerical modeling.

- The second reason is that it shows an example of a system, which buckles in a given "direction", but stabilize in another "direction". By direction, we mean a certain field of displacement. For linear problems, a proportional loading $k.\sigma_0$ results in a proportional displacement field $k.u_0$. In this case, a proportional loading might result in proportional displacement $k.u_0$ until k reaches a second bifurcation point k_2^C, above which the solution might be $(k - k_2^C).u_1$.

We might acknowledge that this phenomenon is the major limitation of the design method we propose in the last chapter of this thesis. We want to stay away from those "double bifurcations" as much as possible.

b)   Results for the finite thickness of the substrate layer.

Huang et al. (75) further developed a scaling analysis to account for the finite thickness of the substrate. They showed that the limit of infinitely thick substrates is really good for most variables of the problems, provided $\frac{\overline{E_c}}{\overline{E_s}} > 10^3$ and $\frac{t_c}{t_s} < 50$. The ratio of the thicknesses used in our numerical modeling was chosen to be $\frac{t_c}{t_s} = 200$, to model the limit of thick substrates.
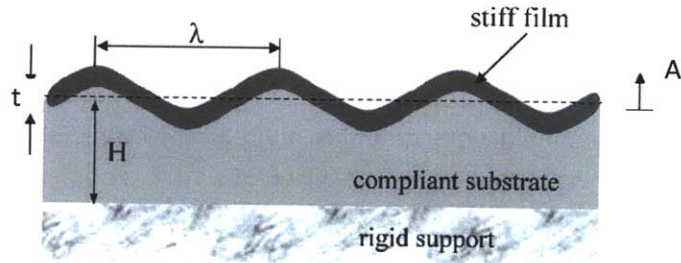
Figure 41: wrinkle of a stiff coating on a compliant support. The nomenclature for Figure 42 is defined as followed: t is the thickness of the coating, H the thickness of the substrate, λ the wave length of the wrinkles and A the deflection of the membrane (from (75))
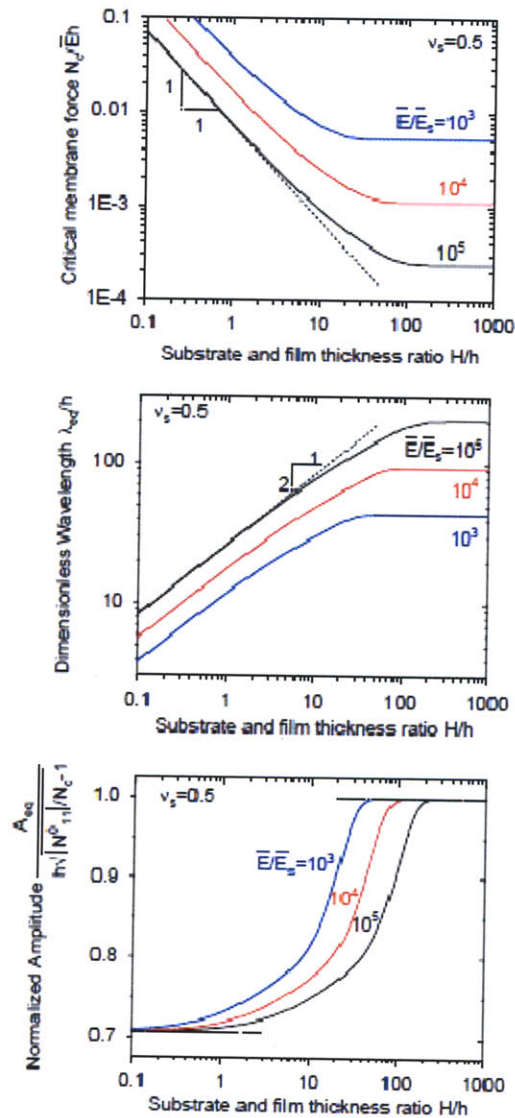
Figure 42: Critical force, wavelength and normalized amplitude are represented as a function of the ratio film thickness to substrate thickness. These plots are computed by scaling law analysis in the context shown in Figure 41 (soft substrate attached to a rigid support). The substrate is taken to be incompressible. (from (75))

They also developed a spectral method to solve the problem of the plate on an elastic substrate. Transforming the equations governing the equilibrium of the plate in the Fourier domain, they solve this dual problem with a fixed-point method. This allows them to efficiently compute the buckled shapes for more multi-axial loadings. We should note that this multi-axial loading is an interesting strategy to obtain more complicated buckling patterns (see the different patterns obtained for multi-axial strains in Figure 43).
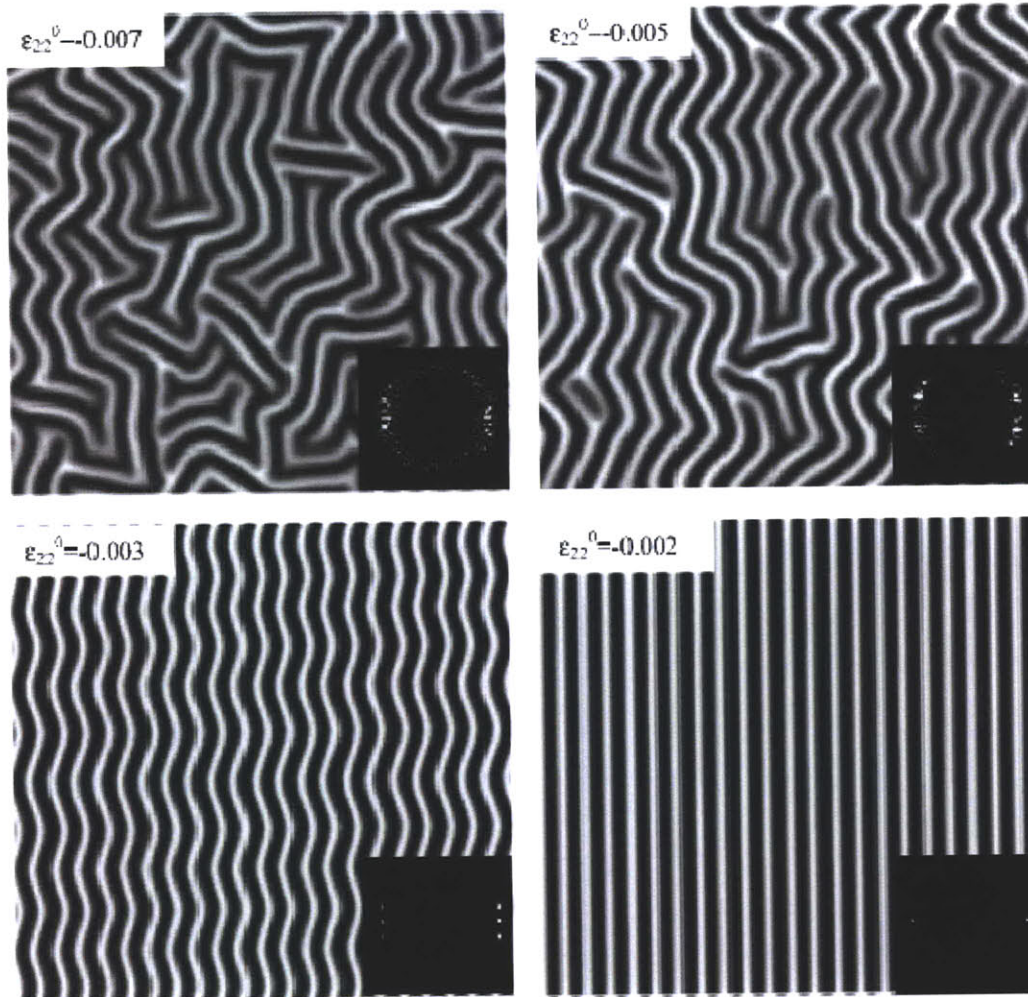
Figure 43: Wrinkle patterns in films subject to anisotropic membrane strains. $\epsilon_{11} = -0.01$ in all cases. The directional preference increases as the strains become more anisotropic, from the labyrinths to the herringbones and to the stripes. The insets plot the wrinkle amplitude in the Fourier space. From (74)

E. iCVD coating and wrinkle formation

To explore the potential of forming wrinkled anti-fouling coating in membranes, we decided to rely on iCVD deposition of a hard coating on a PDMS membrane, with the collaboration of Dr. Gozde Ince Ozaydin, post-doc in prof. Gleason group in Chemical Engineering.

1. Preparation of the samples

a) General idea

The scenario for wrinkle formation is very simple. A soft elastomer substrate is cast, prepared for iCVD coating, and stretched in a sample holder. The stretched sample and sample holder are inserted in the iCVD reactor and a layer of hard coating is deposited on the surface of the substrate. Upon release of the strain of the substrate, the hard coating will be put in compression. Depending on the relative characteristic of the substrate and coating (stiffness, thickness, …), the coating may buckle to release the mechanical energy from the in-plane stresses into bending of the coating and shearing of the substrate.

Casting of a 1mm thick PDMS substrate	Stretching of the substrate with the clamping device (0 to 20%)	iCVD depostion of a layer of EGDA of thickness 0-1 um	Release of the strain -> formation of the wrinkles
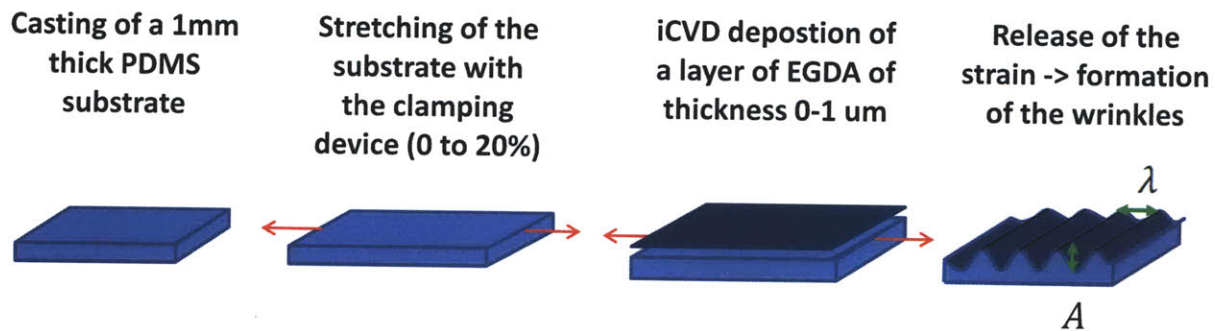
Figure 44: Formation of a wrinkle substrate in 4 steps: a/casting of elastomeric material b/stretching of this substrate c/deposition of a coating d/release of the stretch and wrinkles formation. Note that a biased of stretch could also be imposed to produce a different wrinkle pattern.

b) PDMS substrate

(1)   Preparation of PDMS substrate

PDMS is used for the soft elastomeric substrate. It is prepared from a 15mL of a 10:1 mix of a Poly(dimethylsiloxane) solution and a curing agent from Sigma-Aldrich. The PDMS solution is a mix by Dow Corning, prepared from the SYLGARD® 184 silicone elastomer kit, and contains 3 main components: (Dimethyl, methylhydrogen siloxane), (Dimethyl siloxane- dimethylvinyl-terminated) and (Dimethylvinylated and trimethylated silica).

After stirring, the solution is inserted in a low pressure environment for 10 to 20 min to remove the air bubbles. The solution is then poured onto a 150 mm diameter Petri dish. After an hour of curing time at 60C, the solidified substrate is peeled off the dish, and cut into four 14mm*38mm samples. The thickness is 1mm and, provided the sample are cut from the central region, the thickness is quite homogeneous (+-10%).

(2)   Characterization of the PDMS

We have chosen to work with PDMS for its mechanical characteristics: low Young's modulus, high strain at break and low surface roughness achievable without any special attention. Hence PDMS will serve as an initial substrate for prototyping our proposed method, but it is important to note the applicability of the approach to any other materials.

To determine mechanical properties, we performed tests on a Dynamic mechanical analyzer, the Q800 from TA Instrument.

The first test imposed ramp in strain of 5%/min (the Q800 only controls the engineering strain rate), at a temperature of 28C and measured the force as a function of displacement. The Matlab software is used to process the data. Figure 45 represents one representative true strain/true stress history. The strain is increased until the sample breaks.

PDMS, like most elastomeric materials is non-linear elastic; the tangent stiffness increases with applied strain.

Wrinkle formation can be influenced by the pre-strain of the substrate (before the deposition). The wrinkles form in the very beginning of the release of the strain, from the deformed configuration. For simplicity, we characterize the behavior of the substrate with only one parameter (the so-called initial stiffness or Young's modulus E_s). A more accurate analysis would take into account the non-linear behavior of the PDMS.

The Poisson ratio for this elastomer should be close to .5 (incompressible material). We should note however that the configuration of the machine (furnace must be closed) does not allow the use of a video extensometer to measure this ratio. The strain at break is .6 to .7, mostly due to the propagation of surface edge cracks from one edge of the sample.

The tangent Young's modulus is measured at strains of 0, .25 and .5. Those measurements are repeatable within 10% and $E_{PDMS}(0) = .55$MPa, $E_{PDMS}(0.25) = .75$MPa and $E_{PDMS}(0.5) = 1.01$MPa.
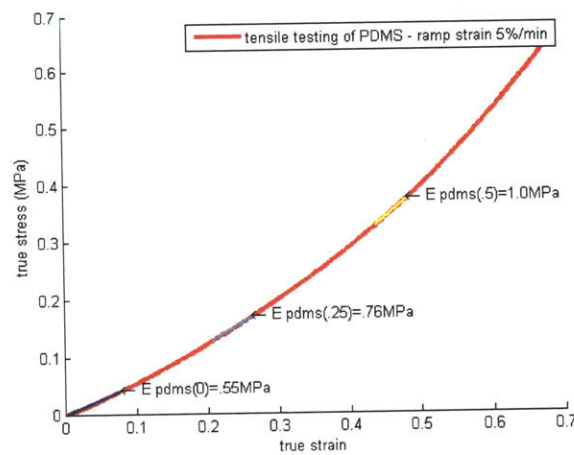
Figure 45: true strain-true stress curve for the PDMS prepared as describe above.

As far as thermal properties are concerned, we perform both a Dynamical Mechanical Analysis (DMA) and a measurement of the coefficient for thermal extension

The first test is performed from room temperature to 130C, and consists of sinusoidal oscillations of amplitude $A_0 = 15\ \mu m$, and frequency $w = 3Hz$:

$$L(t) = L_0 + A_0 * (sin(wt) + 1.25)$$

Assuming a homogeneous strain in the material and small amplitudes of oscillation, we get a linear strain:

$$\epsilon_{xx}(x, y, z, t) = \frac{A_0}{L_0} * (sin(wt) + 1.25)$$

The stress in the material presents a lag, which is usually characterized by δ, and is associated with energy dissipation in the material (76):

$$\sigma = \sigma_a * sin\ (wt + \delta)$$

Then, we define the storage and loss modulus:

$$E' = \frac{\sigma_a\ cos(\delta)}{\epsilon_a} \text{ and } E'' = \frac{\sigma_a\ sin(\delta)}{\epsilon_a}$$

Those two moduli are presented in Figure 46 as a function of the temperature, for the PDMS used in our membrane. The elastomer stiffens with the temperature, and relatively the energy absorbed by the material during one cycle is less and less important, showing the entropic nature of the modulus of rubbery material.
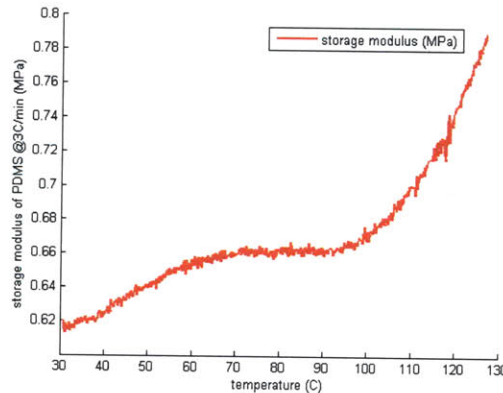
Figure 46: Storage modulus of the bulk PDMS. (1Hz)

Then, we measured the extension of a strip of PDMS when heated above room temperature. A pretension (15kPa) is applied to the sample. This pretension is kept constant while the sample is heated.

The elastic strain is not constant over the range of temperature considered (due to the variation of the stiffness with temperature), and has to be subtracted from the total strain to give the thermal strain: $\epsilon_{total}(T) = \epsilon_{elastic}(T) + \epsilon_{thermal}(T)$. Hence, and neglecting viscoelastic effects, we can compute the coefficient of thermal expansion:

$$k(T) = \frac{d\ \epsilon_{thermal}(T)}{dT} = \frac{d(\epsilon_{total}(T) - \frac{\sigma_0}{\sqrt{E'^2 + E''^2}})}{dT}.$$

This coefficient, corrected by the change in stiffness and the applied tension in the sample over the range of temperature, is pretty constant up to 80C and is close to $420 * 10^{-6}\ K^{-1}$. The resulting thermal strain versus temperature is represented in blue in Figure 47
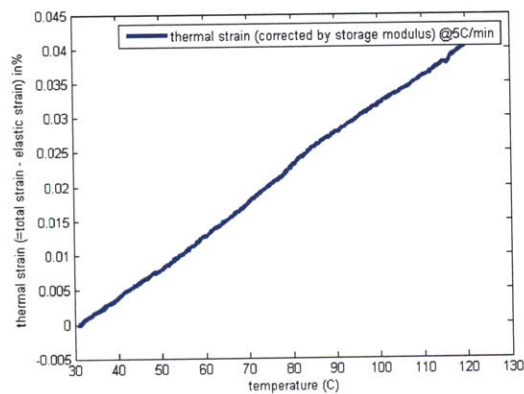
Figure 47: Corrected thermal strain

c) *Coating with EGDA*

(1) Preparation for the iCVD coating

(a) Plasma treatment
The PDMS samples are then plasma treated to obtain a better bonding of the film to the substrate. Plasma treatment creates radicals at the surface of the membrane, which allows the silane to adhere covalently to the substrate.

(b)   Silane evaporation

After plasma treatment, the membrane is placed in a low vacuum environment. Silane is then evaporated in this environment, and reacts with the radicals at the surface of the membrane. This treatment enhances the adhesion of the EGDA coating.

(c)   The stretching device.

In order to deposit the coating on a stretched substrate, we had to design a system for tensioning the PDMS samples. The final design and a photo is shown in Figure 48. Two PVC jaws are moving along two long screws, while the clamping mechanism is actuated by 2 small screws on each clamp.
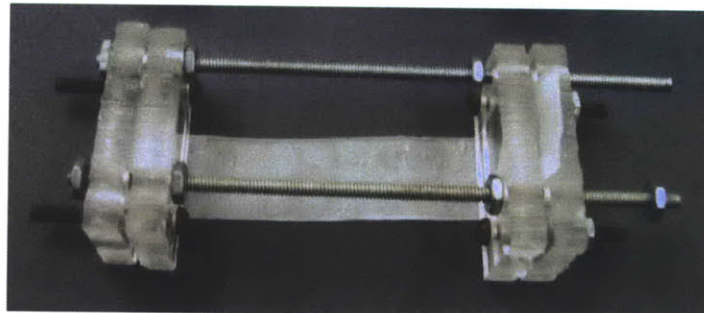
Figure 48: Sample holder designed to stretched PDMS substrate during iCVD coating

This design accommodates several needs:

- The whole sample is maintained in contact with the bottom plate of the reactor, which is cooled down (see Figure 49: iCVD coating technique. From Figure 49 the "backside cooled stage"). It is really important to insure a good control of the temperature of the sample for the quality of the deposition (uniformity of the coating).

- No metal parts touch directly the sample, to avoid conducting the heat of radiation from the filaments to the sample.

- The linear motion of stretching is precise enough to control elongation to hundreds of microns. And the maximum distance separating the two clamps is fixed to 50mm.

(2)   iCVD coating with EGDA

The iCVD (initiated Chemical Vapor Deposition) coating is a low energy coating technique in development in Professor Gleason's group of the Chemical Engineering department of MIT, and the depositions for our samples were carried out by Dr. Gozde Ince-Ozaydin.

During the coating deposition, several chemicals are brought in gaseous phase into a low pressure reactor. As they flow through heated filaments, the initiated species (I_2 on Figure 49) are decomposed into free radicals (I*) with minimal energy input, and will then recombine with the monomer species (M) on the sample to form the polymer coating (77).

This technique has various advantages over other coating techniques. Mainly a great number of different chemicals can be used. Furthermore, it requires only a minimal energy input, and the reaction path is better controlled, resulting in less damage to functional groups during deposition, even at high deposition rate.
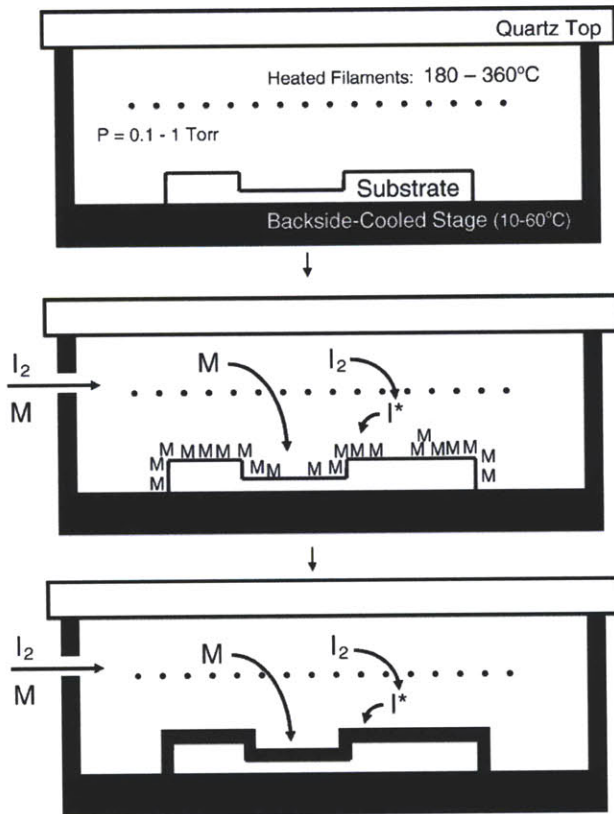
Figure 49: iCVD coating technique. From (77)

(3)   Characterization of mechanical properties of the EGDA hard coating

In addition to the chemistry of the initiated species (I_2) and monomers (M), the flux of those chemicals, we are also controlling the growth rate (or thickness increase of the film). This growth rate is measured in real time by a laser interferometer. This laser is pointed to a control wafer of silicon which is placed close to the sample. We assume that the growth rate is similar on the sample and on the silicon.

For the case of the wrinkled samples produced in this work, the coating is 1µm thick.

In order to test the material properties, we also produce self-standing films of EGDA. Those films must be thick enough to be self standing. The thickness is limited by the time of deposition; the maximum thickness growth rate is on the order 500nm/h. We have chosen to test 3.5 µm thick samples. The films were deposited on a sacrificial layer, which dissolves into water. Since those samples are very thin and brittle, a cardboard frame is used to handle them: the frame is glued to the sample before dissolving the sacrificial layer in water (Figure 50). The cardboard frame is cut just before the test, once both ends of the samples are in the jaws of the Q800 (Figure 51).
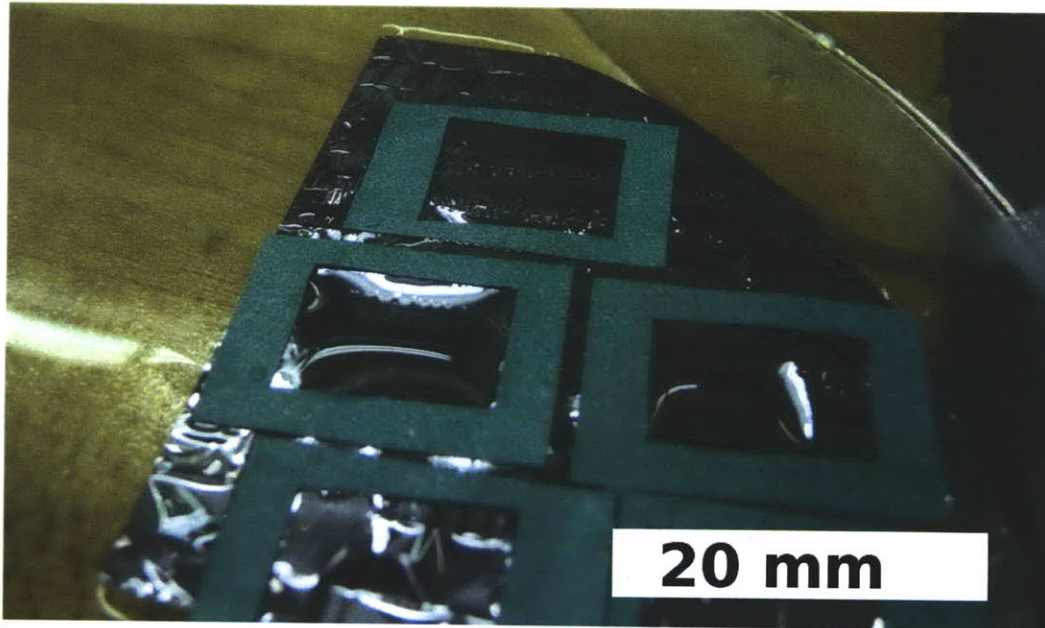
Figure 50: The cardboard frames are glued to the EGDA film. The whole system {silicon wafer, sacrificial layer, EGDA film, cardboard frame) is immersed into water until dissolution of the sacrificial layer and separation of the {film+frame} from the wafer.
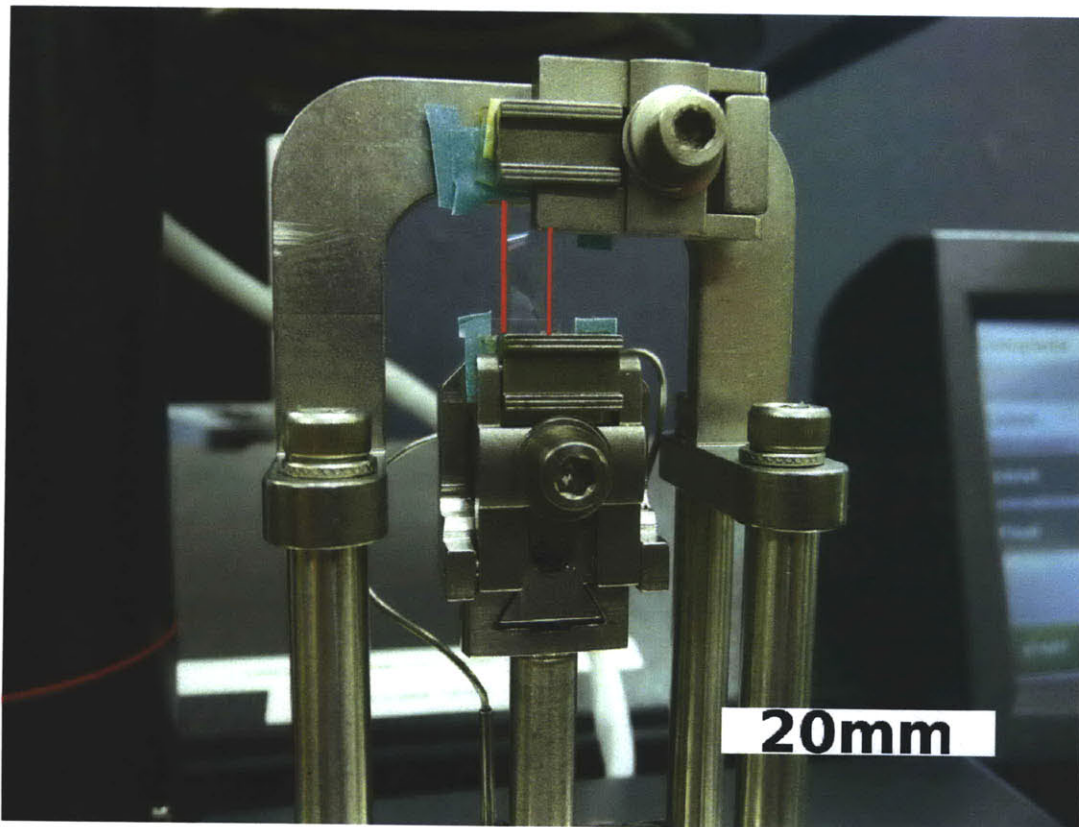
Figure 51: The frame is installed in the jaws of the DMA and the sides of the frame are cut once everything is clamped. The sample (highlighted with red lines) is then loaded with a pre-load force of .001N (for strain-stress tests) or .01N (for DMA tests)

1 %/min strain ramps are performed on EGDA films at room temperature. The stress-strain history for a typical result of this test is shown in Figure 52. The stiff and relatively brittle behavior of EGDA is confirmed; the strain at break is around .03, which corresponds to stresses of 15MPa. The measured stiffness of the EGDA is 775MPa.
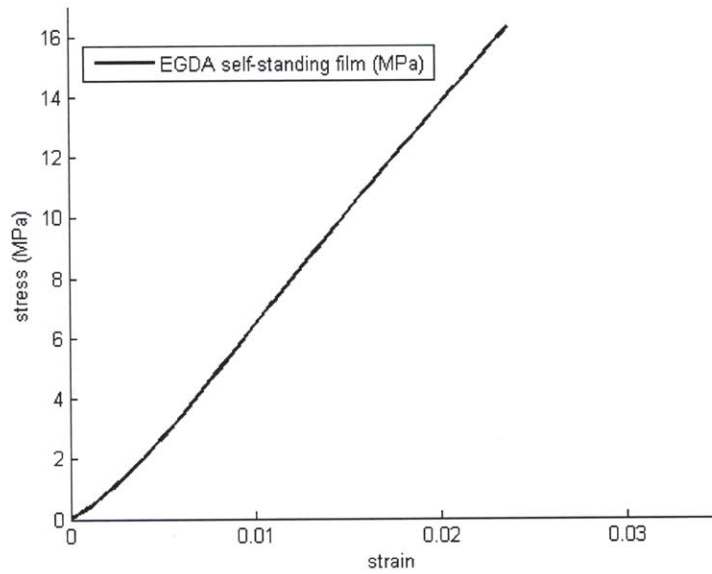
Figure 52: Strain ramp for a self standing film of EGDA (tested on DMA-Q 800 at room temperature).
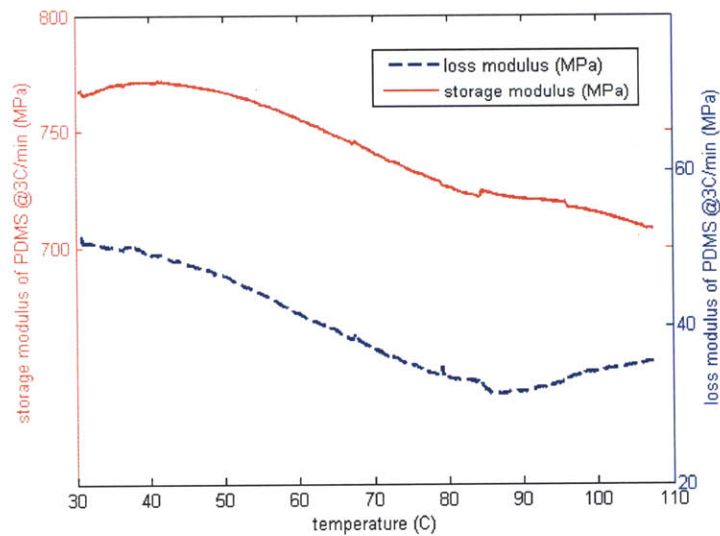
Figure 53: Dynamical Mechanical Analysis of a self-standing film of EGDA (hard coating)

A DMA test was also performed on the EGDA films for low temperature (ambient to 110C). These films are so thin that performing these tests is challenging, and is on the edge of the capability of the DMA.

The input signal was a sinusoid at 1Hz, and controlled in force rather than in strain (0.07N or 10MPa). As shown in Figure 53, the quantitative values compare well with the monotonic stress-strain curve. There is no significant variation of the storage modulus over this temperature range (see Figure 53).

d)   Comparative material properties of the PDMS and EGDA.

While the properties of each material are important, we will show in a dimensionless analysis that the relative mechanical properties, especially the relative stiffness, are determinant for the buckling problem. Assuming similar values of Poisson ratio for the substrate and the coating (i.e. $\nu_s = \nu_c$), we determine that: $\frac{\bar{E}_c(0)}{\bar{E}_s(\epsilon_0)} = \frac{E_c(0)}{E_s(\epsilon_0)} * \frac{1-\nu_s^2}{1-\nu_c^2} = \frac{E_c(0)}{E_s(\epsilon_0)}$ is a function of the pre-strain ϵ_0 of the substrate. It ranges from 1300 for an un-stretched membrane to 800 for a membrane with 50% of pre-strain. However, the wrinkle formation is a result of the buckling and the post buckling problem, and the entire non-linear response is needed to precisely define the final shape of the wrinkles.

During the deposition of the coating, the substrate is maintained at a constant and low temperature. However, the monomers which react to form the coating are going through the filaments before deposition on the sample. Hence, the initial state of stresses in the coating is the result of a complex problem of cooling and chains migration. As the buckling problem is very sensitive to imperfections, we think that a good understanding of this initial problem is paramount to a complete description of the wrinkle formation.

This plot is based on the DMA for each material, and is shown in Figure 54. The relative stiffness of the material decreases with the temperature: 20% drop for 70C. This is due both to the softening of the glassy EGDA and to the entropic stiffening of the rubbery PDMS.
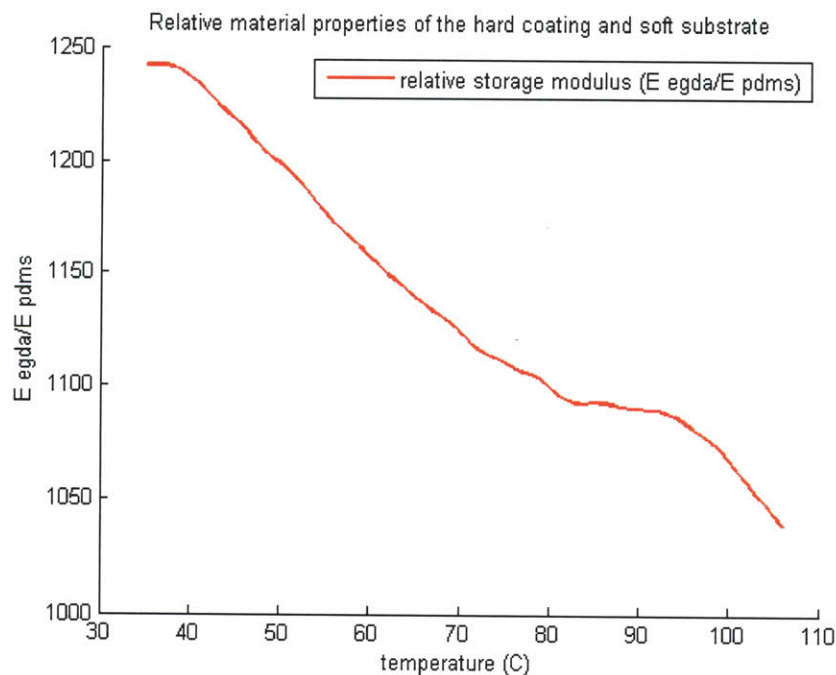
Figure 54: Relative stiffness of the materials (EGDA coating relative to PDMS substrate) as a function of the temperature

e) *Releasing the strain and formation of the wrinkles.*

The last step in the wrinkle formation process is to release the strain from the substrate. This operation is quite delicate, since the coating should not be overstretched. A 3% overstretch (corresponding to few hundreds of microns for our samples) results in breaking the EGDA coating. During the release of the stretch, we may see large defects in the wrinkles; long lines which run through the sample width (i.e. along the main wrinkles.

We are still unsure whether those lines are cracks in the coating (due to over-stretching), regions where the coating is thinner and where the deformation localizes (forming a crease in the coating), or a region where the coating delaminates from the substrate (also resulting in the formation of a crease).

F.   Characterization: Wrinkling of a hard coating on a soft substrate

In this section, we are characterizing the membranes as prepared by the protocol described in II.E. We use optical microscope along with an optical profilometer and a Scanning Electron Microscope to characterize the samples. We characterize the shape of the wrinkled membranes and compare the measurement of wavelength obtained with each technique. The profilometer is also used to measure to the amplitude of the wrinkles.

1.   Microscopy

Optical micrographs of the membrane are taken with a camera associated with a Nikon microscope. The horizontal dimensions on the microscope have been calibrated, with TEM grid Veeco 200 (pitch 125μm).

We are showing images both in the transmitted light mode and in the reflected light mode. The transmitted light mode seems to reduce the field of view and allows to focus on only a part of the sample (eg. Figure 55 a/ shows the focusing on the valley of the wrinkles while the c/ is the same image focused on the peak of the wrinkles). It confirms our intuition that we are not just looking at a flat surface, but at sinusoidal-like features of finite height. Figure 55 shows this phenomena with a single image focuses on 3 different heights of the wrinkles.
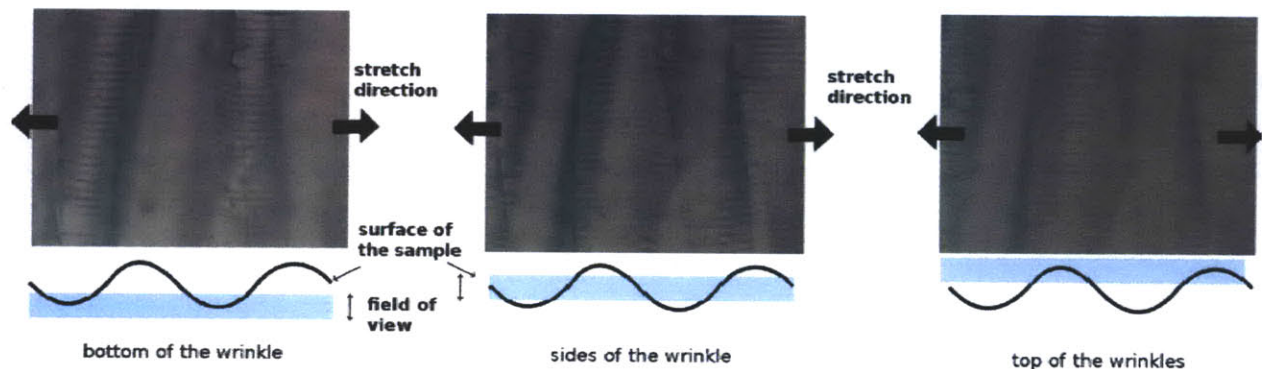
Figure 55: Representation of the finite depth of view. This picture of a single location on a wrinkled membrane is shown focused on a/ the bottom of the wrinkles b/ the sides of the wrinkles c/ the top of the wrinkles.

The low magnification images (Figure 56 a-b) clearly show the primary wrinkles of the longest wavelength, which run perpendicular to the stretch direction. Those wrinkles have a low wavelength and are not perfectly regular **34μm (+-10μm)**. In this case, the finite depth of field allowed us to distinguish peaks and valleys of the sinusoid, which is not obvious in the transmitted light mode.

At higher magnification, wrinkles perpendicular to the long wavelength wrinkles (i.e. aligned with the stretch direction) become apparent (Figure 56 e-f-g-h). These wrinkles of much shorter wavelength, just above **2.2μm (+-.2μm)**, seems to be more regularly spaced than the primary wrinkles.

Reflected light microscope	Trasnmitted light microscope.

5X	Stretch direction ← → 375 um	Stretch direction ← → 375 um
20X	Stretch direction ← → 100 um	Stretch direction ← → 100 um
40X	Stretch direction ← → 48 um	Stretch direction ← → 48 um

100X

Stretch direction

23 um

Stretch direction

23 um
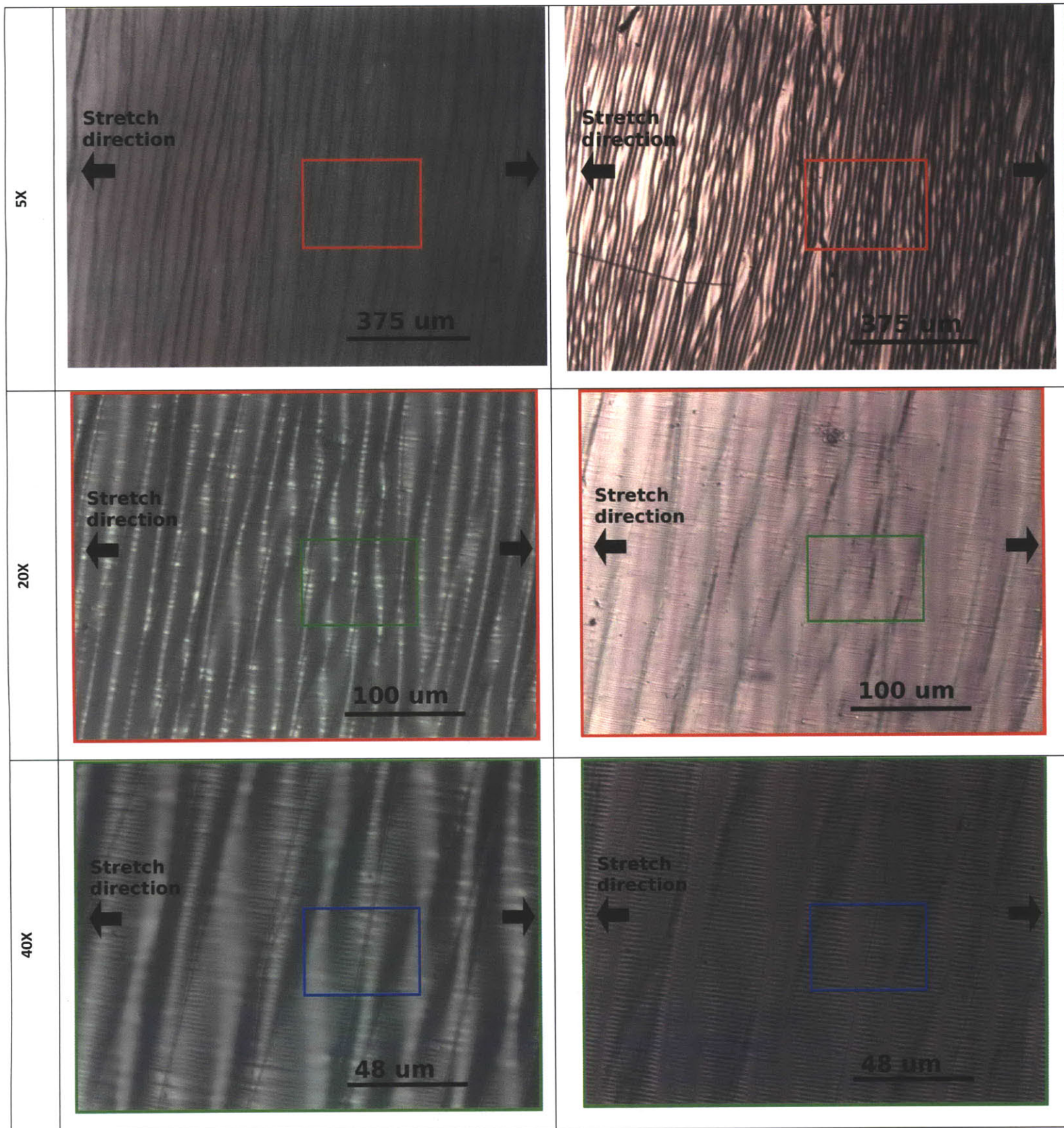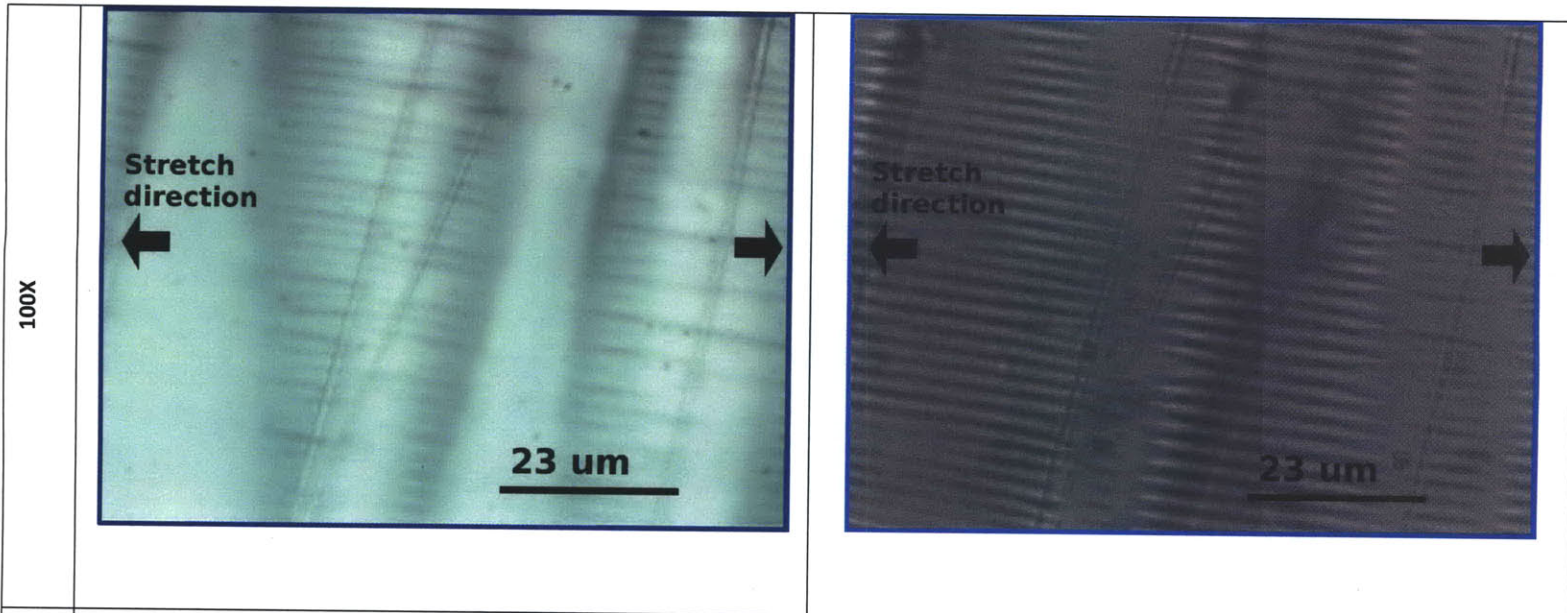
Figure 56: Observation of wrinkles with optical microscope at magnification of 5X (a,b) 20X (c,d) 40X (e,f) and 100X (g,h) for reflected (a,c,e,g) and transmitted light (b,d,f,h).

2. Optical white light profilometer

In order to measure the amplitude of the wrinkles, we use an optical profilometer, the noncontact Scanning White Light Interferometer NewView 5032 by Zygo. Based on the peak of maximum intensity of the fringes of interference, the profilometer outputs a 3D image of the surface of our membrane. Depending on the lens (20X and 50X) and the magnification (.4X to 2X) chosen, those images cover a surface from $70 * 50\ \mu m^2$ up to $800 * 600\ \mu m^2$. The horizontal resolution depends on the magnification and ranges from 30nm to 300nm, while the vertical resolution is under .1nm. The main limitation of this technique is the difficulty to image tilted surfaces, since the light is not reflected on the sensor if the surface is not horizontal. As shown in the Figure 57, most peaks and valleys of the wrinkles can be imaged, but the rest of the pattern is undetected: it is black in the height image (top left image in Figure 57) and grey in the 3D image (top right image in Figure 57). In the subsequent profilometry images, the top part of the wrinkles is highlighter in red while the bottom part is in red, in order to facilitate the interpretation of these images. A profile of the wrinkles is also shown in black at the top of each image.

a) *Measurement of wavelength and amplitude of the wrinkles by profilometry*
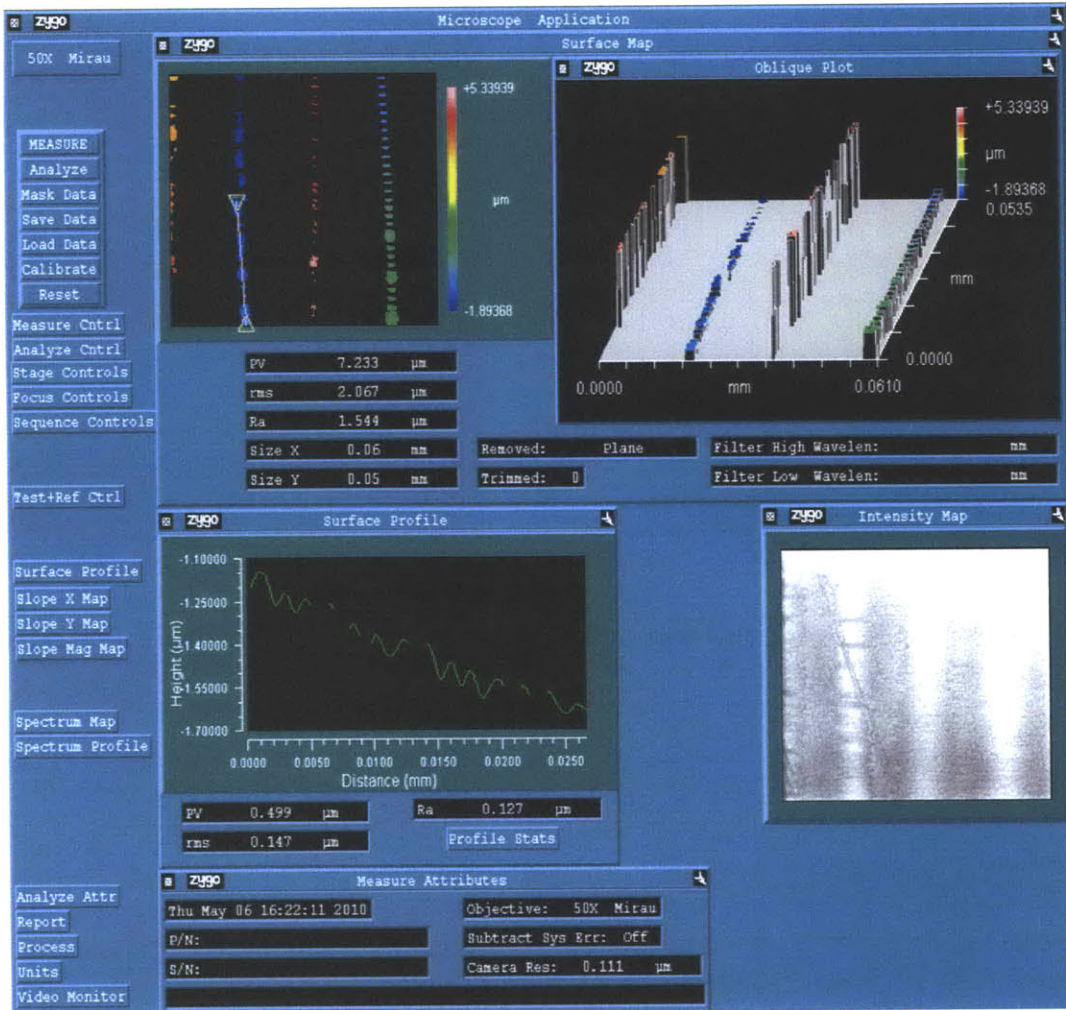
Figure 57: the Zygo profilometer outputs a 600*400 pixels images with, for each pixel an information of height and an information of light intensity. This information is displays with a 2D color plot of the height along with a 3D representation of this image and a profile of a section (along the path between the triangular waymark). The intensity is displayed on the bottom right corner.

The measurements via optical profilometry confirm the microscopy qualitative observations for wrinkles on top of stretched membranes:

- Long wrinkles run perpendicular to the direction of the stretch. Those wrinkles run all across the sample.

- If we zoom in, we can also image the small perpendicular wrinkles. Their wavelength is much smaller than the long wrinkles, but also more regular than the wavelength of the large wrinkles (less statistical dispersion of these wavelengths). Furthermore, we observe that they are not limited to one peak or one valley but extend on hundreds of microns in length.

magnification	(40%) stretched membrane

Low	
Mid	
High	
	Figure 58: Profilometry images: 40% strain is applied horizontally in those images. From top to bottom, the magnification is increased. The color of each pixel represents the height measured at this location. In the black areas the measure was not possible. The alternative blue and orange colors show the peak and valley of the wrinkles
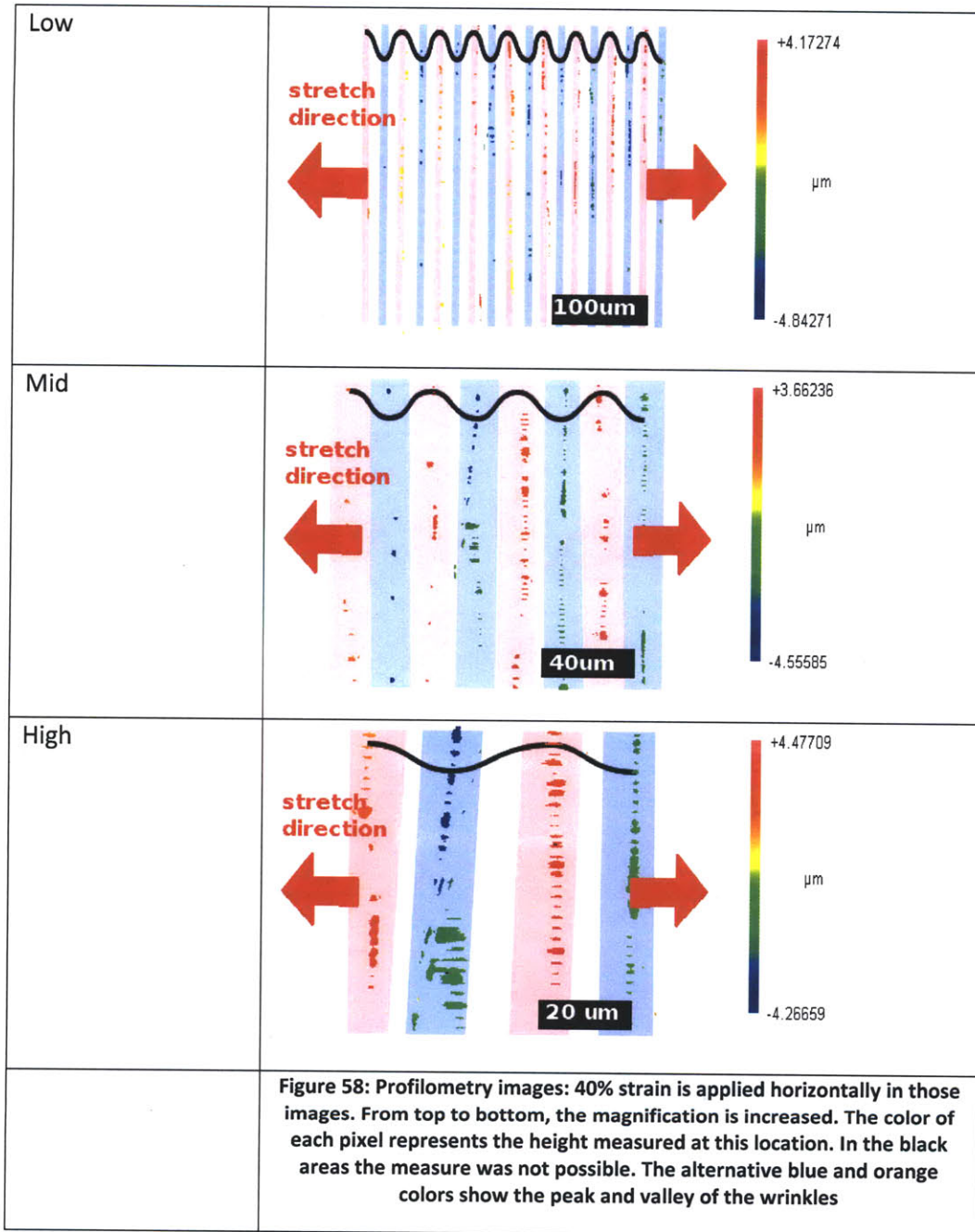
magnification	(10% strain) stretched membrane	unstretched membrane

Low		
Mid		
High		
	Figure 59: Profilometry images: 10% stretch is applied horizontally in those images. From top to bottom, the magnification is increased. The color of each pixel represents the height measured at this location. In the black areas the measure was not possible. The alternative blue and orange colors show the peak and valley of the wrinkles	**Figure 60: Profilometry images. No stretch is applied before the formation of the membrane. The two level of wrinkles are still been seen. We are not expecting any wrinkle formation; however, thermal expansion mismatch along the effect of gravity may induce a slight straining of the membrane which results in those wrinkles.**

b)   Influence of the strain

The influence of the pre-strain has also been studied qualitatively, with 3 different stretches: no strain; mid strain (15%) and high strain (40%). For each stretch, wrinkles of two different length scales are forming.

It should be noted that the higher the stretch, the higher the amplitude of the wrinkles, and the more tilted the surface of those wrinkles. This is why the unstretched membrane can be imaged very well (very little black zones corresponding to points where the profilometer cannot read the height), while the stretched membranes are more difficult to image. Furthermore, we think that the wave observed for 0% strain are due to a very slight strain due to the configuration of the clamps.

We report the measurements of wavelength and amplitude for the 3 level of stretch in Table 2.

strain	wavelength (µm)		amplitude (µm)		wavelength (µm)		amplitude (µm)	
0%	39	(±2.0)	.8	(±.3)	2.0	(±.1)	.1	(±.05)
10%	34	(±1.0)	3.9	(±.2)	2.0	(±.1)	.1	(±.05)
40%	37	(±2.6)	5.7	(±1.1)	1.9	(±.1)	.07	(±.03)

Table 2 : Measurements of the wavelength and amplitude of the larger and smaller wrinkles for three levels of stretch

There is no significant influence of the stretch on the wavelength of the larger wrinkles (see Figure 61), while the amplitude of the larger wrinkles are very dependent on the stretch (Figure 62).

In order to test the assumption of the buckling in a sinusoidal-like shape, we have represented the theoretical amplitude of the oscillations. If the critical strain and if the in-plane strain of the post-buckling solution are small compared to the applied strain, the amplitude A should be related to the stretch of the membrane:

$$stretch = \frac{1}{\lambda} \int_0^\lambda ds$$

$$= \frac{1}{\lambda} * \int_0^\lambda \sqrt{1 + \left(\frac{dy}{dx}\right)^2} \, dx$$

$$= \frac{1}{\lambda} * \int_0^\lambda \sqrt{1 + \left(\frac{2\pi A}{\lambda} \sin\left(\frac{2\pi}{\lambda}x\right)\right)^2} \, dx$$

$$= \int_0^1 \sqrt{1 + \left(2\pi \frac{A}{\lambda} \sin(2\pi\tilde{x})\right)^2} \, d\tilde{x}$$

We have represented the inverse of this function $stretch = f\left(\frac{A}{\lambda}\right)$ in Figure 62, taking $\lambda = 35\mu m$. This expression has no fitting parameters, and considering the scattering of the measurements of amplitude of the wrinkles and the poor precision in the measure of the pre-strain, it is very reassuring to observe the match between the basics theory and experiments.
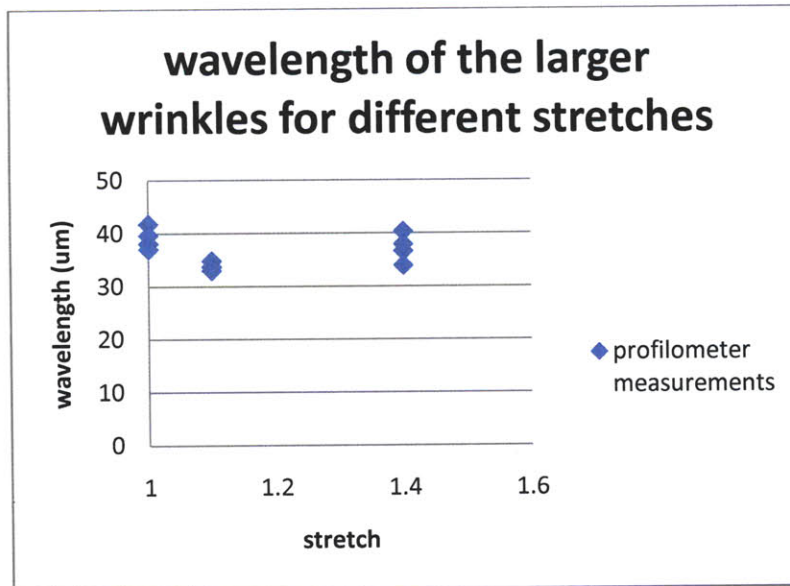
Figure 61: Variation of the wavelength of the larger wrinkles for different stretches, based on profilometer measurements
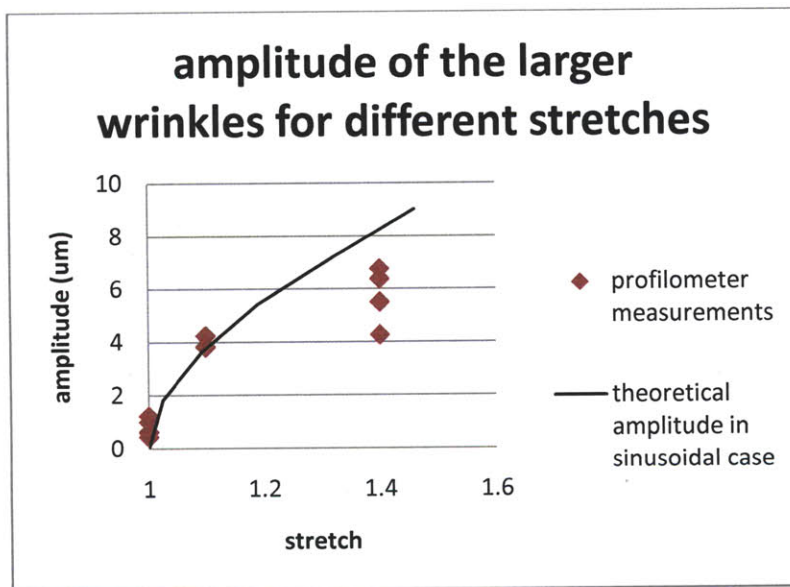
Figure 62: Variation of the amplitude of the larger wrinkles for different stretches, based on profilometer measurements

c)   *Influence of the coating thickness*

The influence of coating thickness has also been studied experimentally.

There is no significant difference in the shape for thinner coatings. The uniaxial straining of the membrane results in the sinusoid-like pattern. However, the wavelength of the sinusoids increases with the thickness of the coating. As summarize in Table 4, the thinner coating (495nm thick) results in short wavelengths for both the long and short wrinkles, as compared to the thicker coating. The ratio of the wavelengths for both coating is close to the ratio of the coating thickness:

$$\frac{\lambda_{long}^{495nm}}{\lambda_{long}^{1000nm}} = \frac{\lambda_{short}^{495nm}}{\lambda_{short}^{1000nm}} = \frac{495nm}{1000nm}$$

	wavelength of longer waves (µm)	wavelength of smaller waves (µm)
thin coating (495nm)	20	1.2
thick coating (1000nm)	37	2

Table 3: Wavelength of the wrinkles for two coating thicknesses, measured by optical profilometry.

Figure 63: Profilometry image of the wrinkles for a coating thickness of 495nm. The longest wavelength is measured to be 20µm while the orthogonal wavelength is 1.2µm.

Figure 64: Profilometry image of the wrinkles for a coating thickness of 1000nm. The longest wavelength is measured to be 37µm while the orthogonal and smaller waves are measured to be 2µm.
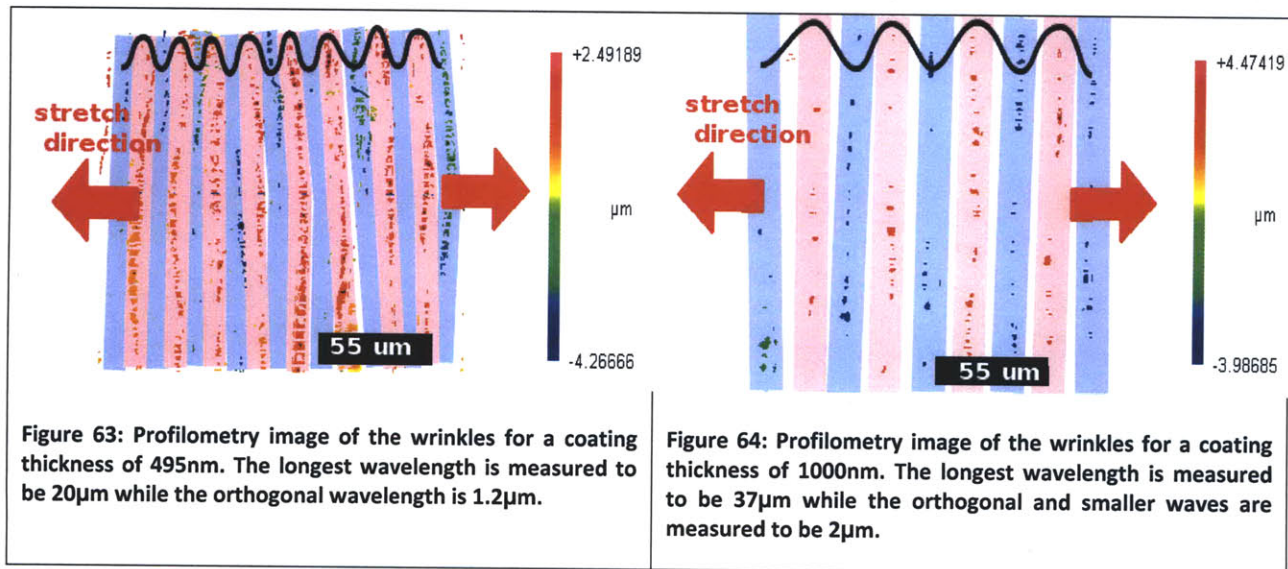
3.   Scanning Electron Microscope

To complete the observation of this sample, Scanning Electron Microscope is used. SEM provides a good visualization of any cracks/defects which run through the sample. The top right corner of Figure 65 shows a representative line of defect, slightly tilted compared to the orientation of the main wrinkles.

It should be noted that those lines of defects are crossed by the shorter wrinkles (i.e. the phase of the wrinkles is the same on both edges, which delimit the defect). It means that the shorter wrinkles were formed prior to the defects.

To conclude definitely on the mechanism of formation of the defect in the wrinkles, a further investigation is needed. More specifically, we plan on improving the characterization of this area by AFM imaging (Atomic Force Microscope).
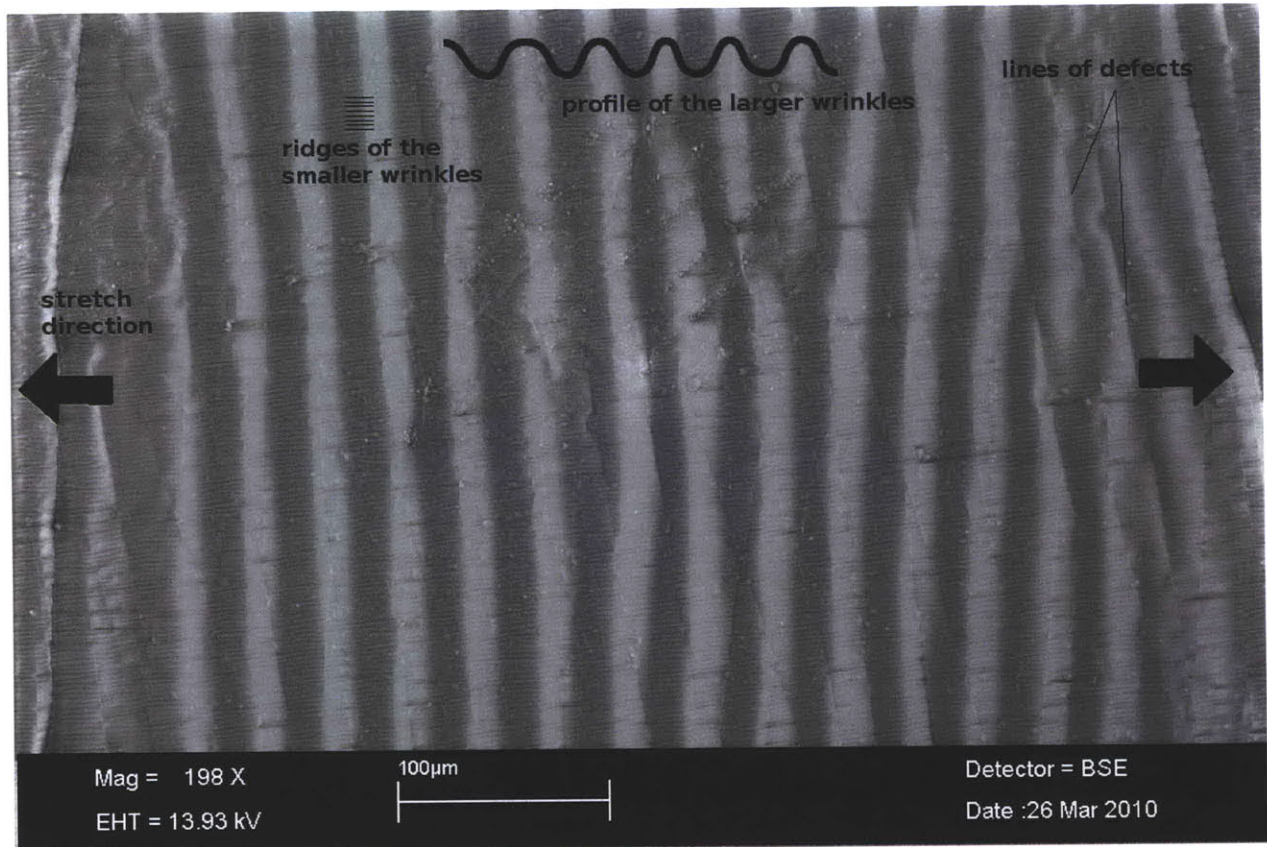
Figure 65: Micrograph of the wrinkles of the EGDA hard coating on top a PDMS substrate. Low spacial frequency wrinkles run in the direction normal to the stretching (vertical white and grey stripes), while higher frequency wrinkles (horizontal white and grey lines) run in the other direction.
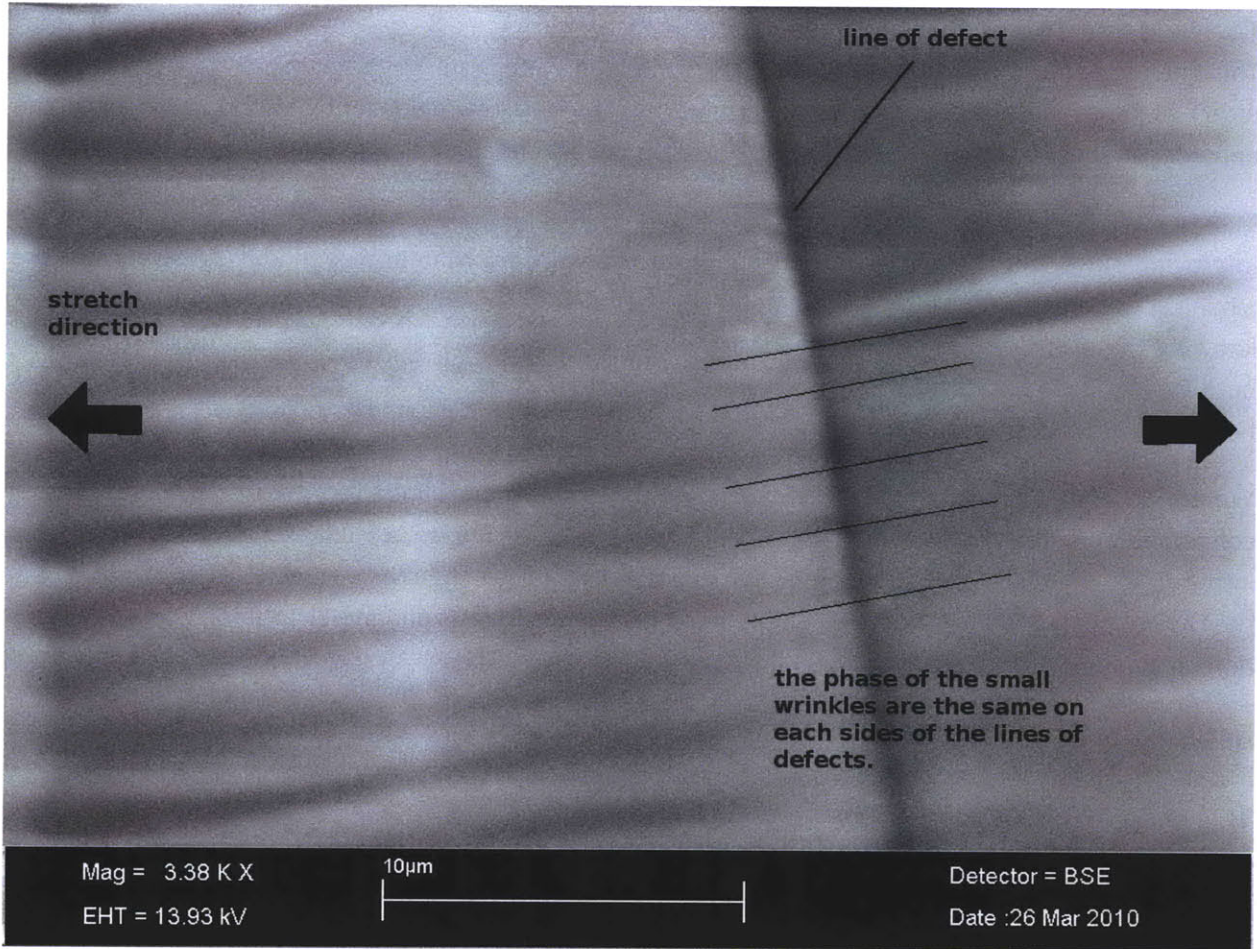
Figure 66: Close up on a line of defect. The small wrinkles seem to run through this line of defect. It is supposed that this line was thus formed after the small wavelength wrinkles.

G. Modeling of the wrinkles

This phenomenon of wrinkling of a hard coating on a soft substrate has been extensively studied (75), either as a mechanism to explain wrinkled patterns (78), or a new engineering method to increase the apparent strain at break of brittle films (79) (i.e. stretchable electronics...).

In this section, we form a dimensionless analysis of the problem of wrinkle formation. More than improving our understanding of the formation of the wrinkle on an homogeneous substrate, we are aiming at obtaining a robust numerical model for the "direct problem". By direct problem, we mean that knowing the elastic properties of the substrate, we should be able to compute the shape of the first buckling mode. Those elastic properties can be homogeneous, as well as in-homogeneous (defined by a field of elastic properties).

We are detailing the assumptions and reasoning that lead to our choices for the modeling (boundary conditions on a representative volume element; method for imposing multiaxial stresses; constraint introduce by the representative volume element...). This model is then tested against existing theories in the case of uniaxial buckling of a coating of homogeneous thickness and material properties on top of a homogeneous elastic substrate.

Finally, we are showing that the numerical model and the theory match the experimental data.

1. Finite element modeling

a) Dimensionless problem

(1) Two numerical formulations

A vast literature has introduced theoretical models for unidirectional wrinkles on soft and uniform substrates. Those theories have since been confirmed by experiments, either for thin metallic coatings on a soft elastomeric substrates or for hard polymeric shells on a soft polymeric core. Unfortunately, for more complex loadings (multi-axial loading), geometries (pattern substrate) or non-uniform material properties (of the substrate or the film) only numerical techniques can predict accurately the buckling shape of the coating.

Two approaches are possible to model this problem numerically:

- modeling the coating as a plate on an elastic foundation (see Figure 67)

- modeling the full 3D problem, with a compliant substrate layer and a stiff coating.

plate on an elastic foundation

stiff coating on a soft substrate

Figure 67: Two possible modelings for the problem: a/ plate laid on top of an elastic foundation b/hard coating (shell or 3D continuum modeling of the coating) on top of a substrate

There is obviously a trade-off between time of computing (in favor of the first option) and versatility and completeness (second approach). We have chosen the second one for more versatility, especially toward introduction of defects or patterns onto the substrate.

(2)   Imposing the pre-strain

For every numerical problem, a loading path and control parameter has to be chosen. There are again two equivalent ways to see the problem: either we start with a configuration of a strained substrate and release the strain (Figure 68), or we might start with a compressive force in the coating and release it (Figure 69). The latter case happens during a change in temperature, if the coefficients of thermal expansion between the two materials are not equal.

Indeed, those two ways to see the problems are both used to obtain the wrinkled pattern:

- Either the deposition of the stiff coating is done on a strained substrate. We call this the DOSS method (Deposition On Stretched Substrate). The stress in compression in the coating (before bifurcation) is $\sigma = -\frac{E}{1-\nu} \ln\left(1 + \frac{\Delta l}{l_0} - \frac{\delta l}{l_0}\right)$, where l_0 is the length of the sample, Δl is the pre-stretch and δl the stretch release at the bifurcation point.

- Or the wrinkles are due to thermal mismatch of the coefficient of thermal expansion. This is the TSC case (Thermally strained coating). If the deposition of the stiff coating is done at high temperature, when the temperature goes down to room temperature, the coating is held in compression with an in-plane stress: $\sigma = -\frac{E}{1-\nu} \int_{T_1}^{T_2} \left(\alpha_s(T) - \alpha_c(T)\right) dT$.

We mentioned that those two cases are equivalent for the buckling problem. It means that the DOSS with a pre-strain equal to the critical pre-strain (ie $\delta l = \Delta l$) is similar to applying the "critical change of temperature" in the TSC problem.

Though, the post-buckling solution may be different. Also, experimentally, the applied pre-strain $\frac{\Delta l}{l_0}$ is always greater than the critical pre-strain $\frac{\delta l}{l_0}$. Hence, the buckling does not happen around the free equilibrium (i.e. the one predicted with TSC or DOSS with $\delta l = \Delta l$) but around a strained equilibrium

configuration (the sample is still on the clamp during the wrinkle formation). This is the reason why it is important in practice, for relatively large applied pre-strains, to have a tangent stiffness modulus around the pre-strain state: $l + \Delta l$ (which is close to the critical equilibrium where the bifurcation happens).

We choose the TSC approach for the numerical simulations.

Situation 1	Situation 2
Figure 68: The substrate (a) is stretched by the exact critical pre-strain (b), before coating (c) and releasing of the stretch (d). [(d) is exactly at the bifurcation point, and there are wrinkles of infinitely small amplitude around the represented equilibrium position].	Figure 69: The substrate (a) is coated and heated so that compressive stresses develop in the coating (b) until it reaches the bifurcation point (d). This bifurcation point is exactly the same as in Figure 68.d. With this loading, it is possible to go above the critical point and form wrinkles of finite amplitude (e)

(3) Dimensionless problem

(a) Variables of the problem and Buckingham Pi-theorem
A dimensionless analysis is carried out to obtain a robust numerical problem. The dimensionless formulation is formed for isotropic linear material and in the case of uni-directional loading.

The main parameters of the problems are the stiffness of the materials E_c, E_s, the finite thickness of the coating and substrate t_c, t_s, along with the parameters to impose the force $\Delta T, \alpha_{therm}$. As discussed earlier, the stiffness of the material are parameters which encompass both the Young's modulus and the Poisson ratio (mainly the effective Young's modulus $\frac{E}{1-\nu}$). The coefficient of thermal expansion is really a parameter to impose the stresses, via the constraint of an expansion mismatch: $\alpha_{therm} = (\alpha_c - \alpha_s)$. With this convention, $\Delta T > 0$, would be the difference between the temperature of deposition and the temperature when the wrinkles are forming.

On the other hand, we are looking to determine the wavelength of the wrinkles λ, the amplitude A and the buckling load (per unit width) in the in-plane direction N.

	Length	Mass	Time	Temperature
t_c	1	0	0	0
t_s	1	0	0	0
E_c	-1	1	-2	0
E_s	-1	1	-2	0
α_{therm}	0	0	0	-1
ΔT	0	0	0	1
λ	1	0	0	0
A	1	0	0	0
N	0	1	-2	0

Table 4: Dimension of the variables of the simplified problem

The rank of the system of dimensions (Table 4) is 3. As a result, the Buckingham Pi-theorem implies that 3 dimension parameters have to be chosen, and there exist a relation between 6 independent dimensionless variables.

Let $t_c, E_c, \Delta T$ be the dimension parameters.

Then, we form the following dimensionless variables:

- Relative substrate stiffness: $R1 = \left(\frac{E_s}{E_c}\right)^{-1}$
- Relative wavelength: $R2 = \frac{\lambda}{t_c}$
- Relative amplitude of the oscillations: $R3 = \frac{A}{t_c}$
- Thermal pre-strain: $R4 = \alpha . \Delta T$
- Relative buckling force per unit width (or critical strain): $R5 = \frac{N}{E_c * t_c}$
- Relative thickness: $R6 = \frac{t_s}{t_c}$

And the Pi theorem proves the existence of a function f such that:

$$f(R1, R2, R3, R4, R5, R6) = 0$$

(b)   Formulation in Finite Element code.
For the Finite Element Analysis, we have used the commercially available code ABAQUS. We have imposed a coating thickness of 1, a coating stiffness of 1300 and a variation of temperature of 1. Those are the reference values. Knowing that the actual coating is 1 μm and the stiffness of the coating is 775MPa, we can conclude that 1 unit in length represent 1 μm and 1 unit in pressure is .6MPa. We do not actually use the temperature for the buckling problem, but only for the post-buckling solution.

(c)   Dimensionless analysis
Furthermore, we know that the wavelength of the oscillations is not independent of the other variables. As a result, there exists f (different from the previous one, but let's keep the same notation) such that:

$$R2 = f(R1, R3, R4, R5, R6)$$

We are interested in the limit of thick substrate, i.e. for $R6 \rightarrow \infty$. It rules $R6$, the relative thickness of substrate and coating, out of the problem.

Furthermore, we are making the assumption of linear buckling. It means that the state of stress of the buckle shape is taken to be the state of stress in the pre-buckling solution, for a magnitude of the load equal to the critical load. Thus, the in plane force is $N = E_c . t_c . \alpha . \Delta T$. It forms the constraint : $R5 = R4$. This means that the thermal strain is equal to the critical strain.

We are studying the buckling problem, not the post-buckling at this stage. As a result, we only consider the limit of infinitesimally small amplitude: R3 → 0.

Finally, the bifurcation point is detected as the smallest eigenvalue of the second derivative of the potential energy in the displacement field (cf III B). And as a result, this introduces another condition between the parameter: R5=g(R1,R2).

Under these assumptions, the complex problem of buckling is reduced to finding two scalar functions:

$$R2 = f(R1) \text{ and } R5 = f(R1)$$

Expressing the dimensionless ratio in the initial variable, this analysis shows that:

$$\lambda = t_c . f\left(\frac{E_c}{E_s}\right) \text{ and } N = E_c * g\left(\frac{E_c}{E_s}\right)$$

,where f and g are two scalar functions to be defined.

> This dimensionless analysis is different from the scaling law analysis. The initial assumption is that the buckled shape can be represented by two parameters (λ and A). However, no approximations are made on the 3D strain fields.

b) Numerical solution

(1) Stresses and strains are uniform in a sample

Before any finite element modeling, we have to consider the questions of symmetry, periodicity and ratio of different length scales, to know what volume to model and what type of elements are appropriate.

We first model the tensioning of the membrane in the grips to assess the influence of the gripping conditions. We assume that this membrane has the geometrical and material parameters of the PDMS substrate: $t_s = 1mm$, $width = 14mm$ and $length = 38mm$, and $E_c = .75MPa$ and $v = .49$. Since the thickness is less than a tenth of the other dimension, we have chosen to model the membrane by plane stress elements of thickness 1 (ie the dimensions are scaled by the thickness). More precisely, the 4-node bilinear CPS4R element type was chosen. We should note that a hyper-elastic model could have been used here, but the elastic model gives a good first order approximation.

We show the strain and stress contour in the PDMS substrate, at a 20%pre-strain (Figure 70, Figure 71 and Figure 72). As expected, there is a 20mm*14mm region in the middle of the membrane in which the strain and stress fields are uniform. We have performed all of our measurements in the experimental section within this area. Furthermode, we should note that in this region and due to the nearly incompressible model chosen, the strain in the normal direction is roughly half the strain in the loading direction (and in compression for the tensile loading).
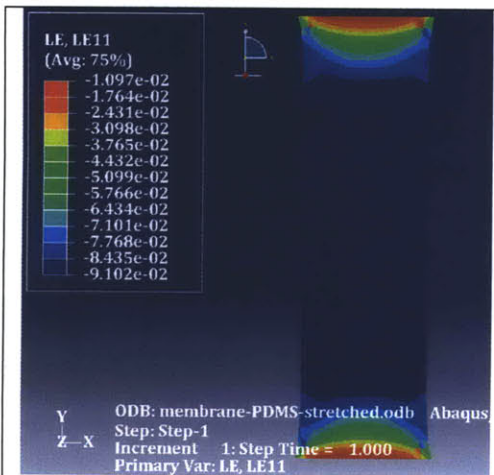
| Figure 70: logarithmic strain field in the stretched PDMS substrate, normal to the loading direction for a pre-stretched of 20% | Figure 71: Logarithmic strain field in the stretched PDMS substrate, in loading direction for a pre-stretched of 20% | Figure 72: Mises equivalent stress field in the PDMS substrate at 20% of pre-stretched. |
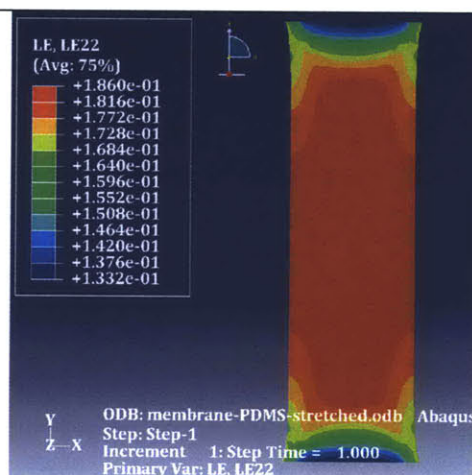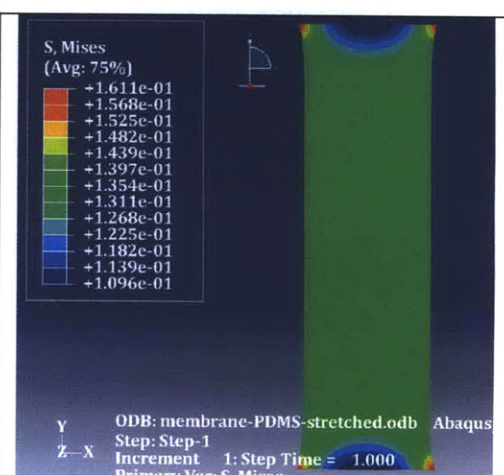
This simulation proves that instead of modeling the whole membrane, we can extract a small representative volume element. We may apply to this representative volume element periodic boundary conditions and a macroscopic transformation gradient equal to the one obtained in this analysis.

(2)   Mesh and boundary conditions.

(a)   mesh
We have moved from 2D to 3D to model the wrinkles on the surface of the coating samples.

For the 3D model, we have chosen to represent a portion of substrate of 200*200*200 units of substrate, with a coating layer modeled by shell elements of thickness 1 (because the thickness of the coating is taken to be 1, a unit is 1μm). It means that the substrate is 200 times thicker than the coating, which should be sufficient to model the thick substrate limit. Also, the elements are 8 node three-dimensional elements, with reduced integration (C3D8R) for the substrate, and 4 node shell elements (S4R) for the coating. The shape of the first buckling mode is pretty independent of the type of element (reduce integration or not, number of integration point in the thickness and type of integration rule), so we settled for a reduced formulation, with Simpson rule and 5 integration points.

Those rectangular elements proved to give "better results" than tetragonal elements. Though, they are not easy to coarsen. In fact, as shown in Figure 73, only the direction normal to the coating is "coarsen". A total of 82160 nodes are used.
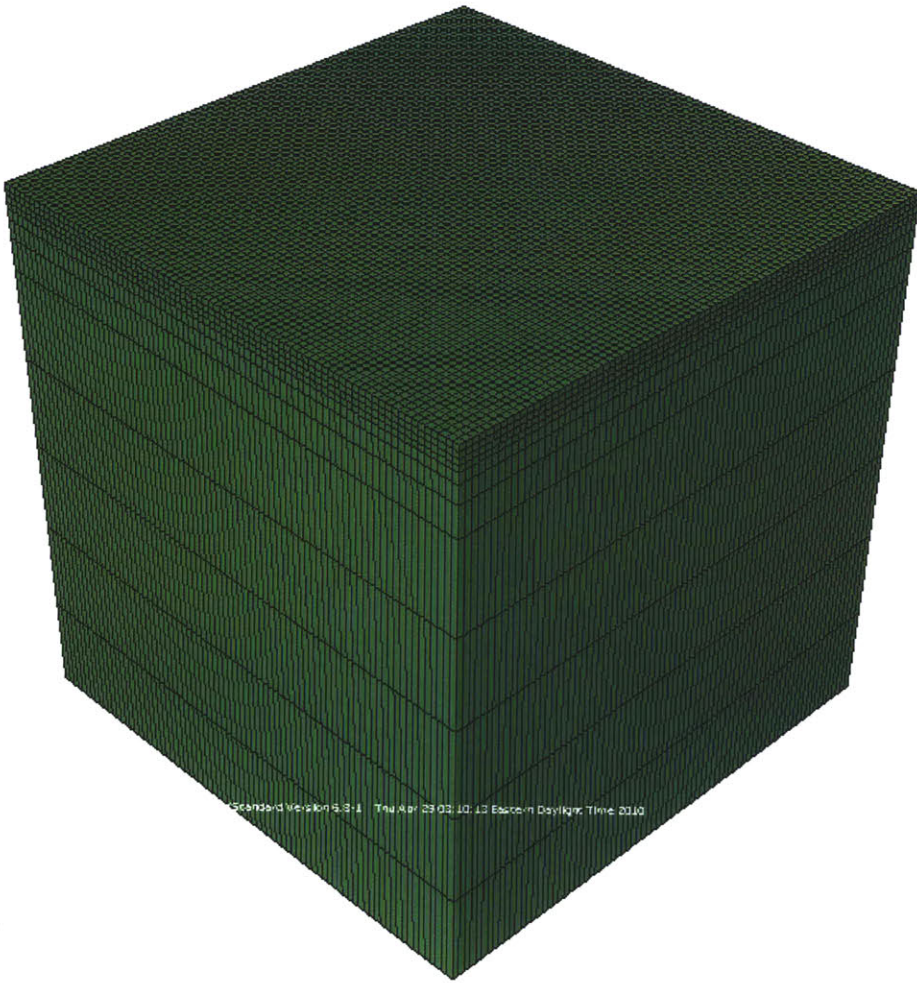
Figure 73: Mesh and geometry used for the modeling of the wrinkles; the mesh is made of 8 nodes elements and is refined close to the coating. The elements on the surface are 2.5*2.5*2.5 while the ones further away are 2.5*2.5*34.

(b)   Boundary conditions

The boundary conditions have been one of the big issues of this modeling. We have studied 4 types of conditions for the representative volume element (the surfaces normal to e_x and e_z): pinned, free, symmetric and periodic.

(i)   equations for periodic boundary conditions

The periodic boundary conditions were directly written into the *.inp file with a Matlab routine, by imposing equations between the displacement of matching nodes. More precisely, let A be a point of a "periodic surface" (Figure 74). We find the node B, such that $b = a + OO'$. With Figure 74, we understand that B is both on the right surface of the considered portion and on the left surface of the next representative volume element. As a result, we find the relation:

$$u_b - u_a = (u_b - u_{o'}) + (u_{o'} - u_o) + (u_o - u_a)$$

$$= (u_{o'} - u_o)$$

$$= F.OO'$$

Where F is the transformation gradient imposed to the macro-structure. To impose this relation for continuum elements, we introduce a reference node, say O'. Then,

$$\{for\ all\ nodes\ a \in \mathring{A}\ and\ b \in \mathcal{B}, such\ that\ b - a = OO'we\ impose\ u_a^i = u_b^i - u_{O'}\}$$

For structural elements, we should additionally impose a condition on the rotation degree of freedom. For instance, assuming that shell elements are applied on the top surface on Figure 74, we should impose on edge E1 and E2 (oriented by $\vec{t}$) the additional condition:

$$\{for\ all\ nodes\ c \in \mathcal{E}_1\ and\ d \in \mathcal{E}_2, such\ that\ d - c = OO'we\ impose\ \theta_a^{\vec{t}} = \theta_b^{\vec{t}}\}$$
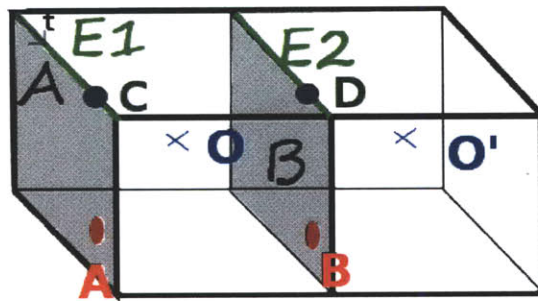
Figure 74: Periodic boundary conditions: two representative volume elements

Figure 75 (with free boundary conditions applied on the sides) shows an interesting phenomenon with a solution of bending of the coating before the buckling. Physically, this phenomenon of bilayer bending is describing very well the membrane as a whole. Though, the wrinkles have a much smaller length scale than the width or length of the sample. As a result, this phenomenon does not describe what happens locally.

(ii)   choice between the different boundary conditions for the representative volume element
The pinned boundary conditions are constraining too much the development of proper and homogeneous patterns.
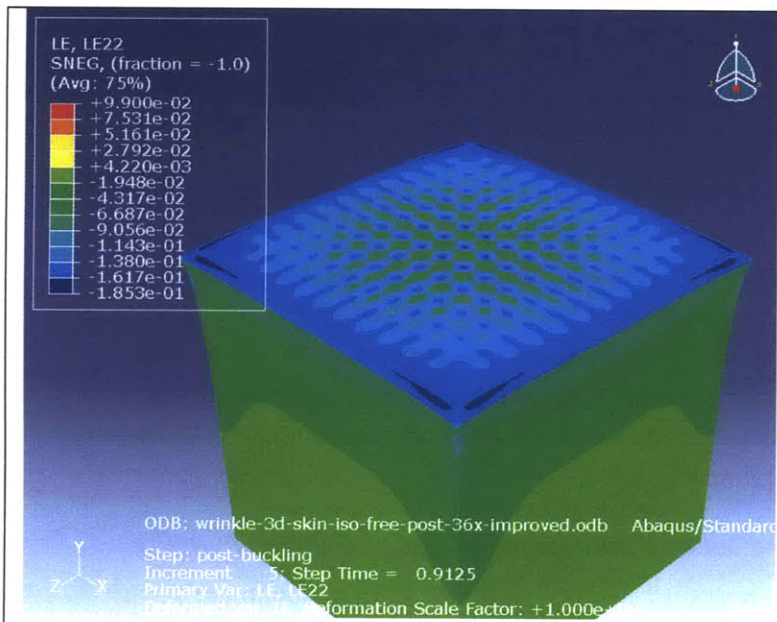
Figure 75: First buckling mode of a representative volume element with a hard coating put into compression by thermal expansion mismatch. Free boundary conditions are applied on the sides of this representative volume element (RVE).
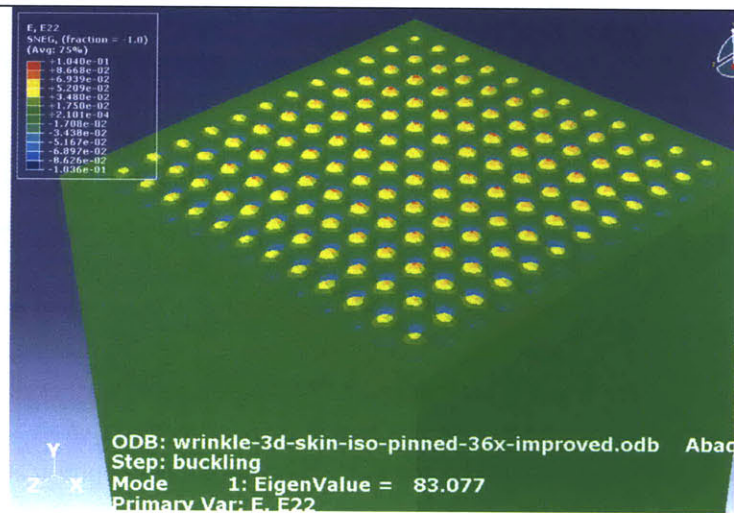
Figure 76: First buckling mode for pinned boundary conditions applied on sides of the RVE.
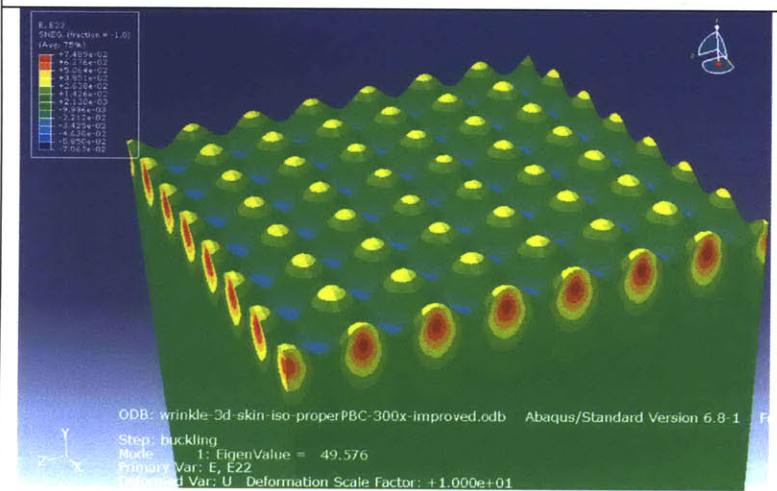
Figure 77: First buckling mode for the Periodic Boundary conditions applied on the sides of the RVE
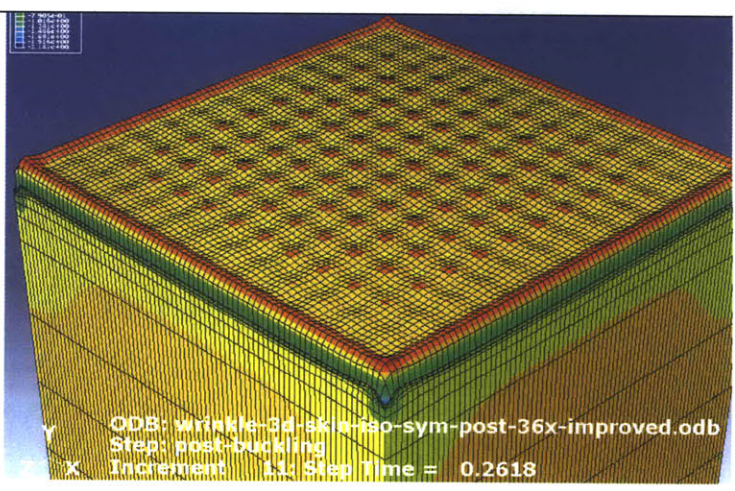
Figure 78: First buckling mode for the Symmetric boundary conditions applied on the sides of the RVE

(c)   Constraint on the wavenumber

It is important to note that both periodic boundary conditions, symmetric boundary conditions and pinned boundary conditions constrain the wavenumber to be an integer and hence the predicted wavelength will be limited to be the length of a RVE divided by some integer value. It may affect the prediction of the actual wavelength.

Figure 79,Figure 80, Figure 81,Figure 82,Figure 83 are showing the transition between a wave number of 6 and 7, as the ratio R1 increases. When there is no constraint (i.e. the wave number is an integer), the numerical solution displays a buckling in a mode where all the wrinkles are of similar amplitude Figure 79. If we had an infinitely large representative element, we would see wrinkles of the same wavelength. As R1 increases, the wave number decreases. Though, our simulations still suppose that the representative volume element is periodic. Hence, it over-constrains the numerical solution. It results in a shape that has no physical meaning Figure 80. By further increasing the relative stiffness of the coating and substrate, R1, we will reach the middle of the transition region where the wave number is 6.5: Figure 81. The two waves in the center are merging into one. Once again, this has no physical meaning, and it is very depend from the size of the representative element. Decreasing further the wave number, we observe the end of this "transition region" Figure 82, until we reach an integer wave number Figure 83, where the numerical solution is the physical solution.

Hence, it should be noted that the precision of the determination of the wavelength of the wrinkles is affected: the maximum precision should be $error_\lambda = 200 * \left(\frac{1}{k} - \frac{1}{k-1}\right)$, where k is the wavenumber.

Furthermore, we can show analytically that the buckling force (or R5) is an increasing function of the relative stiffness, R1. We should note that it does not hold true for the simulations: Figure 80 and Figure 81 show that $\alpha * R5_{R1=340} = 72.913$ while $\alpha * R5_{R1=360} = 72.973$. This is due to the fact that the buckling of the numerically constraint coating requires more force than it does in reality (if we were to consider an infinitely large representative element). However, the buckling force seems to be bounded by the two situations of integer wave number just below and above:

$$R5_{floor(wavenumber)} < R5_{wavenumber} < R5_{floor(wavenumber)+1}.$$

This is of importance because for large wave numbers, it is difficult to impose a ratio R1 such that the wave number is an integer. However, the sequence $f(n) = R5_n - R5_{n+1}, with\ n \in \mathbb{N}$ is converging to zero. So even though we are not in situation where the wavenumber is an integer, the estimation error for the buckling force is minimal for large wave numbers:

$$error_{R5} = R5_{wavenumber}^{numerical} - R5_{wavenumber}^{theoretical}$$

$$R5_{floor(wavenumber)}^{numerical} - R5_{wavenumber}^{theoretical} < error < R5_{floor(wavenumber)+1}^{numerical} - R5_{wavenumber}^{theoretical}$$

$$R5_{floor(wavenumber)}^{theoretical} - R5_{wavenumber}^{theoretical} < error < R5_{floor(wavenumber)+1}^{theoretical} - R5_{wavenumber}^{theoretical}$$

$$R5_{floor(wavenumber)}^{theoretical} - R5_{floor(wavenumber)+1}^{theoretical} < error < R5_{floor(wavenumber)+1}^{theoretical} - R5_{floor(wavenumber)}^{theoretical}$$

$$|error_{R5}| < f(n)$$

It means that provided the representative element contains "enough" wrinkles, the estimation of the force and the estimation of the wavelength is correct, even though the shape is not really "physical" due to the constraint, unless the exact wavelength is allowed in the chosen RVE.
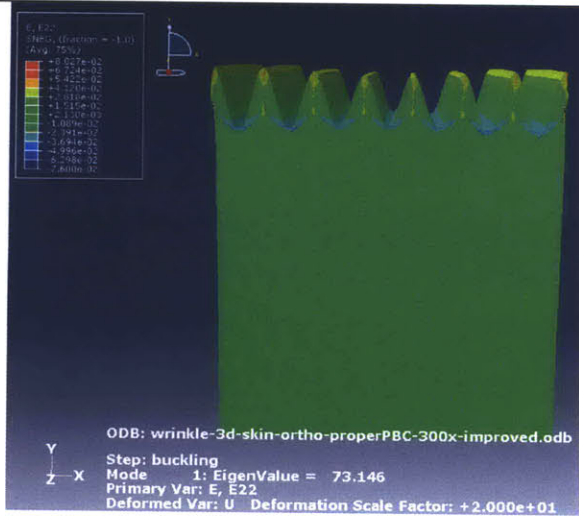
Figure 79: Uniaxial stretch for R1=300. 7 wrinkles of equal amplitude are forming. The constraint on the wave number is "slight" and the wavelength computed in larger representative elements should be
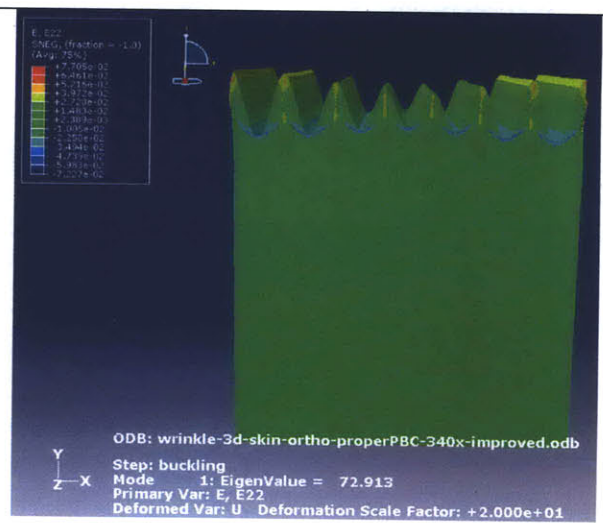
Figure 80: Uniaxial stretch for R1=340. 7 wrinkles are forming on the representative volume element. Due to the constraint on the wave number, wave of smaller amplitudes are forming in the center
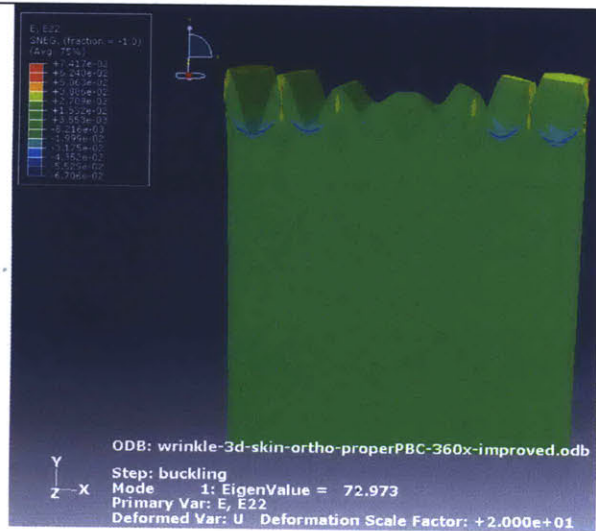
Figure 81: Uniaxial stretch for R1=360. 6 wrinkles are forming. The middle wrinkle is irregular, and seems to accommodate the constraint on the wavenumber; The eigenvalue is larger than the one obtained for R1=340.
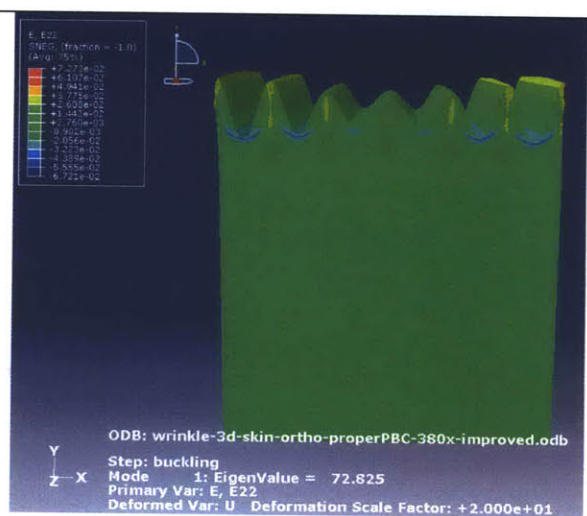
Figure 82: Uniaxial stretch for R1=380. 6 wrinkles are forming. The amplitude of the wrinkles is irregular, due to the constraint on the wavenumber.
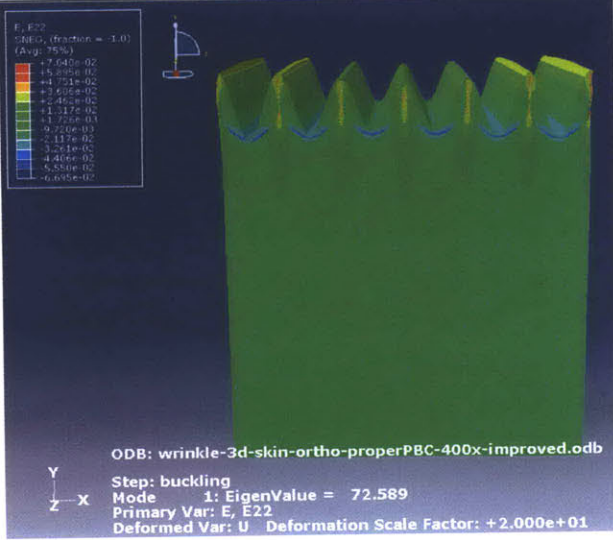
Figure 83: Uniaxial stretch for R1=400. 6 wrinkles of equal amplitude are forming. It means that the wavenumber constraint is "slight".

(3)   Buckled coating

We now have a problem well defined. We use Abaqus simulations to determine the function f that link the dimensionless parameters. We will also check the assumption we made. Again, we have shown under certain assumptions that there must exist a function f such that: $f(R1, R2) = 0$ with $R1 = \frac{E_c}{E_s}$, $R2 = \frac{\lambda}{t_c}$.

We should also consider the variation with the Poisson ratio of the coating, since we were not able to measure this experimentally v_c.

(a)   Variation of E_c keeping R1 constant

The first series of simulation is more of a sanity check: the relative stiffness, $R1 = \frac{E_c}{E_s}$, is kept constant while E_s and E_c are increased. The Poisson coefficients are set up to: $v_c = 0.45$ and $v_s = 0.49$, the dilatation coefficient is orthotropic: (0.004;-0.002;0). This coefficient corresponds to the uniaxial loading, as we have seen in II.G.1.b)(1). For each simulation, we are counting the number of wrinkles to determine the wavelength. The eigenvalue given by Abaqus is the proportional load (i.e. temperature) at the bifurcation point. As a result, we compute $N = E_c.t_c.\alpha.eigenvalue$.
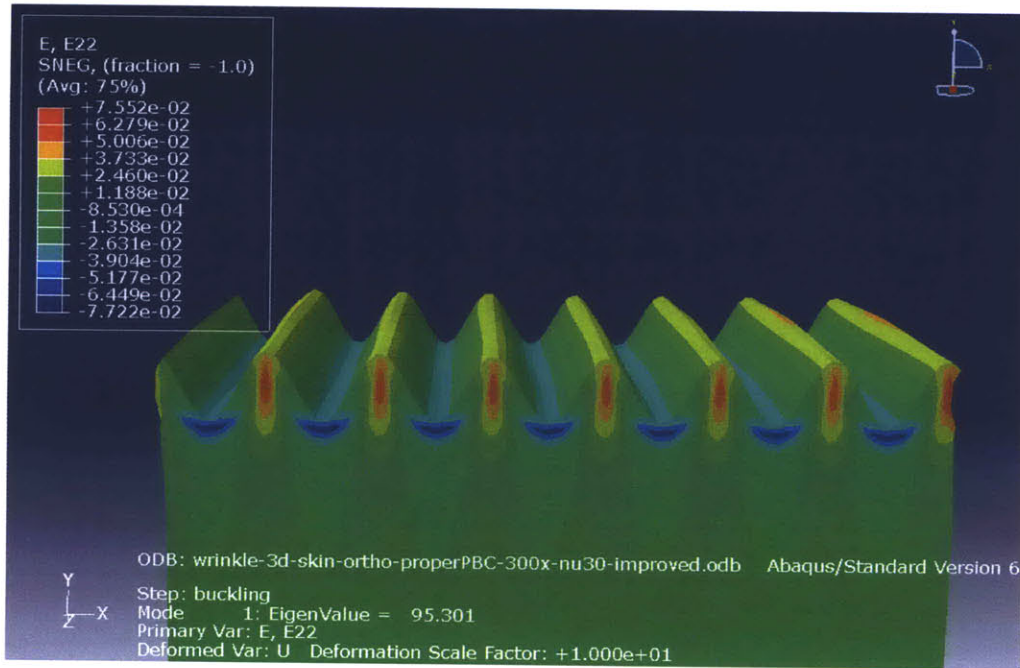
Figure 84: Field of vertical displacement for the simulation 2.

The results of those simulations are shown in Table 5. As expected, the critical strain R5 and the relative wavelength R2 are constant. We should note that one of the simulations did not converge after 300 iterations. We don't have any explanation.

Simulation	1	2	3	4
Es	0.036	0.36	/	36
Ec	1.3	13	/	1300
k	12+2	12+2	/	12+2
Lambda	15	15	/	15
$\dfrac{N}{E_c}$	155.3	155.3	/	155.3
$R1 = \dfrac{E_c}{E}$	0.028	0.028	/	0.028
$R2 = \dfrac{\lambda}{t_c}$	15	15	/	15
$R5 = \dfrac{N}{t_c\,E_c}$	.62	.62	/	.62

Table 5: Simulation results: the relative stiffness R1 and thickness R6 are kept constant but the absolute value of E_s and E_c are changed. As expected, the simulation predicts the same wavelength and critical strain for every case.

Poisson ratios do not appear in our dimensionless analysis. We decided to run a series of simulations to decide of the role of the Poisson ratio of the coating on the buckling load and wavelength. Unfortunately, the buckling could not be performed with less than 300 iterations for low Poisson coefficient. The results are shown in the Table below, and plotted in Figure 85. The conclusion here is that the Poisson ratio of the coating does not seem to have that big of an influence on the shape and critical load.

Simulation	5	6	7	8	9
E_s	.5	.5	.5	.5	.5
E_s	150	150	150	150	150
k	7	7	7	7	7
λ	28.5	28.5	28.5	28.5	28.5
N	95.3	95.3	95.3	96.2	95.3
$R1 = \dfrac{E_c}{E}$	300	300	300	300	300
$R2 = \dfrac{\lambda}{t_c}$	28.6	28.6	28.6	28.6	28.6
$R5 = \dfrac{N}{t_c\, E_c}$	.38	.38	.38	.39	.38
ν_c	0.3	0.4	0.45	0.47	0.49

Table 6: Influence of the Poisson ratio of the coating on wavelength and buckling load (keeping R1 constant)
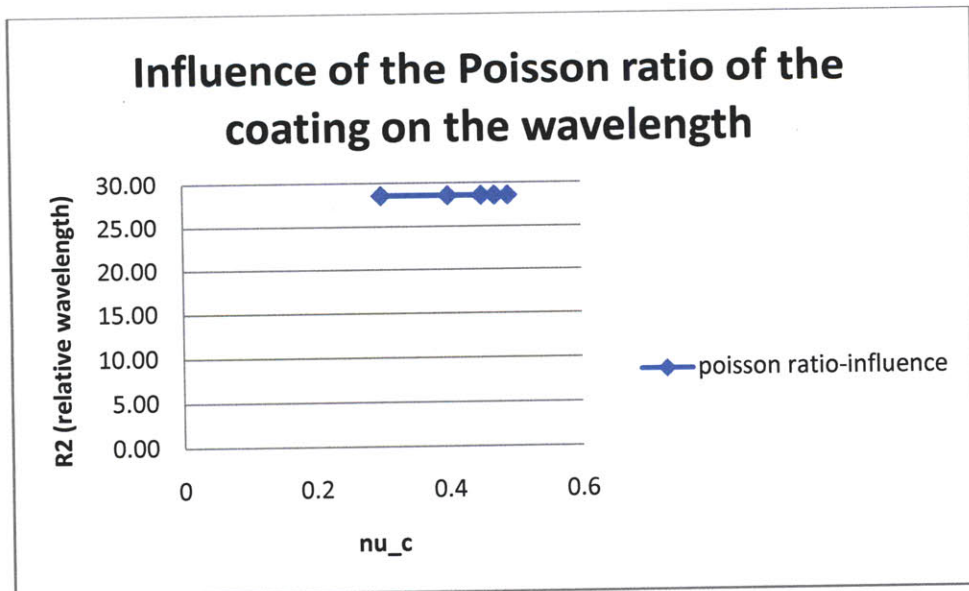
Figure 85: Influence of the Poisson ratio of the coating on the wavelength of the wrinkles

$$\begin{cases} R2 = 5.2 * R1^{.32} \\ R5 = 6.1 * R1^{-0.64} \end{cases}$$

We observe that those simulations confirm the results obtain analytically by scaling analysis for the wavelength. However, the critical force outputs by the numerical simulations are confirmed for stiffness ratio up to 100. Then, the variation with the the ratio R1 diverge from the scaling law analysis.
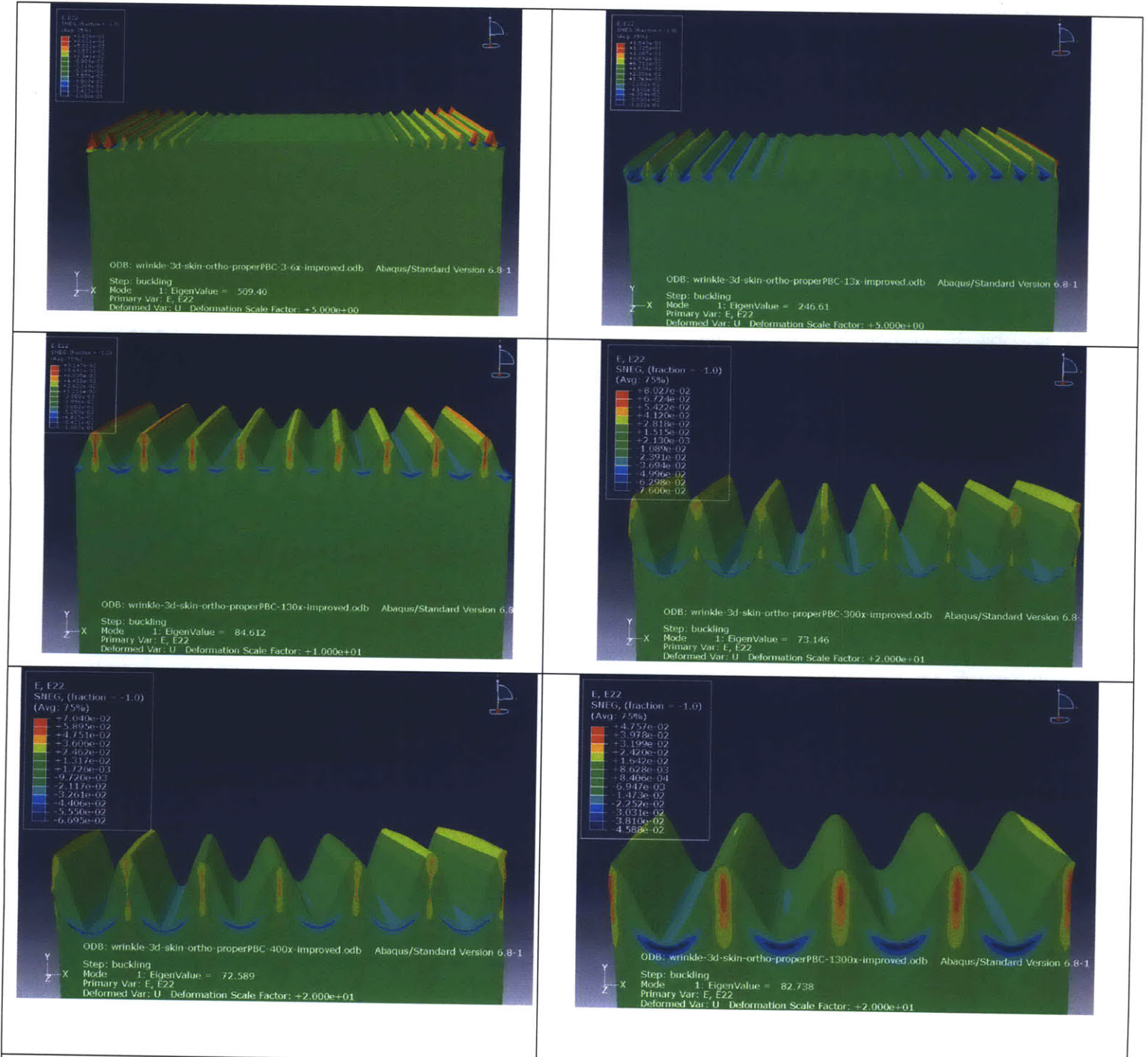
Figure 86: Buckled shapes for 4 values of the parameter R1 (everything constant otherwise). a/ R1=3.6 ; b/ R1=13 ; c/ R1=130; d/ R1=300; e/

Simulation	10	11	12	13	14	15	16	17	18
Es	360.0	325	100.0	36	32.5	10.0	4.3	3.25	1
Ec	1300.0	1300	1300.0	1300.0	1300.0	1300.0	1300.0	1300.0	1300.0
k	26.0	25	18.0	13	13.0	9.0	7	6	4
lambda	7.7	8.0	11.1	15.4	15.4	22.2	28.6	33.3	50.0
N	509.4	482	246.6	141.67	134.5	84.6	73.15	72.56	82.738
R1	3.61	4.00	13.00	36.11	40.00	130.00	302.33	400.00	1300.0
R2	7.69	8.00	11.11	15.38	15.38	22.22	28.57	33.33	50.00
R5	2.04	1.93	0.99	0.57	0.54	0.34	0.29	0.29	0.33

Table 7: An analysis of the influence of R1 is shown here. The coating stiffness is kept constant while the stiffness of the substrate is increased. The wavenumber, k, is defined as the number of wave in a RVE. The wavelength is the inverse of the wavenumber and N is the eigenvalue output by Abaqus. R1,R2 and R5 are computed from those parameters
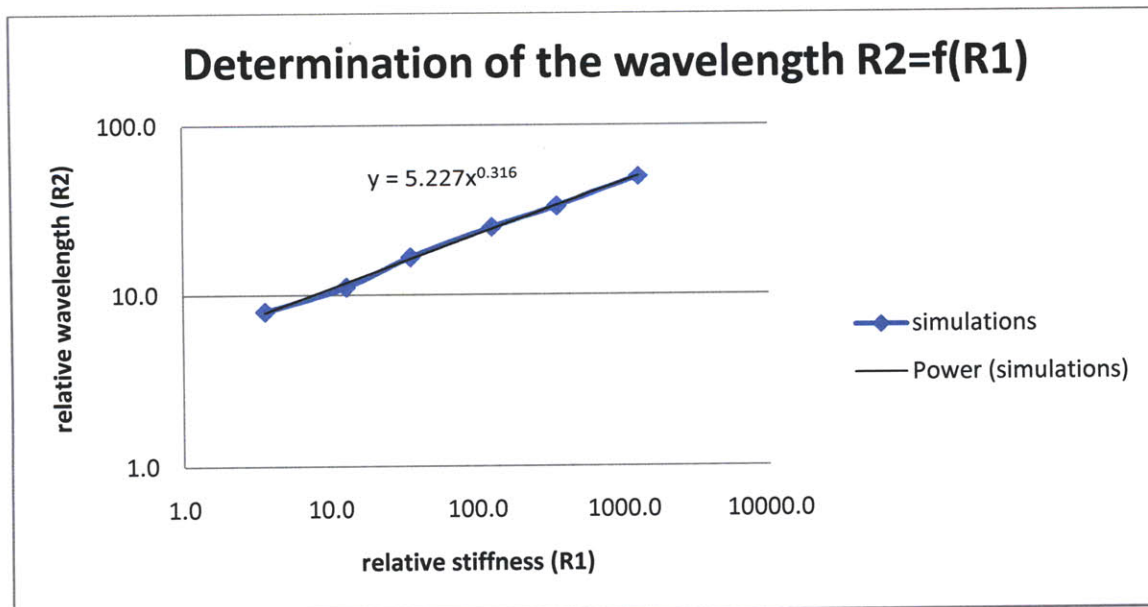
Figure 87: The dimensionless wavelength R2 is shown as a function of R1.
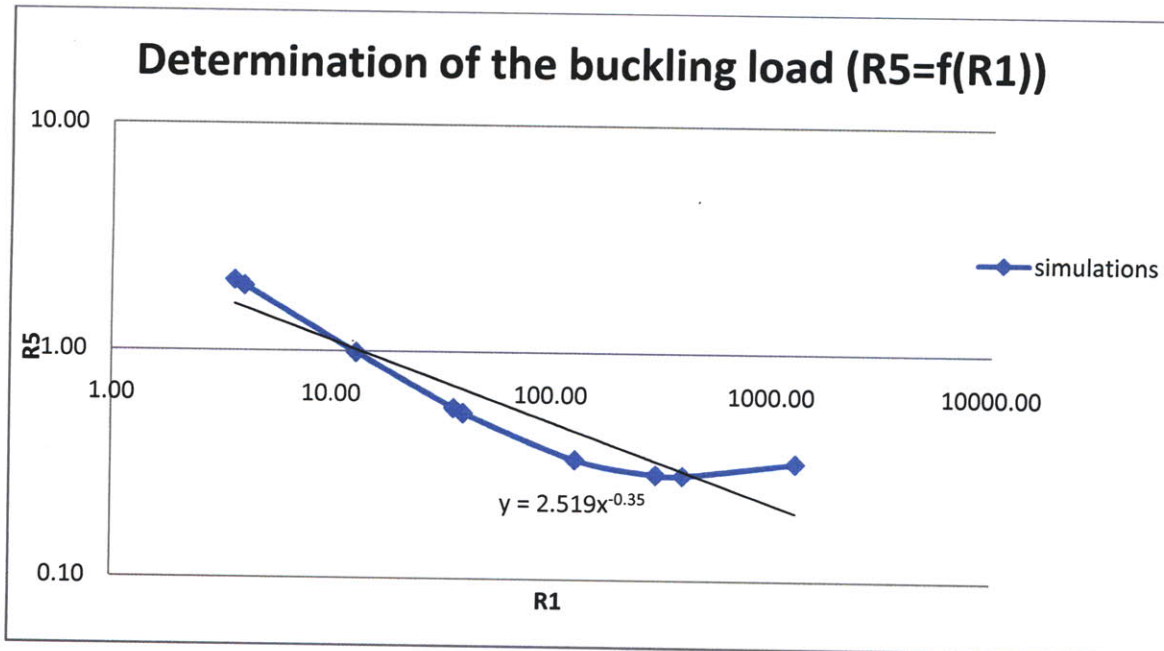
Figure 88: Determination of the critical load (R5=f(R1))

(4) Non-uniaxial stretching

To complete the testing of our numerical modeling, we compute the post-buckling solution of a membrane with an isotropic straining. We use the same RVE as before with the periodic boundary conditions. The stiffness ratio R1 is taken to be 300, and the relative thickness of the coating is R6=.005. We should note that the predicted wavelength in this isotropic case is the same as the wavelength in the orthotropic case (corresponding to the same relative stiffness R1).

As predicted by the theory, the mode associated with the lowest buckling load is the checkerboard. However, if we run a post-buckling analysis, the system will go from this checkerboard pattern to the Herringbone pattern when the load is increased above a certain value. This was predicted by Chen et al. (74): the Checkerboard pattern has a lower buckling load. However, when the load is increased further, the energy of the Herringbone patterns is lower than the energy of the checkerboard.

The final post-buckling solution also matches the "shape" of the Herringbone pattern observed experimentally: one leg of the zigzag pattern encompasses four of the initial bumps of the buckling shape. As a result, the distance between two consecutive zigzag patterns is equal to the wavelength of the bumps predicted by the buckling solution, but the legs of those zigzag is four times larger.
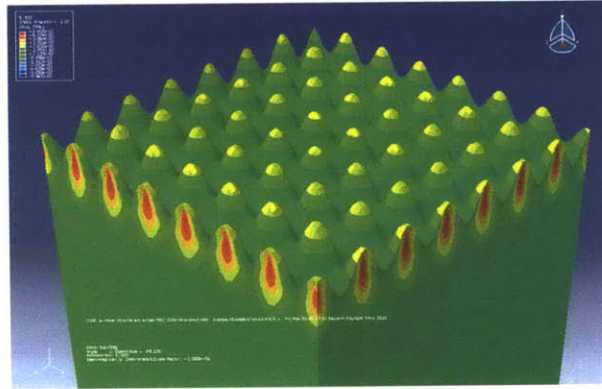
Figure 89: The first buckling mode for the bi-axial stretching of the membrane is the checkerboard pattern
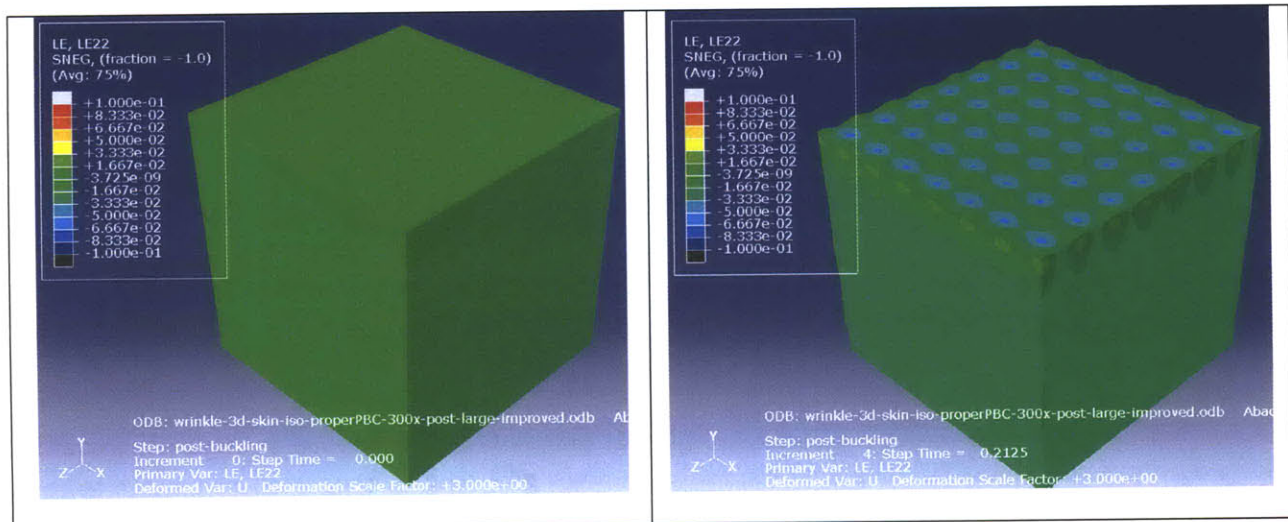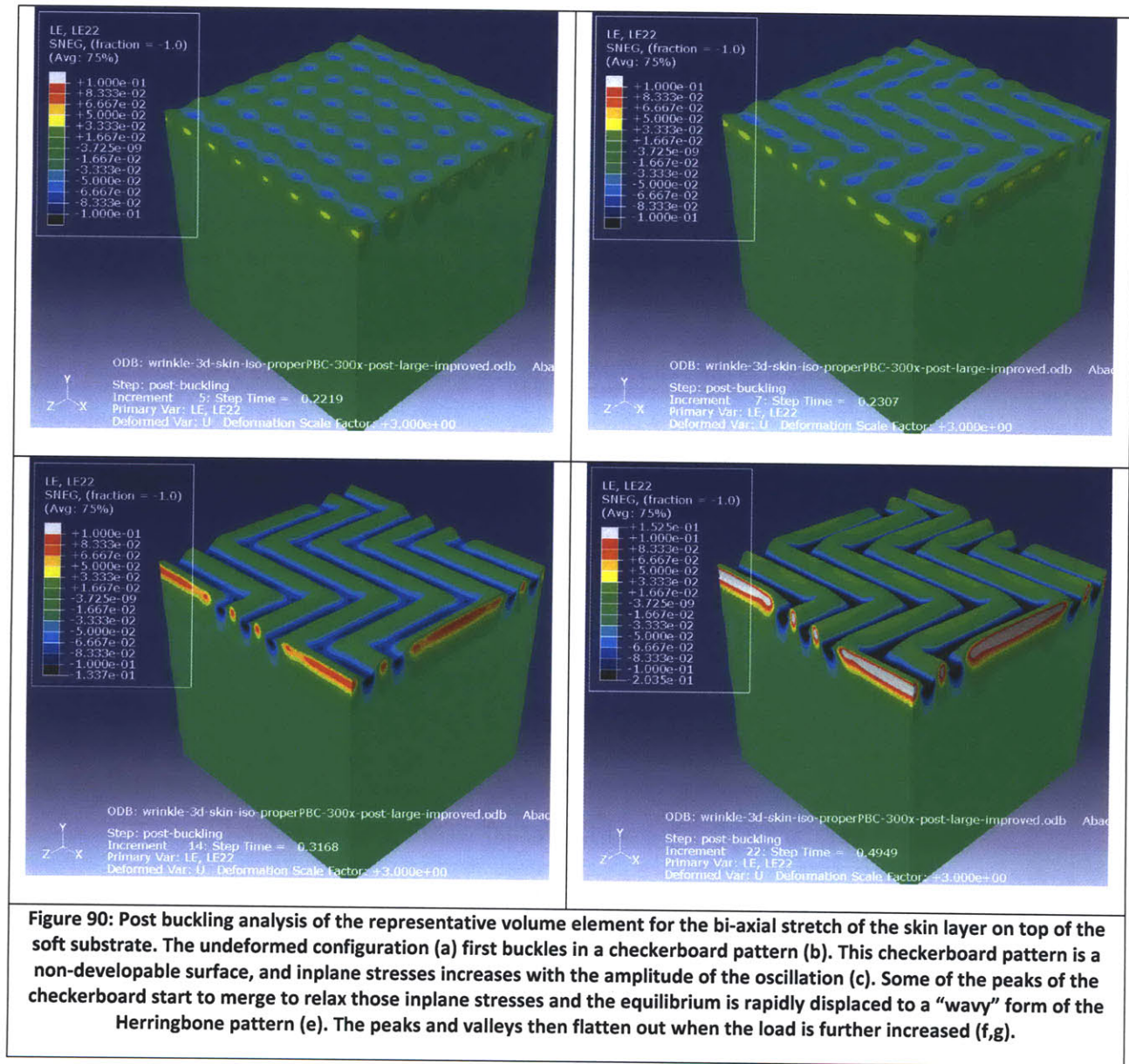
Figure 90: Post buckling analysis of the representative volume element for the bi-axial stretch of the skin layer on top of the soft substrate. The undeformed configuration (a) first buckles in a checkerboard pattern (b). This checkerboard pattern is a non-developable surface, and inplane stresses increases with the amplitude of the oscillation (c). Some of the peaks of the checkerboard start to merge to relax those inplane stresses and the equilibrium is rapidly displaced to a "wavy" form of the Herringbone pattern (e). The peaks and valleys then flatten out when the load is further increased (f,g).

2.   Experiments, theory and simulation

a)   *Theory and simulations*

In (74), Chen et Huchinson find out two essential relations in the approximation of thick substrate and linear buckling:

$$\begin{cases} \dfrac{\sigma_c}{\bar{E}} = \dfrac{1}{4} * \left(3 * \dfrac{\bar{E}_s}{\bar{E}}\right)^{\frac{2}{3}} \\ \lambda = 2.\pi.t.\left(\dfrac{\bar{E}_c}{3 * \bar{E}}\right)^{\frac{1}{3}} \end{cases}$$

We compare the conclusions of our simulations and the theory (derived from a scaling analysis) developed by Chen (74) in Table 8 with the following notations (where R1 is the relative stiffness of the two materials, R5 the critical strain and R2 the relative wavelength):

$$\begin{cases} R5 = \alpha R1^{\beta} \\ R2 = \gamma . R1^{\delta} \end{cases}$$

The theory (74) leads to:

$$\begin{cases} \alpha_{analytical} = \dfrac{1}{4} * 3^{\frac{2}{3}} * (1 - v_c^2)^{-\frac{1}{3}} * (1 - v^2)^{-\frac{2}{3}} \\ \beta_{analytical} = \dfrac{-2}{3} \\ \gamma_{analytical} = 2.\pi.2^{-\frac{1}{3}} \\ \gamma_{analytical} = \dfrac{1}{3} \end{cases}$$

constant	Theory (Huchinson)	Numerical solution
α	.66	3.8 (for R1<100)
β	-.67	-.55 (for R1<100)
γ	4.3	5.1
δ	.33	.31

Table 8: Comparison of analytical 2D solution in plane stress and the numerical simulations

It proves that the simulations capture really well the variations between the dimensionless parameters R1, R2 and R5. However, there is a discrepancy in the prediction of the critical load between the theory and the simulations. The critical force predicted by the simulation is five times more important than the one predicted in the Hutshinson's analysis. Furthermore, as the relative stiffness of the coating is increased, the critical strains predicted by the simulations seem to differ from the prediction given by the scaling analysis. The difference might be due to the in-plane strain the substrate. As the stiffness ratio is increase above 1000, the in-plane compressive strain of the compliant substrate (which is "only" 200 thicker than the coating in our simulations) might no longer be negligible.

b) Experiments

If we substitute the material parameters of EGDA and PDMS in the analytical model, we obtain:

$$\lambda_{analytical} = 2.\pi.t_c.\left(\frac{E_c}{3*E_s}\right)^{\frac{1}{3}}$$

$$= 2.\pi.1\mu m.\left(\frac{775}{3*E_{PDMS}}\right)^{\frac{1}{3}}$$

Assuming that the tangent stiffness of the PDMS is 1.0 MPa, we get $\lambda_{analytical} = 40\mu m$.

On the other hand, the simulation predicts a wavelength for the larger wavelength $\lambda_{simulation} = 42\mu m$

The observed wavelength for our sample was $\lambda_{experimental} = 38\mu m$. Considering the experimental imprecision (in the applied pre-strain, the geometrical dimensions or the conditions of deposition), those results prove that both the scaling analysis and the simulations predict well the wrinkles we see on the membranes. This quantitative comparison between simulations and experiments also proves that the "direct method" to compute the shape of the buckled coating is quite robust. We show a more complex simulation for this direct method in the next chapter: the substrate is no longer kept homogeneous but exhibits local stiffening (due to an increase in crosslink density). This results in the possibility to direct the waves. We are showing a comparison between our simulations and the experiments made by Huck et al. (80).

However, we should note that neither the simulation, nor the theory by Hutchinson predict the smaller wavelength wrinkles.

H. Conclusion

This second chapter addresses three important points:

- A short literature review for the role of artificial micro-patterning in anti-fouling and fouling release properties.
- A proof of concept and characterization of the pattern surface obtained after iCVD deposition of a "chemically optimize" coating onto a strained substrate.
- Design of a robust numerical simulation to model the wrinkle formation of a stiff coating on a compliant substrate.

I.   Bibliography for chapter II

1. **World Health Organization.** *Guideline for drinking water (3rd edition).* 2006.

2. **Robert Engelman (Population Action International).** *People in the balance- Population and Natural resources at the Turn of the Millennium.* 2000.

3. **(US), National Research Council.** *Review of the desalination and water purification technology roadmap.* s.l. : Committee to Review the Desalination and Water Purification, 2002.

4. **Cashman, Preene.** *Groundwater lowering in construction: a practical guide.* s.l. : Spon press, 2001.

5. Water Quality Association, Glossary . [Online] as of October 2009. http://www.wqa.org/.

6. **Pearce.** *When the Rivers Run Dry: Water--The Defining Crisis of the Twenty-first Century .* s.l. : Beacon Press books, 2006.

7. *Ashkelon desalination plant — A successful challenge.* **Sauvet-Goichon.** 2007, Desalination, Vol. 203, pp. 75–81.

8. *Handbook of Inorganic Chemical Compounds.* s.l. : McGraw-Hill, 2003.

9. *Enhancing RO system performance utilizing antiscalants.* **Ghafour.** 2002, Desalination, Vol. 153, pp. 149-153.

10. *Limits of RO recovery imposed by calcium phosphate precipitation.* **Greenberg.** 2005, Desalination, Vol. 183 , pp. 273–288.

11. **Dow water solution.** *Filmtech reverse osmosis membrane: Technical manual.* 2003.

12. *Engineering design of Skikda Seawater Desalination Plant, Desalination and Water Treatment.* **Fanjul.** 2009, Desalination and Water Treatment, Vol. 7, pp. 206–213.

13. *Reverse osmosis desalination: Water sources, technology, and today's challenges.* **Greenlee.** 2009, Water Research, Vol. 43, pp. 2317-2348.

14. *Second law analysis of a reverse osmosis plant in Jordan.* **Aljundi.** 2009, Desalination, Vol. 239, pp. 207-215.

15. *State of the art of reverse osmosis desalination.* **Fritzmann.** 2007, Desalination, Vol. 216, pp. 1-76.

16. *Development of the fourth generation energy recovery device. A CTO's Notebook.* **Stover.** 2004, Desalination, Vol. 165, pp. 313-321.

17. *Effect of recent technological developments on SWRO incorporated in the Red-Dead project.* **Glueckstern.** 2009, Desalination and Water treatment, Vol. 5, pp. 132-136.

18. *Hollow fine fiber vs. spiral-wound RO desalination membranes Part 2: Membrane autopsy.* **Butt.** 1997, Desalination, Vol. 109 , pp. 83-94.

19. *Modeling the impacts of feed spacer geometry on reverse osmosis and nanofiltration processes.* **Gilllen.** 2009, Chemical Engineering Journal, Vol. 149, pp. 221–231.

20. *Spiral wound modules and spacers Review and analysis.* **Ribeiro.** 2004, Journal of Membrane Science, Vol. 242, pp. 129–153.

21. *Characterization of a zigzag spacer for ultrafiltration.* **Schwinge.** 2000, Journal of Membrane Science, Vol. 172, pp. 19–31.

22. *Study of the effects of spacer geometry in membrane feed channels using three-dimensional computational flow modeling.* **Shakaib.** 2007, Journal of membrane science, Vol. 297, pp. 74-89.

23. *Biofouling of reverse osmosis membranes: Role of biofilm-enhanced osmotic pressure.* **Herzberg.** 2007, Journal of Membrane Science, Vol. 295, pp. 11–20.

24. **Dow Chemical.** *Technical manual, Form No. 609-00071-0309.*

25. **Hoff, Jacobus Henricus van 't.** *Osmotic pressure and chemical equilibrium, Nabel lecture.* 1901.

26. *A new thin-film composite seawater reverse osmosis membrane.* **Cadotte.** 32, 1980, Desalination, pp. 25-31.

27. *Development of crosslinked fully aromatic polyamide ultra-thin composite membranes for seawater desalination.* **Kurihara.** 1994, Desalination, pp. 133-144.

28. *Reformulation of the solution-diffusion theory of reverse osmosis .* **Paul.** 2004, Journal of membrane science, Vol. 241, pp. 371-389.

29. **Cadotte.** *Interfacially synthesized reverse osmosis membrane. 4,277,344* 1981.

30. *Effect of membrane chemistry and coating layer on physiochemical properties of thin film composite polyamide RO and NF membranes.* **Tang.** 2009, Desalination, Vol. 242, pp. 168-182.

31. *Impacts of support membrane structure and chemistry on polyamide-polysulfone interfacial composite membranes.* **Ghosh.** 2009, Journal of Membrane Science, Vol. 336, pp. 140-148.

32. *New membrane developments expanding the horizon for the application of reverse osmosis technology.* **Gerard.** 1998, Desalination, Vol. 119, pp. 47-55.

33. *Surface properties of Reverse Osmosis Membrane.* **Yao.** 2007, Journal of Applied polymer science, Vols. 105-3, pp. 1261 – 1266.

34. *Effect of skin layer surface on the flux behavior of RO membranes.* **Hirose.** 1996, Journal of membrane science, Vol. 121, pp. 209-215.

35. *Role of membrane surface morphology in colloidal fouling of cellulose acetate and composite aromatic polyamide reverse osmosis membranes.* **Elimelech.** 1997, Journal of membrane science, Vol. 127, pp. 101-109.

36. *Leading Edge Technology on Commercially Available Membranes vs. Innovative Membranes in the R&D Stages.* Asilomar, CA : s.n., Feb. 2009. ACS conference.

37. *The Reaction of Cellulose Acetate with Acetic Acid and Water.* **Hiller.** 1953, Journal of polymer science, Vols. 10-4, pp. 385-423.

38. *Optimization of the intermittent chlorine injection (ICI) method for seawater desalination RO plants.* **Fujiwara.** 2008, Desalination, Vol. 229, pp. 231-244.

39. *Kinetic study of the hydrolysis of cellulose acetate in the pH range of 2-10.* **Kenneth.** 1966, Journal of applied polymer science, Vol. 10, pp. 825-832.

40. **Baker.** *Membrane technology and application.* s.l. : Jahn Wiley and sons editions , 2004.

41. *Study on hypochlorite degradation of aromatic polyamide reverse osmosis membrane.* **Kang.** 2007, Journal of membrane science, Vol. 300, pp. 165-171.

42. **Zhou.** *Simulations of Polymeric Membrane Formation in 2D and 3D.* s.l. : PhD thesis at MIT , 2006.

43. *Transport properties of cellulose acetate osmotic membranes.* **Lonsdale.** 1965, Journal of applied polymer science, Vol. 9, pp. 1341-1362.

44. *Experimental study of water and salt fluxes through reverse osmosis membranes.* **Zhou.** 2005, Environment science technology, Vol. 39, pp. 3382-3387.

45. *Non-linear behavior of permeate flux in full-scale reverse osmosis process.* **Tay.** 2005, Journal of environmental engineering, pp. 1481-1487.

46. **Mudler.** chap. 4: Transport in membrane. *Basic principle of membrane technology.* s.l. : Kluwer academic publishers, 1996.

47. *Effect of porous support fabric on osmosis through a Loeb-Sourirajan type asymmetric membrane.* **Loeb.** 1997, Journal of Membrane Science, Vol. 129, pp. 243-249.

48. *Concentration polarization in ultrafiltration and reverse osmosis: a critical review.* **Sablani.** 2001, Desalination, Vol. 141, pp. 269-289.

49. *Estimation of mass transfer coefficient using a combined nonlinear membrane transport and film theory model.* **Murthy.** 1997, Desalination, Vol. 109, pp. 39-49.

50. **Mudler.** chap. 7: Polarisation phenomena and membrane fouling. *Basic principle of membrane technology.* s.l. : Kluwer academic publishers, p. 1996.

51. *Modeling concentration polarization in reverse osmosis processes.* **Kim.** 2005, Desalination, Vol. 186, pp. 111-128.

52. **Amjad.** *Reverse Osmosis; Membrane Technology, Water Chemistry and Industrial Application.* [ed.] Van Nostrand Reinhold. 1992.

53. **Costa, Da.** *Fluid flow and mass transfer in spacer-filled channels for ultrafiltration, PhD thesis.* s.l. : School of chemical engineering and industrial engineering, University of New South Wales, 1993.

54. *Fouling of reverse osmosis and ultrafiltration membranes: a critical review.* **Goosen.** 2004, Separation Science and Technology, Vol. 39 (10), pp. 2261-2298.

55. *Marine epibiosis. I.Fouling and antifouling: some basics aspects.* **Wahl.** 1989, Mar. Ecol. Prog. Ser. , Vol. 58, pp. 175-189.

56. *Boron removal from desalinated seawater and brackish water by improved electrodialysis.* **Oren.** 2006, Desalination, Vol. 199, pp. 52–54.

57. *Boron removal from seawater using FILMTECTM high rejection SWRO membranes.* **Redondo.** 2003, Desalination, Vol. 156, pp. 229-238.

58. **Miller.** *Review of Water Ressources and Desalination Technoloies.* Sandia National Laboratories. 2003.

59. *Marine epibiosis. I.Fouling and antifouling: some basics aspects.* **Wahl.** 1989, Mar. Ecol. Prog. Ser. , Vol. 58, pp. 175-189.

60. Volume 4: Marine and Industrial Biofouling. *Surface Modification Approach to Control Biofouling, Marine and Industrial Biofouling.* s.l. : Springer Series on Biofilms.

61. *Settlement of Ulva Zoospores on Patterned Fluorinated and PEGylatedMonolayer Surfaces.* 2008, Langmuir, Vol. 24, pp. 503-510.

62. *Engineered Nanoforce Gradients for Inhibition of Settlement (Attachment) of Swimming Algal Spores.* **Schumacher.** Langmuir : s.n., 2008, Vol. 24, pp. 4931-4937.

63. *Bioinspiration—the solution for biofouling control?* 2009, Bioinsp. Biomim. , Vol. 4, p. 015007.

64. *Approaches in designing non-toxic polymer surfaces to deter marine biofouling.* 2009, Soft matter, Vol. 5, pp. 4088–4100.

65. **Fleming.** Biofouling in RO systems. [book auth.] Amjad. *Reverse Osmosis. Membrane Technology Water Chemistry and Industrial Applications.* s.l. : Van Nostrand Reinhold, 1993.

66. *Bioinspiration—the solution for biofouling control?* **Ralston.** 2009, Bioinsp. Biomim., Vol. 4, pp. 1-9.

67. *A preliminary approach to epidermal antimicrobial defense in the Delphinidae.* **Meyer.** 2004, Marine Biology, Vol. 144, pp. 841–844.

68. *The influence of Natural Surface Microtopographies on Fouling.* **Bers.** 2004, Biofouling, Vol. 20, pp. 43-51.

69. *Learning from nature: Non-toxic biofouling control by.* **A. Kesel, R. Liedert.** 2007. Comparative Biochemistry and Physiology, Part A 146 ; A7–BIOMIMETICS AND BIOMECHANICS — SMART SOLUTIONS FROM NATURE. pp. S129–S141.

70. *Cells lying on a bed of microneedles: An approach to isolate mechanical force.* 4, 2003, PNAS (Proc. of Nat. Ac. of Science), Vol. 100, pp. 1484–1489.

71. *Engineering Shark skin and other solutions.* **Ball.** 1999, Nature, Vol. 400, pp. 507-509.

72. *Development and Testing of Hierarchically Wrinkled Coatings for Marine Antifouling.* **Efimenko.** 2009, Applied material and interface, Vol. 1;5, pp. 1031–1040.

73. **Wierzbicki.** *Lecture notes for the class "Plate and Shells" at MIT.* s.l. : MIT, 2009.

74. *Herringbone Buckling Patterns of Compressed Thin Films on Compliant Substrates.* **Chen.** 2004, Journal of Applied Mechanics, Vol. 71, pp. 597-603.

75. *Nonlinear analyses of wrinkles in a film bonded to a compliant substrate.* **Huang.** 2005, Journal of the Mechanics and Physics of Solids, Vol. 53, pp. 2101–2118.

76. **Dowling.** 15.10: Energy dissipation in materials. *Mechanical behavior of materials, engineering methods for deformation, fracture and fatigue.* 1999.

77. *Initiated chemical vapor deposition (iCVD) of polymeric nanocoatings.* **Gleason.** 2007, Surface & Coatings Technology, Vol. 201, pp. 9400–9405.

78. *Wrinkled surface topographies of electrospun polymer fibers.* **Wang.** 2009, Appl. Phys. Lett., Vol. 94, p. 151916.

79. *A Stretchable Form of Single-Crystal Silicon for High-Performance Electronics on Rubber Substrates.* **Khang.** 2006, science, Vol. 311.

80. *Ordering of Spontaneously Formed Buckles on Planar.* **Huck.** 2000, langmuir, Vol. 16.

81. —. **Wilhelm T. S. Huck, Ned Bowden, Patrick Onck, Thomas Pardoen, John W. Hutchinson and George M. Whitesides.** 2000, langmuir, Vol. 16, pp. 3497-3501.

82. **Anand, L.** *Mechanics of solids, Lecture notes (MIT 2.071).* 2009.

83. **Nguyen, Q.S.** *Stability and nonlinear solid mechanics.* s.l. : Wiley, 2000.

84. **R., Cook.** *Concepts and applicatoins of Finite Element Analysis, second edition.* s.l. : John Wiley, 1974.

85. **Moler, Cleve.** Eigenvalues and Singular Values. *Numerical Computing with MATLAB.* s.l. : Mathworks, 2004.

86. **Organization), UNESCO-WWAP (World Health.** *World Health Report, Water, a shared responsibility.* 2006.

87. *The search for a chlorine-resistant reverse osmosis Membrane.* **Glater.** 1994, Desalination, Vol. 95, pp. 325-345.

88. *Backwash of RO spiral wound membranes.* **Sagiv.** 2005, Desalination, Vol. 179, pp. 1-9.

89. *Overview of systems engineering approaches for a large-scale seawater desalination plant with a reverse osmosis network.* **Kim.** 2009, Desalination, Vol. 238, pp. 312-332.

90. *Pilot Tests of Multibore UF Membrane at Addur SWRO Desalination Plant, Bahrain.* **Bu-Rashid.** 2007, Desalination, Vol. 203, pp. 229–242.

91. **Wilf.** *Guidebook, membrane desalination technology, Reverse Osmosis, Nanofiltration and Hybrid Systems Process, Design, Applications and Economics .* ISBN 0-86689-065-3.

92. *UF membranes for RO desalination pretreatment.* **Wolf.** 2005, Desalination, Vol. 182 , pp. 293–300.

93. *Le dessalement des eaux par osmose inverse: l'expérience de Véolia Water.* **Gaid.** 2007, Desalination, Vol. 203, pp. 1–14.

94. *Microscopy as a tool for analysis of membrane failure and fouling.* **Roever, De.** 2007, Desalination, Vol. 207, pp. 35–44.

95. **Organization, World Health.** chap 7: Microbial aspects. *Guideline for drinking water (3rd edition),.* 2006.

96. *Pretreatment for desalination of seawater from an open intake by dual-media filtration: Pilot testing and comparison of two different media.* **Mitrouli.** 2008, Desalination, Vol. 222, pp. 24–37.

97. *Seawater filtration for fouling prevention under stormy conditions.* **Tenzer.** 1999, Desalination, Vol. 125, pp. 77-88.

98. *Performance of the Gabès desalination plant.* **Fethi.** 2001, Desalination, Vol. 136, pp. 263–272.

99. *UF/MF as RO pre-treatment: the real benefit.* **Bonnélye.** 2008, Desalination, Vol. 222, pp. 59–65.

100. *Theoretical optimization of spiral-wound and capillary nanofiltration modules.* **Meer, Van der.** 1997, Desalination, Vol. 113, pp. 129-146.

101. *Modeling concentration polarization in reverse osmosis spiral wound elements.* **Marinas.** 1996, Journal of environmental Eng. , pp. 292-298.

102. *Biofouling of spiral-wound nanofiltration and reverse osmosis membranes: A feed spacer problem.* **Vrouwenvelder.** 2009, water research, Vol. 43, pp. 583-594.

103. **Schwinge.** *Experimental & simulation studies of fluid flow in spacer-filled channels in spiral wound modules, Ph.D. Thesis.* s.l. : School of Chemical Engineering and Industrial Chemistry, University of New South Wales, 2003.

104. **GOSS, V.G.A.** *Snap buckling, writhing and loop formation in twisted rods, PhD thesis.* s.l. : Center for Nonlinear Dynamics, University College London, 2003.

105. **Millard P., Ballard A.** *Modelling of slender structures, lecture note.* Palaiseau : Ecole Polytechnique, 2008.

106. *Using Euler buckling springs for vibration isolation.* **Winterflood.** 2002, Class. Quantum Grav., Vol. 19, pp. 1639–1645.

CHAPTER III: Micro-patterning, tailoring the wrinkled surface topology

A. Content

B.   Introduction

We have seen in the previous chapter some of the basic elements of strategies to create an anti-fouling coating. When using the "stiff coating on a compliant substrate" technique, the literature is essentially limited to the use of wrinkles in one direction or at most the herringbones or "random and uncontrolled" type of geometries. Here, we consider the opportunity to optimize the pattern and shape of wrinkles by tuning the properties of the substrate.

C.   Patterning the wrinkled topology

1.   Previous work.

Huck et al. (81) were the firsts to use photochemical reactions to direct the wrinkles obtained during the buckling step. The basics system consists of a compliant PDMS substrate with a stiff gold coating. Figure 91 shows their direct approach: they generated several photomasks, which provided a difference in crosslink density and hence PDMS stiffness in the PDMS regions that were unmasked as compared to masked regions. The UV light primarily affects a photosensibilizer (a solution of benzophenone in dichloromethane) in which PDMS was soaked, and creates free radicals upon irradiation; these radicals cross-link PDMS, and hence results in hard domains. However, it was noted by Huck et al. (81) that the UV treatment is not uniform in thickness.

A thin gold coating was then deposited onto the substrate, at high temperature (100C). Upon cooling, shrinkage in the elastomer places the fold film under isotropic compressive stress, which finally resulted in the buckling of the gold film. Figure 91 shows four examples for this method. The photolithographic masks, hence the local stiffness of the substrate, were taken to be periodic and are shown on the right of the optical micrograph for each case in Figure 91. The wrinkles are "directed" by the in-homogeneities in the stiffness of the substrate.

This approach gives a good insight and physical understanding of various wrinkle patterns which can be created.
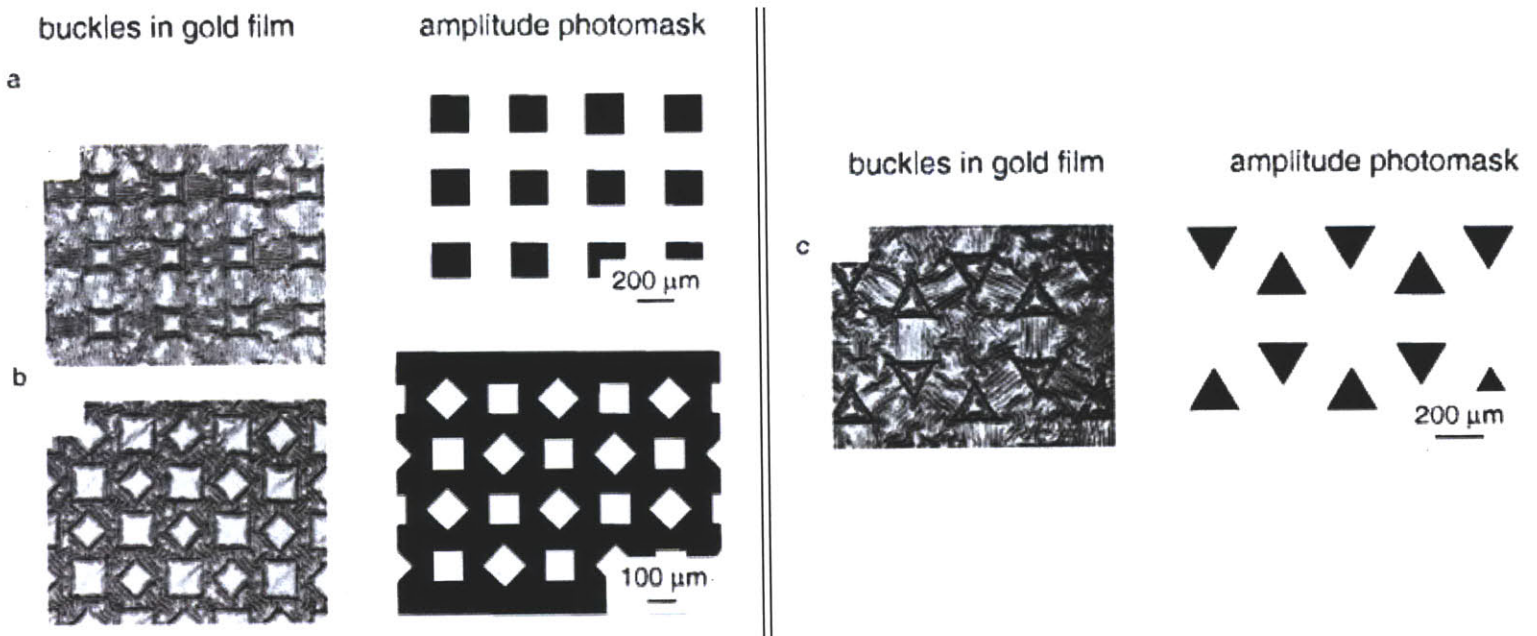
Figure 91: different photolithographic masks (a,b,c right picture) and resulting buckled shape (a,b,c left picture). The wrinkles tend to concentrate on the compliant area of the substrate. From (81)

2.   Our numerical simulation for this technique.

The simulation approach and methods introduced in Chapter two can be used to predict the pattern and shape of the wrinkles of the stiff coating. For example purposes, we show here a few simulations corresponding to the situation a/ of Huck et al. experiments in Figure 91.

We are expecting that a sample prepared from a periodic photomask will results in a periodic pattern for the buckled shape of the coating. Furthermore, to maximize the resolution of the mesh, we decided to consider only one periodic unit of photomask per RVE (see Figure 92: the blue line is both a periodic unit of the photomask and the contour in the horizontal direction of a RVE considered).
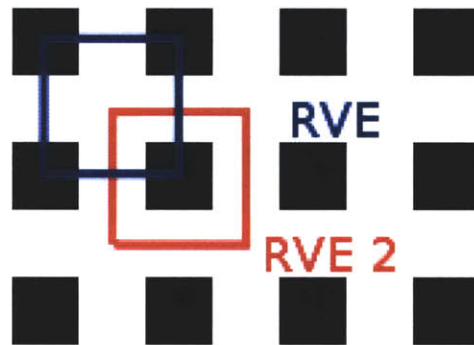
Figure 92: Representation of the stiffened regions (in black) and the unstiffened regions (in white). Two RVE have been compared: the Red is centered on a stiff region while the blue is centered on a compliant region.

For the cases presented in this chapter, there exist stiff and compliant areas in the substrate, as well as a hard coating. More precisely, for the modeling of the periodic square pattern, we define 4 different material properties:

- the coating (transparent red in Figure 93) is modeled by shell elements with stiff material properties $E_{coating}$.
- the substrate is prepared and soaked in a photosensibilizer solution. This solution only diffuses in a thin layer (thickness t_{photo} as represented in Figure 93), the rest (in orange in Figure 93) has the material properties of the PDMS: E_{PDMS}.
- The volume of the substrate where the photosensibilizer has diffused by that has been masked is slightly stiffer than the PDMS: $E_{masked} > E_{PDMS}$.
- Finally, the volume with photosensibilizer which has been exposed to UV is the stiffest part of the substrate: $E_{unmasked} > E_{masked}$.
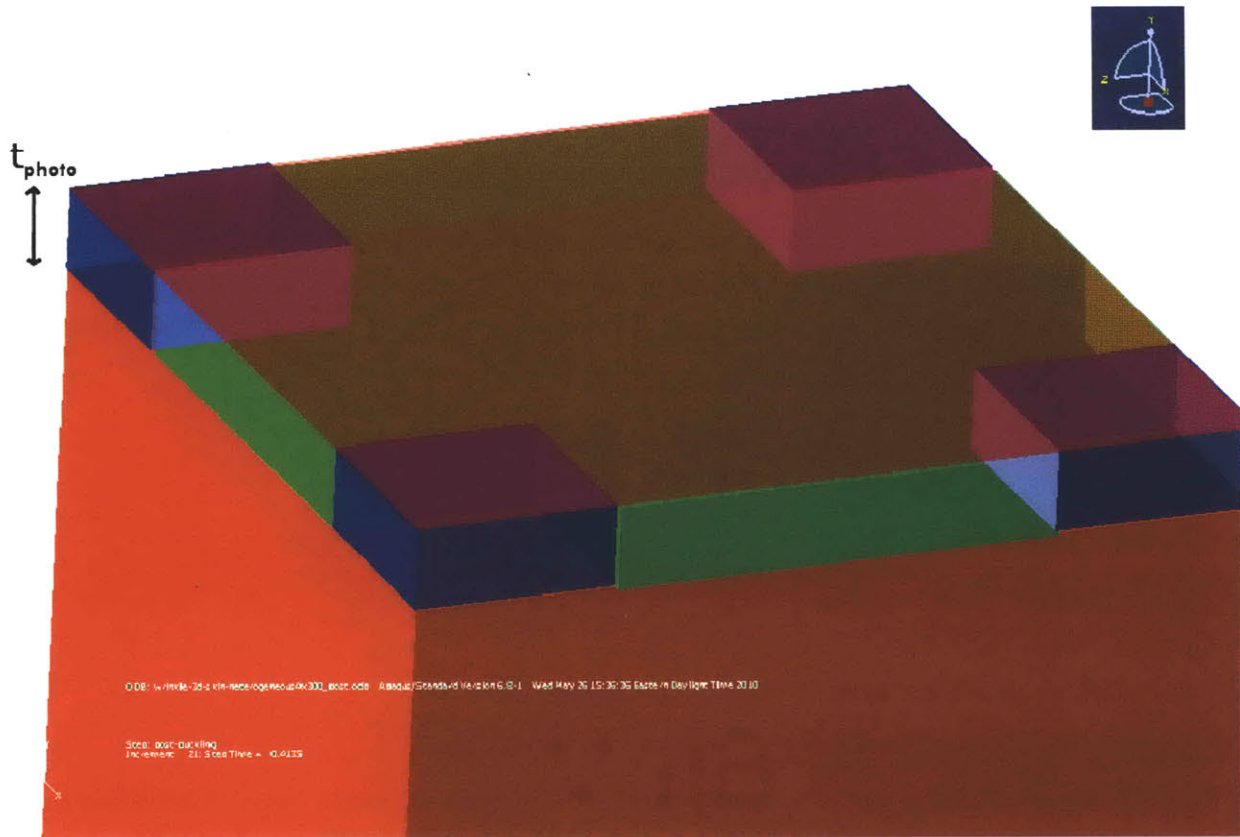
Figure 93: Four different material properties are defined in one Representative Volume Element (RVE): the orange on the bottom is the region of the substrate where the photosensibilizer did not diffuse (i.e. the depth is greater than the thickess of the diffusion layer of the photosensibilizer t_{photo}). This section of the substrate is compliant (E_{PDMS}). The green part represents the volume of the substrate in which the photosensibilizer did diffuse but that was masked during the UV treatment. As a result, it is a bit stiffer than the bulk PDMS ($E_{masked} > E_{PDMS}$) but less than the volume in blue, which was treated with the photosensibilizer and has been exposed to UV light ($E_{unmasked} > E_{masked}$).

Experimentally, as well as in our simulations, the patterns were obtained with isotropic straining of the membrane (due to the mismatch of the coefficient of thermal expansion between the coating and the substrate).

The number of parameters to tune for the simulations is greater than for uniaxial straining with homogeneous substrates:

- $\frac{E_{masked}}{E_{PDMS}}$, the relative stiffness of the photosensibilized unexposed region
- $\frac{E_{unmasked}}{E_{PDMS}}$, the relative stiffness of the photosensibilized exposed region
- $\frac{E_{coating}}{E_{PDMS}}$, the relative stiffness of the coating
- $\frac{t_{photo}}{t_{coating}}$, the relative thickness of the diffusion layer of the photosensibilizer

a) Influence of the Representative Volume Element (RVE) chosen

The first set of simulations have been made with two RVE extracted from the same stiffness pattern. One RVE is centered on a compliant region (blue in Figure 92) while the other one is centered on a stiff region (red in Figure 92).

In order to simplify this study, we are imposing, in this section, uniform material properties through the substrate thickness. In other words, $t_{photo} = t_{substrate}$: the UV and the photosensibilizer penetrate through the whole thickness of the substrate. Furthermore, $\frac{E_{coating}}{E_{masked}} = 70$, $\frac{E_{unmasked}}{E_{masked}} = 2$ and $\frac{t_{coating}}{t_{substrate}} = \frac{1}{200}$.

These two RVEs predict similar wrinkle patterns: unidirectional-like wrinkles (sinusoids) are bridging stiff areas while the stiff domains are flat and the compliant domain in between four stiff domains is exhibiting an isotropic-like wrinkling (checkerboard buckling solution), see Figure 94 and Figure 95. However, the constraint for the RVEs on the wavenumber is slightly different. We think this is the reason why the compliant-centered RVE is exhibiting less noise in the bridge between two stiff regions. The difference in the two buckling solutions, induced by chosing two different RVE, results in the two post-buckling shapes to be slightly different (see Figure 96 and Figure 97). As expected, the isotropic checkerboard in the compliant domains bifurcates again in a Herringbone like pattern, constraint by the hard domain.

In Figure 97, the central and compliant region is still a checkerboard like pattern. This happens because the transition from checkerboard to Herringbone is not achieved at the last step. We are imposing a given pre-strain of 10%. However, due to the relatively coarse meshes (finer meshes would require more computational power than available), the simulations always stop before this 10% strain, when an equilibrium cannot be found with the required precision. Depending on the simulation, this final step might be after the transition region from the checkerboard to Herringbone-like pattern (see Figure 96) or before it (Figure 97).

We note that the desired wave pattern is one with waves perpendicular to the edges of the stiff regions as observed in Figure 95 and Figure 97. The constraint on the wavelength, as well as the potential imperfections in real case, leads to different patterns, as seen in Figure 94 and Figure 96.
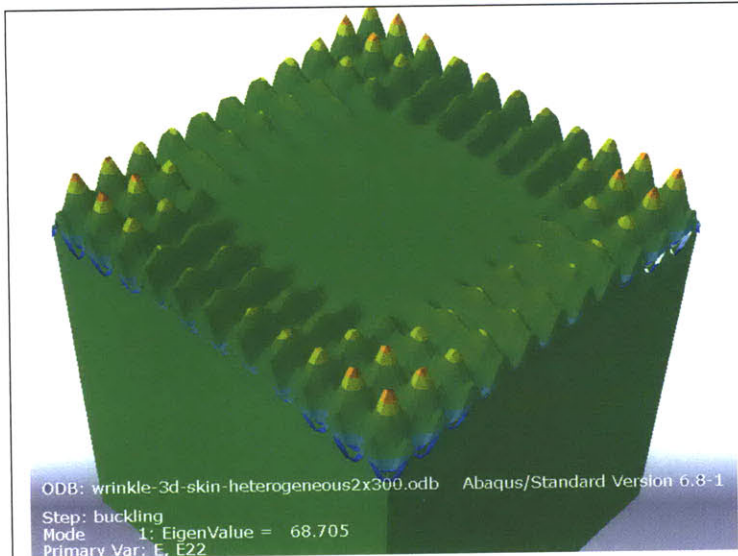
Figure 94: buckling solution for the RVE centered on the stiff area of the substrate. On the stiff substrate, the film will not buckle and will stay flat. The compliant section bridging two stiff sections (the RVE has periodic boundary conditions and hence we have to imagine that this RVE is repeated several times) is showing unidirectional-like wrinkles. The compliant regions on the four corner exhibit a checkerboard pattern.
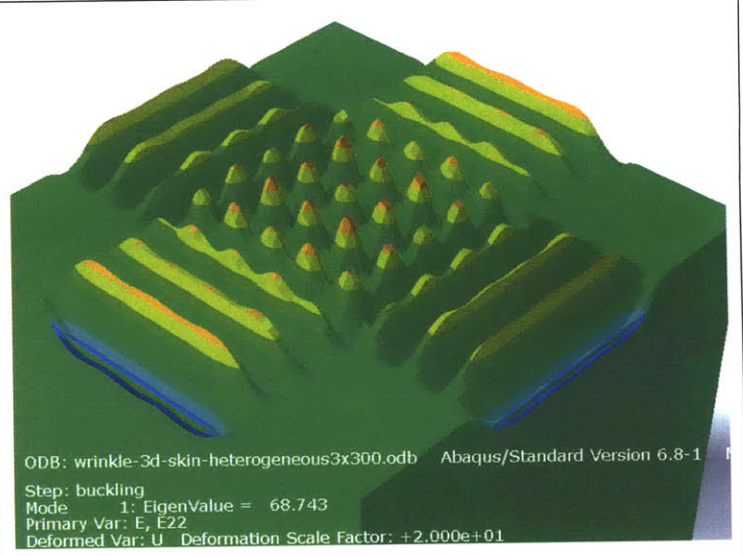
Figure 95: Buckling solution for the RVE centered on the soft area of the substrate On the stiff substrate, the film will not buckle and will stay flat. The compliant section bridging two stiff sections is showing unidirectional-like wrinkles. The compliant region in the middle exhibits a checkerboard pattern.
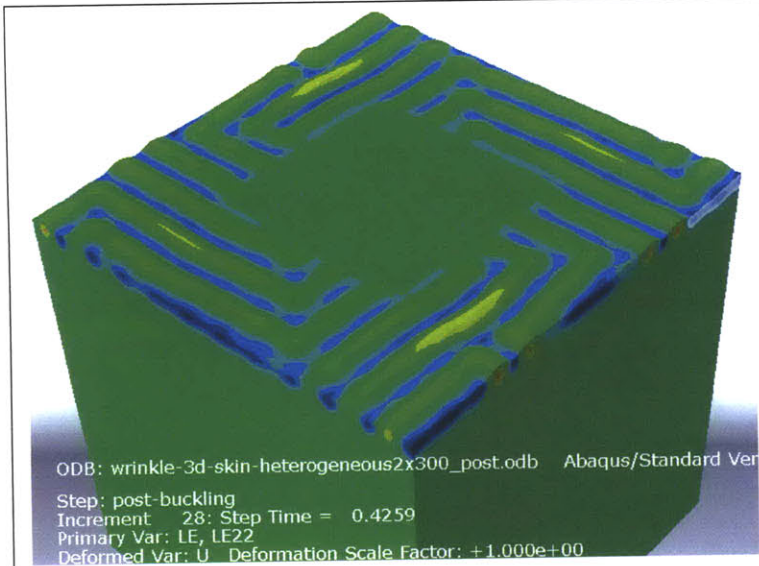
Figure 96: Post-buckling pattern for a RVE centered on a stiff region.
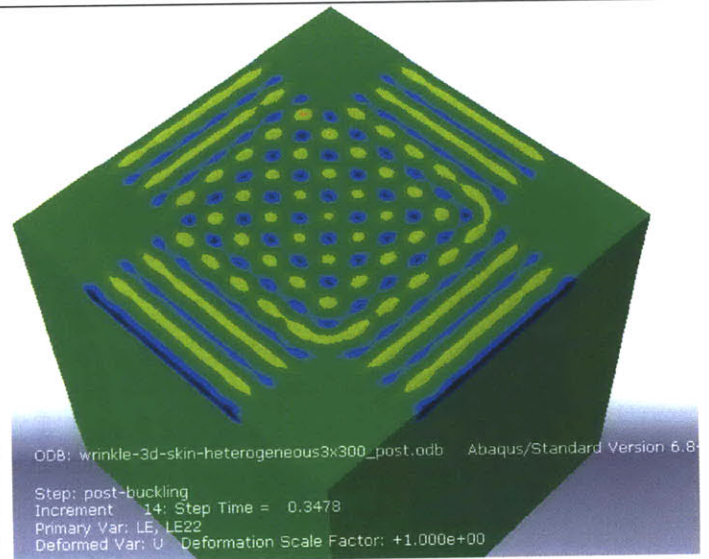
Figure 97: Post-buckling pattern for a RVE centered on a stiff region.

Periodic boundary conditions are defined on the RVEs. As a result, we can assemble several RVEs together to reconstruct larger portion of the periodic substrate (portion with several periodic units). The qualitative description of the observed patterns is quite accurate as compared to the patterns observed

experimentally by Huck et al. (81): see Figure 98, Figure 99 and Figure 100. There are two main issues differences between the experiments and the pattern predicted by the simulation: the hard domains also buckle experimentally, and the predicted wavelength of the wrinkles is larger than the observed one. We are showing in the next two sections that introducing a finite thickness for the diffusion of the photosensibilizer addresses the first issue, while tuning the stiffness ratio addresses the later issue.
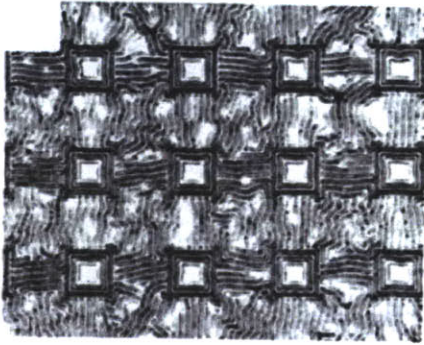
Figure 98: Wrinkles observed experimentally for a gold coating on a PDMS substrate treated to exhibit periodic square stiffened regions. (from (81))
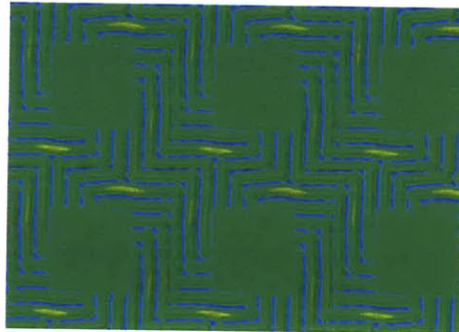
Figure 99: Wrinkles observed by the simulation centered on a stiff region (for the same stiffen pattern as Figure 98)
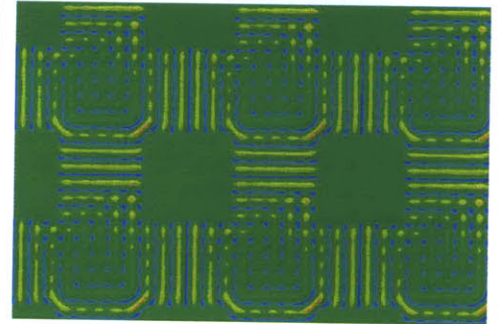
Figure 100: Wrinkles observed by the simulation centered on a compliant region (for the same stiffen pattern as Figure 98)

b) Influence of the thickness of the diffusion layer for the photosensibilizer

The previous simulations were based on material properties uniform in thickness. It means that the photosensibilizer can penetrate all the way though the PDMS layer and the UV radiation also penetrate through the sample. Huck et al. showed that this assumption was questionable, and most likely, only a thin layer was affected by the photosensibilizer. This diffusion layer thickness t_{photo} is most likely the limiting phenomenon and we may consider that the UV treatment affect uniformly this layer, as shown in Figure 93.

We are showing here the changes predicted by the simulations as the diffusion layer thickness t_{photo} is varied: 200 (throughout the substrate), 20 (1/10 of the thickness of the substrate) and finally 2.5 (this corresponds to 2.5μm, the assumed thickness in the paper by Huck et al. (81)). Every other parameter is kept constant. More precisely, $\frac{E_{masked}}{E_{PDMS}} = 1.72$, $\frac{E_{unmasked}}{E_{PDMS}} = 3.6$, $\frac{E_{coating}}{E_{PDMS}} = 12$. The elements of the stiffen part (unmasked) of the substrate are shown for each case in Figure 101, Figure 102 and Figure 103. The thickness of the masked region but with the photosensibilizer is the same as the thickness of these stiff areas.
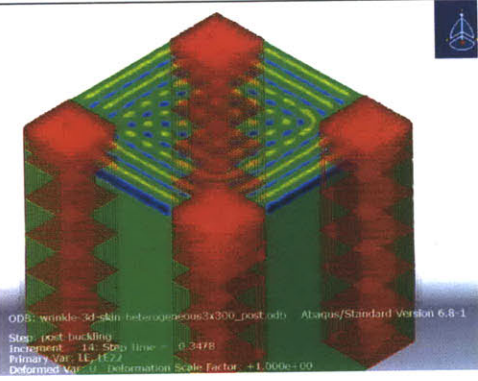
Figure 101: The elements of the stiff unmasked region are shown in red. For this simulation, it goes throughout the substrate. This models the case of a uniform diffusion of the photosensibilizer in the substrate. The rest of the substrate is modeled
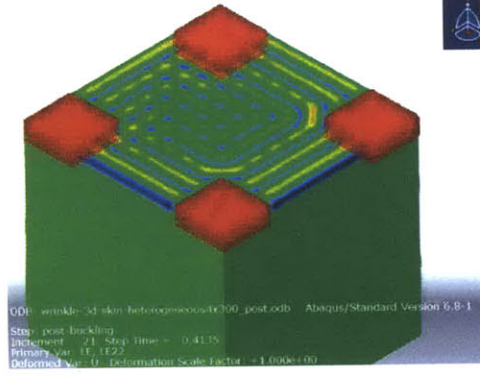
Figure 102: The elements of the stiff unmasked region are shown in red. With the masked elements, these elements form a layer of thickness t_{photo}. Under these elements, there exists a section with even more compliant material properties E_{PDMS} (of thickness $t_{substrate} - t_{photo}$)
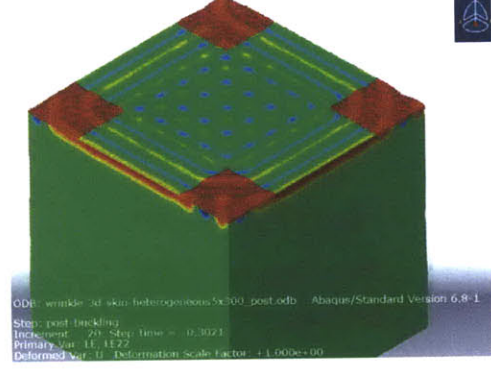
Figure 103: The elements of the stiff unmasked region are shown in red. This region is composed of only one layer of elements. The rest of the top elements are assigned the material properties of the masked region E_{masked}. Under this first layer of elements, there exists a section with even more compliant material properties E_{PDMS} (of thickness $t_{substrate} - t_{photo}$)

We should note that the value of $\frac{E_{coating}}{E_{PDMS}}$ used in the simulations was computed from the experimental values by imposing the same plate bending stiffness in simulations and experiments, where the bending stiffness is $D \sim E_{coating} \cdot t_{coating}^3$.

Assuming a stiffness of $E_{PDMS}(experimental) = .5 MPa$ for the PDMS, this relation leads to:

$$\frac{E_{coating}(simulation)}{E_{PDMS}(simulation)} = \frac{E_{gold}(experimental)}{E_{PDMS}(experimental)} \cdot \left(\frac{t_{coating}(experimental)}{t_{coating}(simulation)} \right)^3$$

Those parameters are summarized in Table 9.

simulation #	3	4	5
t_{photo}	200	20	2.5
$t_{coating}$	1	1	1
$\frac{E_{PDMS}}{E_{masked}}$	/	.6	.6
$\frac{E_{unmasked}}{E_{masked}}$	2.1	2.1	2.1
$\frac{E_{coating}}{E_{masked}}$	70	70	70

Table 9: Parameters used in the simulations for the influence of the diffusion of the photosensibilizer on the wrinkle pattern

As shown in Figure 104, Figure 105 and Figure 106, the buckling analysis for the three cases are very much similar: flat coating on the stiff regions, wrinkles in between and checkerboard in the center compliant region.
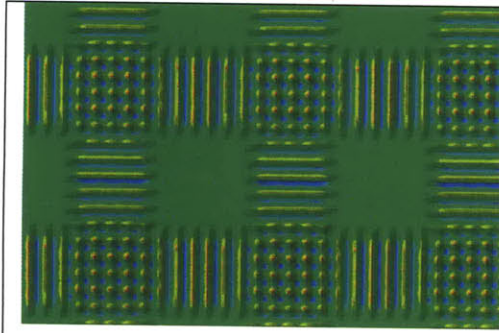
Figure 104: Buckling analysis for a diffusion of the photosensibilizer throughout the substrate $t_{photo} = 200$.	Figure 105: Buckling analysis for a diffusion of the photosensibilizer on a medium thickness $(t_{photo} = 20)$	Figure 106: Buckling analysis for a diffusion of the photosensibilizer only on surface $(t_{photo} = 2.5)$
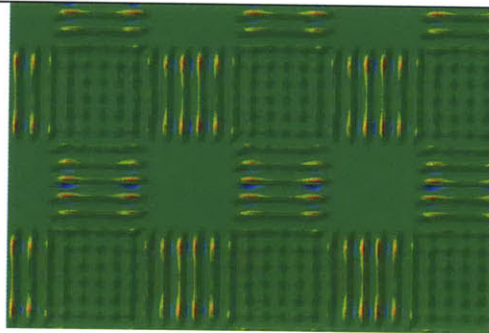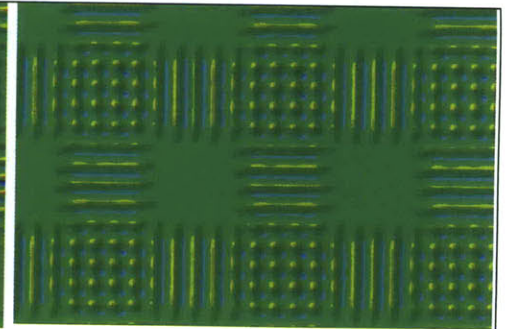
However, the post-buckling analysis reveals a difference between those three cases: If the photosensibilizer affects only a surface region, it might be favorable to form wrinkles on top of the stiff substrate, very soon after the wrinkles on top of the compliant regions. This is what we observe in Figure 109: the wrinkles developped on the compliant substrate. As the loading increases, the the wrinkles becomes of finite amplitude. Instead of continuing to grow in amplitude, the predicted shape involves the buckling of the coating on top of the stiff regions (which was not the case for thick treated regions Figure 107 and Figure 108).
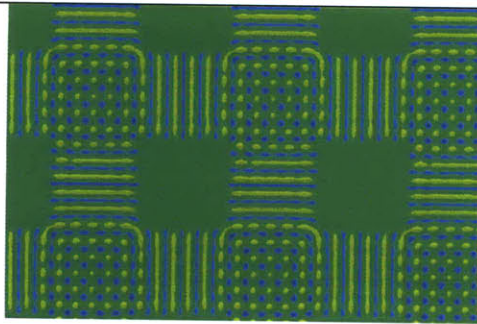
Figure 107: Post-buckling analysis for a uniform treatment of the substrate by the photosensibilizer . The wrinkles only form on top of compliant regions of the substrate.	Figure 108: Post-buckling analysis for a mild diffusion of the photosensibilizer in the substrate $(t_{photo} = 20\mu m)$. The predicted solution is very close to the one in Figure 107. This was expected since the buckling only affects the top part of the substrate, and the deeper material properties are less important.	Figure 109: Post-buckling analysis for a very shallow diffusion of the photosensibilizer in the substrate $(t_{photo} = 2.5\mu m)$. Wrinkles are forming on the stiff regions very soon after the apparition of the first wrinkles on the compliant regions. This is expected wince the buckling problems mostly feels the PDMS which has not been affected by the photosensibilizer.
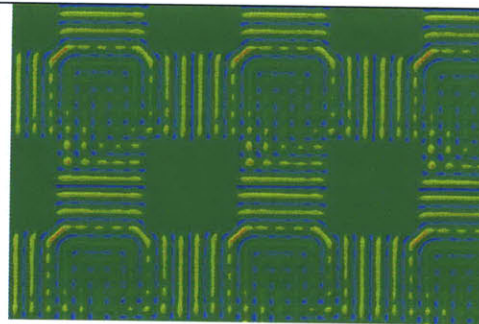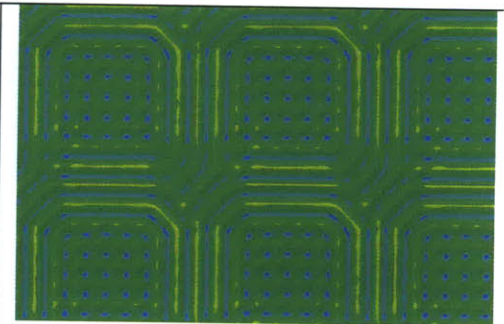
c) *Influence of the stiffness of the coating*

A last set of simulations was set up to observe the difference of shape with the ratio of stiffness (coating versus substrate: $\frac{E_{coating}}{E_{marked}}$) or with the thickness of the coating. We have chosen the model with a mild diffusion of the photosensibilizer (i.e. intermediate case in the previous set of simulations, with $t_{photo} = 20$).

Once again, the general buckling pattern observed is quite insensitive to the stiffness ratio (flat area on top of the stiff areas and a combination of unidirectional and isotropic wrinkles on the compliant areas). However, the size of the waves as well as the precise shape of the wrinkles for the post-buckling solutions (branching, zigzag and Herringbone patterns...) does vary with this stiffness ratio.
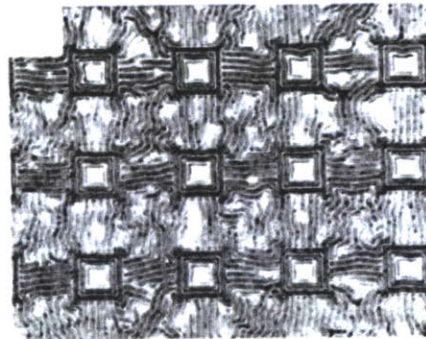
Figure 110:Wrinkles observed experimentally for a gold coating on a PDMS substrate treated to exhibit periodic square stiffened regions. (from (81))

| **Figure 111: Post-buckling solution for $\frac{E_{coating}}{E_{masked}} = 14$. Eighteen waves are forming in one RVE.** | **Figure 112: Wrinkles observed by the simulation for a stiffness ratio $\frac{E_{coating}}{E_{masked}} = 23$. Fifteen waves are forming in one RVE.** | **Figure 113: Wrinkles predicted by the post-buckling solution by the simulation for a stiffness ratio $\frac{E_{coating}}{E_{masked}} = 70$. Eleven waves are forming in one RVE.** |
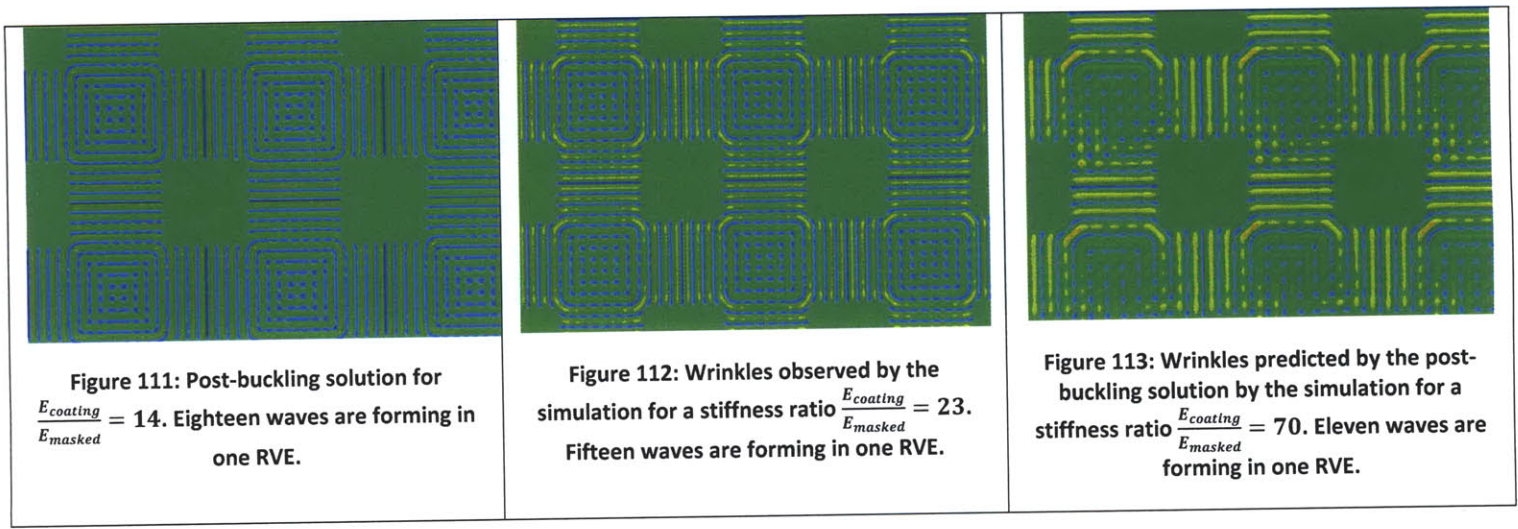
d) *Bifurcation away from checkerboard pattern.*

As we have observed, one of the typical numerical issues associated with this post-buckling analysis is the transition from a Checkerboard pattern to a Herringbone or more random pattern. This transition involves several bifurcations (one per case of the checkerboard). Furthermore, if the numerical solution does not bifurcate at the correct step, it might be locked in an unstable solution.

To overcome this issue, we have tried to use a Riks analysis. This type of analysis is usually used in post-buckling analysis of systems that might exhibit negative stiffness matrices. The result is only slightly better than the normal analysis. Furthermore, the Riks analysis is not appropriate when too many bifurcations might exist.

The comparison between a Riks and a normal analysis is shown in Figure 114 and Figure 115.
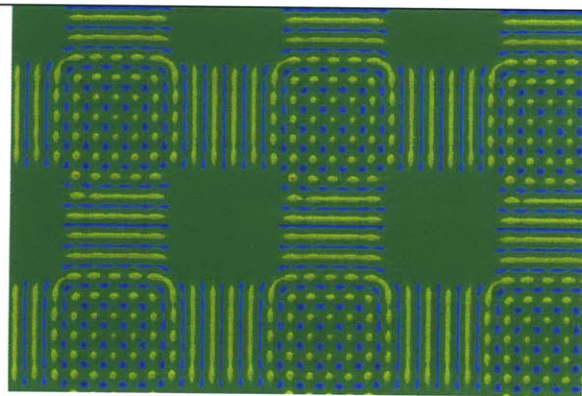
Figure 114: Regular post-buckling analysis: The analysis is interrupted before the transition from Checkerboard to Herringbone, due to numerical convergence problem.
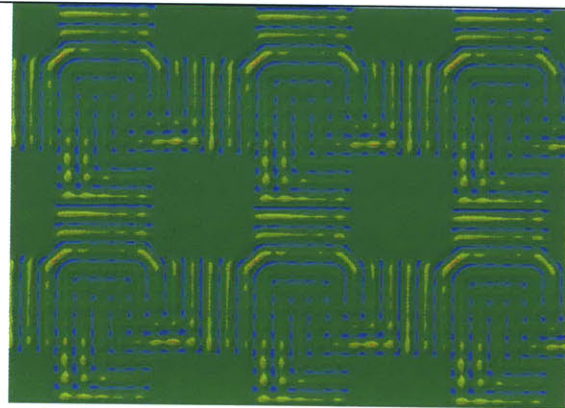
Figure 115: Riks post-buckling analysis: The analysis is interrupted when the Checkerboard turns into Herringbone, due to numerical convergence problem. The improvement over the regular analysis is not that significant.

To conclude this section, we should also note that the stiffening is achieved with UV treatment and a photosensibilizer, experimentally. As a result, the interfaces between the treated and untreated areas may not be well defined. Also, the non-uniformity of the stiffening in the depth might affect the observed wrinkled pattern. This is why it would be beneficial to find more precise control of the stiffening mechanism used experimentally to obtain even less discrepancies between simulations and experiments.

D. Patterning the wrinkle topology: Inverse Design Approach, from a two parameters system to the theory in 3D elasticity

1. The proposed idea: inverse design.

a) *Inverse design: how to create a desired micro-topography on membranes,*

We are proposing in the rest of this thesis a new design design paradigm for creating a desired micro-topography on membrane.

The flow of this proposed design process is shown in Figure 116: A compliant substrate is treated according to a photomask. The rest of the process is identical to the process describe in Chapter two, which wsa used to create our samples: the substrate is strained before deposition of a stiff coating. Upon realese of the strain, the coating will buckle, affecting the micro-topography of the membrane.

The key step is to determine the proper photomask. Instead of using trial and error method to fabricate the photomask, we investigate a deterministic method or algorithm to do so. More specifically, this method aims at determine the substrate stiffness pattern, hence the photomask, needed to obtain a desired wrinkled topography. This is the inverse problem of the problem solved in the first section of this chapter (knowing a stiffness pattern of the substrate, can we compute the final buckling shape of a stiff coating that would be deposited on this strained substrate).

We should also note that the stiffness of the substrate is not the only parameters that can be controlled. More complex pre-stress (unidirectional straining, multiaxial straining, thermal straining or even straining due to body forces generated with magnet) might further increase the complexity of the achievable patterns.

Proposed numerical inverse design method

| A compliant substrate is casted on a flat surface and may be dipped into a photosensibilizer | The substrate is UV-treated. The photomask used is created according to the inverse design method. | A coating is then deposited, either at high temperature or on a strained substrate | Upon decrease of the temperature (or release of the strain), the desired pattern is formed on the surface of the substrate. |

Figure 116: Flow chart for the reversal design: we propose to generate an optimal "stiffness map" for the substrate in order to obtain patterns as close as possible from the desire shape.

b)   *From a sequential to continuous roll to toll process.*

Compared to conventional processes for patterning substrates (e.g. mold casting), one of the huge advantages of this method, adding to the ones already explored in chapter two (e.g. versatility, chemistry independence, tenability, quality of the wrinkles), is that it can be made a truly continuous roll to roll process. We are providing an example of a continuous line using this method, in Figure 117 where:

- a compliant substrate can be obtained by drawn out of a polymer bath (1 in Figure 117).
- a photomask can be synchronize with the membrane, achieving a local stiffening of the substrate in a continuous process (2 in Figure 117).
- the straining can be achieved by tensioning the membrane or by raising the temperature (3 in Figure 117).
- the coating can be obtained by evaporation (iCVD...) in a low pressure section of this process, or even by dip coating (4 in Figure 117).
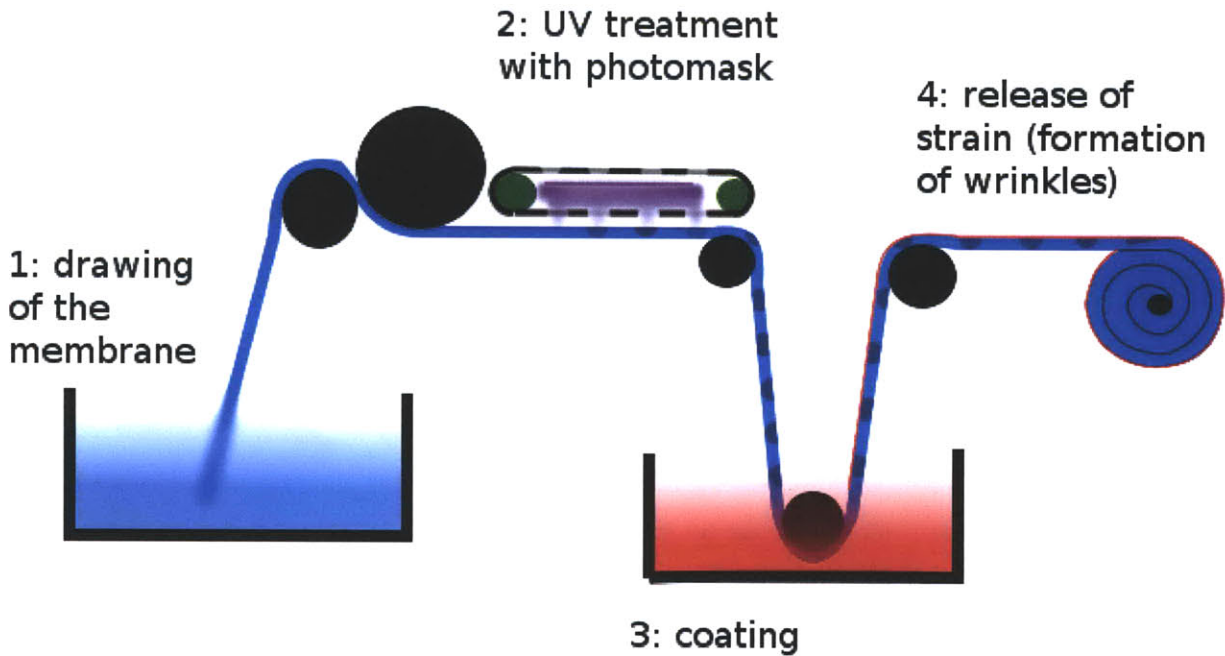
Figure 117: An example of a continuous process for membrane micro-patterning: after drawing of a substrate from a coagulation bath (1), a continuous UV treatment (2) is used to stiffen the membrane. It is then strained (thermally or mechanically with the rolls resistance) and coating (3) [a dip coating is represented here]. Finally, upon release of the strain, the desired pattern is form at the surface of the membrane.

c) *Mathematical formulation of the inverse problem.*

The key step is the design of the algorithm to determine the substrate stiffness pattern needed to obtain a desired wrinkled topography. We are formulating this idea more mathematically here.

Let

- $u(x, y, z)$ *in* Ω be the displacement field.
- $m(u(x, y, z))$ be a measure of the displacement fields,
- $u_{obj}(x, y, z)$ be the objective displacement field.
- $C(x, y, z)$ be the local material properties (of the substrate and/or the coating)
- and $\mathcal{L}(C(x, y, z))$ be the displacement field associated with the first buckling mode for those material properties.

Then, the problem is to find the local material properties $C(x, y, z)$ that minimizes $m(\mathcal{L}(C(x, y, z)) - u_{obj}(x, y, z))$

Some important concepts and notations are reviewed in the subsequent sections. A model of mechanical conservative system with two parameters is introduced. This allows us to understand which the appropriate measure $m(u(x,y,z))$ should be chosen for our problem.

Then, the direct problem of the buckling and post-buckling is presented for 3D elasticity, along with the inverse formulation for the design of material properties needed to produce a desired shape function.

Finally, we are showing an algorithm that we developed to direct the buckling of an elastic beam on a compliant elastic foundation.

2. Direct problem of buckling

a) A simplified version of our proposed approach for control of the buckling direction: buckling of a two parameter conservative system

(1) Description of the problem and potential energy

Before going into any further details, we are showing the details of our design method on a conservative system with two parameters. This simple example provides an enlightening version of the full problem, since it allows us to better understand and draw the non-linear potential function as a function of the parameters.

The system is composed of two bars of length L_1 and L_2 connected by hinges and rotation springs of stiffness k_1 and k_2 (see Figure 118). The parameters used to describe the system are θ_1 and θ_2.
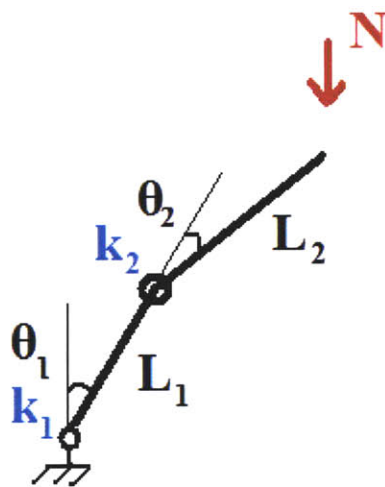
Figure 118: Two bar systems for the study of buckling: bar 1 is connected at one end to the ground by an hinge of stiffness k1 and at the other end to bar 2 with a stiffness k2

A force N is applied on the top of bar #2, in the vertical direction. This defines both the **path of loading** $\mathcal{L}$ (vertical force on top of bar 2), and the **control parameter,** N, on this path (the magnitude of the force in compression).

The physical intuition of this problem is that the structure can take 3 positions: either the bars stays aligned with the force, or an angle is created with the vertical, such that the torque created by the applied force is in equilibrium with the springs. We understand that if (θ_1, θ_2) is an equilibrium position, then the symmetric $(-\theta_1, -\theta_2)$ is also one. Thus, we label those 3 **equilibrium paths**:

- $\wp_0$, with $\theta_1 = \theta_2 = 0$ is the pre-buckling solution.
- $\wp_1$, with $\theta_1 > 0$.
- $\wp_{-1}$, with $\theta_1 < 0$.
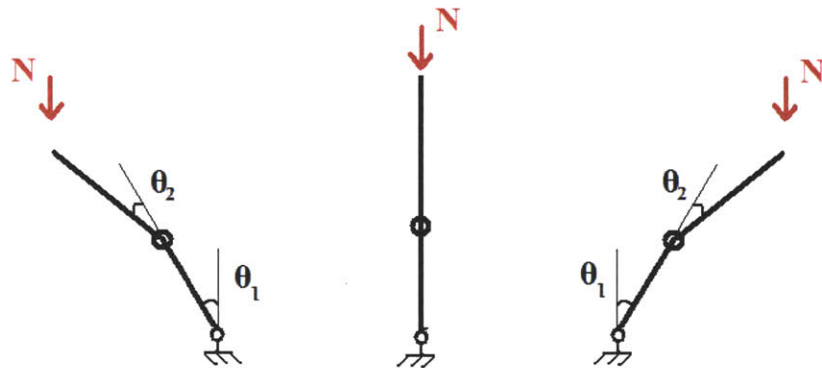
Figure 119: Representation of the 3 "equilibrium paths" for a given force N. a/ is a stable equilibrium and is along $\wp_{-1}$, b/ is an unstable equilibrium along $\wp_0$ and c/ is a stable equilibrium along $\wp_1$.

The potential energy is the sum of the energy stored in the two springs and the work of the external force (here the force N times the vertical displacement of the top most point):

$$\Pi(N, \theta_1, \theta_2) = \frac{1}{2}k_1\theta_1^2 + \frac{1}{2}K_2\theta_2^2 - N * [L_1(1 - \cos(\theta_1)) + L_2(1 - \cos(\theta_1 + \theta_2))]$$

We then compute the first order differential function in the "displacement parameter" θ_1 and θ_2. This differential function is computed at the point (N, θ_1, θ_2).

$$\Pi_{,u|@(N,\theta_1,\theta_2)}: (\widetilde{\theta_1}, \widetilde{\theta_2})$$
$$\rightarrow k_1\theta_1\widetilde{\theta_1} + K_2\theta_2\widetilde{\theta_2} - N * \left[L_1\widetilde{\theta_1}\cos(\theta_1) + L_2\widetilde{\theta_1}\cos(\theta_1 + \theta_2) + L_2\widetilde{\theta_2}\cos(\theta_1 + \theta_2)\right]$$

Then, the second order differential of the potential energy is:

$$\Pi_{,uu|@(N,\theta_1,\theta_2)}: \left(\widetilde{\theta_1}, \widetilde{\theta_2}, \widetilde{\theta_1}.\widetilde{\theta_2}\right)$$

$$\rightarrow k_1\overline{\theta_1}\widetilde{\theta_1} + K_2\overline{\theta_2}\widetilde{\theta_2} - N$$

$$* \left[L_1\overline{\theta_1}\,\widetilde{\theta_1}\cos(\theta_1) + L_2\overline{\theta_1}\,\widetilde{\theta_1}\cos(\theta_1 + \theta_2) + L_2\overline{\theta_2}\,\widetilde{\theta_1}\cos(\theta_1 + \theta_2)\right.$$

$$\left. + L_2\overline{\theta_1}\,\widetilde{\theta_2}\cos(\theta_1 + \theta_2) + L_2\overline{\theta_2}\,\widetilde{\theta_2}\cos(\theta_1 + \theta_2)\right]$$

It can be written under the matrix form:

$$\Pi_{,uu}(N, \theta_1, \theta_2)\left[\left[\widetilde{\theta_1}, \widetilde{\theta_2}\right], \left[\overline{\theta_1}.\overline{\theta_2}\right]\right]$$

$$= \left[\widetilde{\theta_1}, \widetilde{\theta_2}\right] \begin{bmatrix} \dfrac{\partial \Pi}{\partial \theta_1^2} & \dfrac{\partial \Pi}{\partial \theta_1 \partial \theta_2} \\[2mm] \dfrac{\partial \Pi}{\partial \theta_1 \partial \theta_2} & \dfrac{\partial \Pi}{\partial \theta_2^2} \end{bmatrix} \begin{bmatrix} \overline{\theta_1} \\ \overline{\theta_2} \end{bmatrix}$$

$$= \left[\widetilde{\theta_1}, \widetilde{\theta_2}\right] \begin{bmatrix} k_1 - N.(L_1.\cos(\theta_1) + L_2.\cos(\theta_1 + \theta_2)) & -N.L_2.\cos(\theta_1 + \theta_2) \\ -N.L_2.\cos(\theta_1 + \theta_2) & k_2 - N.(L_2.\cos(\theta_1 + \theta_2)) \end{bmatrix} \begin{bmatrix} \overline{\theta_1} \\ \overline{\theta_2} \end{bmatrix}$$

To detect the bifurcation point on the path $\wp_0$, the determinant of this matrix on the pre-buckling path $\wp_0$, (i.e. for $\theta_1 = \theta_2 = 0$) is computed as a function of N. The first root N_c of this determinant is the critical load; the point $(\theta_1(N_c), \theta_2(N_c), N_c)$ is called the bifurcation point. For this very simple example, we can draw the potential energy in the coordinate system $(\theta_1, \theta_2, \Pi)$ along the path of loading $\mathcal{L}$ as a function of the control parameter N.

(2)   The direct problem for this two parameter system

For this system, the "direct problem" is very simple and consists of:

Find the direction of buckling $[\theta_{1,obj}, \theta_{2,obj}]$ for two given spring stiffness (k_1, k_2).

The eigenvector $\theta_c = [\theta_{c_1}, \theta_{c_2}]$ associated with the 0 eigenvalue is the "direction" in which the buckling will occur. In this case, if we denote by $K = \Pi_{,uu}(N, \theta_1, \theta_2)$ the matrix of the second order differential of the potential energy, the first line of the eigenvalue problem results in the equation: $K_{11} * \theta_{c_1} + K_{12} * \theta_{c_2} = 0$.

$$[K] * [\theta_c] = [0]$$

Hence, the "direction of buckling" is

$$[\theta_{c_1}, \theta_{c_2}] = \frac{1}{\sqrt{1 + \left(\frac{K_{11}(N_c,0,0)}{K_{12}(N_c,0,0)}\right)^2}} * [1, -\frac{K_{11}(N_c,0,0)}{K_{12}(N_c,0,0)}].$$

It provides the relation between $\theta_1 = \theta_{c_1}$ and $\theta_2 = \theta_{c_2}$ at the bifurcation. Not surprisingly, this direction can be tuned by the stiffness of the springs (k_1, k_2). To simplify the notation, we can normalize θ_1 and θ_2. We denote by $\theta_{ratio} = \frac{\theta_2}{\theta_1}$ the ratio of the angles at the bifurcation points. Similarly, we can normalize the stiffness k_1 and k_2: $k = \frac{k_2}{k_1}$.

For instance, for bars of equal length, we can show that:

$$\theta_{ratio}(k) = \frac{-2*k+\sqrt{1+4*k^2}}{-1-2*k+\sqrt{1+4*k^2}}.$$

This function is shown in Figure 120.
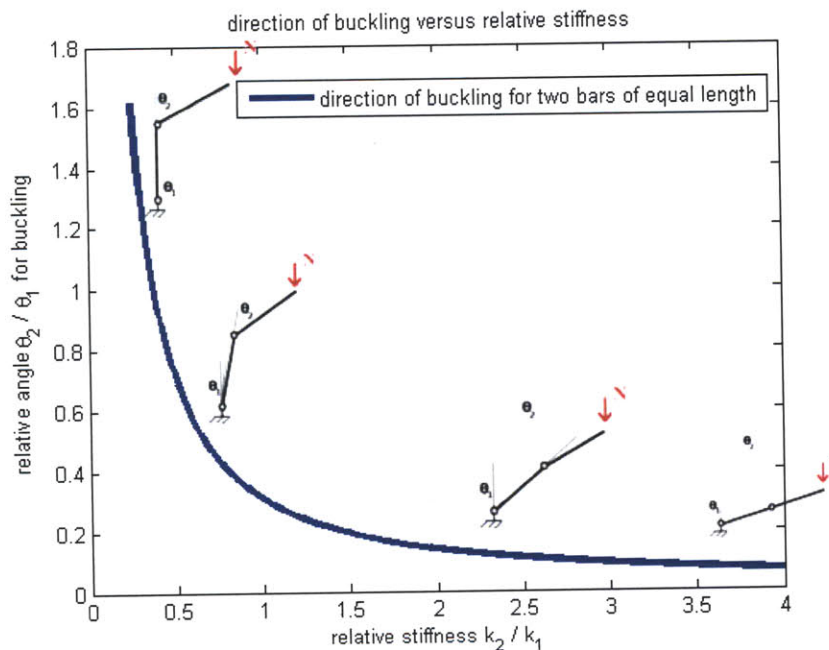
Figure 120: Direction of buckling for a system of two bars of equal length. The ratio $\frac{\theta_1}{\theta_2}$ is represented versus the ratio of stiffness of the springs $\frac{k_1}{k_2}$.

This direction of buckling can also be "read" directly on the full potential function at the critical load. We are representing in Figure 121 the potential energy of the system versus θ_1 and θ_2, at the critical load for different ratio of the spring stiffness at the two hinges.

- When $k_2 \ll k_1$ (situation a/ in Figure 121), the structure is not stiff in the direction $[\theta_1, \theta_2] = [0,1]$; the potential energy is does not increase in this direction. In the other hand, the system is very stiff in the direction $[\theta_1, \theta_2] = [1,0]$ (the potential energy is quadratic in θ_1 and increases a lot as we depart from $\theta_1 = 0$).

- When $k_2 \gg k_1$ (situation g/ in Figure 121), it is the opposite. A small increase in θ_1 does not result in a significant increase in the energy. However, a small increase in θ_2 results in a large increase in energy. As a result, the buckling will occur in the direction $[\theta_1, \theta_2] = [0,1]$

- For the situations in between, there is always a direction $[\theta_1, \theta_2] = [1, \theta_{ratio}]$ in which the stiffness is zero (no increase in the potential energy when the system is displaced in this direction). This is the buckling direction.
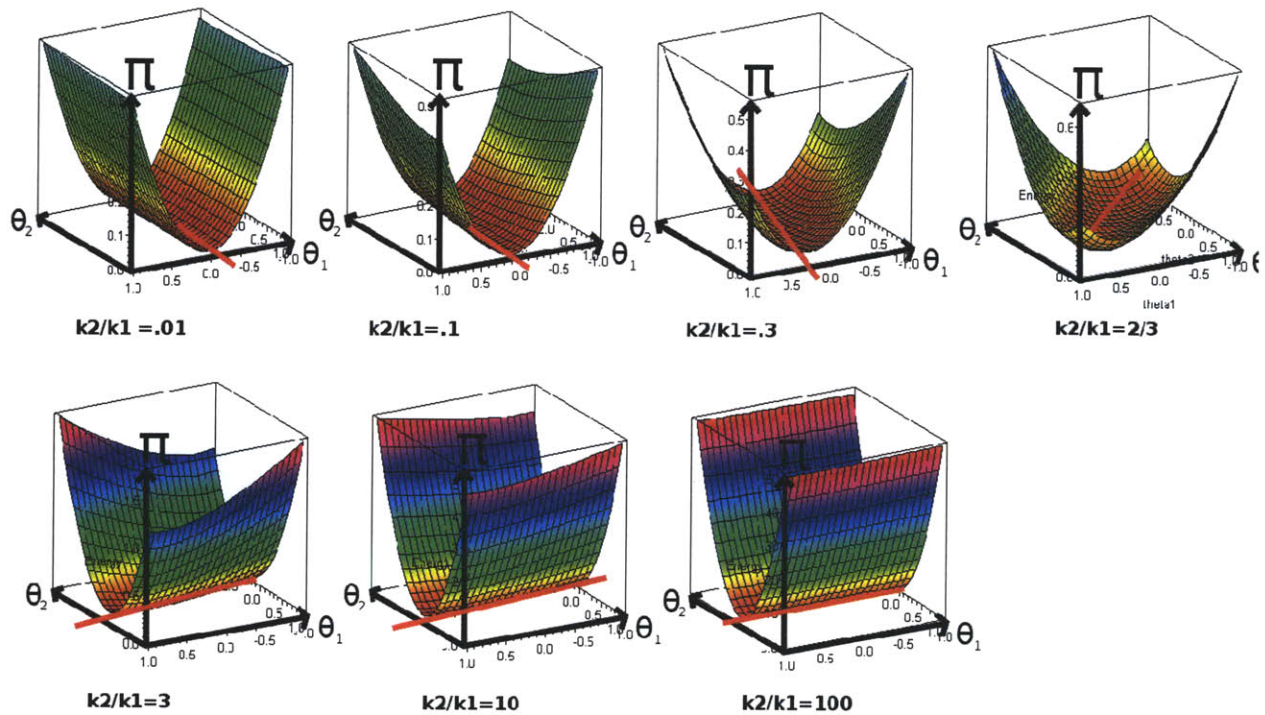
Figure 121: The potential function at the smallest critical load is represented versus θ_1 and θ_2. The direction of the buckling is changed by varying the ratio of the spring stiffness k2/k1 from .01 to 100 (from the top left to the bottom right). The ratio of $\frac{\theta_2}{\theta_1}$ varies from infinity (top left) to 0 (bottom right).

(3)   Representation of the energy function as a function of the load parameter: N.

The Maple software is used to compute and plot the potential energy for a two bar system with bars of length 1, and $k_2 = 2 * k_1 = 2$.

The three path of equilibrium are represented in Figure 122. The load N is plotted versus the angle of the first bar θ_1. $\wp_0$ is shown in blue, $\wp_1$ in green and $\wp_{-1}$ in red (Figure 122).

In Figure 123, we represent the non-linear potential energy $\Pi(N, \theta_1, \theta_2)$ for three values of N ($N = 0, N = N_c$ and $N > N_c$) in the (θ_1, θ_2) coordinates. $\wp_0$ is stable from A to B (this path is in a well of

potential), and unstable later (saddle point in C). $\wp_1$ and $\wp_{-1}$ are both stable (at least up to the value of N chosen). $\wp_1$ is the symmetric of $\wp_{-1}$.
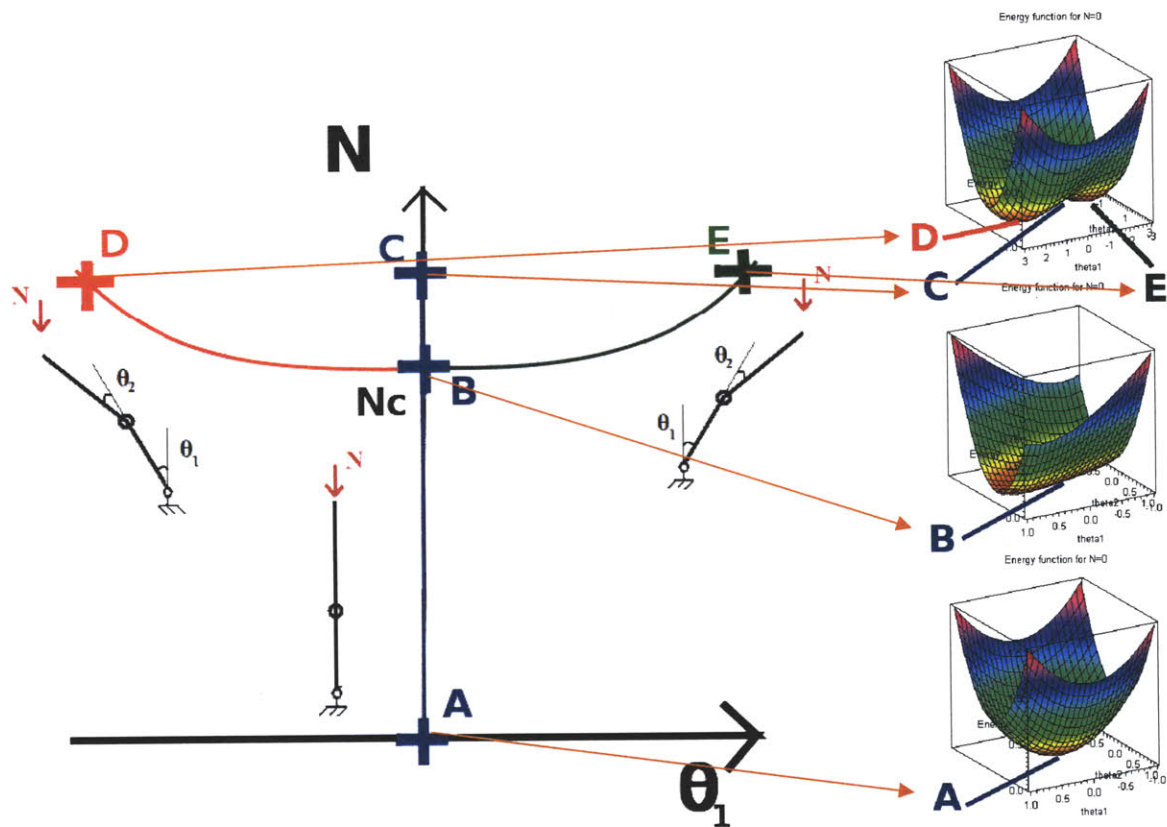
Figure 122: equilibrium path (P0 in blue, P1 in green, P-1 in red) in the (N, θ_1) coordinate. This plot is obtained by finding the equilibriums for each value of the load (in Figure 123, those points are the local minima or maxima) and reporting them in this schematics.

Figure 123: Potential energy for 3 values of N (N=0; N=N_c and N>N_c). The equilibrium points are the local minima and maxima of the potential function. For every value of the force, N, a potential function can be drawn, a the extrema of this function is reported onto Figure 122

(4)   The inverse problem of spring design.

Similarly, we understand that we can tune the relative stiffness k_{ratio} of the two springs to have the system buckle in a given direction $[\theta_{1,obj}, \theta_{2,obj}]$.

The inverse problem is defined as the function $k_{ratio}(\theta_{ratio})$. For the same problem (two bars of unit length), we can show that:

$$k_{ratio}(\theta_{ratio}) = \frac{1 + \theta_{ratio}}{\theta_{ratio} * (2 + \theta_{ratio})}$$

However, we should keep in mind that the magnitudes of θ_1 or θ_2 are not part of the buckling problem, but part of the post-buckling problem (ie $N > N_c$). To fit in the framework that we develop in the later paragraph, this magnitude of θ_1 or θ_2 is related to the control parameter on the equilibrium path $\wp_1$. This path $\wp_1$ is a straight line in the (θ_1, θ_2) coordinates, defined by what the direction of buckling, while $N > N_c$ is the control parameter on this loading path.

b)   *Rigorous approach to buckling of conservative systems: a non-linear phenomenon*

A rigorous and general formulation of the buckling is more involving than the usual linear elastic problem of small deformation.

Linear elasticity is widely used for its simplicity and the uniqueness of the solution u for a given situation (body forces b, displacement $\hat{u}$ and traction $\hat{t}$ boundary conditions applied on a given shape Ω with defined material properties $\mathbb{C}$). The case of buckling arises when several solutions exist to a given situation. Hence, we should depart from the case of linear elasticity to capture buckling.

This concept is précised in the following section in the case of a conservative system.

(1)   Potential energy, principal of minimal potential energy and stability

For every conservative system, we define the **potential energy** equal to the free energy minus the work of the external forces (body forces and boundary tractions). In the following, we assume that the Potential energy is differentiable.

$$\Pi(\sigma, u, \hat{u}, \hat{t}, b) = U(\sigma, u) - W_e(u, \hat{t}, b)$$

The **principle of minimal potential energy** states that for every kinematically admissible field $\tilde{u}$, $\Pi(u, t, \hat{u}, b, \mathbb{C}) \leq \Pi(\tilde{u}, \hat{t}, \hat{u}, b, \mathbb{C})$, with equality when $u - \tilde{u}$ is a rigid body motion. It results that $\frac{\partial \Pi(u + \alpha.v, t, \hat{u}, b, \mathbb{C})}{\partial \alpha} = 0$ and $\frac{\partial^2 \Pi(u + \alpha.v, t, \hat{u}, b, \mathbb{C})}{\partial \alpha^2} \geq 0$ for all v kinematically admissible (82).

Lejeune-Dirichlet's theorem (83) states that an equilibrium u is stable if Π **is locally strictly minimum in** u. Then the **equilibrium is stable** if the second derivative of the energy in the displacement is positive definite, i.e. $\Pi_{,uu}[\delta u, \delta u] > 0$, for all δu. Physically, it means that the eigenvalues of the stiffness matrix

around the local state have all positive real parts (in fact, the stiffness matrix is symmetric, so the eigenvalues are real).

(2) Path of loading

To better represent buckling, we often refer to a **path of loading**. It is a scalar parameterization of a given loading. We will write this path: $\mathcal{L} = \{\widehat{trac}(s), \hat{u}(s), b(s), s \in \mathbb{R}\}$ or for proportional loading $\mathcal{L} = \{s * T_o, \hat{u} + s * \widehat{U_0}, b + s * b_0, s \in \mathbb{R}\}$; s is the control parameter and $\{\frac{d\widehat{trac}}{ds}(s), \frac{d\hat{u}}{ds}(s), \frac{db}{ds}(s), s \in \mathbb{R}\}$ or $\{T_0, \widehat{U_0}, b_0\}$ is the direction of loading.

> For instance, in the case of an Euler Buckling, the magnitude of the force at the top of the beam is usually used as the control parameter for the path of loading. $N = \int_{section(l)} trac(x,y,z)\, dy\, dz$ is the analytical expression of this control parameter that describes the curve $\mathcal{L}$. The curve itself is a straight line in the set of admissible traction conditions, oriented by the vector $\{\tau\ traction\ on\ S_t\ such\ that\ \int_{section(l)} trac(x,y,z)\, dy\, dz\ is\ colinear\ to\ e_x\}$.

(3) bifurcation and buckling

For buckling problems, it is assumed that the configuration is loaded along a certain **equilibrium path** $\wp_i = \{s * T_o, \hat{u} + s * \widehat{U_0}, b + s * b_0, s \in \mathbb{R}\}$. To simplify the notation, we replace the full situation $(trac + s * T_o, b + s * b_0, \hat{u} + s * \widehat{U_0}, \mathbb{C})$ by its control parameter s.

> We have seen with the example of Euler buckling that there might exist several paths of equilibrium solution $\wp_i$ (which are called the "buckling modes i") corresponding to one path of loading (the force at the top of the column). Those paths can be stable (mode 1), or partially stable (mode 0).

Every position of the path $\wp_i$ is a position of equilibrium. As a result, along the paths $\wp_i$, the properties on the derivatives of the potential still hold: $\frac{\partial \Pi(u(s)+\alpha.v,s,\mathbb{C})}{\partial \alpha} = 0$ and $\frac{\partial^2 \Pi(u(s)+\alpha.v,s,\mathbb{C})}{\partial \alpha^2} > 0$, for all v kinematically admissible $and\ s$.

A static bifurcation point is the intersection of at least two of the loading and equilibrium paths $(\wp_i(\mathcal{L}))$. Physically, it is an equilibrium that can be reached by at least two different directions. So u is a static bifurcation point if and only if there exist $(\wp_1, \wp_2, \mathcal{L}_1, \mathcal{L}_2)$ such that $u = u_1(s_1) = u_2(s_2)$ where $(trac_1 + s_1 * T_1, b_1 + s_1 * b_1, \widehat{u_1} + s_1 * \widehat{U_1}, \mathbb{C})= (trac_2 + s_2 * T_2, b_2 + s_2 * b_2, \widehat{u_2} + s_2 * \widehat{U_2}, \mathbb{C})$ and $u_1 \in \wp_1, u_2 \in \wp_2$.

For instance the bifurcation point of an Euler buckling can be reached by unloading a "mode 1", by unloading the unstable "mode 0" down the buckling load or by loading the "mode 0" up to the buckling load.

(4)   Detection of bifurcation point

From Lejeune-Dirichlet's theorem, we infer that to the general problem of bifurcation is equivalent to finding the singularities of $\Pi_{,uu}(u, \hat{u}, \hat{t}, b, \mathbb{C})$. It leads to the generalized eigenvalue problem: Find X eigenvector solution of $\Pi_{,uu}[X, \delta u] = 0$ for all δu, around an equilibrium position.

X defines a direction in the space of displacement fields. Physically, this displacement can be added to the pre-buckling solution at the bifurcation point, without changing the potential energy of the system: it is a direction of zero-stiffness.

Usually, the detection of bifurcation are often perform along an equilibrium path $\wp$. The control parameter s is increased until we find a solution to the eigenvalue problem around the equilibrium $u_0(s)$: {find X, $\Pi_{,uu}(u_0(s), s)[X, \delta u] = 0$}.

3.   Buckling of elastic structures.

a)   Detecting the critical load

The previous section provides a rigorous framework for buckling of any conservative system, especially elastic structures. The formal equations of the buckling problem are derived and the physical meaning of "linear buckling" is defined in the next section.

The Green strain tensor is defined by:

$$E = \frac{1}{2}(F^T F - 1), \text{with } F = (\frac{dx}{dX}).$$

This strain is composed of a linear and a bilinear function of the displacement field:

$$\epsilon_{ij} = \frac{1}{2}(u_{i,j} + u_{j,i}) + \frac{1}{2}u_{i,j} \cdot u_{j,i}$$

$$\epsilon = e(u) + q(u, u)$$

We assume that the material behaves elasticically, i.e. the free energy function is $W(\epsilon) = \frac{1}{2}\epsilon : C : \epsilon$. The Kirchhoff stress function is then: $\sigma = W_{,\epsilon} = C : \epsilon$. The potential energy, for a loading path $\{\widehat{trac}(\lambda), \lambda \in \mathbb{R}\}$, in absence of body forces is:

$$\Pi(u,\lambda) = \int_{\Omega} W(\epsilon(u))d\Omega - \int_{S_t} \widehat{trac}(\lambda) . u \, dA$$

We introduce the same control parameter λ for the pre-buckling path of equilibrium and the path of loading for the structure: $\Pi_{,u}(u(\lambda), \lambda)[\delta u] = 0$ for all δu

We compute:

$\Pi_{,u}(u(\lambda), \lambda)[\delta u]$

$$= \int_{\Omega} \{ \left(e(u(\lambda)) + q(u(\lambda), u(\lambda))\right) : C : \left(e(\delta u) + q(u(\lambda), \delta u)\right) \} d\Omega$$

$$+ \int_{\Omega} \widehat{trac}(\lambda) . \delta u . dA$$

Then, the **critical point** is the smallest value λ such that: there exists X(x,y,z) displacement field such that $\mathbf{\Pi_{,uu}(u(\lambda), \lambda)[X, \delta u] = 0}$ for all δu.

By computing this second order differential, we find that:

$\Pi_{,uu}(u(\lambda), \lambda)[\delta u_1, \delta u_2]$

$$= \int_{\Omega} \{ \left(e(\delta u_1) + q(\delta u_1, u(\lambda))\right) : C : \left(e(\delta u_2) + q(u(\lambda)_2, \delta u)\right) \} d\Omega$$

$$+ \int_{\Omega} \{ \left(e(u(\lambda)) + q(u(\lambda), u(\lambda))\right) : C : \left(q(\delta u_1, \delta u_2)\right) \} d\Omega$$

or, because $e(u(\lambda) + q(u(\lambda), u(\lambda)) : C = \sigma(\lambda)$

$$\Pi_{,uu}(u(\lambda), \lambda)[X, \delta u] = \int_{\Omega} \{ \left(e(\delta u) + q(u(\lambda), \delta u)\right) : C : \left(e(X) + q(u(\lambda), X)\right) + \sigma(\lambda) : q(\delta u, X) \} d\Omega$$

This is the energetic formulation of the critical point. This function is composed of 3 terms:

- $K_1[X_1, X_2] = \int_{\Omega} e(X_1) : C : e(X_2) d\Omega$. This is the operator "stiffness" for linear elastic systems
- $K_2(\sigma(\lambda))[X_1, X_2] = \int_{\Omega} \sigma(\lambda) : q(X_1, X_2) d\Omega$. This term is the stiffness associated with the stress field of the pre-buckling solution, and the non-linear components of the strain. It does not depend on the displacement field $u(\lambda)$.

- $K_3\big(u(\lambda)\big)[X_1, X_2] = \int_\Omega q(u(\lambda), \delta u) : C : \big(e(X) + q(u(\lambda), X)\big) + e(\delta u) : C : q(u(\lambda), X)\, d\Omega.$ This term is the stiffness associated with other part of the non-linear component of the strain.

b)   The finite element case.

(1)   Tangent stiffness matrix and stress stiffness matrix

Based on this energetic formulation, the finite element formulation can be formed. The elastic stiffness matrix K is used. We also define a tangent stiffness matrix: $K_{\sigma;u}(U(\lambda), \lambda)$ such that:

$$K_2(\sigma(\lambda)) + K_3\big(u(\lambda)\big) = \delta U_{global}^T . K_{\sigma;u}(U(\lambda), \lambda) . X_{global}$$

This tangent stiffness is composed of a stress stiffness (associated with $K_2(\sigma(\lambda))$) and a non-linear displacement stiffness (associated with $K_3(u(\lambda))$)

Let U be the vector of global displacements of the nodes of an equilibrium position. X_{global} and δU_{global}^T are any two vectors of the global displacements, kinematically admissible, and λ is the control parameter on the loading path. The second order differential of the potential energy is:

$$\Pi_{,uu}(u(\lambda), \lambda)[X, \delta u] \approx \delta U_{global}^T \big(K + K_{\sigma;u}(U(\lambda), \lambda)\big) . X_{global}$$

$\delta U_{global} . \big(K + K_{\sigma;u}(U(\lambda), \lambda)\big) . X_{global} = 0$ for all δU_{global}. The relation holds for each individual component of the vector. As a result:

$$\big(K + K_{\sigma;u}(u(\lambda), \lambda)\big) . X_{global} = 0$$

The eigenvector X_{global} can again be interpreted as a direction of zero stiffness.

We should note that:

- The first term is the usual stiffness matrix. In elasticity, the stiffness is positive definite. So in itself, it is not enough to get the buckling.
- The other terms have a dependency in λ.

(2)   Linear buckling

In (84), Cook simplifies the problem by supposing that $K_{\sigma;u}(u(\lambda), \lambda)$ does not depend on $u(\lambda)$. This means that $K_3\big(u(\lambda)\big)$, the non-linear displacement stiffness, is neglected. The tangent stiffness is then equal to the stress stiffness:

$$K_{\sigma;u}(u(\lambda), \lambda) = K_\sigma\big(\sigma(\lambda)\big)$$

The linear buckling assumption is used in many finite element codes. It supposes that the stress field in the buckling mode is the same as the stress field in the pre-buckling solution, for a load equal to the critical load. [This assumption is made, for instance, in the case of buckling of columns. The force in the direction of the beam is supposed to be constant and equal to N_c, the load applied on top.]

He further introduces a linearization of the stresses for proportional loadings. Then

$$K_{\sigma;u}\ (u(\lambda),\lambda) = \lambda.K_\sigma$$

Finally, the buckling problem is equivalent to finding (λ_c, X_c) such that $(K + \lambda_c.K_\sigma).X_c = 0$

λ_c is the critical load, and X_c is the direction of buckling (a direction which yields to zero forces).

c)   Output for buckling analysis

For most application, buckling is a failure mode. Hence, the question to be answered is the question of the critical load, in our notation: λ_c.

For some other applications, like energy absorber by buckling (car-crashes …) the important information is the rate of dissipation, related to the stiffness of the buckled structure or $(K + \lambda_c.K_\sigma)$.

In our case, we want to be able to **control the buckled shape**. So it is a control of the direction of buckling, X_c.

4.   The proposed methodology to solve the problem: residual forces

The reversal design method is a method to optimize the properties of a material to have a stable equilibrium path that goes through a given shape.

a)   Residual forces to direct the direction of buckling

(1)   Body forces- a inspiring element

Body forces are often kept aside of the full 3D case by textbooks, mostly for clarity reasons. However, body forces do not change the detection of the bifurcation (i.e. second derivative of the energy), but only the path of equilibrium so $u(\lambda)$ and $\sigma(\lambda)$!

If we suppose that we are in the hypothesis of the linear buckling, we know that:

$$\Pi_{body-force}(u, \lambda) = \int_{\Omega} u(\lambda): K: u(\lambda)\, d\Omega + \int_{\Omega} u(\lambda): K_{\sigma}: u(\lambda)\, d\Omega + \int_{\Omega} f.u(\lambda)\, d\Omega$$

It leads to:

$$\Pi_{body-force,u}(u, \lambda)[\delta u] = \int_{\Omega} u(\lambda): K: \delta u\, d\Omega + \int_{\Omega} u(\lambda): K_{\sigma}: \delta u\, d\Omega + \int_{\Omega} f.\delta u\, d\Omega$$

And the second derivative is:

$$\Pi_{body-force,uu}(u, \lambda)[\delta u, X] = \int_{\Omega} X: K: \delta u\, d\Omega + \int_{\Omega} X: K_{\sigma}: \delta u\, d\Omega, \text{ for all } [\delta u, X]$$

In this formulation, we can see that only the stress field σ depends on the body forces, b. The term $\int_{\Omega} f.u(\lambda)\, d\Omega$ does not contribute to the buckling analysis. So if we add body forces to the linear buckling problem considered by Cook (84), we form the new problem:

Find the smallest eigenvalue λ_c and the eigenvector X_c such that $(K + \lambda_c.K_{\sigma,b}(f)).X_c = 0$

Only the stress stiffness matrix depends on the body forces b.

(2)   Residual forces- a mathematical concept

(a)   Definition for of residual forces in finite element

Instead of adding body forces, we introduce the mathematical concept of residual forces.

Those forces are not taken into account in the stress-stiffness matrix K_{σ}, but are used to direct the buckling in the direction of our desired shape U_{obj}. In other words, for a desired shape U_{obj}, we define the residual forces $F_r(u_{obj})$ as:

$$F_r(u_{obj}) = (K + \lambda_c.K_{\sigma}).u_{obj}$$

For the limit case $F_r(u_{obj}) = 0$, we know that the direction of the buckling will be u_{obj}.

(b)   The residual forces are the dual quantity of the objective function for the potential energy

These residual forces have a physical meaning. They are the dual quantities of the displacements for the potential energy.

We have seen that the buckling mode was a direction of zero stiffness, or a displacement which could be added to the pre-buckling solution without changing the energy. On the other hand, the objective shape is not, in general, associated with a zero stiffness. More precisely, the increase of energy when u_{obj} is added to the pre-buckling solution is $\delta\Pi = F_r(u_{obj}).U_{obj}$. Minimizing the residual forces means minimizing the energy increase when the objective function is added to the pre-buckling solution. In the limit of zero residual forces, the energy is not increased when the objective displacement is added to the pre-buckling solution. This objective function is then the buckling mode!

(c)   Definition of the residual force as an operator

These residual forces have been introduced in the finite element case. However, the same concept may apply in the continuous problem. In this case, we have to define the residual forces as an operator on the displacement fields. An implicit definition of these residual forces is the following: $fr_{u_{obj}}[X] = \Pi_{,uu}(u(\lambda))[u_{obj}, X]$, where X is a displacement field. And as a result, the energy increase when u_{obj} is added to the pre-buckling solution is: $\delta\Pi = fr_{u_{obj}}[u_{obj}]$.

We know by the theorem of representation that this operator of residual forces can be represent by a function $f_{u_{obj}}[u_{obj}]$, such that $fr_{u_{obj}}[X] = \Pi_{,uu}(u(\lambda))[u_{obj}, X] = \int_{\Omega} f_{obj}(x,y,z).X(x,y,z)d\Omega$. We call this function the field of residual forces.

(d)   Residual forces for a two parameter-systems

On the two parameters system introduced in II.D.2.a), $fr_{u_{obj}}[u_{obj}]$ is the second derivative of the potential function in the direction u_{obj}, at the point (0,0). We represent the potential function for different stiffness ratio of the two springs in Figure 124.

We also represent the potential function at the critical point in the direction $(\theta_1, \theta_2) = (1,1)$ for different ratio of the spring stiffness Figure 125. This is just a section cut of the previous potential in the plane normal to (1,1,0). The residual forces are associated with the second order derivative of this curve at $(\theta_1, \theta_2) = (0,0)$. For a ratio of spring stiffness of 2/3, this second derivative is zero. In this situation, the objective direction $(\theta_1, \theta_2) = (1,1)$ is the direction of buckling.
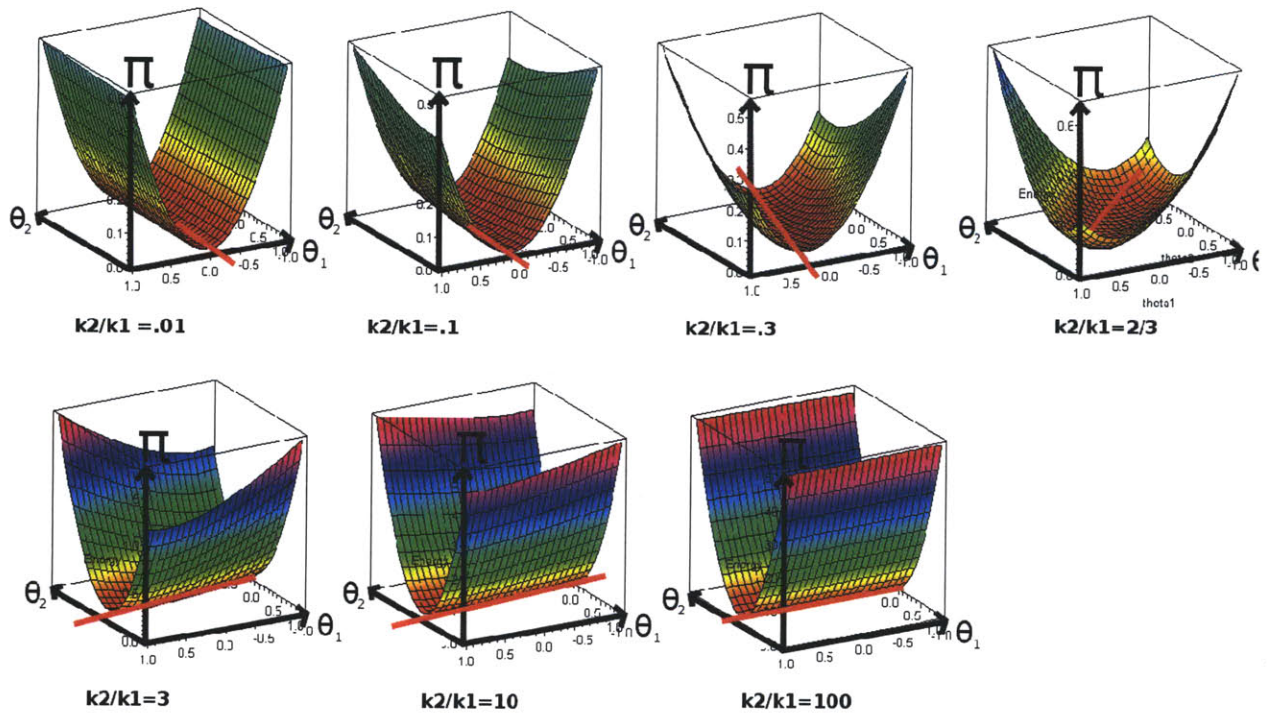
Figure 124: Potential function for the two parameter system for different ratio of the spring constant

Potential energy functions in the direction (θ1,θ2)=(1,1)
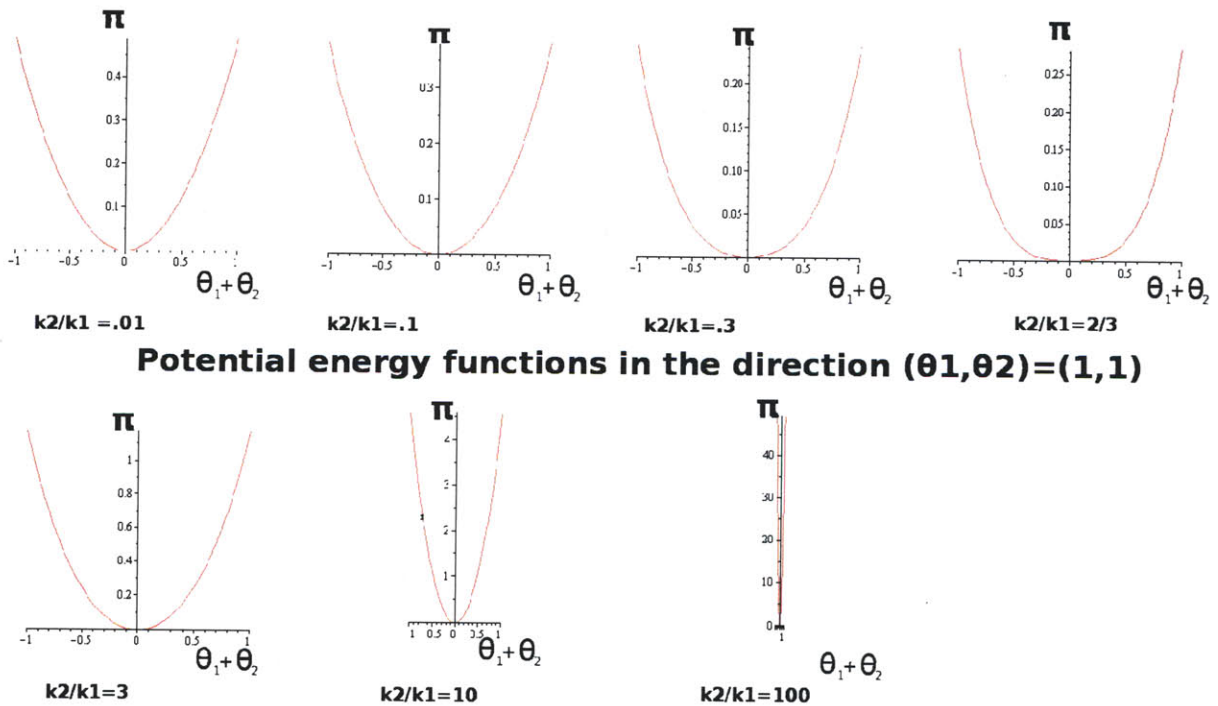
Figure 125: Potential function for the two parameter system, in the direction $(\theta_1, \theta_2)=(1,1)$, for different ratio of spring constant. This graph is a section of the graph in Figure 124

b)   *A good measure for our problem*

The introduction of this chapter mentions the need for a measure for the optimization problem.

(1)   Displacement and energy

It would be very convenient to measure how close the solution is from the objective shape, directly on the shape. Mainly, using the conventional second degree norm on the displacement: $m_u(u - u_{obj}) = \sqrt{\int_\Omega \left(u(x,y,z) - u_{obj}(x,y,z)\right)^2 d\Omega}$. This norm is very impractical for buckling solutions. As we have observed, static buckling implies great changes of shape for small variation of the control parameter on the loading path (ie critical load). It means that at the critical load, $f := \lambda \to m_u(u(\lambda) - u_{obj})$ is not a continuous function. For instance, at the buckling point, $m_u(u(\lambda), u(\lambda + \delta\lambda))$ can have a limit non nul for $\delta\lambda \to 0$. This is due to the fact that the stiffness is zero in the buckling direction, and depending of higher order terms in the energy, the stable solution at $\lambda + \delta\lambda$ can be very different to the stable solution at λ.

A better norm in our set of solutions is the difference of energy between the objective function and the solution of the buckling. $m_\Pi(u, u_{obj}) = \min_\lambda \left(\Pi(u_{obj}, \lambda) - \Pi(u, \lambda)\right)$. We know that the energy is continuous in λ. Though, as underlined in the example of buckling with 2 parameters Figure 123, we can have $m_\Pi(u_1(N), u_{-1}(N)) = 0$ without $u_1(N) = u_{-1}(N)$. This is the case of the two symmetric path, leading to the same energy for two symmetric shape. m_Π is thus only a semi-norm.

(2)   Intensity of residual forces

Instead, we decided to use the concept of residual forces. To form a scalar, we take the norm of the field of residual forces:

$$m_{fr}(u - u_{obj}) = \sqrt{\int_\Omega \left(f_{u_{obj}}(x,y,z)\right)^2 d\Omega}$$

If we are using finite element, we have an analytical expression:

$$m_{Fr}(U - U_{obj}) = \sqrt{\sum_{i=1}^{\#elmt} \left((K + \lambda_c . K_{\sigma(u)}).u_{obj}\right)^2}$$

Furthermore, we have shown that if $m_{fr}(u - u_{obj}) = 0$ the direction of buckling is u_{obj}.

It does not mean that the final stable equilibrium is u_{obj} itself. Furthermore, we believe that for non-pathologic cases, a bifurcated equilibrium path has rather a constant direction (if the branch does not bifurcate itself).

However, as we have seen in II.D, with the checker-board patterns, which bifurcate into the Herringbone, this might not always be the case.

c)   *Decomposition into an orthonormal base.*

Can this method be implemented at a reasonable calculation cost?

If we recall the problem is the following:

Find the material properties $C(x, y, z)$ and critical load λ that minimizes $m_{fr}(u(\lambda) - u_{obj})$.

Equivalently, the finite element version is:

Find $\mathbb{C}_i$ (the material constant of element i) such that $\sum_{i=1}^{\#elmt} \left((K + \lambda_c . K_{\sigma(u)}) . u_{obj} \right)^2$ is minimum.

Both problems are very complicated. The continuous case is a minimization in a function. The discrete case is parametric minimization with a number of variables equal to the number of elements of our mesh.

An easy method to solve this problem is to decouple the problem. This requires to find the proper spectral decomposition (eigenfunctions for the continuous case or eigenvector for the discrete case) of the cost function.

If we find such eigenvectors, the cost function is transformed into:

$$cost(\mathbb{C}_i) = cost(\mathbb{C}_1, \mathbb{C}_2, \dots, \mathbb{C}_e)$$
$$= cost_1(\mathbb{C}_1) + cost_2(\mathbb{C}_2) + \dots + cost_e(\mathbb{C}_e)$$

Each material parameter is then defined by the one-dimension minimization problem find $\mathbb{C}_1$ such that $cost_1(\mathbb{C}_1)$ is minimum.

> We should be aware that the material properties are usually positive. Lagrangian multipliers might be required to impose this condition.

> Instead of this decomposition, we might also use other advanced technique for minimization (simulated annealing, gradient method, Monte-Carlo method...)

E. Toys problems: A formulation adapted to the design of wrinkled membranes

In order to test this method, we have designed a toy problem. This toy problem is adapted to the wrinkling problem. Huck et al. (81) have shown that buckling of a hard coating on a soft substrate can be modeled by a stiff elastic plate on a soft elastic foundation. Instead of 2D, this model can be simplified in a 1D problem of the buckling of a beam maintained by an elastic foundation (Figure 126).

We are introducing two algorithms:

- The first one compute the direct problem in finite differences (given an elastic foundation distribution, what is the shape of the buckling mode)
- The second one computes the inverse problem, also in finite differences. It relies on the definition of the cost function and the optimum material properties developed in II.D.3.b)

We then test those algorithms as follow:

- Comparison of the optimal properties given by the algorithm for the inverse problem, and the initial stiffness map, with an analytical solution for one precise stiffness map (the elastic foundation is taken to be zero stiffness everywhere apart in the center where it is taken to be 1).

We are showing that the algorithm globally converges toward the given "stiffness map" (except at the boundaries, for reasons that we are trying to explain in a last section).

1. Algorithms for the direct and inverse problems of the buckling of a column on an elastic foundation, using finite differences.

a) Direct problem.
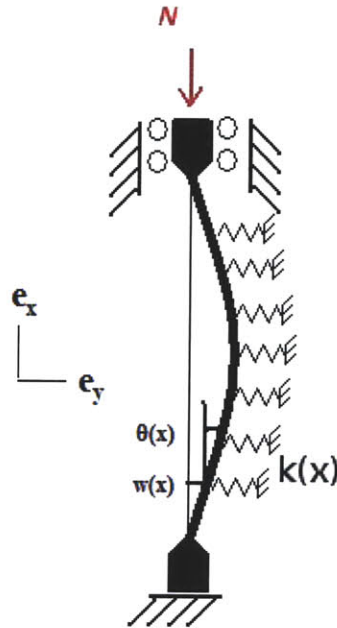
Figure 126: Nomenclature of the adapted toy problem: buckling of a column on an elastic foundation. The elastic foundation is modeled by springs of stiffness k(x). The deflection at x is named w(x) while the angular rotation of the section of the column is $\theta(x)$. A force N is exerted vertically at the top of the column. The section of the column has an area S(x) and the second moment of inertia is I(x). The column has a length L.

The problem involves a beam in compression with an axial force $-F.e_x$ on top. The nomenclature for this problem is described in Figure 126: the beam is characterized by the displacement field of the neutral axis $(u(x), w(x), \theta(x))$.

The assumption of small rotations and finite displacements classically results in two kinematics relations:

$$\theta = \frac{dw}{dx}$$

$$\kappa = -\frac{d\theta}{dx}$$

and three equilibrium equations:

$$\frac{du(x)}{dx} = 0$$

$$V(x) = \frac{dM}{dx} - N * \theta$$

$$\text{and } k(x) * w(x) = \frac{dV}{dx}.$$

Then, the Hooke's law for an elastic material gives:

$$M(x) = EI(x).\kappa(x)$$

$$\text{and } N(x) = ES(x).\frac{du(x)}{dx}.$$

Finally, the imposed boundary conditions are:

$$N(L) = N; u(0) = 0$$

$$M(L) = M(0) = 0; w(L) = w(0) = 0.$$

Under the assumption of linear buckling, the state of stress in the beam is the same as the pre-buckling solution i.e. the force N(x) is uniform and equal to N, in the buckled state.

As a result, it leads to the fourth order differential equation:

$$\frac{d^4w}{dx^4} + \frac{N}{EI} \cdot \frac{d^2w}{dx^2} = \frac{k}{EI} \cdot w \quad \text{for } x \in [0, L]$$

We then form the discrete formulation of the problem. The interval $[0, L]$ is divided into n intervals of equal length.

$$\frac{1}{(n+1)^4}(w_{i-2} - 4w_{i-1} + 6w_i - 4w_{i+1} + w_{i+2}) + \frac{N}{EI(n+1)^2}(w_{i-1} + 2w_i - w_{i+1}) = \frac{1}{EI} \cdot k_i w_i, \text{ for all}$$
$$i \in \{3, n-2\}$$

As for the first and last two nodes:

$$w_0 = w_n = 0$$

Usually, the condition of zero moment in 0 and L are considered by introducing supplementary nodes: w_{-1} and w_{n+1}, such that

$$-w_{-1} + 2w_0 - w_1 = 0$$

$$-w_{n-1} + 2w_n - w_{n+1} = 0$$

Combine with the condition in displacement at node 0 and n, we get:

$$w_{-1} = -w_1$$

$$w_{n+1} = -w_{n-1}$$

Those two equations are then included in the general equation to eliminate the displacement of the introduced nodes w_{-1} and w_{n+1}:

$$(n+1)^4(w_{n-3} - 4w_{n-2} + 5w_{n-1} - 4w_n) + \frac{N(n+1)^2}{EI}(-w_{n-2} + 2w_{n-1} - w_n) = \frac{1}{EI} \cdot \mathrm{k}_{n-1} w_{n-1}$$

$$(n+1)^4(w_0 - 4w_1 + 5w_2 - 4w_3) + \frac{N(n+1)^2}{EI}(-w_1 + 2w_2 - w_3) = \frac{1}{EI} \cdot \mathrm{k}_2 w_2$$

It results in the following system:

$$\left[\begin{pmatrix} 1 \\ -4 & 5 & -4 & 1 \\ 1 & -4 & 6 & -4 & 1 \\ & \ddots & \ddots & \ddots & \ddots & \ddots \\ & & \ddots & \ddots & \ddots & \ddots & \ddots \\ & & & \ddots & \ddots & \ddots & \ddots & \ddots \\ & & & 1 & -4 & 6 & -4 & 1 \\ & & & & 1 & -4 & 5 & -4 \\ & & & & & & & 1 \end{pmatrix} + \frac{N}{(n+1)^2 EI} \begin{pmatrix} 0 \\ -1 & 2 & -1 \\ & \ddots & \ddots & \ddots \\ & & \ddots & \ddots & \ddots \\ & & & \ddots & \ddots & \ddots \\ & & & & \ddots & \ddots & \ddots \\ & & & & & -1 & 2 & 1 \\ & & & & & & & 0 \end{pmatrix} - \frac{(n+1)^4}{EI} \begin{pmatrix} 0 \\ & k_2 \\ & & \ddots \\ & & & k_{n-1} \\ & & & & 0 \end{pmatrix} \right] * (w_i) = 0$$

We introduce the notation K_M, K_σ and K_{spring} for the three previous matrices. The system can be rewritten:

$$\left(\left(K_M - K_{spring} \right) + load. K_\sigma \right). W = 0$$

or, provided that $K_M - K_{spring}$ is not singular:

$$\left(\left(K_M - K_{spring} \right)^{-1}. K_\sigma + \frac{1}{load} Id \right). W = 0$$

This is to say, the direct problem is equivalent to finding the largest eigenvalue λ and eigenvector W of $\left(K_M - K_{spring} \right)^{-1}. K_\sigma$. Then, the critical load is equal to $N = \frac{1}{\lambda} * \frac{EI}{(n+1)^2}$, and the shape of the buckling mode is W.

We are representing the first three buckling modes, without elastic foundation, in Figure 127. The analytical shape is a sinusoid. The difference between the shape predicted by the numerical algorithm and a sinusoid (analytical solution for mode 1) is plotted in Figure 128. While the predicted shape is globally quite accurate (the maximum difference between the analytical and the predicted shape is 10^{-4} smaller than the amplitude of the deflection), the relative precision is less, near the boundary, (where the deflection is the smallest and the error the more important). We think that this problem is due to the "poor condition" of the problem of eigenvalue. As described in (85), the eigenvalue problem is very sensitive to perturbations. Our problem is very close to the example chosen by the C. Moler (85) to highlight the sensitivity of the eigenvalue problem (a perturbation of the size of the floating-point roundoff error on one of the coefficient of the matrix might result in a change of unity in the computed eigenvalue!). Going from an eigenvalue problem to singular value decomposition might be a solution to increase the precision of this algorithm, as advised by (85).

However, we should note that this error does not depend on the magnitude of the coefficients $K_M(1,1)$ and $K_M(n,n)$ which have been chosen arbitrarily.

Figure 127: Shape of the first three buckling modes of a column, without any elastic foundation. The black curve is associated with the smallest critical load and will then happen first. The blue curve is the second mode while the red is the third. Their critical load is more important than the one of the first mode. As a result, unless exception, only the first mode will be observed.
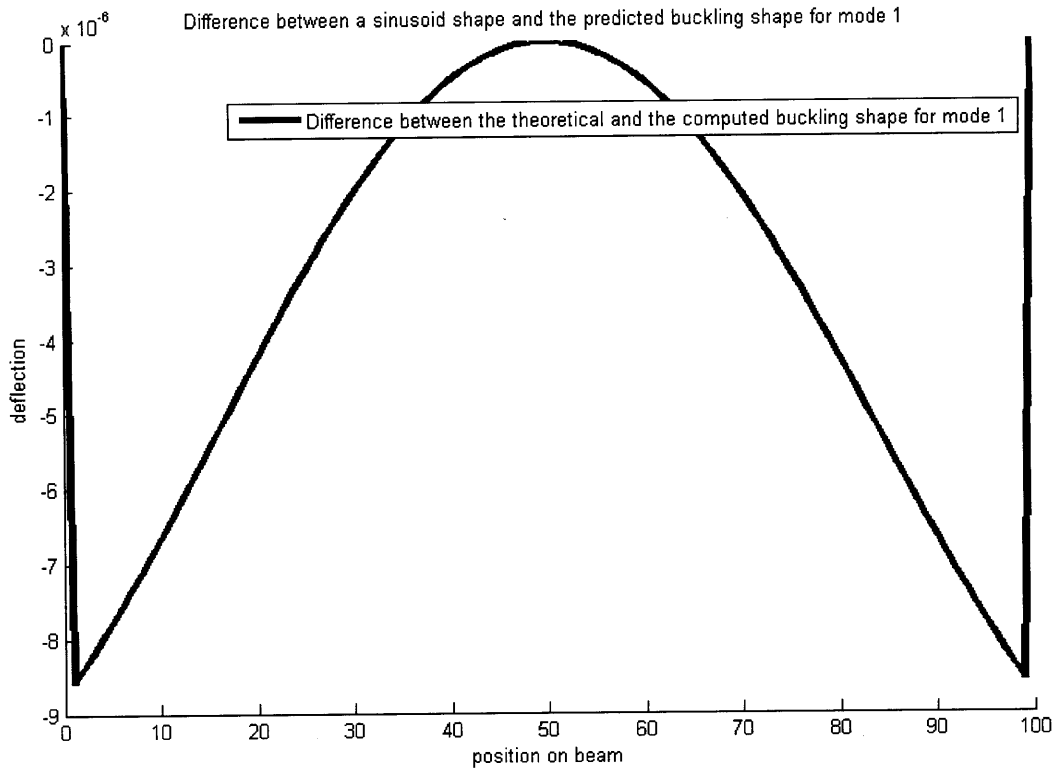
Figure 128: This plot represents the difference between an arc of sinusoid (expected buckling shape for a column without elastic foundation) and the mode 1 predicted by the algorithm. The precision in displacement is very good (maximum error is 10^{-5}). However, this proves the existence of "numerical errors" when Matlab performs the eigenvalue problem.

This analysis is the first sanity test of our direct algorithm. We develop another analytical solution with a spring at the center of the column, in the subsequent sections. But before that, we are showing the second algorithm, which performs the inverse method (determination of the foundation knowing the buckling shape).

b) Inverse problem.

For the inverse problem, we are introducing the concept of residual force, in the direction of a desired buckling shape u_{obj}.

More especially, the vector of residual forces is:

$$\mathrm{p} = \left(\left(K_M - K_{spring} \right) + load. K_\sigma \right). u_{obj}$$

Then, the objective function is assumed to be

$$cost(\{k_i, i \in [2..n]\}) = p^T. p$$

The problem of minimization can be found analytically here, since:

$$\frac{\partial cost}{\partial k_i} = 2 * p^t . \frac{\partial p}{\partial k_i}$$

Furthermore:

$$\frac{\partial p}{\partial k_i} = [i \otimes i] * u_{obj}$$

(no summation on the i)

Hence:

$$\frac{\partial cost}{\partial k_i} = 2 * \left(u_{obj}^T . K_M + N * u_{obj}^T . K_\sigma - u_{obj}^T * \text{diag}(k_j) \right) : \left([i \otimes i] * u_{obj} \right) \text{ (no summation on the i)}$$

$$\frac{\partial cost}{\partial k_i} = 2 * \left(u_{obj}^T . K_M \right)_i . \left(u_{obj} \right)_i + 2 * N * \left(u_{obj}^T . K_\sigma \right)_i \left(u_{obj} \right)_i - \frac{k_i}{EI} * \left(u_{obj} \right)_i^2$$

$\frac{\partial cost}{\partial k_i}$ does not depend on k_j for $j \neq i$. It means that the cost function is already decoupled, or that the $(k_j, j = 1..e)$ is already the spectral decomposition of the cost function.

The cost function is a second degree polynomial function, positive. So its minimum is achieved when the derivative is null: $\frac{\partial cost}{\partial k_i} = 0$ for all $i \in [1, n]$. As a result, the optimal material properties of the substrate are found by the analytical expression:

$$k_i = \frac{EI \left[\left(u_{obj}^T . K_M \right)_i + N * \left(u_{obj}^T . K_\sigma \right)_i \right]}{\left(u_{obj} \right)_i}$$

The algorithm for the inverse method is only the implementation of this result. Given an objective function u_{obj} and the matrices K_M, K_σ, we are able to define the function of the elastic foundation.

c) *Improved algorithm for the adapted problem.*

step 1:   Step 2:   Step 3:   Step 4:

Choose a desired buckled shape

Prescibe springs (body forces) to force a homogeneous beam into the desired shape

Prescribe a tuned material in order to relax the springs

Get the final shape without any spring! This is your buckle mode right here.

$$U_{obj}(x) \qquad f_r(x) \qquad k(x)$$
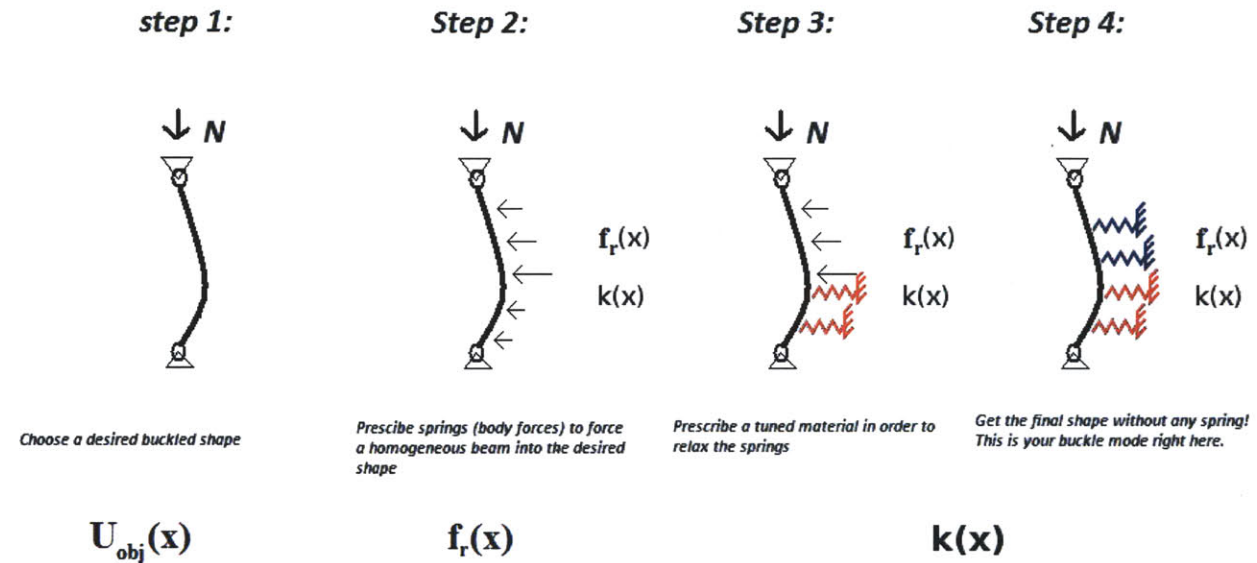
Figure 129: Adapted version of the algorithm for buckling of a beam on an elastic foundation

We should note that an analytical solution may not be found for every problem (especially more complex 2D or 3D problems). Instead, a simple optimization algorithm might be used to minimize the residual forces and define an optimal property for the elastic foundation, as shown in Figure 129.

2. Test of the algorithms.

a) *Definition of the stiffness map*

To test the two algorithms, we introduce a problem with a non-zero elastic foundation that can be analytically determined.

We assign the stiffness of the foundation to be 0 everywhere but in $\frac{L}{2}$ where it is 1. This problem models the case of a beam with one spring of stiffness 1 at $x = \frac{L}{2}$. This situation is represented in Figure 130.
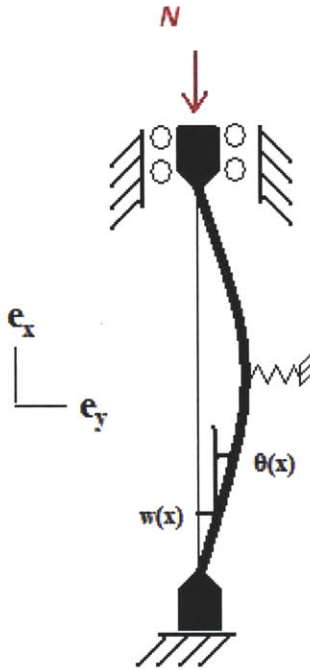
Figure 130: Buckling of a column with a spring in the middle. The notations are the same than the one introduced in Figure 126

b)   *Analytical solution*

Building upon the previous section, we know that the equations modeling the buckling of this column are:

$$\frac{d^4w}{dx^4} + \frac{N}{EI} \cdot \frac{d^2w}{dx^2} = 0 \text{ for } x \in [0, \frac{L}{2}]$$

$$\frac{d^4w}{dx^4} + \frac{N}{EI} \cdot \frac{d^2w}{dx^2} = 0 \text{ for } x \in [\frac{L}{2}, L]$$

This results in a solution defined in $[0, \frac{L}{2}]$ and $[\frac{L}{2}, L]$.

$$w(x) = A_1 \sin\left(\sqrt{\frac{N}{EI}} x\right) + B_1 \cos\left(\sqrt{\frac{N}{EI}} x\right) + C_1 x + D_1, \text{ for } x \text{ in } [0, \frac{L}{2}]$$

$$w(x) = A_2 \sin\left(\sqrt{\frac{N}{EI}} x\right) + B_2 \cos\left(\sqrt{\frac{N}{EI}} x\right) + C_2 x + D_2, \text{ for } x \text{ in } [\frac{L}{2}, L]$$

We should point out that the solution on the two intervals are perfect sinusoids. However, the critical load will be affected by the spring. Hence, the final buckled shape is going to be a piecewise function made of two arcs of sinusoids intercepting at $\frac{L}{2}$. The stronger the spring, the higher the critical load for the first mode. On the other hand, the critical point for the second mode (for which the deflection at $\frac{L}{2}$ is

equal to zero) is not affected by the spring constant. As a result, as the spring constant is increased, the shape of the mode associated with the lowest energy is composed of two arc of sinusoid, and snaps into the "second mode" if the spring constant is raised over a certain value.

To determine the critical load, we establish the continuity equations at $x = \frac{L}{2}$

$$w(\tfrac{L}{2}+) = w(\tfrac{L}{2}-) ;$$

$$\theta(\tfrac{L}{2}+) = \theta(\tfrac{L}{2}-) \Rightarrow \frac{dw}{dx}(\tfrac{L}{2}-) = \frac{dw}{dx}(\tfrac{L}{2}+)$$

$$M(\tfrac{L}{2}+) = M(\tfrac{L}{2}-) \Rightarrow EI\frac{d^2w}{dx^2}(\tfrac{L}{2}-) = EI\frac{d^2w}{dx^2}(\tfrac{L}{2}+)$$

$$V(\tfrac{L}{2}+) = V(\tfrac{L}{2}-) \Rightarrow -EI\frac{d^3w}{dx^3}\left(\tfrac{L}{2}-\right) + N*\theta\left(\tfrac{L}{2}-\right) = -EI\frac{d^3w}{dx^3}(\tfrac{L}{2}+) + N*\theta\left(\tfrac{L}{2}+\right) + k*w\left(\tfrac{L}{2}\right)$$

And boundary conditions:

$$w(L)=0 ;$$
$$M(L)=0 \Rightarrow \frac{d^2w}{dx^2}(L) = 0;$$
$$N(L)=N$$

$$w(0)=0 ;$$
$$M(0)=0 \Rightarrow \frac{d^2w}{dx^2}(L) = 0;$$

$$u(0)=0;$$

Those equations lead to the following system for the unknown parameters.

$$
\begin{pmatrix}
0 & 1 & 0 & 1 & 0 & 0 & 0 & 0 \\
0 & \sqrt{\frac{N}{EI}} & 0 & 0 & 0 & 0 & 0 & 0 \\
\sin\!\left(\sqrt{\frac{N}{EI}}\frac{L}{2}\right) & \cos\!\left(\sqrt{\frac{N}{EI}}\frac{L}{2}\right) & \frac{L}{2} & 1 & -\sin\!\left(\sqrt{\frac{N}{EI}}\frac{L}{2}\right) & -\cos\!\left(\sqrt{\frac{N}{EI}}\frac{L}{2}\right) & -\frac{L}{2} & -1 \\
\sqrt{\frac{N}{E_A I}}\cdot\cos\!\left(\sqrt{\frac{N}{EI}}\frac{L}{2}\right) & -\sqrt{\frac{N}{E_A I}}\cdot\sin\!\left(\sqrt{\frac{N}{EI}}\frac{L}{2}\right) & 1 & 0 & -\sqrt{\frac{N}{E_B I}}\cdot\cos\!\left(\sqrt{\frac{N}{EI}}\frac{L}{2}\right) & \sqrt{\frac{N}{E_B I}}\cdot\sin\!\left(\sqrt{\frac{N}{EI}}\frac{L}{2}\right) & -1 & 0 \\
-N*\sin\!\left(\sqrt{\frac{N}{EI}}\frac{L}{2}\right) & -N*\cos\!\left(\sqrt{\frac{N}{EI}}\frac{L}{2}\right) & 0 & 0 & N*\sin\!\left(\sqrt{\frac{N}{EI}}\frac{L}{2}\right) & N*\cos\!\left(\sqrt{\frac{N}{EI}}\frac{L}{2}\right) & 0 & 0 \\
k*\sin\!\left(\sqrt{\frac{N}{EI}}\frac{L}{2}\right) & k*\cos\!\left(\sqrt{\frac{N}{EI}}\frac{L}{2}\right) & k*\frac{L}{2}+N & k & 0 & 0 & -N & 0 \\
0 & 0 & 0 & 0 & \sin\!\left(\sqrt{\frac{N}{EI}}L\right) & \cos\!\left(\sqrt{\frac{N}{EI}}L\right) & L & 1 \\
0 & 0 & 0 & 0 & -N*\sin\!\left(\sqrt{\frac{N}{EI}}L\right) & -N*\cos\!\left(\sqrt{\frac{N}{EI}}L\right) & 0 & 0
\end{pmatrix}
*
\begin{pmatrix} A_1 \\ B_1 \\ C_1 \\ D_1 \\ A_2 \\ B_2 \\ C_2 \\ D_2 \end{pmatrix}
=
\begin{pmatrix} 0 \\ 0 \\ 0 \\ 0 \\ 0 \\ 0 \\ 0 \\ 0 \end{pmatrix}
$$

For the system to have a non-zero solution, the determinant of the matrix should be zero. We compute the first buckling mode (i.e. the first annulation of the determinant of the matrix as a function of N), as well as the eigenvector associated with the eigenvalue 0.

It leads to a symmetric solution only slightly different from the free Euler buckling of a column. Euler critical load for this beam maintained by a spring is 11.9 while it was 9.8 with a "natural beam". Numerically, Maple computes a bifurcation point for N=11.88911149 and the constants for this problem are:

$$
\begin{pmatrix} A_1 \\ B_1 \\ C_1 \\ D_1 \\ A_2 \\ B_2 \\ C_2 \\ D_2 \end{pmatrix}
=
\begin{bmatrix}
0.594338589474801559 \\
2.490282782504852740^{-16} \\
0.3127956106132226027 \\
4.020115538535364490^{-11} \\
0.566645719463812036 \\
-0.179306964571846972 \\
-0.312795610681659953 \\
0.312795610662712276
\end{bmatrix}
$$

Where the solution is the piecewise function:

$$w(x) = A_1 \sin\!\left(\sqrt{\frac{N}{EI}}x\right) + B_1 \cos\!\left(\sqrt{\frac{N}{EI}}x\right) + C_1 x + D_1, \text{ for } x \text{ in } \left[0,\frac{L}{2}\right]$$

$$w(x) = A_2 \sin\!\left(\sqrt{\frac{N}{EI}}x\right) + B_2 \cos\!\left(\sqrt{\frac{N}{EI}}x\right) + C_2 x + D_2, \text{ for } x \in \left[\frac{L}{2},L\right]$$

As observed earlier on the equation themselves, this solution is composed of two arcs of sinusoids that intersect at $\frac{L}{2}$. WE are representing one situation in Figure 131.
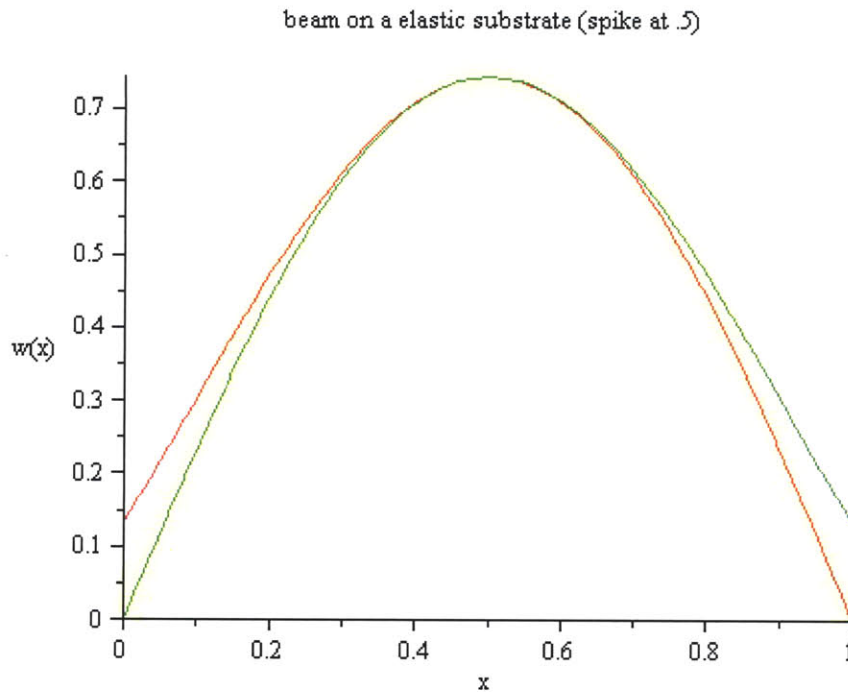
Figure 131: Deflection of a beam on an elastic substrate (spike at L/2). This function is defined piecewise [green: solution on [0,.5]; red: solution on [.5,1]; yellow: position of the neutral axis of the beam on [0,1]

c) *Testing of the inverse problem.*

To test the algorithm of the inverse problem, we implement the shape found analytically in Matlab. The nodes are evenly spaced: $x_i = L * \frac{i}{n-1}$ (with n=100) and the objective shape function input in the algorithm is a bare discretization of the analytical one:

$$(U_{obj})_i = w(x_i) = A_1 \sin\left(\sqrt{\frac{N}{EI}}x_i\right) + B_1 \cos\left(\sqrt{\frac{N}{EI}}x_i\right) + C_1 x_i + D_1, \text{for } i \in \left[0; \frac{n}{2}\right]$$

$$(U_{obj})_i = w(x_i) = A_2 \sin\left(\sqrt{\frac{N}{EI}}x_i\right) + B_2 \cos\left(\sqrt{\frac{N}{EI}}x_i\right) + C_2 x_i + D_2, \text{for } i \in \left[\frac{n}{2}; n\right]$$

The algorithm predicts a reasonable stiffness map for the elastic foundation Figure 132. By reasonable, we mean that away from the boundaries, the stiffness map shows a spike at L/2, just like the theoretical solution.

Though, we can observe that the magnitude of this map (i.e. spring constant) is not correct. This magnitude is not a huge problem. The problem could be scaled by the critical load.

However, some of the spring constants are negative. This is due to the fact that we did not impose the condition of the material properties to be all positive. The added constraint would have resulted in the exact stiffness map taken at the beginning.
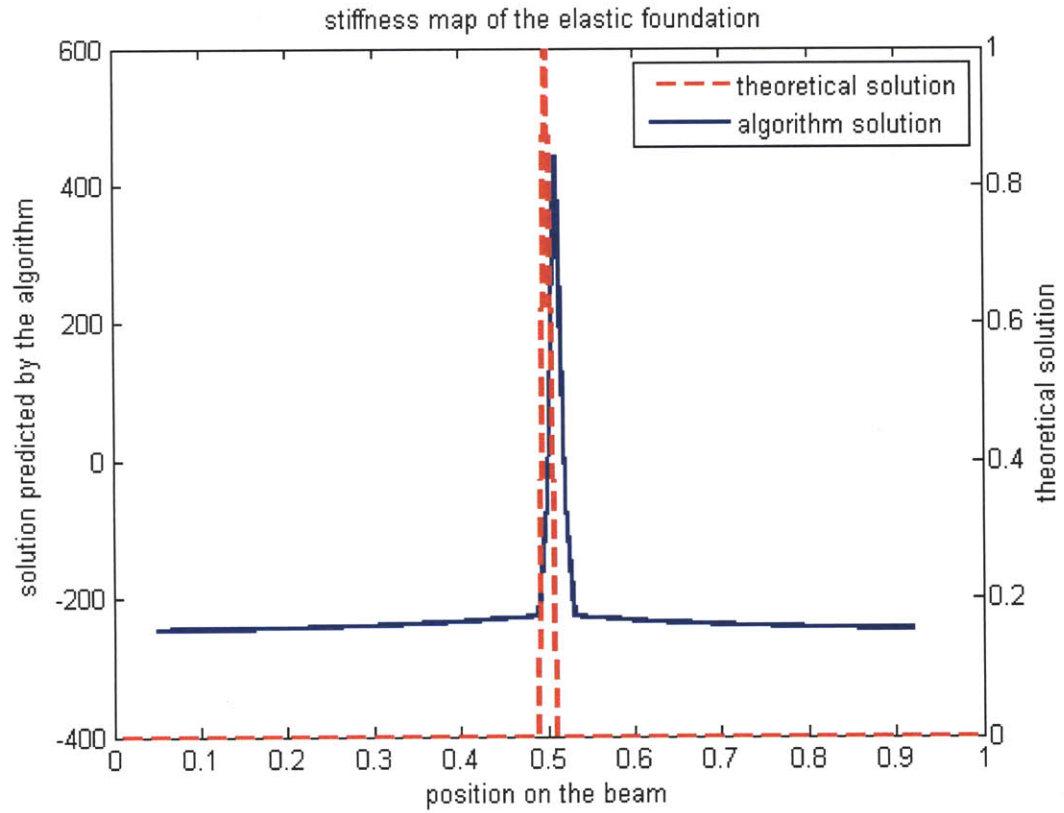
Figure 132: Stiffness map of the elastic foundation for the adapted formulation. The shape predicted by the algorithm (blue) is compared to the theoretical solution (red dashed line).

F. Conclusion

This third chapter introduces the new design paradigm: directing the buckling of a stiff coating through local and controlled alteration of the material properties of a soft substrate.

The 3D numerical simulation was tested against experimental observation by Huck et al. This simulation is solving the "direct problem", meaning predicting the shape of the buckling for material properties.

The later sections of this chapter address the "inverse problem": what should be the material properties of the substrate to obtain a desired buckling shape. This problem is very fundamental, and to the best of the author's knowledge, has not been tackled before. Considering the number of unknown parameters, we can prove that this inverse problem does not always admit a solution. As a result, we introduce a concept of residual forces along with an adapted cost function, to formulate this inverse problem as a minimization problem.

G.   Bibliography

1. **World Health Organization.** *Guideline for drinking water (3rd edition).* 2006.

2. **Robert Engelman (Population Action International).** *People in the balance- Population and Natural resources at the Turn of the Millennium.* 2000.

3. **(US), National Research Council.** *Review of the desalination and water purification technology roadmap.* s.l. : Committee to Review the Desalination and Water Purification, 2002.

4. **Cashman, Preene.** *Groundwater lowering in construction: a practical guide.* s.l. : Spon press, 2001.

5. Water Quality Association, Glossary . [Online] as of October 2009. http://www.wqa.org/.

6. **Pearce.** *When the Rivers Run Dry: Water--The Defining Crisis of the Twenty-first Century .* s.l. : Beacon Press books, 2006.

7. *Ashkelon desalination plant — A successful challenge.* **Sauvet-Goichon.** 2007, Desalination, Vol. 203, pp. 75–81.

8. *Handbook of Inorganic Chemical Compounds.* s.l. : McGraw-Hill, 2003.

9. *Enhancing RO system performance utilizing antiscalants.* **Ghafour.** 2002, Desalination, Vol. 153, pp. 149-153.

10. *Limits of RO recovery imposed by calcium phosphate precipitation.* **Greenberg.** 2005, Desalination, Vol. 183 , pp. 273–288.

11. **Dow water solution.** *Filmtech reverse osmosis membrane: Technical manual.* 2003.

12. *Engineering design of Skikda Seawater Desalination Plant, Desalination and Water Treatment.* **Fanjul.** 2009, Desalination and Water Treatment, Vol. 7, pp. 206–213.

13. *Reverse osmosis desalination: Water sources, technology, and today's challenges.* **Greenlee.** 2009, Water Research, Vol. 43, pp. 2317-2348.

14. *Second law analysis of a reverse osmosis plant in Jordan.* **Aljundi.** 2009, Desalination, Vol. 239, pp. 207-215.

15. *State of the art of reverse osmosis desalination.* **Fritzmann.** 2007, Desalination, Vol. 216, pp. 1-76.

16. *Development of the fourth generation energy recovery device. A CTO's Notebook.* **Stover.** 2004, Desalination, Vol. 165, pp. 313-321.

17. *Effect of recent technological developments on SWRO incorporated in the Red-Dead project.* **Glueckstern.** 2009, Desalination and Water treatment, Vol. 5, pp. 132-136.

18. *Hollow fine fiber vs. spiral-wound RO desalination membranes Part 2: Membrane autopsy.* **Butt.** 1997, Desalination, Vol. 109 , pp. 83-94.

19. *Modeling the impacts of feed spacer geometry on reverse osmosis and nanofiltration processes.* **Gilllen.** 2009, Chemical Engineering Journal, Vol. 149, pp. 221–231.

20. *Spiral wound modules and spacers Review and analysis.* **Ribeiro.** 2004, Journal of Membrane Science, Vol. 242, pp. 129–153.

21. *Characterization of a zigzag spacer for ultrafiltration.* **Schwinge.** 2000, Journal of Membrane Science, Vol. 172, pp. 19–31.

22. *Study of the effects of spacer geometry in membrane feed channels using three-dimensional computational flow modeling.* **Shakaib.** 2007, Journal of membrane science, Vol. 297, pp. 74-89.

23. *Biofouling of reverse osmosis membranes: Role of biofilm-enhanced osmotic pressure.* **Herzberg.** 2007, Journal of Membrane Science, Vol. 295, pp. 11–20.

24. **Dow Chemical.** *Technical manual, Form No. 609-00071-0309.*

25. **Hoff, Jacobus Henricus van 't.** *Osmotic pressure and chemical equilibrium, Nabel lecture.* 1901.

26. *A new thin-film composite seawater reverse osmosis membrane.* **Cadotte.** 32, 1980, Desalination, pp. 25-31.

27. *Development of crosslinked fully aromatic polyamide ultra-thin composite membranes for seawater desalination.* **Kurihara.** 1994, Desalination, pp. 133-144.

28. *Reformulation of the solution-diffusion theory of reverse osmosis .* **Paul.** 2004, Journal of membrane science, Vol. 241, pp. 371-389.

29. **Cadotte.** *Interfacially synthesized reverse osmosis membrane. 4,277,344* 1981.

30. *Effect of membrane chemistry and coating layer on physiochemical properties of thin film composite polyamide RO and NF membranes.* **Tang.** 2009, Desalination, Vol. 242, pp. 168-182.

31. *Impacts of support membrane structure and chemistry on polyamide-polysulfone interfacial composite membranes.* **Ghosh.** 2009, Journal of Membrane Science, Vol. 336, pp. 140-148.

32. *New membrane developments expanding the horizon for the application of reverse osmosis technology.* **Gerard.** 1998, Desalination, Vol. 119, pp. 47-55.

33. *Surface properties of Reverse Osmosis Membrane.* **Yao.** 2007, Journal of Applied polymer science, Vols. 105-3, pp. 1261 – 1266.

34. *Effect of skin layer surface on the flux behavior of RO membranes.* **Hirose.** 1996, Journal of membrane science, Vol. 121, pp. 209-215.

35. *Role of membrane surface morphology in colloidal fouling of cellulose acetate and composite aromatic polyamide reverse osmosis membranes.* **Elimelech.** 1997, Journal of membrane science, Vol. 127, pp. 101-109.

36. *Leading Edge Technology on Commercially Available Membranes vs. Innovative Membranes in the R&D Stages.* Asilomar, CA : s.n., Feb. 2009. ACS conference.

37. *The Reaction of Cellulose Acetate with Acetic Acid and Water.* **Hiller.** 1953, Journal of polymer science, Vols. 10-4, pp. 385-423.

38. *Optimization of the intermittent chlorine injection (ICI) method for seawater desalination RO plants.* **Fujiwara.** 2008, Desalination, Vol. 229, pp. 231-244.

39. *Kinetic study of the hydrolysis of cellulose acetate in the pH range of 2-10.* **Kenneth.** 1966, Journal of applied polymer science, Vol. 10, pp. 825-832.

40. **Baker.** *Membrane technology and application.* s.l. : Jahn Wiley and sons editions , 2004.

41. *Study on hypochlorite degradation of aromatic polyamide reverse osmosis membrane.* **Kang.** 2007, Journal of membrane science, Vol. 300, pp. 165-171.

42. **Zhou.** *Simulations of Polymeric Membrane Formation in 2D and 3D.* s.l. : PhD thesis at MIT , 2006.

43. *Transport properties of cellulose acetate osmotic membranes.* **Lonsdale.** 1965, Journal of applied polymer science, Vol. 9, pp. 1341-1362.

44. *Experimental study of water and salt fluxes through reverse osmosis membranes.* **Zhou.** 2005, Environment science technology, Vol. 39, pp. 3382-3387.

45. *Non-linear behavior of permeate flux in full-scale reverse osmosis process.* **Tay.** 2005, Journal of environmental engineering, pp. 1481-1487.

46. **Mudler.** chap. 4: Transport in membrane. *Basic principle of membrane technology.* s.l. : Kluwer academic publishers, 1996.

47. *Effect of porous support fabric on osmosis through a Loeb-Sourirajan type asymmetric membrane.* **Loeb.** 1997, Journal of Membrane Science, Vol. 129, pp. 243-249.

48. *Concentration polarization in ultrafiltration and reverse osmosis: a critical review.* **Sablani.** 2001, Desalination, Vol. 141, pp. 269-289.

49. *Estimation of mass transfer coefficient using a combined nonlinear membrane transport and film theory model.* **Murthy.** 1997, Desalination, Vol. 109, pp. 39-49.

50. **Mudler.** chap. 7: Polarisation phenomena and membrane fouling. *Basic principle of membrane technology.* s.l. : Kluwer academic publishers, p. 1996.

51. *Modeling concentration polarization in reverse osmosis processes.* **Kim.** 2005, Desalination, Vol. 186, pp. 111-128.

52. **Amjad.** *Reverse Osmosis; Membrane Technology, Water Chemistry and Industrial Application.* [ed.] Van Nostrand Reinhold. 1992.

53. **Costa, Da.** *Fluid flow and mass transfer in spacer-filled channels for ultrafiltration, PhD thesis.* s.l. : School of chemical engineering and industrial engineering, University of New South Wales, 1993.

54. *Fouling of reverse osmosis and ultrafiltration membranes: a critical review.* **Goosen.** 2004, Separation Science and Technology, Vol. 39 (10), pp. 2261-2298.

55. *Marine epibiosis. I.Fouling and antifouling: some basics aspects.* **Wahl.** 1989, Mar. Ecol. Prog. Ser. , Vol. 58, pp. 175-189.

56. *Boron removal from desalinated seawater and brackish water by improved electrodialysis.* **Oren.** 2006, Desalination, Vol. 199, pp. 52–54.

57. *Boron removal from seawater using FILMTECTM high rejection SWRO membranes.* **Redondo.** 2003, Desalination, Vol. 156, pp. 229-238.

58. **Miller.** *Review of Water Ressources and Desalination Technoloies.* Sandia National Laboratories. 2003.

59. *Marine epibiosis. I.Fouling and antifouling: some basics aspects.* **Wahl.** 1989, Mar. Ecol. Prog. Ser. , Vol. 58, pp. 175-189.

60. Volume 4: Marine and Industrial Biofouling. *Surface Modification Approach to Control Biofouling, Marine and Industrial Biofouling.* s.l. : Springer Series on Biofilms.

61. *Settlement of Ulva Zoospores on Patterned Fluorinated and PEGylatedMonolayer Surfaces.* 2008, Langmuir, Vol. 24, pp. 503-510.

62. *Engineered Nanoforce Gradients for Inhibition of Settlement (Attachment) of Swimming Algal Spores.* **Schumacher.** Langmuir : s.n., 2008, Vol. 24, pp. 4931-4937.

63. *Bioinspiration—the solution for biofouling control?* 2009, Bioinsp. Biomim. , Vol. 4, p. 015007.

64. *Approaches in designing non-toxic polymer surfaces to deter marine biofouling.* 2009, Soft matter, Vol. 5, pp. 4088–4100.

65. **Fleming.** Biofouling in RO systems. [book auth.] Amjad. *Reverse Osmosis. Membrane Technology Water Chemistry and Industrial Applications.* s.l. : Van Nostrand Reinhold, 1993.

66. *Bioinspiration—the solution for biofouling control?* **Ralston.** 2009, Bioinsp. Biomim., Vol. 4, pp. 1-9.

67. *A preliminary approach to epidermal antimicrobial defense in the Delphinidae.* **Meyer.** 2004, Marine Biology, Vol. 144, pp. 841–844.

68. *The influence of Natural Surface Microtopographies on Fouling.* **Bers.** 2004, Biofouling, Vol. 20, pp. 43-51.

69. *Learning from nature: Non-toxic biofouling control by.* **A. Kesel, R. Liedert.** 2007. Comparative Biochemistry and Physiology, Part A 146 ; A7–BIOMIMETICS AND BIOMECHANICS — SMART SOLUTIONS FROM NATURE. pp. S129–S141.

70. *Cells lying on a bed of microneedles: An approach to isolate mechanical force.* 4, 2003, PNAS (Proc. of Nat. Ac. of Science), Vol. 100, pp. 1484–1489.

71. *Engineering Shark skin and other solutions.* **Ball.** 1999, Nature, Vol. 400, pp. 507-509.

72. *Development and Testing of Hierarchically Wrinkled Coatings for Marine Antifouling.* **Efimenko.** 2009, Applied material and interface, Vol. 1;5, pp. 1031–1040.

73. **Wierzbicki.** *Lecture notes for the class "Plate and Shells" at MIT.* s.l. : MIT, 2009.

74. *Herringbone Buckling Patterns of Compressed Thin Films on Compliant Substrates.* **Chen.** 2004, Journal of Applied Mechanics, Vol. 71, pp. 597-603.

75. *Nonlinear analyses of wrinkles in a film bonded to a compliant substrate.* **Huang.** 2005, Journal of the Mechanics and Physics of Solids, Vol. 53, pp. 2101–2118.

76. **Dowling.** 15.10: Energy dissipation in materials. *Mechanical behavior of materials, engineering methods for deformation, fracture and fatigue.* 1999.

77. *Initiated chemical vapor deposition (iCVD) of polymeric nanocoatings.* **Gleason.** 2007, Surface & Coatings Technology, Vol. 201, pp. 9400–9405.

78. *Wrinkled surface topographies of electrospun polymer fibers.* **Wang.** 2009, Appl. Phys. Lett., Vol. 94, p. 151916.

79. *A Stretchable Form of Single-Crystal Silicon for High-Performance Electronics on Rubber Substrates.* **Khang.** 2006, science, Vol. 311.

80. *Ordering of Spontaneously Formed Buckles on Planar.* **Huck.** 2000, langmuir, Vol. 16.

81. —. **Wilhelm T. S. Huck, Ned Bowden, Patrick Onck, Thomas Pardoen, John W. Hutchinson and George M. Whitesides.** 2000, langmuir, Vol. 16, pp. 3497-3501.

82. **Anand, L.** *Mechanics of solids, Lecture notes (MIT 2.071).* 2009.

83. **Nguyen, Q.S.** *Stability and nonlinear solid mechanics.* s.l. : Wiley, 2000.

84. **R., Cook.** *Concepts and applicatoins of Finite Element Analysis, second edition.* s.l. : John Wiley, 1974.

85. **Moler, Cleve.** Eigenvalues and Singular Values. *Numerical Computing with MATLAB.* s.l. : Mathworks, 2004.

86. **Organization), UNESCO-WWAP (World Health.** *World Health Report, Water, a shared responsibility.* 2006.

87. *The search for a chlorine-resistant reverse osmosis Membrane.* **Glater.** 1994, Desalination, Vol. 95, pp. 325-345.

88. *Backwash of RO spiral wound membranes.* **Sagiv.** 2005, Desalination, Vol. 179, pp. 1-9.

89. *Overview of systems engineering approaches for a large-scale seawater desalination plant with a reverse osmosis network.* **Kim.** 2009, Desalination, Vol. 238, pp. 312-332.

90. *Pilot Tests of Multibore UF Membrane at Addur SWRO Desalination Plant, Bahrain.* **Bu-Rashid.** 2007, Desalination, Vol. 203, pp. 229–242.

91. **Wilf.** *Guidebook, membrane desalination technology, Reverse Osmosis, Nanofiltration and Hybrid Systems Process, Design, Applications and Economics .* ISBN 0-86689-065-3.

92. *UF membranes for RO desalination pretreatment.* **Wolf.** 2005, Desalination, Vol. 182 , pp. 293–300.

93. *Le dessalement des eaux par osmose inverse: l'expérience de Véolia Water.* **Gaid.** 2007, Desalination, Vol. 203, pp. 1–14.

94. *Microscopy as a tool for analysis of membrane failure and fouling.* **Roever, De.** 2007, Desalination, Vol. 207, pp. 35–44.

95. **Organization, World Health.** chap 7: Microbial aspects. *Guideline for drinking water (3rd edition),.* 2006.

96. *Pretreatment for desalination of seawater from an open intake by dual-media filtration: Pilot testing and comparison of two different media.* **Mitrouli.** 2008, Desalination, Vol. 222, pp. 24–37.

97. *Seawater filtration for fouling prevention under stormy conditions.* **Tenzer.** 1999, Desalination, Vol. 125, pp. 77-88.

98. *Performance of the Gabès desalination plant.* **Fethi.** 2001, Desalination, Vol. 136, pp. 263–272.

99. *UF/MF as RO pre-treatment: the real benefit.* **Bonnélye.** 2008, Desalination, Vol. 222, pp. 59–65.

100. *Theoretical optimization of spiral-wound and capillary nanofiltration modules.* **Meer, Van der.** 1997, Desalination, Vol. 113, pp. 129-146.

101. *Modeling concentration polarization in reverse osmosis spiral wound elements.* **Marinas.** 1996, Journal of environmental Eng. , pp. 292-298.

102. *Biofouling of spiral-wound nanofiltration and reverse osmosis membranes: A feed spacer problem.* **Vrouwenvelder.** 2009, water research, Vol. 43, pp. 583-594.

103. **Schwinge.** *Experimental & simulation studies of fluid flow in spacer-filled channels in spiral wound modules, Ph.D. Thesis.* s.l. : School of Chemical Engineering and Industrial Chemistry, University of New South Wales, 2003.

104. **GOSS, V.G.A.** *Snap buckling, writhing and loop formation in twisted rods, PhD thesis.* s.l. : Center for Nonlinear Dynamics, University College London, 2003.

105. **Millard P., Ballard A.** *Modelling of slender structures, lecture note.* Palaiseau : Ecole Polytechnique, 2008.

106. *Using Euler buckling springs for vibration isolation.* **Winterflood.** 2002, Class. Quantum Grav., Vol. 19, pp. 1639–1645.

FUTURE WORK

While we are showing a prototype and proof of concept of the patterning in the Chapter two, few steps need to be taken to make this a successful technology.

At the theoretical level, we have shown that the 3D problem of buckling was almost identical to the 1D problem. However, we did not derive any analytical expression, or write a minimization algorithm for this inverse problem in the general case. We think this step is not so far ahead of this work, and should be completed to give this new design method its full strength. It might be decomposed in two steps:

- Deriving the wrinkling of a plate on an elastic substrate is a first small, yet very important step. This case would be sufficient for the example of the patterning of membranes. Patterning the surface of substrates would be applicable not only to reverse osmosis membranes, but could serve a large variety of applications:
  - membranes: micro- and ultra-filtration membranes, used for seawater pre-treatment or in reclamation plants, might also hugely benefit from this technology since bio-foulants are of greater size and use searching mechanisms
  - coatings: coating of ship hulls with micro-patterned films to mitigate macro-fouling can also be a huge and beneficial application.
  - creating new micro-devices: we have seen how this new design paradigm could be substituted to the traditional "photolithography-etching-casting" process. From biological chips to MEMS, number of small devices could be custom-made with this method.
- Deriving the full 3D algorithm for directing buckling would be even more beneficial, to create full 3D features and control their buckling shape.

Aside from recreating the patterned surfaces that have been shown in Chapter III with the iCVD coating, three experimental questions should be addressed:

- Process optimization: The sample preparation (precision of the material treatment, uniformity of the coating thickness, uniformity of material properties, and absence of cracks...) should be better controlled. A first step could be to try and obtain very steady wrinkles in the unidirectional case.
  The second step is to optimize the control of the material properties of the substrate. The experiments prove that it was possible to treat the PDMS to have two material properties (stiff regions and compliant ones). Instead, a continuum of material properties (for instance by replacing black and white masks by grayscale photo-masks) would expand the range of "possible topography", i.e. the shape that can be created with this method. This set of "possible

topography" would also be extended by improving the "contrast" of the material properties (i.e. the gradient of material properties)

- Permeation properties of substrate: So far, our prototypes involve a dense substrate. In order to apply this technology to membrane filtration, without degrading too much the permeation properties of current membranes, we have to substitute a porous material to this dense substrate. We could potentially benefit from a gradient in porosity of the support layer to control the material properties of the substrate.

- Fouling test: We are confident that the results obtained on anti-fouling behavior of pattern membrane will hold for our sample. However, we still need to prove this on our samples. Also, we mentioned that we were expecting improvement in the prediction and understanding of fouling behavior, as more and more studies focus on bio-fouling. The design

At the conceptual level, this method of controlling the shape of an object by changing its material properties looks very promising. For instance, active materials (which can reversibly change their mechanical properties with temperature, light or magnetic and chemical signals) could be used in combination with this design method to invent structures that can change shape: from bio-chips to microfluidic devices and MEMS fabrication, numerous fields could benefit from this technology.

CONCLUSION

This work emphasizes the need for more efficient membranes for water desalination. A comprehensive review of RO plants has raised one of the keys factor in reverse osmosis: bio-fouling. Both researches on marine species and on engineered membranes suggest that chemistry and micro-topography play an important role in the deterrence of bio-fouling.

For instance, wrinkled membranes have been proven to be less affected by macro-fouling. iCVD deposition was used to create wrinkled membranes that could benefit both from a tuned topography and an optimized chemistry. The wrinkle formation was studied by comparing theory, experiments and results obtained by numerical simulation.

Going further in mimicking biological anti-fouling surfaces, we are showing a process that can be used to produce different topography, by treated substrate prior to coating. We are comparing the results of our numerical simulation and the shape obtained experimentally in a paper by Huck et al.. Then, we are setting the foundation of an inverse method to generate a "stiffness map" needed to obtain a given micro-topology. This method is based on a concept of residual forces, which we introduce and validate in a simplified model.

We conclude this work with perspectives and future works that we regard as important to make a successful technology out of this promising concept.

TABLE OF ILLUSTRATIONS

LIST OF TABLES